Linear Stability Analysis of Non-Reacting and Reacting Elliptical Jets

by

Shiling Huang

Dissertation submitted to the Faculty of the

Virginia Polytechnic Institute and State University

in partial fulfilment of the requirements for the degree of

Doctor of Philosophy

in

Mechanical Engineering

APPROVED:

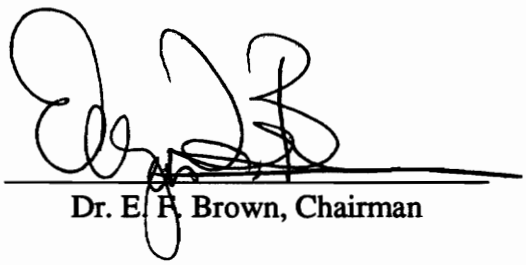

Dr. E. R. Brown, Chairman

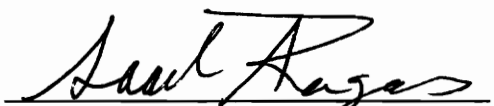

Dr. S. A. Ragab

Dr. U. Vandsburger

Dr. W. F. Ng

Dr. C. L. Dancey

April, 1994

Blacksburg, Virginia

Linear Stability Analysis of Non-Reacting and Reacting Elliptical Jets

by

Shiling Huang

Committee Chairman: Dr. E. F. Brown
Department of Mechanical Engineering

(ABSTRACT)

A spatial linear stability analysis of circular and elliptical jets has been carried out. For the circular jet, the Michalke's shooting method has been extended to the case with a swirling basic flow. For the elliptical jet, an algebraic eigenvalue problem has been formulated by applying the Chebyshev and Fourier spectral collocation method to the disturbance equations of the flow expressed in a generalized cylindrical coordinate system. The resulting algebraic eigenvalue problem was solved using the inverse power method. The approach developed is capable of handling the influences of different distributions of the momentum thickness, swirl, and heat release. In addition to studying the stability properties of the elliptical jet in comparison with those of a circular jet, the linear stability analysis has been used to obtain the insight into the entrainment process. A possible way to enhance the entrainment of elliptical jets has been suggested.

Acknowledgements

I wish to express my sincere gratitude and appreciation to my advisor Professor Eugene F. Brown for his advice, guidance, understanding, encouragement, confidence, and support. Without his help I could not have completed this research and my Ph.D. study. I would like to thank Dr. S. A. Ragab from whom I learned the linear stability analysis and with whom I had had many stimulating discussions. Thanks are also due to Dr. E. F. Brown, Dr. S. A. Ragab, Dr. U. Vandsburger, Dr. W. F. Ng and Dr. C. L. Dancey for serving as members of my advisory committee. I would also thank Dr. R. Kriz for providing numerical flow visualization facilities without which this research would not have been possible.

I wish to express my special thanks to my parents, Yanwei Huang and Qimei Wu for their full-hearted and constant support toward the completion of my higher and graduate education. I would also like to thank my wife's parents Yan Luo and Shuqin Zhang for their support.

I am indebted to my wife, Wei Luo, for the support she has given to me during my Ph.D. study. I am very grateful to the many sacrifices she made during this period.

The research described in this dissertation was sponsored by the Mechanics Division of the Office of Naval Research under Grant No. N0014-92-J-1272.

Table of Contents

Chapter 1. Introduction

1.1 Jet Flows

Jets are unbounded fluid streams which travel at higher speeds than their surroundings. Jets are found in combustors, propulsion systems, fiber fabrication and transmission systems. These are only a few of many industrial processes where an improved understanding of the characteristics of jet flow will result in improved component efficiency and reduced risk to the environment.

Let us take a special example. In the combustion chamber of most gas turbine engines fuel in the form of a gaseous jet meets with the air which surrounds it is ignited and burns. It is desirable that this process take place in as short a length as possible. This requires that the jet fuel mix with its surroundings rapidly and thoroughly. The mixing process begins with the large scale engulfment of the surrounding air by vortical structures which result from the rolling up of the shear layer at the edge of the jet. The induction of the surrounding fluid into the jet which begins here and continues downstream is called entrainment. This is often distinguished from mixing in which already entrained fluid is brought into contact with the jet on a finer scale basis and ultimately at a molecular level. Molecular level mixing is a necessary requirement for chemical reactions to occur.

The roll up process is itself preceded by exponentially growing disturbances in the streamwise direction which are driven by the so called Kelvin Helmholtz instability. This entire process which begins with the Kelvin Helmholtz instability, proceeds through vortex rollup, vortex merging, and mixing transition eventually leads to breakdown into fine scale turbulence. To this process, combustion (to the extent that the molecular mixing has occurred) must be added if improvements in the design of combustion systems is to be pursued on a rational basis.

Experiments have shown [Ho and Gutmark,1987] that jets of elliptical geometry exhibit enhanced mixing characteristics in contrast to their circular counterparts.

The purpose of this research is to investigate the early stages of the entrainment process in jet flows, to identify and investigate the origin of those features of the flow which are responsible for this increased entrainment, and in addition, to explore how these features of the flow can be manipulated, so that even higher levels of entrainment can be achieved. In particular, passive means for achieving desired effects will be sought in order to avoid complications of active control systems.

1.2 Linear Stability Analysis of Planar Shear Layers

For circular jets and planar shear layers, it has been known for many years that

linear stability analysis provides an accurate model of the early stages of the mixing process. And, in fact, depending upon the initial shear layer thickness, features of the flow field located many diameters downstream of the nozzle exit may still bear features which are reminiscent of the structures which are predicted by this technique [Brown and Roshko, 1974]. The purpose of this research is to perform a linear stability analysis of three dimensional jets, in particular elliptical jets, in which the effects of swirl and combustion are included in order to identify the phenomena which are responsible for their enhanced entrainment. This work has been regarded as complimentary to both experiments and numerical simulations which show large differences in entrainment, but little in the way of explanation for why these differences occur.

Linear stability analysis had its beginnings in the nineteenth century with the work of Rayleigh who solved a linearized form of equations of fluid flow. This has come to be known as linear stability analysis. In linear stability analysis, the flow is assumed to consist of a time independent, but spatially varying, basic flow and a spatially and temporally varying perturbation component. In the Rayleigh's work and in what is reported here, the basic flow is assumed to be parallel, that is, invariant in the streamwise direction. To investigate the stability of the basic flow, questions which govern the evolution of small perturbations to the basic flow are written. This can be done by linearizing the governing equations which describe the fluid motion. The problems in which the temporal evolution of the spatially periodic perturbations is sought are referred to as temporal stability analysis. In spatial stability analysis, the spatial evolution of

temporally periodic disturbances is sought. Both the temporal and spatial stability analysis can be carried out for a specified spatial or temporal frequency by assuming that the disturbances vary exponentially in time for temporal stability analysis and exponentially in streamwise direction for the spatial stability analysis. This is known as the normal mode assumption. Linear stability analysis then predicts the temporal and spatial scale of these disturbances. The equations which describe the behavior of the normal modes reduce to a second order differential equation called the Rayleigh's equation if viscosity is neglected, or a fourth order differential equation called the Orr-Sommerfield equation if viscosity is included. These equations are homogeneous differential equations and, along with the boundary condition which specifies the behavior of the disturbance at infinity, constitute an eigenvalue problem. The relation between the real and imaginary portion of the eigenvalue and the temporal or spatial frequency is the dispersion relation which provides the growth rate and the phase speed of the disturbance. The eigenfunction provides the spatial distribution of the disturbance.

For planar shear layers, Rayleigh [Sherman, 1990] established that the necessary condition for inviscid instability is that there exists a inflection point in the streamwise basic velocity. Later, Fjortoft [Sherman, 1990] proved a more general necessary condition for instability, i.e., $U''(U - U_s) \leq 0$ in which U_s is the basic flow velocity at an inflection point, and U'' is the second order derivative of the basic velocity across the shear layer. Howard [Sherman, 1990] found that the location of the eigenvalue satisfy a semicircle theorem which gives a range of the real and imaginary part of the complex

phase speed.

More recently, Michalke [1965] studied the temporal and spatial stability characteristics of planar shear layers. An analytical asymptotic solution was used as the boundary condition for the integration of the Rayleigh's equation using the fourth-order Runge-Kutta method from both sides of the shear layer. This integration was carried out from an initial approximation for the unknown eigenvalue. The requirement that the solution at the shear layer should match, that is, the solution and its derivative should be the same independent of whether the shear layer is approached from above or below, can be regarded as a nonlinear algebraic equation for the eigenvalue. Newton's method was used to obtain the solution of this nonlinear equation. The eigenfunction was computed using an additional integration after the eigenvalue had been obtained. This process is called the shooting method. The results showed that the shear layer was temporally unstable only in a range of spatial wave frequencies. There exist two neutral frequencies at which the growth rates of the shear layer are zero. Michalke also presented a spatial instability analysis [1966] for the planar shear layer with a similar method and obtained similar results. Streak lines were plotted which showed the initial development of vortical structures.

Recently, Grosch and Jackson [1991] studied the inviscid spatial stability characteristics of a three-dimensional mixing layers. They found that the three-

dimensional stability problem of a shear layer can be transformed to a two dimensional stability problem. A universal dispersion relation curve was found and can be used to find the growth rate of the shear layer with any other parameter.

1.3 Linear Stability Analysis of Circular Jets

The solution of the linear stability problem for a circular jet is viewed as a linear combination of an infinite number of solutions each with an eigenfunction having a periodic azimuthal dependency. The process of defining these dependencies is called mode classification. Accordingly, the solution of the mode in which the eigenfunction has the least azimuthal variation is the axisymmetrical mode or $m = 0$ mode. Batchelor and Gill [1962] analyzed the temporal stability of axisymmetrical jets with a streamwise velocity profile which was obtained by solving the Navier-Stokes equation assuming that the jet was formed due to a force at a point in the unbounded flow. Since the source of jet was assumed to be at a point, the analysis was valid only in the far field. However, they extended the necessary condition of the instability of the planar shear flow to the axisymmetrical jet flow and found a similar relationship for the range of complex phase speed similar to Howard's theorem. They also demonstrated that there is one and only one neutral disturbance wave with a non-zero wave number. Lessen and Singh [1973] found that axisymmetrical shear-layers are more stable than corresponding planar shear layers. Michalke [1981, 1984] carried out a spatial linear stability analysis of circular

jets. He used the shooting method and asymptotic solution at large and small radius expressed as the modified Bessel functions of the first and second kinds to find the pressure eigenfunction. The eigenfunctions for other variables such as velocity components were derived from this pressure eigenfunction. Various ratios of the jet radius (which is defined as the radius at the location where the basic velocity is half of that at the center line) to the jet momentum thickness, R/θ, were considered. The basic temperature and density profiles were related by the Busemann-Crocco relationship [Schlichting, 1966]. Similar to the planar shear layer, he found that the circular jet is also unstable in only a certain range of frequencies. The growth rate was larger for a larger values of R/θ. The phase speed of the axisymmetrical mode increases with decreasing R/θ. The effect of increasing the Mach number is to reduce the growth rate at higher frequencies. The growth rate at lower frequencies and the phase speed are unchanged. One reason suggested for the decreased growth rate for higher Mach numbers is that part of the disturbance energy is absorbed by compressibility of the fluid.

The effect of low levels of swirl on the temporal stability of a circular jet was investigated by Khorrami [1991] using the spectral collocation method. This resulted in an algebraic matrix equation which contained the eigenvalue as a parameter. By re-organizing the equation, the terms involving the eigenvalue were moved to the right hand side and a generalized algebraic eigenvalue problem was formulated. He used the QZ algorithm to obtain the eigenvalues and eigenfunctions of interest. The swirl was found to dramatically increase the growth rate of the mode with high azimuthal wave numbers.

The stabilizing effect of higher Mach number is greatly reduced due to the swirl. The spectral collocation method was also used by Macaraeg et al. [1989] and Khorrami [1989] to investigate the stability of the compressible circular shear layer. With the shooting method, Wu, Farokhi and Taghavi [1991] investigated theoretically and experimentally the stability of the swirling circular jet with a top-hat velocity profile and found that the higher the positive azimuthal wave number, the less spatially unstable the jet is; the higher the negative azimuthal wave number, the more spatially unstable the jet becomes.

1.4 Linear Stability Analysis of Elliptical Jets

An elliptical jet is a jet which has a constant velocity contours of elliptical cross-section. The semi-major axis is denoted by A and the semi-minor axis is denoted by B. The aspect ratio of an elliptical jet is defined as A/B. The experiments of Ho and Gutmark [1987] demonstrated that elliptical jet of aspect ratio of 2 exhibits higher level of entrainment than corresponding circular jets. The enhanced entrainment of elliptical jet has been thought to be a result of the non-symmetrical evolution of the vortical structures. Another important feature of the elliptical jet is that the entrainment is larger at the minor axis than at the major axis. Because of this, the elliptical jet becomes less elliptical until at some point in the downstream direction that the major axis becomes the minor axis and the minor axis becomes the major axis. This axis switching usually occurs

for several times before the elliptical jet becomes a circular jet in the far downstream region [Hussain, 1989]. The linear stability analysis of elliptical jet enables one to understand the early development of the vortical structures and to suggest ways of enhancing the non-uniformity. It is conjectured that this will enhance the entrainment process.

Crighton [1973] found an exact solution for an spatial and temporal stability characteristics of an elliptical jet with a top-hat velocity profile in terms of the Mathieu functions in an elliptical coordinate system. He found that increasing the aspect ratio greatly reduces the growth rate of the lateral modes, regardless of whether the disturbance grows spatially or temporally; the mode which is antisymmetrical to the major axis has the larger growth rate if its disturbances grow spatially; and the mode which is symmetric about the major axis has a smaller growth rate.

Morris and Miller [1984, 1986] also gave the solution of the stability problem of an elliptical jet with a top hat and continuous velocity profiles in terms of Mathieu's functions. Similar to Crighton, they found that for the elliptical jets of tophat velocity profile, the mode which is antisymmetrical about the minor axis has the larger growth rate. For continuous velocity profiles, they used the shooting method. They found that the minimum momentum thickness is an important factor in influencing the stability property of the elliptical jet. Unfortunately, the shear layer distribution was pre-

determined by the aspect ratio and it is impossible to change the shear layer distribution in this approach. In Morris and Miller's work, the minimum momentum thickness occurred on the major axis, thus it is not surprising that they found the pressure fluctuation are greatest on the major axis. They speculated that the roll-up would occur on the major axis, but not on the minor axis as a result of maximum disturbance amplitude on the major axis.

In order to study the stability of the elliptical jet with arbitrary momentum thickness distribution around the jet periphery, Koshigoe, Tubis and Ho [1986, 1987, 1988] developed a generalized shooting method for a jet of arbitrary shape using the Green's function method and the generalized shooting method. In the region where the basic velocity is a constant, it is possible to associate the derivative of the pressure eigenfunction to the pressure eigenfunction itself by the use of Green's function. In this way, it is no longer necessary to adopt asymptotic solutions near the center line and at a large radial coordinate. The computational effort was greatly reduced by decomposing the pressure eigenfunction into four different modes, the so called ++, +-, -+, and -- modes. Because each of these modes contains some symmetry about the major and minor axis, it is only necessary to carry out the computation in one quadrant. They postulated three criteria which they felt promoted the vortex interaction. By examining the streaklines which were generated from the eigenfunctions, they saw that the rollups on the major axis occurred further downstream than the ones on the minor axis.

For the same problem, Baty and Morris [1989] used a conformal mapping technique and wrote the stability equation in terms of the radial and azimuthal coordinates of a general orthogonal coordinate system. By using Chebyshev spectral collocation method, a set of ordinary differential equations of in terms of the radial coordinate were formulated. The resulting ordinary differential equations were then integrated from a large and small radial coordinate to the shear layer and a matching condition was applied similar to the generalized shooting method used by Koshigoe. The matching condition at the shear layer can again be viewed as a non-linear algebraic equation in terms of the eigenvalue which was solved using the Newton's method. In addition to examining the traditional dispersion relationship and the distribution of the eigenfunction, they used the result of the linear stability analysis to provide a turbulent closure scheme.

1.5 Stability of Jets with Combustion

The modeling of the combustion is a very difficult task. This is not surprising since dozens of chemical species and many more (hundreds) chain reactions are involved in a typical combustion process [Gupta, 1985]. With today's computing power, it is difficult to keep track of the variations of so many chemical species. Fortunately, if only the flow field is the main concern, one can get reasonable results by assuming that only one equivalent chemical reaction and three chemical species i.e. the fuel, the oxidizer and

the product are involved in the combustion process. In some cases, even ignoring the chemical reaction and assuming that the only effect of the combustion is heat release can give good results.

Mahalingam, et al [1989] studied the stability of a low-speed chemically reacting jet flow. The governing equations were modified using the low Mach number assumption in order to relieve the time step requirement. The basic steady flow field was obtained numerically [McMurtry, et al. 1985], and the stability analysis was carried out using the shooting method. The effect of the combustion was included through its influence on the basic flow field, and the generation of a heat source in the stability analysis. They found that the primary influence of combustion is to vary the basic flow, and its direct influence on the stability characteristics is small. The heat release makes the flow more stable. The rate at which the chemical reaction occurs does not have a significant influence on the stability.

When the amount of heat release is significant, three modes were found for a reacting circular jet by Shin and Ferziger [1991], Jackson and Grosch [1990], and Planche, at el [1992]. The explanation for the three modes was that when the amount of heat release was high, the basic temperature became high and the basic density became low at the shear layer, causing $(U'/T)'$ to have three inflection points. Here U and T denote the basic velocity and temperature in the flow. The prime denotes the spatial

derivative across the shear layer. However, in the case with no heat release, the basic density was constant for the incompressible flow, and $(U'/T)'$ had only one inflection point. The modes that correspond to the inflection points located in the lower and higher basic velocity sides were called the slow and fast mode, while the mode which corresponds to the shear layer was refereed to as the central mode. In addition to the non-premixed flame, Mahalingam, et al. [1991] examined the stability of premixed flames and found that flows are generally more stable with increased heat release. In addition, they found that the chemical reaction (that is, the change in the chemical species) is unimportant in the growth of the instability of the flow and can be ignored. This was also verified by the calculations of Mukunda and Drummond [1992].

1.6 Goal of this Research

In order to understand the features of the early development of the vortical structures which are thought to greatly influence the entrainment of elliptical jets, it is necessary to carry out a comprehensive study which considers the influence of many parameters , such as the momentum thickness and its distribution, swirl, and heat release. Linear analysis will be used as the tool and attention will therefore be focused in the near field. The questions of why elliptical jets have larger entrainment than corresponding circular jets will be answered.

First, a spatial stability analysis of a swirling circular jet will be developed. The motivation of this effort is that the swirl is one of the means to influence the jet stability properties. By introducing the swirl, it is possible to enhance some particular modes. This work provides a starting point for solution of the elliptical jet problem.

Using linear stability analysis, a parametric study of elliptical jet flows will then be developed. Influence of swirl, momentum thickness and its distribution, and aspect ratio will be considered for different modes. The effect of heat release, activation energy and chemical reaction rate will also be examined. To illustrate the formation of flow structures of the jet flow, various flow visualizations will be performed. Comparing the features of a circular and elliptical jet in a consistent fashion will be presented and a passive means for increasing the entrainment of elliptical jets will be suggested on the basis of the parameters explored.

Chapter 2. Stability Analysis of the Circular Jet

2.1 Introduction

In order to compare the results of the stability analysis of elliptical jets with those of circular jets, a stability analysis of circular jets was first carried out. Khorrami et al. [1991] carried out a temporal stability analysis of a swirling circular jet with continuous basic streamwise velocity, and a spatial stability analysis of a swirling circular jet with a top hat basic streamwise velocity profile. In this chapter, the spatial stability analysis of the circular jet with a continuous basic velocity profile and a swirl will be given. Specifically, the purpose of doing the stability analysis of a circular jet is:

1. to analyze the influence of the swirl on the spatial stability characteristics of the circular jet for a continuous basic velocity profile; and

2. to give a convenient tool for the stability analysis of the circular jet which can be used to verify the stability analysis code for the elliptical jet, and to provide an initial solution of the elliptical jet eigenvalue problem.

2.2 Formulation of Eigenvalue Problem

Following the approaches of many investigators, the dissipative effects such as viscosity and diffusivity will be neglected. Assuming that the flow is inviscid and incompressible, Euler's equations can be expressed in the circular cylindrical coordinate system as follows:

$$\frac{\partial v_r}{\partial t} + v_r\frac{\partial v_r}{\partial r} + v_\theta\frac{\partial v_r}{r\partial\theta} + v_z\frac{\partial v_r}{\partial z} - \frac{v_\theta^2}{r} = -\frac{\partial p}{\partial r} \tag{2.1}$$

$$\frac{\partial v_\theta}{\partial t} + v_r\frac{\partial v_\theta}{\partial r} + v_\theta\frac{\partial v_\theta}{r\partial\theta} + v_z\frac{\partial v_\theta}{\partial z} + \frac{v_\theta v_r}{r} = -\frac{\partial p}{r\partial\theta} \tag{2.2}$$

$$\frac{\partial v_z}{\partial t} + v_r\frac{\partial v_z}{\partial r} + v_\theta\frac{\partial v_z}{r\partial\theta} + v_z\frac{\partial v_z}{\partial z} = -\frac{\partial p}{r\partial z} \tag{2.3}$$

$$\frac{1}{r}\frac{\partial(rv_r)}{\partial r} + \frac{1}{r}\frac{\partial v_\theta}{\partial\theta} + \frac{\partial v_z}{\partial z} = 0 \tag{2.4}$$

where r, θ and z are the circular cylindrical coordinates in the radial, azimuthal and streamwise direction; v_r, v_θ and v_z are the three velocity components in these three directions, respectively. In Equations (2.1)-(2.4), all the lengths are non-dimensionalized by R, the jet radius, which is defined as the radial coordinate of the location where the basic streamwise velocity is half of the center line basic streamwise velocity U_0; all the velocity components are non-dimensionalized by the basic streamwise velocity at the center line; and the pressure is non-dimensionalized by ρU_0^2.

The velocity and pressure can be assumed to consist of the basic steady part and the disturbance part as

$$v_r = U_r + u_r' \tag{2.5}$$

$$v_\theta = U_\theta + u_\theta' \tag{2.6}$$

$$v_z = U_z + u_z' \tag{2.7}$$

$$p = \bar{p} + p' \tag{2.8}$$

where U_r, U_θ, U_z and $\bar{p}$ are the basic velocity components and the basic pressure. The quantities with a prime are the disturbance quantities. In this chapter, only the following basic parallel velocity profile will be considered:

$$U_r = 0 \tag{2.9}$$

$$U_\theta = U_\theta(r) \tag{2.10}$$

$$U_z = U_z(r) \tag{2.11}$$

That means the radial basic velocity component will be assumed to be zero which is consistent with the parallel jet assumption which requires that the basic flow is independent of the streamwise coordinate. The basic azimuthal and basic streamwise velocities are all assumed to be functions of r, the radial coordinate.

By substituting the expressions of the basic velocity components into Equations (2.1) - (2.4), the equations of the basic velocity and presure can be obtained:

$$-\frac{U_\theta^2(r)}{r} = \frac{\partial \bar{p}}{\partial r} \tag{2.12}$$

$$0 = -\frac{\partial \bar{p}}{r\partial\theta} \tag{2.13}$$

$$0 = -\frac{\partial \bar{p}}{\partial z} \tag{2.14}$$

Under the assumption of the above basic velocity profiles, the basic pressure is not a constant, but a function of r. However, if the magnitude of the azimuthal basic velocity is small, the variation of the basic pressure with r is small and the basic pressure can be regarded as constant.

Now substitute Equations (2.5)-(2.8) into Equations (2.1)-(2.4), subtracting the Equations for the basic flow (2.12)-(2.14), and neglecting the quadratic and higher order terms, Euler's equations are reduced to the following linearized form for the disturbance quantities:

$$\frac{\partial u_r'}{\partial t} + U_\theta(r)\frac{\partial u_r'}{r\partial\theta} + U_z(r)\frac{\partial u_r'}{\partial z} - \frac{2U_\theta(r)u_\theta'}{r} = -\frac{\partial p'}{\partial r} \tag{2.15}$$

$$\frac{\partial u_\theta'}{\partial t} + u_r' \frac{dU_\theta(r)}{dr} + U_\theta(r)\frac{\partial u_\theta'}{r\partial\theta} + U_z(r)\frac{\partial u_\theta'}{\partial z} + \frac{U_\theta(r)u_r'}{r} = -\frac{\partial p'}{r\partial\theta} \tag{2.16}$$

$$\frac{\partial u_z'}{\partial t} + u_r' \frac{dU_z(r)}{dr} + U_\theta(r)\frac{\partial u_z'}{r\partial\theta} + U_z(r)\frac{\partial u_z'}{\partial z} = -\frac{\partial p'}{r\partial z} \tag{2.17}$$

$$\frac{u_r'}{r} + \frac{\partial u_r'}{\partial r} + \frac{1}{r}\frac{\partial u_\theta'}{\partial\theta} + \frac{\partial u_z'}{\partial z} = 0 \tag{2.18}$$

Now substituting the normal mode representation of the disturbance quantities

$$u_r' = u_r(r)e^{i(\alpha z + m\theta - \omega t)} \tag{2.19}$$

$$u_\theta' = u_\theta(r)e^{i(\alpha z + m\theta - \omega t)} \tag{2.20}$$

$$u_z' = u_z(r)e^{i(\alpha z + m\theta - \omega t)} \tag{2.21}$$

$$p' = p(r)e^{i(\alpha z + m\theta - \omega t)} \tag{2.22}$$

into the equations for the velocity and pressure disturbances (2.15) - (2.18), we can get the equations for the disturbance eigenfunctions u_r, u_θ, u_z and p:

$$u_r W(r)\, i - \frac{2U_\theta(r)}{r}u_\theta = -\frac{dp}{dr} \tag{2.23}$$

$$u_r\left(\frac{dU_\theta(r)}{dr} + \frac{U_\theta(r)}{r}\right) + u_\theta W(r)\, i = -\frac{p}{r}im \tag{2.24}$$

$$u_r \frac{dU_z(r)}{dr} + u_z W(r) i = -pi\alpha \tag{2.25}$$

$$\frac{u_r}{r} + \frac{du_r}{dr} + \frac{1}{r} u_\theta im + u_\theta i\alpha = 0 \tag{2.26}$$

In Equations (2.19)-(2.22), α is the complex wave number. The negative of the imaginary part, $-\alpha_i$ is called the growth rate. Growth rate is the exponential rate with which the disturbances growth in the streamwise direction. The temporal frequency of the disturbance for the particular mode considered is ω which is a real number. $c_{ph} = \omega/\alpha_r$ is called the phase speed which is a measure of how fast the disturbances travel in the streamwise direction and m is the azimuthal wave number. In Equations (2.23)-(2.26), u_r, u_θ, u_z and p are the eigenfunctions of the velocity and pressure disturbances. The eigenfunctions of the disturbances represent the spatial distribution of the disturbance. The task of the linear stability analysis is to find the growth rate, phase speed and the eigenfunctions of the disturbances for a given azimuthal mode at a specified frequency. As has been mentioned in the first chapter, the relationship of the growth rate and phase speed with the frequency is the dispersion relationship. The dispersion relationship and the distribution of the eigenfunction combined determine the stability characteristics of the jet flow. In Equations (2.23)-(2.25), W is defined as:

$$W(r) = -\omega + \frac{U_\theta(r)m}{r} + U_z(r)\alpha \tag{2.27}$$

From Equations (2.23)-(2.26), we can eliminate u_r, u_θ, u_z in favor of p to get a

single second order ordinary differential equation for the pressure disturbance eigenfunction:

$$\frac{d^2p}{dr^2} + C_1\frac{dp}{dr} + C_2 p = 0 \tag{2.28}$$

where

$$C_1 = \frac{1}{r} + \frac{1}{W(r)}\frac{dW(r)}{dr} - \frac{1}{L(r)}\frac{dL(r)}{dr} + \frac{2m}{r^2}\frac{U_\theta(r)}{W(r)} - \frac{m}{r^2 W(r)}U_\theta(r) - \frac{m}{rW(r)}\frac{dU_\theta(r)}{dr} - \frac{\alpha}{W(r)}\frac{dU_z(r)}{dr} \tag{2.29}$$

$$C_2 = \frac{2mU_\theta(r)}{r^3 W(r)} + \frac{2m}{W(r)r^2}\frac{dU_\theta(r)}{dr} - \frac{4mU_\theta(r)}{r^3 W(r)} - \frac{2mU_\theta(r)}{r^2 W(r)L(r)}\frac{dL(r)}{dr} - \frac{m^2}{r^2} - \frac{2m\alpha U_\theta(r)}{r^2 W(r)^2}\frac{dU_z(r)}{dr} + \frac{\alpha^2 L(r)}{W(r)^2} \tag{2.30}$$

$$L(r) = -W(r)^2 + \left(\frac{dU_\theta(r)}{dr} + \frac{U_\theta(r)}{r}\right)\frac{2U_\theta(r)}{r} \tag{2.31}$$

with the following boundary condition:

$$r \to 0: \qquad p = \text{finite} \tag{2.32}$$

$$r \to \infty: \qquad p = 0 \tag{2.33}$$

Equations (2.28) can be regarded as a generalization of the Rayleigh's equation which includes the presence of the swirl.

2.3 Solution of the Eigenvalue Problem

The solution of the eigenvalue problem represented by Equation (2.28) is difficult because of the boundary conditions, Equations (2.32)-(2.33). Fortunately, it can be noticed that as $r \to 0$ and ∞, Equation (2.28) becomes a modified Bessel equation:

$$\xi^2 \frac{d^2 p}{d\xi^2} + \xi \frac{dp}{d\xi} + p\,(-\xi^2 - m^2) = 0 \qquad (2.34)$$

$$r \to 0$$

$$\xi = \frac{\alpha}{W(0)} \sqrt{-L(0)}\, r \qquad (2.35)$$

$$\eta^2 \frac{d^2 p}{d\eta^2} + \eta \frac{dp}{d\eta} + p\,(-\eta^2 - m^2) = 0 \qquad (2.36)$$

$$r \to \infty$$

$$\eta = \frac{\alpha}{W(\infty)} \sqrt{-L(\infty)}\, r \qquad (2.37)$$

Therefore it is possible to use the solutions of the modified Bessel equations as the boundary conditions. The boundary condition should satisfy the requirement that the disturbance should be finite at the jet center line and disappear at the infinity. This requirement is equivalent to the requirement that the pressure eigenfunction should be finite at the jet center line and disappear at the infinity. The modified Bessel equation has two particular solutions, I_m and K_m. The general solution of the modified Bessel equation

is a linear combination of these two particular solutions. Since I_m is finite at the jet center line and infinite at the infinity, I_m should have no contribution to the asymptotic solution of Equation (2.28) at a large radius. In the same way, since K_m is infinite at the jet center line and finite at the infinity, K_m should have no contribution to the asymptotic solution of Equation (2.28) at a small radius. So the boundary conditions which Equation (2.28) should satisfy are:

$$r \to 0: \qquad p = I_m(\xi) = I_m\left(\frac{\alpha}{W(0)}\sqrt{-L(0)}\, r\right) \tag{2.38}$$

$$r \to \infty: \qquad p = K_m(\eta) = K_m\left(\frac{\alpha}{W(\infty)}\sqrt{-L(\infty)}\, r\right) \tag{2.39}$$

In the actual solution of the eigenvalue problem the asymptotic solutions are used at a small non-zero radius R_1 and large finite radius R_2. This is a good approximation since at these locations the variation of the basic velocity profiles with the radius is extremely small. The adaptive-step-size Runge-Kutta method is used to integrate Equation (2.28). The intergration was carried out in two regions, one which starts at R_1 near the center line moves outward, and the other which starts at a large radius and moves inward. Because the pressure eigenfunction must be continuous and smooth everywhere, p must satisfy the following compatibility condition at the jet radius R:

$$F(\alpha) = p_2(R)\frac{dp_1(R)}{dr} - p_1(R)\frac{dp_2(R)}{dr} = 0 \tag{2.40}$$

where p_1 and p_2 are the pressure eigenfunctions at the jet radius which are obtained

from these integrations. In Equation (2.40), $F(\alpha)$ can be regarded as a non-linear function of complex variable α which is the eigenvalue. Equation (2.40) is solved using the Newton's method. The process proceeds as follows:

1. give an initial guess for α for a specified value of ω and m;

2. integrate Equation (2.28) from R_1 to R to get $p_1(R)$ and $\frac{dp_1(R)}{dr}$;

3. integrate Equation (2.28) again from R_2 to R using a negative step to obtain $p_2(R)$ and $\frac{dp_2(R)}{dr}$;

4. evaluate $F(\alpha)$ using Equation (2.40);

5. if $F(\alpha)$ is close to 0, the guessed α is the correct eigenvalue, then compute the eigenfunction and end the solution process;

6. if $F(\alpha)$ is not close to 0, update α according to

$$\alpha_{new} = \alpha_{guess} - \frac{F(\alpha_{guess})}{F'(\alpha_{guess})}$$

and proceed to step 2.

After the eigenvalue α and the pressure eigenfunction p are obtained, the eigenfunctions of the other variables can be found by using the following equations:

$$u_r = -\frac{dp}{dr}\frac{W(r)}{L(r)}i - \frac{p}{r^2}\frac{2imU_\theta(r)}{L(r)} \tag{2.41}$$

$$u_\theta = \frac{p}{r}\frac{mW(r)}{L(r)} + \frac{dp}{dr}\left(r\frac{dU_\theta(r)}{dr} + U_\theta(r)\right)\frac{1}{rL(r)} \tag{2.42}$$

$$u_z = \frac{dp}{dr}\frac{1}{L(r)}\frac{dU_z(r)}{dr} + p\left[\frac{2mU_\theta(r)}{r^2L(r)W(r)}\frac{dU_z(r)}{dr} - \frac{\alpha}{W(r)}\right] \tag{2.43}$$

The total vorticity can be found by using

$$\Gamma_r = \varepsilon\left(\frac{1}{r}u_z(r)im - u_\theta(r)i\alpha\right)e^{i(\alpha z+m\theta-\omega t)} \tag{2.44}$$

$$\Gamma_z = \frac{dU_\theta(r)}{dr} + \frac{U_\theta(r)}{r} + \varepsilon\left(\frac{du_\theta}{dr} - \frac{1}{r}u_r im + \frac{u_\theta}{r}\right)e^{i(\alpha z+m\theta-\omega t)} \tag{2.45}$$

$$\Gamma_\theta = -\frac{dU_z(r)}{dr} + \varepsilon\left(u_r i\alpha - \frac{du_z}{dr}\right)e^{i(\alpha z+m\theta-\omega t)} \tag{2.46}$$

where ε is a constant that represent the level of disturbances at z=0.

2.4 Validation of Code

The code verification is carried out for the growth rate and the phase speed of m=0 mode and m=1 mode of a circular jet using Michalke's second basic streamwise velocity profile:

$$U_z(r) = 0.5\left\{1 + \tanh\left[\frac{1}{4}\frac{R}{\theta}\left(\frac{R}{r} - \frac{r}{R}\right)\right]\right\} \tag{2.47}$$

where R is the jet radius; θ is the momentum thickness.

For $R/\theta = 10$, the growth rates of the $m = 0$ and $m = 1$ modes from the code developed by the author are given in Figure 2.1. Also shown in the figure are Michalke's growth rates which was read from the figures in Michalke's paper. From Figure 2.1, excellent agreement between the present calculations and Michalke's results is evident.

2.5 Effects of Swirl

For the non-swirling circular jet, Michalke, among others, demonstrated that the stability is strongly influenced by the momentum thickness. Other parameters which influence the the flow include the form of the basic streamwise velocity. In addition, the swirl also changes the stability characteristics of the jet. In the following, the influence of the swirl on the stability properties of an incompressible inviscid circular jet with Michalke's second basic streamwise velocity, Equation 2.47, will be investigated. The

basic azimuthal velocity used in this investigation is:

$$U_\theta(r) = \frac{\Gamma}{2\pi r}\left[1 - e^{-r^2}\right] \tag{2.48}$$

where Γ is a parameter with which the maximum basic azimuthal velocity can be varied. In the calculations described here, the maximum basic azimuthal velocity was set to 6% of the maximum basic streamwise velocity.

Figure 2.2 shows the basic streamwise velocity as a function of radial coordinate for $R/\theta = 10$. Figure 2.3 shows basic azimuthal velocity for the same momentum thickness.

Let us first look at the results of the stability analysis for the fundamental mode ($m = 0$). Figure 2.4 and 2.5 show the scaled non-dimensionalized growth rates $-\alpha_i\theta$ and phase speeds $\frac{c_{ph}}{U_z(0)}$ against the scaled non-dimensionalized frequency $\frac{\omega\theta}{U_z(0)}$ for the cases in which the swirl is zero and 6%. It is easy to see that the curves which corresponds to the $m = 0$ mode of the circular jet with no swirl and 6% swirl are almost identical. So, the dispersion relationship of this mode is independent of the basic azimuthal velocity. In addition to the dispersion relationship, we can also look at the distribution of the eigenfunction. Figure 2.6 shows that the streamwise velocity eigenfunctions are also the same for the cases with and without the swirl. However, that the dispersion relationships and the eigenfunctions are the same for the $m = 0$ mode

whether or not there is a swirling basic velocity does not mean that the flows with no swirl and the 6% swirl are the same. This is because the basic flows are different. Similar results have also be obtained by Khorrami [1991] although he used different basic streamwise and azimuthal velocity profiles.

Next, let us examine the behavior of the first azimuthal mode ($m = 1$). Figures 2.7 and 2.8 are the plots of the nondimensional growth rates and phase speeds for $m = 1$ mode of the circular jet with and without swirl against the nondimensional frequency. We can immediately see that in the high frequency region, the growth rate of the $m = 1$ modes are almost the same, while in the low frequency region the growth rate of the $m = 1$ mode was reduced by the swirl. For this mode, the swirl increased the phase speed as is shown in Figure 2.8. That means the disturbances of the swirling first azimuthal mode travel faster in the presence of swirl.

That the growth rate of the $m = 1$ mode of the circular jet with swirl is smaller than that without swirl is a result of the azimuthal directions of the swirl and the disturbance propagation being the same. Here the direction of the disturbance propagation is determined by the sign of m, the azimuthal wave number. When m is positive, the disturbances travel in the same azimuthal direction of the swirl. If the jet flows out of the paper, the disturbances of the positive mode travel in the counterclockwise direction.

Even though the dispersion relationship of the $m = 1$ mode is altered by the addition of the basic azimuthal velocity, the streamwise velocity eigenfunction is not changed. This can be seen clearly in Figure 2.9 in which these eigenfunctions are compared.

From Figures 2.10 and 2.11 in which the growth rates and phase speeds of the $m = -1$ modes are shown for both the non-swirling and swirling circular jet, we see that the result of $m = -1$ mode is opposite to the result of $m = 1$ mode. That is, the growth rate in the high frequency region is not changed by the swirl and the growth rate in the low frequency region is increased by the swirl. This increase in growth rate can be explained by the azimuthal direction of the disturbance being opposite to that of the swirl. Contrary to the $m = 1$ mode, the phase speed of the $m = -1$ mode was decreased by the swirl. Finally, we can again look at the streamwise velocity eigenfunction of the $m = -1$ mode plotted in Figure 2.12. Similar to the $m = 1$ mode, the eigenfunctions of the $m = -1$ were almost unchanged by the swirl.

In summary, we have seen that the swirl does not change the stability properties of the $m = 0$ mode. The influence of the swirl of the first azimuthal modes is on the growth rate and phase speeds. The eigenfunctions distribution was the same regardless if there is a basic swirling velocity. Therefore, the swirl does not change the flow structures of the circular jet.

Chapter 3. Stability Analysis of Elliptical Jets

3.1 Introduction

In this chapter the approach used in the linear stability problem of elliptical reacting jet will be described. It is assumed that the stability properties of the jet are non-dissipative, which means that the viscosity, conductivity, diffusion, etc., only influence the basic flow and therefore not included in the stability analysis

To simplify the analysis, it is assumed that the only effect of combustion is heat release and that the combustion can be modeled by an equivalent global, three species, single step finite rate Arrhenius chemical reaction, i.e.:

$$\nu_1[F] + \nu_2[O] \rightarrow \nu_3[P] \tag{3.1}$$

where [F], [O] and [P] represent the three species, i.e., the fuel, oxidizer and the product of the chemical reaction and ν_1, ν_2 and ν_3 are the stoichmetric coefficient of these species. In addition to the above assumptions, the mass fractions of the species are assumed to be steady. This is because the primary interest of this research is the examination of the flow field, rather than the variations of the chemical species. These assumptions about the combustion process in the flow are justified by Mahalingam, et al. [1989] in their stability analysis of a circular jet.

Because of the presence of swirl, the partial differential equations of the disturbance can no longer be reduced to an ordinary differential equation as Koshigoe [1986, 1987], Morris [1988] and Baty [1989] did. Therefore, it is necessary to handle the continuity, momentum and energy equations and the equation of state at the same time. Also because of the swirl, some of the symmetry properties of the elliptical jet no longer exist. So, it is impossible to use the pressure eigenfunction based mode classification schemes which Crighton [1973], Morris [1988] and Koshigoe [1986,1987] have used.

In the current work, a matrix method was used to obtained the solution of the stability problem. To simplify the analysis and reduce the resolution requirements, the linear stability analysis was performed in a generalized non-orthogonal cylindrical coordinate system. This is because the basic streamwise velocity can be assumed to be constant on lines of constant radial coordinate, so that fewer grid points are needed in the azimuthal direction. The governing equations for the disturbance eigenfunctions are then discretized using the Chebyshev spectral collocation method in the radial direction and Fourier spectral collocation method in the azimuthal direction. The resulting governing equations, together with the boundary conditions, constitute an algebraic eigenvalue problem which was solved using the inverse power method. The search for the eigensolution of an elliptical jet with a specified aspect ratio is started with the solution of the eigenvalue problem of a circular jet which is obtained using the method described in the last chapter and the aspect ratio was progressively increased until the required value was reached. Although the matrix method has the disadvantage of requiring a large

amount of memory, it requires no asymptotic solutions and therefore can be used for a greater range of problems.

3.2 Generalized Cylindrical Coordinate System

The coordinate system is important because the linear stability analysis of the elliptical jet will be greatly simplified if it is properly defined. In this work, a non-orthogonal elliptical coordinate system will be used. This coordinate system is used to overcome the difficulties present in the standard elliptical coordinate system which Morris [1986] used to carry out the linear stability analysis for an elliptical jet. These difficulties are: (1). It is impossible to distribute the momentum thickness around the jet periphery such that the momentum thickness is smaller on the minor axis than on the major axis because of the particular elliptical coordinate system used. This is a major disadvantage for linear stability analysis of elliptical jets, because Hussain [1989], Ho and Gutmark [1987] have demonstrated that a naturally formed elliptical jet has a minimum momentum thickness on the minor axis and maximum momentum thickness on the major axis. (2). The jet center line maps to a planar surface which is difficult for basic swirl to be defined. By using the non-orthogonal elliptical coordinate system, this problem can be avoided.

Even though Baty and Morris [1989] overcame the difficulties of the standard

orthogonal elliptical coordinate system by numerically generating an orthogonal elliptical coordinate system by using a conformal mapping technique, this approach was not used here because it is unnecessarilly complicated for an elliptical jet of moderate aspect ratio. In fact, for high aspect ratio jets both the non-orthogonal coordinate system used here and Baty's method have difficulties, because in the minor axis (present method) and major axis (Baty's method) regions the resolution may be insufficient.

The other advantage of using this non-orthogonal coordinate system is that the influence of variable jet geometries, such as the aspect ratio, momentum thickness, and momentum thickness distribution, can be easily taken into account by adjusting the parameters which define the coordinate system. Since the non-orthogonal elliptical coordinate system is a special case of the generalized cylindrical coordinate system, the generalized cylindrical coordinate system will be described first. Then a special form of the generalized cylindrical coordinate system will be given to accommodate the elliptical jet requirements. By giving other special forms to this generalized cylindrical coordinate system, it is also possible to carry out the linear stability analysis of jet with arbitrary cross-sectional shape if it is symmetrical about the major and minor axis, such as a rectangular jet.

As a first step the governing equations will be written in the generalized cylindrical coordinate system. These equations will be derived and the associated metric tensor and

Christoffel symbol will be identified. In addition, an approach will be described to adjust the parameters in the definition of the generalized coordinate system to properly distribute the momentum thickness around the periphery of an elliptical jet with a specified aspect ratio.

The generalized cylindrical coordinate system used is defined as follows:

$$x = \bar{x}^1 = x(x^1, x^2) = x(\mu, \theta) \tag{3.2}$$

$$y = \bar{x}^2 = y(x^1, x^2) = y(\mu, \theta) \tag{3.3}$$

$$z = \bar{x}^3 = z \tag{3.4}$$

where x, y and z are Cartesian coordinates which are denoted as $\bar{x}^1$, $\bar{x}^2$ and $\bar{x}^3$, respectively; x^1, x^2 and x^3 are the generalized cylindrical coordinates which will also be denoted by μ, θ and z, respectively.

The covariant metric tensor of this generalized coordinate system can be determined by

$$g_{ij} = \frac{\partial \bar{x}^k}{\partial x^i} \frac{\partial \bar{x}^l}{\partial x^j} \bar{g}_{kl} \tag{3.5}$$

The contravariant metric tensor can be obtained from the covariant metric tensor as follows:

$$\left[g^{ij}\right] = \left[g_{ij}\right]^{-1} = \frac{1}{g_{11}g_{22} - g_{12}^2}\begin{bmatrix} g_{22} & -g_{12} & 0 \\ -g_{12} & g_{11} & 0 \\ 0 & 0 & g_{11}g_{22} - g_{12}^2 \end{bmatrix} \tag{3.6}$$

Once the metric tensor is known, the Christoffel symbol can be determined from

$$\Gamma_{ij}^{k} = g^{kl}\frac{1}{2}\left[\frac{\partial g_{il}}{\partial x^{j}} + \frac{\partial g_{jl}}{\partial x^{i}} - \frac{\partial g_{ij}}{\partial x^{l}}\right] \tag{3.7}$$

One of the useful properties of the metric tensor and the Christoffel symbol is that they are symmetric about the covariant indices, i.e.

$$g_{ij} = g_{ji} \tag{3.8}$$

$$g^{ij} = g^{ji} \tag{3.9}$$

and

$$\Gamma_{ij}^{k} = \Gamma_{ji}^{k} \tag{3.10}$$

Since the third component of the generalized cylindrical coordinate system is a linear coordinate, many components of the metric tensor and Christoffel symbol are zero. The non-zero components of these quantities are listed in the following:

$$g_{11} = \left[\frac{\partial x}{\partial \mu}\right]^2 + \left[\frac{\partial y}{\partial \mu}\right]^2 \tag{3.11}$$

$$g_{12} = g_{21} = \frac{\partial x}{\partial \mu}\frac{\partial x}{\partial \theta} + \frac{\partial y}{\partial \mu}\frac{\partial y}{\partial \theta} \tag{3.12}$$

$$g_{22} = \left[\frac{\partial x}{\partial \theta}\right]^2 + \left[\frac{\partial y}{\partial \theta}\right]^2 \tag{3.13}$$

$$g^{11} = \frac{\left[\frac{\partial x}{\partial \theta}\right]^2 + \left[\frac{\partial y}{\partial \theta}\right]^2}{\left[\frac{\partial x}{\partial \mu}\frac{\partial y}{\partial \theta} - \frac{\partial x}{\partial \theta}\frac{\partial y}{\partial \mu}\right]^2} \tag{3.14}$$

$$g^{12} = g^{21} = -\frac{\frac{\partial x}{\partial \mu}\frac{\partial x}{\partial \theta} + \frac{\partial y}{\partial \mu}\frac{\partial y}{\partial \theta}}{\left[\frac{\partial x}{\partial \mu}\frac{\partial y}{\partial \theta} - \frac{\partial x}{\partial \theta}\frac{\partial y}{\partial \mu}\right]^2} \tag{3.15}$$

$$g^{22} = \frac{\left[\frac{\partial x}{\partial \mu}\right]^2 + \left[\frac{\partial y}{\partial \mu}\right]^2}{\left[\frac{\partial x}{\partial \mu}\frac{\partial y}{\partial \theta} - \frac{\partial x}{\partial \theta}\frac{\partial y}{\partial \mu}\right]^2} \tag{3.16}$$

$$\Gamma^1_{11} = \frac{1}{2}\left[g^{11}\frac{\partial g_{11}}{\partial x^1} + 2g^{12}\frac{\partial g_{12}}{\partial x^1} - g^{12}\frac{\partial g_{11}}{\partial x^2}\right] \tag{3.17}$$

$$\Gamma^1_{12} = \frac{1}{2}\left[g^{11}\frac{\partial g_{11}}{\partial x^2} + g^{12}\frac{\partial g_{22}}{\partial x^1}\right] \tag{3.18}$$

$$\Gamma_{12}^{1} = \frac{1}{2}\left[g^{11}\frac{\partial g_{12}}{\partial x^2} + 2g^{12}\frac{\partial g_{22}}{\partial x^2} - g^{11}\frac{\partial g_{22}}{\partial x^1} \right] \tag{3.19}$$

$$\Gamma_{11}^{2} = \frac{1}{2}\left[g^{12}\frac{\partial g_{11}}{\partial x^1} + 2g^{22}\frac{\partial g_{12}}{\partial x^1} - g^{22}\frac{\partial g_{11}}{\partial x^2} \right] \tag{3.20}$$

$$\Gamma_{12}^{2} = \frac{1}{2}\left[g^{12}\frac{\partial g_{11}}{\partial x^2} + g^{22}\frac{\partial g_{22}}{\partial x^1} \right] \tag{3.21}$$

$$\Gamma_{22}^{2} = \frac{1}{2}\left[2g^{12}\frac{\partial g_{12}}{\partial x^2} + g^{22}\frac{\partial g_{22}}{\partial x^2} - g^{12}\frac{\partial g_{22}}{\partial x^1} \right] \tag{3.22}$$

Up to this point, the definition of the generalized coordinate can be applied in the stability analysis of the jets of any cross sectional shape if they are symmetrical about both the x and y axis of the Cartesian coordinate system.

For the elliptical jet, it is necessary to use a special form of the generalized coordinate system. In the following calculations a non-orthogonal elliptical coordinate system which is used is defined by:

$$x = \left\{ a\mu - k_1\left[\tanh(c_1(\mu - 1)) + 1 \right] + e \right\}\cos\theta \tag{3.23}$$

$$y = b\mu \sin\theta \tag{3.24}$$

where parameters a, b, k_1, c_1, and e are are adjusted so that the lines of constant μ are

ellipses of the desired aspect ratio and so that the desired momentum thicknesses on the x axis (which is regarded as the major axis) and y axis (which is regarded as the minor axis) are produced. This is necessary because in order to use fewer grid points in the azimuthal direction, it is better to assign equal basic streamwise velocity on the ellipses on which the generalized radial coordinate μ is a constant. In this chapter, all the lengths are non-dimensionalized by the equivalent jet radius which is defined as the square root of the product of the semi-lengths of major and minor axes. The result is that the cross-sectional area of the jet is π. To determine the desired parameters in the definition of the generalized cylindrical coordinate system, the following conditions must be met:

1. the area within $\mu \leq 1$ must be π; This requires that all jets have the same flow area;
2. the aspect ratio (which is the ratio of the major axis to the minor axis when μ is unity) is at the given value AR;
3. the physical momentum thickness on the x axis is at the given value θ_x;
4. the physical momentum thickness on the y axis is at the given value θ_y;
5. $x = 0$ when $\mu = 0$;
6. $c_1 \theta_\mu = 0.2$.

where θ_μ is the momentum thickness measured in μ; θ_x and θ_y are momentum thicknesses on the major and minor axes.

Since the major axis is at $\theta = 0$ and the minor axis is at $\theta = \frac{\pi}{2}$. The x coordinate on

the major axis and the y axis on the minor axis can be represented as

$$x\,|_{\text{major}} = a\mu - k_1\left[\tanh(c_1(\mu-1))+1\right] + e \tag{3.25}$$

$$y\,|_{\text{minor}} = b\mu \tag{3.26}$$

According to the expressions for the Cartesian coordinate on the major and minor axis in terms of the generalized radial coordinate μ, the above criteria for determining the parameters of the elliptical coordinate can be put into the following mathematical form:

$$b\,(a - k_1 + e) = 1 \tag{3.27}$$

$$AR = \frac{a - k_1 + e}{b} \tag{3.28}$$

$$\frac{\theta_y}{\theta_x}\left[a\theta_\mu - 2k_1\tanh(c_1\frac{\theta_\mu}{2})\right] = b\theta_\mu \tag{3.29}$$

$$c_1\theta_\mu = 0.2 \tag{3.30}$$

$$\theta_y = b\theta_\mu \tag{3.31}$$

$$-k_1\left[\tanh(-c_1)+1\right] + e = 0 \tag{3.32}$$

There are five parameters in the definition of the generalized cylindrical coordinate system. However, we have six equations and seven unknowns. Therefore, we need to specify one of the seven parameters to close the set of the equations. How this parameter

needs to be determined depends on the method of comparison of the results of the linear stability analysis for the circular and elliptical jets. In the subsequent chapter, two methods of comparison will be given. One is based on maintaining equal minimum momentum thickness for both the circular jet and elliptical jet, and the other on maintaining equal momentum area which is defined as the integral of the momentum thickness around the jet periphery, $\int \theta dl$ where l is the arc (peripheral) length.

For comparison based on the equal minimum momentum thickness, if the momentum thickness on the minor axis is smaller than that on the major axis, θ_y needs to be supplied; otherwise θ_x needs to be supplied.

For equal momentum area, it is necessary to supply the ratio of the momentum thickness on the minor axis to the momentum thickness on the major axis. The momentum thickness on the minor axis can be determined in the following: Let θ_{cir} denote the momentum thickness of the circular jet with uniform momentum thickness, then the momentum area of the circular jet is

$$\Delta area_{cir} = 2\pi\theta_{cir} \tag{3.33}$$

The momentum area of an elliptical jet which in this case is set equal to $\Delta area_{cir}$ can be approximated for the above definition by

$$\Delta \text{area}_{\text{ell}} = \pi(A + \frac{1}{2}\theta_x)(B + \frac{1}{2}\theta_y) - \pi(A - \frac{1}{2}\theta_x)(B - \frac{1}{2}\theta_y) \tag{3.34}$$

$$= \pi(A\theta_y + B\theta_x)$$

where A and B are the semi-major and semi-minor axis. Since the non-dimensional equivalent jet radius is unity,

$$A = \sqrt{AR} \tag{3.35}$$

and

$$B = \frac{1}{\sqrt{AR}}. \tag{3.36}$$

By requiring the momentum areas of the circular jet and the elliptical jet are equal to each other, that is

$$\Delta \text{area}_{\text{cir}} = \Delta \text{area}_{\text{ell}} \tag{3.37}$$

we can find the momentum thickness of the elliptical jet on the x axis as

$$\theta_x = \frac{2\theta_{\text{cir}}}{\sqrt{AR}\,\frac{\theta_y}{\theta_x} + \frac{1}{\sqrt{AR}}} \tag{3.38}$$

The above procedure was used to determine the parameters defining the coordinate system. The resulting Cartesian coordinates on the major and minor axes given by Equations 3.25 and 3.26 are plotted in Figure 3.1 for the case of an elliptical jet of aspect

ratio of 2 and uniform momentum thickness which corresponds to a circular jet of $\frac{R}{\theta_{cir}} = 14.14$.

Figures 3.2 to 3.6 are the plots of the distributions of the momentum thicknesses around the jet peripheries for the following five cases:

1. $AR = 1, \quad \theta_y/\theta_x = 1.0;$
2. $AR = 2, \quad \theta_y/\theta_x = 1.0;$
3. $AR = 2, \quad \theta_y/\theta_x = 0.8;$
4. $AR = 2, \quad \theta_y/\theta_x = 1.2;$
5. $AR = 3, \quad \theta_y/\theta_x = 1.0;$

3.3 Governing Equations in Generalized Cylindrical Coordinate System

In this section, the eigenvalue problem of the inviscid incompressible jet flow will be derived. Let q represent either pressure, a velocity component, temperature, or density, then

$\tilde{q}$ = dimensional

$\hat{q}$ = nondimensional

$\overline{q}$ = nondimensional basic

q' = nondimensional disturbance

q = nondimensional eigenfunction

and we define

$\hat{t} = t$ nondimensional time

$\hat{x}^1 = x^1 = \mu$ nondimensional generalized radial coordinate

$\hat{x}^2 = x^2 = \theta$ nondimensional generalized azimuthal coordinate

$\hat{x}^3 = x^3 = z$ nondimensional streamwise coordinate

Furthermore, if a quantity has superscript, it is a tensor, otherwise it is a scalar.

In the Cartesian coordinate system, the continuity, momentum, energy equations and the equation of state can be expressed in the following form:

$$\frac{\partial \tilde{\rho}}{\partial t} + \frac{\partial(\tilde{\rho}\tilde{u}^j)}{\partial \tilde{x}^j} = 0 \tag{3.39}$$

$$\tilde{\rho}\left[\frac{\partial \tilde{u}^i}{\partial \tilde{t}} + \tilde{u}^j \frac{\partial \tilde{u}^i}{\partial \tilde{x}^j}\right] = -\frac{\partial \tilde{p}}{\partial \tilde{x}^j} g^{ij} \tag{3.40}$$

$$(i = 1, 2, 3)$$

$$\tilde{\rho} c_p \left[\frac{\partial \tilde{T}^i}{\partial \tilde{t}} + \tilde{u}^j \frac{\partial \tilde{T}^i}{\partial \tilde{x}^j}\right] - \left[\frac{\partial \tilde{p}^i}{\partial \tilde{t}} + \tilde{u}^j \frac{\partial \tilde{p}^i}{\partial \tilde{x}^j}\right] = -\omega_1 \Delta h^0_{f,1} - \omega_2 \Delta h^0_{f,2} - \omega_3 \Delta h^0_{f,3} \tag{3.41}$$

$$\tilde{p} = \tilde{\rho} R_M \tilde{T} \tag{3.42}$$

where

$$R_M = R_u \left[\frac{Y_1}{W_1} + \frac{Y_2}{W_2} + \frac{1 - Y_1 - Y_2}{W_3}\right] \tag{3.43}$$

$$\omega_1 = -W_1 \nu_1 B \tilde{T}^{\alpha_k} e^{-\frac{E_a}{R_u \tilde{T}}} \left[\frac{\tilde{\rho} Y_1}{W_1}\right]^{\nu_1} \left[\frac{\tilde{\rho} Y_2}{W_2}\right]^{\nu_2} \tag{3.44}$$

$$\omega_2 = -W_2 \nu_2 B \tilde{T}^{\alpha_k} e^{-\frac{E_a}{R_u \tilde{T}}} \left[\frac{\tilde{\rho} Y_1}{W_1}\right]^{\nu_1} \left[\frac{\tilde{\rho} Y_2}{W_2}\right]^{\nu_2} \tag{3.45}$$

$$\omega_3 = W_3 \nu_3 B \tilde{T}^{\alpha_k} e^{-\frac{E_a}{R_u \tilde{T}}} \left[\frac{\tilde{\rho} Y_1}{W_1}\right]^{\nu_1} \left[\frac{\tilde{\rho} Y_2}{W_2}\right]^{\nu_2} \tag{3.46}$$

W_1 = molecular weight of the fuel (3.47)

W_2 = molecular weight of the oxidizer (3.48)

W_3 = molecular weight of the product (3.49)

$$Y_1 = \text{mass fraction of the fuel} \tag{3.50}$$

$$Y_2 = \text{mass fraction of the oxidizer} \tag{3.51}$$

$$R_u = \text{universal gas constant} \tag{3.52}$$

$$E_a = \text{activation energy} \tag{3.53}$$

The dimensional form of the governing equations can be nondimensionalized with the parameters at the jet center line. The dimensional quantities are related to the nondimensional quantities in the following:

$$\tilde{\rho} = \hat{\rho}\rho_0 \tag{3.54}$$

$$\tilde{T} = \hat{T}T_0 \tag{3.55}$$

$$\tilde{p} = \hat{p}\rho_0 U_z(0)^2 \tag{3.56}$$

$$\tilde{u}^i = \hat{u}^i U_z(0) \tag{3.57}$$

$$(i = 1, 2, 3)$$

$$\tilde{x}^i = \hat{x}^i R = x^i R \tag{3.58}$$

$$(i = 1, 2, 3)$$

$$\tilde{t} = \hat{t}\frac{R}{U_z(0)} = t\frac{R}{U_z(0)} \tag{3.59}$$

where ρ_0, T_0 and $U_z(0)$ are the density, temperature and streamwise velocity at the jet

center line; R is the equivalent jet radius defined as $\sqrt{AB}$. The governing equations can now be expressed in the following nondimensional form:

$$\frac{\partial \hat{\rho}}{\partial t} + \frac{\partial (\hat{\rho}\hat{u}^j)}{\partial \tilde{x}^j} = 0 \tag{3.60}$$

$$\hat{\rho}\left[\frac{\partial \hat{u}^i}{\partial t} + \hat{u}^j \frac{\partial \hat{u}^i}{\partial \hat{x}^j}\right] = -\frac{\partial \hat{p}}{\partial x^j} g^{ij} \tag{3.61}$$

$$(i = 1, 2, 3)$$

$$\hat{\rho} c_p \left[\frac{\partial \hat{T}^i}{\partial t} + \hat{u}^j \frac{\partial \hat{T}^i}{\partial x^j}\right] - (k-1)M^2 \left[\frac{\partial \hat{p}}{\partial t} + \hat{u}^j \frac{\partial \hat{p}}{\partial x^j}\right]$$

$$= -\frac{D_a H}{W_1 \nu_1 c_p T_0} Y_1^{\nu_1} Y_2^{\nu_2} \hat{\rho}^{\nu_1+\nu_2} \hat{T}^{\alpha_k} e^{-\frac{E_a}{R_u T_0 \hat{T}}} \tag{3.62}$$

$$kM^2 \hat{p} = \hat{\rho}\hat{T} \tag{3.63}$$

where M is the Mach number at the jet center line; D_a is the Damkholer number which represents the rate the chemical reaction occurs in contrast to the convective rate of the flow; and H is the heat of reaction:

$$M = \frac{U_z(0)}{\sqrt{kR_M T_0}} \tag{3.64}$$

$$D_a = \frac{R}{U_z(0)} \frac{W_1 \nu_1}{W_1^{\nu_1} W_2^{\nu_2}} B T_0^{\alpha_k} \rho_0^{\nu_1+\nu_2-1} \tag{3.65}$$

$$H = -W_1 \nu_1 h^0_{f,1} - W_2 \nu_2 h^0_{f,2} + W_3 \nu_3 h^0_{f,3} \tag{3.66}$$

The above equations can be expressed in the generalized coordinate system by replacing $\frac{\partial(\hat{\rho}\hat{u}^j)}{\partial x^j}$ with $\frac{\partial(\hat{\rho}\hat{u}^j)}{\partial x^j} + \Gamma^j_{kj}\hat{\rho}\hat{u}^k$ and $\frac{\partial(\hat{u}^j)}{\partial x^j}$ with $\frac{\partial(\hat{u}^j)}{\partial x^j} + \Gamma^j_{kj}\hat{u}^k$.

Expanding the governing equations and making use of the fact that some components of the Christoffel symbol and metric tensor are zero, we obtain the continuity, momentum and energy equations, and the equation of state in the generalized cylindrical coordinate:

$$\frac{\partial\hat{\rho}}{\partial t} + \frac{\partial(\hat{\rho}\hat{u}^1)}{\partial x^1} + \frac{\partial(\hat{\rho}\hat{u}^2)}{\partial x^2} + \frac{\partial(\hat{\rho}\hat{u}^3)}{\partial x^3} + \Gamma^1_{11}\hat{\rho}\hat{u}^1 + \Gamma^2_{12}\hat{\rho}\hat{u}^1 + \Gamma^1_{12}\hat{\rho}\hat{u}^2 + \Gamma^2_{22}\hat{\rho}\hat{u}^2 = 0 \tag{3.67}$$

$$\hat{\rho}\frac{\partial\hat{u}^1}{\partial t} + \hat{\rho}\hat{u}^1\frac{\partial\hat{u}^1}{\partial x^1} + \hat{\rho}\hat{u}^2\frac{\partial\hat{u}^1}{\partial x^2} + \hat{\rho}\hat{u}^3\frac{\partial\hat{u}^1}{\partial x^3} + \hat{\rho}\Gamma^1_{11}\hat{u}^1\hat{u}^1 + 2\hat{\rho}\Gamma^1_{12}\hat{u}^2\hat{u}^1 + \hat{\rho}\Gamma^1_{22}\hat{u}^2\hat{u}^2 = -g^{11}\frac{\partial\hat{p}}{\partial x^1} - g^{12}\frac{\partial\hat{p}}{\partial x^2} \tag{3.68}$$

$$\hat{\rho}\frac{\partial\hat{u}^2}{\partial t} + \hat{\rho}\hat{u}^1\frac{\partial\hat{u}^2}{\partial x^1} + \hat{\rho}\hat{u}^2\frac{\partial\hat{u}^2}{\partial x^2} + \hat{\rho}\hat{u}^3\frac{\partial\hat{u}^2}{\partial x^3} + \hat{\rho}\Gamma^2_{11}\hat{u}^1\hat{u}^1 + 2\hat{\rho}\Gamma^2_{12}\hat{u}^2\hat{u}^1 + \hat{\rho}\Gamma^2_{22}\hat{u}^2\hat{u}^2 = -g^{12}\frac{\partial\hat{p}}{\partial x^1} - g^{22}\frac{\partial\hat{p}}{\partial x^2} \tag{3.69}$$

$$\hat{\rho}\frac{\partial \hat{u}^3}{\partial t}+\hat{\rho}\hat{u}^1\frac{\partial \hat{u}^3}{\partial x^1}+\hat{\rho}\hat{u}^2\frac{\partial \hat{u}^3}{\partial x^2}+\hat{\rho}\hat{u}^3\frac{\partial \hat{u}^3}{\partial x^3}=-\frac{\partial \hat{p}}{\partial x^3} \tag{3.70}$$

$$\hat{\rho}\left[\frac{\partial \hat{T}}{\partial t}+\hat{u}^1\frac{\partial \hat{T}}{\partial x^1}+\hat{u}^2\frac{\partial \hat{T}}{\partial x^2}+\hat{u}^3\frac{\partial \hat{T}}{\partial x^3}\right]$$

$$-(k-1)M^2\left[\frac{\partial \hat{p}}{\partial t}+\hat{u}^1\frac{\partial \hat{p}}{\partial x^1}+\hat{u}^2\frac{\partial \hat{p}}{\partial x^2}+\hat{u}^3\frac{\partial \hat{p}}{\partial x^3}\right]$$

$$=-\frac{D_a H Y_1^{\nu_1} Y_2^{\nu_2}}{W_1 \nu_1 c_p T_c}\hat{\rho}^{\nu_1+\nu_2}\hat{T}^{\alpha_k}e^{-\frac{E_a}{R_u T_0 \hat{T}}} \tag{3.71}$$

$$kM^2\hat{p}=\hat{\rho}\hat{T} \tag{3.72}$$

Since

$$x^1=\mu, \qquad x^2=\theta, \qquad x^3=z \tag{3.73) - (3.75}$$

$$\hat{u}^1=\hat{u}_\mu, \qquad \hat{u}^2=\hat{u}_\theta, \qquad \hat{u}^3=\hat{u}_z \tag{3.76) - (3.78}$$

the above equations can be re-expressed as

$$\frac{\partial \hat{\rho}}{\partial t}+\frac{\partial(\hat{\rho}\hat{u}_\mu)}{\partial \mu}+\frac{\partial(\hat{\rho}\hat{u}_\theta)}{\partial \theta}+\frac{\partial(\hat{\rho}\hat{u}_z)}{\partial z}+\Gamma_{11}^1\hat{\rho}\hat{u}_\mu+\Gamma_{12}^2\hat{\rho}\hat{u}_\mu$$

$$+\Gamma_{12}^1\hat{\rho}\hat{u}_\theta+\Gamma_{22}^2\hat{\rho}\hat{u}_\theta=0 \tag{3.79}$$

$$\hat{\rho}\frac{\partial \hat{u}_\mu}{\partial t} + \hat{\rho}\hat{u}_\mu\frac{\partial \hat{u}_\mu}{\partial \mu} + \hat{\rho}\hat{u}_\theta\frac{\partial \hat{u}_\mu}{\partial \theta} + \hat{\rho}\hat{u}_\mu\frac{\partial \hat{u}_\mu}{\partial z} + \hat{\rho}\Gamma^1_{11}\hat{u}_\mu\hat{u}_\mu$$

$$+ 2\hat{\rho}\Gamma^1_{12}\hat{u}_\theta\hat{u}_\mu + \hat{\rho}\Gamma^1_{22}\hat{u}_\theta\hat{u}_\theta = -g^{11}\frac{\partial \hat{p}}{\partial \mu} - g^{12}\frac{\partial \hat{p}}{\partial \theta} \tag{3.80}$$

$$\hat{\rho}\frac{\partial \hat{u}_\theta}{\partial t} + \hat{\rho}\hat{u}_\mu\frac{\partial \hat{u}_\theta}{\partial \mu} + \hat{\rho}\hat{u}_\mu\frac{\partial \hat{u}_\theta}{\partial \theta} + \hat{\rho}\hat{u}_z\frac{\partial \hat{u}_\theta}{\partial z} + \hat{\rho}\Gamma^2_{11}\hat{u}_\mu\hat{u}_\mu$$

$$+ 2\hat{\rho}\Gamma^2_{12}\hat{u}_\theta\hat{u}_\mu + \hat{\rho}\Gamma^2_{22}\hat{u}_\theta\hat{u}_\theta = -g^{12}\frac{\partial \hat{p}}{\partial \mu} - g^{22}\frac{\partial \hat{p}}{\partial \theta} \tag{3.81}$$

$$\hat{\rho}\frac{\partial \hat{u}_z}{\partial t} + \hat{\rho}\hat{u}_\mu\frac{\partial \hat{u}_z}{\partial \mu} + \hat{\rho}\hat{u}_\theta\frac{\partial \hat{u}_z}{\partial \theta} + \hat{\rho}\hat{u}_z\frac{\partial \hat{u}_z}{\partial z} = -\frac{\partial \hat{p}}{\partial z} \tag{3.82}$$

$$\hat{\rho}\left[\frac{\partial \hat{T}}{\partial t} + \hat{u}_\mu\frac{\partial \hat{T}}{\partial \mu} + \hat{u}_\theta\frac{\partial \hat{T}}{\partial \theta} + \hat{u}_z\frac{\partial \hat{T}}{\partial z}\right]$$

$$-(k-1)M^2\left[\frac{\partial \hat{p}}{\partial t} + \hat{u}_\mu\frac{\partial \hat{p}}{\partial \mu} + \hat{u}_\theta\frac{\partial \hat{p}}{\partial \theta} + \hat{u}_z\frac{\partial \hat{p}}{\partial z}\right]$$

$$= -\frac{D_a H Y_1^{\nu_1} Y_2^{\nu_2}}{W_1 \nu_1 c_p T_c}\hat{\rho}^{\nu_1+\nu_2}\hat{T}^{\alpha_k} e^{-\frac{E_a}{R_u T_0 \hat{T}}} \tag{3.83}$$

$$kM^2\hat{p} = \hat{\rho}\hat{T} \tag{3.84}$$

The governing equations for the basic steady flow can be obtained by replacing the quantities with a "$\hat{}$" with quantities with a "$\bar{}$", eliminating the partial derivatives with respect to time, and making use of the parallel flow assumption. This gives (according to Equations 3.79 - 3.83):

$$\frac{\partial \bar{\rho}\bar{u}_\theta}{\partial \theta} + \Gamma_{12}^1 \bar{\rho}\bar{u}_\theta + \Gamma_{22}^2 \bar{\rho}\bar{u}_\theta = 0 \tag{3.85}$$

$$\bar{\rho}\Gamma_{22}^1 \bar{u}_\theta^2 = -g^{11}\frac{\partial \bar{p}}{\partial \mu} - g^{12}\frac{\partial \bar{p}}{\partial \theta} \tag{3.86}$$

$$\bar{\rho}\bar{u}_\theta \frac{\partial \bar{u}_\theta}{\partial \theta} + \bar{\rho}\Gamma_{22}^2 \bar{u}_\theta^2 = -g^{12}\frac{\partial \bar{p}}{\partial \mu} - g^{22}\frac{\partial \bar{p}}{\partial \theta} \tag{3.87}$$

$$0 = 0 \tag{3.88}$$

$$\bar{\rho}\bar{u}_\theta \frac{\partial \bar{T}}{\partial \theta} + \bar{\rho}\bar{u}_z \frac{\partial \bar{T}}{\partial z} - (k-1)M^2 \bar{u}_\theta \frac{\partial p}{\partial \theta}$$

$$= -C_e \bar{\rho}^{\nu_1 + \nu_2} \bar{T}^{\alpha_k} e^{-\frac{E_a}{R_u T_0 \bar{T}}} \tag{3.89}$$

$$kM^2 \bar{p} = \bar{\rho}\bar{T} \tag{3.90}$$

The above equations represent the continuity equation, the momentum equations in the radial, azimuthal and streamwise directions, the energy equation, and the equation of state. Note that the momentum equation in the streamwise direction is satisfied automatically.

Assuming that the parameters of the flow, such as velocity, pressure can be decomposed into their basic steady parts and the disturbance parts, i.e.

$$\hat{q} = \bar{q} + q' \tag{3.91}$$

we can change the governing equations into a form in terms of the disturbances, where the quantities with a prime denote the disturbance quantities. Next, the governing equations are linearized, thus limiting the calculation to the near field where the disturbances to the basic flow are small. This procedure results in a set of equations which contains the basic flow quantities as well as the disturbance quantities. By subtracting the governing equations of the basic flow, the governing equations for the disturbance quantities can be obtained:

$$\frac{\partial \rho'}{\partial t} + \frac{\partial \bar{\rho} u'_\mu}{\partial \mu} + \frac{\partial \bar{\rho} u'_\theta}{\partial \theta} + \frac{\partial \bar{\rho} u'_z}{\partial z} + \frac{\partial \rho' \bar{u}_z}{\partial z} + \Gamma^1_{11} \bar{\rho} u'_\mu$$
$$+ \Gamma^2_{12} \bar{\rho} u'_\mu + \Gamma^1_{12} \bar{\rho} u'_\theta + \Gamma^1_{12} \rho' \bar{u}_\theta + \Gamma^2_{22} \bar{\rho} u'_\theta + \Gamma^2_{22} \rho' \bar{u}_\theta = 0 \tag{3.92}$$

$$\bar{\rho} \frac{\partial u'_\mu}{\partial t} + \bar{\rho} \bar{u}_\theta u \frac{\partial u'_\mu}{\partial \theta} + \bar{\rho} \bar{u}_z \frac{\partial u'_\mu}{\partial z} + 2\Gamma^1_{12} \bar{u}_\theta u'_\mu + 2\Gamma^1_{22} \bar{u}_\theta u'_\theta$$
$$= - g^{11} \frac{\partial p'}{\partial \mu} - g^{12} \frac{\partial p'}{\partial \theta} \tag{3.93}$$

$$\bar{\rho} \frac{\partial u'_\theta}{\partial t} + \bar{\rho} u'_\mu \frac{\partial \bar{u}_\theta}{\partial \mu} + \bar{\rho} \bar{u}_\theta \frac{\partial u'_\theta}{\partial \theta} + \bar{\rho} u'_\theta \frac{\partial \bar{u}_\theta}{\partial \theta} + \rho' \bar{u}_\theta \frac{\partial \bar{u}_\theta}{\partial \theta} + \bar{\rho} \bar{u}_z \frac{\partial u'_\theta}{\partial z}$$
$$+ 2\bar{\rho} \Gamma^2_{12} \bar{u}_\theta u'_\mu + 2\bar{\rho} \Gamma^2_{22} \bar{u}_\theta u'_\theta = - g^{12} \frac{\partial p'}{\partial \mu} - g^{22} \frac{\partial p'}{\partial \theta} \tag{3.94}$$

$$\bar{\rho} \frac{\partial u'_z}{\partial t} + \bar{\rho} u'_\mu \frac{\partial \bar{u}_z}{\partial \mu} + \bar{\rho} \bar{u}_\theta \frac{\partial u'_z}{\partial \theta} + \bar{\rho} \bar{u}_z \frac{\partial u'_z}{\partial z} = - \frac{\partial p'}{\partial z} \tag{3.95}$$

$$\bar{\rho}\frac{\partial T'}{\partial t}+\bar{\rho}u'_{\mu}\frac{\partial \bar{T}}{\partial \mu}+\bar{\rho}\bar{u}_{\theta}\frac{\partial T'}{\partial \theta}+\bar{\rho}u'_{\theta}\frac{\partial \bar{T}}{\partial \theta}+\rho'\bar{u}_{\theta}\frac{\partial \bar{T}}{\partial \theta}+\bar{\rho}\bar{u}_{z}\frac{\partial T'}{\partial z}$$

$$+\bar{\rho}u'_{z}\frac{\partial \bar{T}}{\partial z}+\rho'\bar{u}_{z}\frac{\partial \bar{T}}{\partial z}-(k-1)M^{2}\left[\frac{\partial p'}{\partial t}+u'_{\mu}\frac{\partial \bar{p}}{\partial \mu}+u'_{\theta}\frac{\partial \bar{p}}{\partial \theta}\right.$$

$$\left.+\bar{u}_{\theta}\frac{\partial p'}{\partial \theta}+\bar{u}_{z}\frac{\partial p'}{\partial z}\right]=x' \tag{3.96}$$

$$kM^{2}p'=\bar{\rho}T'+\rho'\bar{T} \tag{3.97}$$

where

$$x'=-C_{e}\bar{\rho}^{\nu_1+\nu_2}\bar{T}^{\alpha_k}e^{-\frac{E_a}{R_uT_0\bar{T}}}\left[\frac{\nu_1+\nu_2}{\bar{\rho}}\rho'+\left[\frac{\alpha_k}{\bar{T}}+\frac{E_a}{R_uT_0\bar{T}^{2}}\right]T'\right] \tag{3.98}$$

$$C_{e}=-D_{a}Q_{0}Y_{1}^{\nu_1}Y_{2}^{\nu_2} \tag{3.99}$$

$$Q_{0}=\frac{Q}{W_{1}\nu_{1}} \tag{3.100}$$

$$Q=\frac{h^{0}_{f,1}W_{1}\nu_{1}+h^{0}_{f,2}W_{2}\nu_{2}-h^{0}_{f,3}W_{3}\nu_{3}}{c_{p}T_{0}} \tag{3.101}$$

In the above equations, Q is the amount of heat release from the chemical reaction in the flow; Q_0 is the non-dimensional heat release.

The temperature disturbance T' can be eliminated from the governing equations for the disturbance by expressing the disturbance temperature in terms of the pressure and density disturbances using the equation of state:

$$T' = \frac{kM^2}{\bar{\rho}} p' - \frac{\bar{T}}{\bar{\rho}} \rho' \tag{3.102}$$

Since the disturbance temperature does not appear in the continuity and momentum equations, only the energy disturbance equations will be modified:

$$M^2 \frac{\partial p'}{\partial t} - \bar{T} \frac{\partial \rho'}{\partial t} + \left[\bar{\rho} \frac{\partial \bar{T}}{\partial \mu} - (k-1) M^2 \frac{\partial \bar{p}}{\partial \mu} \right] u'_\mu$$

$$+ \left[\bar{\rho} \frac{\partial \bar{T}}{\partial \theta} - (k-1) M^2 \frac{\partial \bar{p}}{\partial \theta} \right] u'_\theta + \bar{\rho} \frac{\partial \bar{T}}{\partial z} u'_z$$

$$+ \left[- \frac{kM^2 \bar{u}_\theta}{\bar{\rho}} \frac{\partial \bar{\rho}}{\partial \theta} + C_e \bar{\rho}^{\nu_1 + \nu_2} \bar{T}^{\alpha_k} e^{-\frac{E_a}{R_u T_0 \bar{T}}} \left(\frac{\alpha_k}{\bar{T}} + \frac{E_a}{R_u T_0 \bar{T}^2} \right) \frac{kM^2}{\bar{\rho}} \right] p'$$

$$+ \left[- \bar{u}_\theta \frac{\partial \bar{T}}{\partial \theta} + \bar{u}_\theta \frac{\bar{T}}{\bar{\rho}} \frac{\partial \bar{\rho}}{\partial \theta} + \bar{u}_\theta \frac{\partial \bar{T}}{\partial \theta} + C_e \bar{\rho}^{\nu_1 + \nu_2} \bar{T}^{\alpha_k} e^{-\frac{E_a}{R_u T_0 \bar{T}}} \frac{\nu_1 + \nu_2}{\bar{\rho}} \right.$$

$$\left. - C_e \bar{\rho}^{\nu_1 + \nu_2} \bar{T}^{\alpha_k} e^{-\frac{E_u}{R_u T_0 \bar{T}}} \left(\frac{\alpha_k}{\bar{T}} + \frac{E_a}{R_u T_0 \bar{T}^2} \right) \frac{\bar{T}}{\bar{\rho}} \right] \rho'$$

$$+ M^2 \bar{u}_\theta \frac{\partial p'}{\partial \theta} + M^2 \bar{u}_z \frac{\partial p'}{\partial z} - \bar{u}_\theta \bar{T} \frac{\partial \rho'}{\partial \theta} - \bar{u}_z \bar{T} \frac{\partial \rho'}{\partial z} = 0 \tag{3.103}$$

Since the solution of stability problem of the elliptical jet is not unique (which will be discussed later), it is necessary to use the normal mode assumption in order to be able to obtain the solution related to a specified azimuthal symmetry. However, the azimuthal variations of the disturbances are no longer represented in a sinusoidal form which was adopted in the stability analysis of the circular jet. This is because the non-uniformity of

the elliptical jet makes the eigenfunction non-uniform and non-sinusoidal. Thus the azimuthal variations of the eigenfunctions are incorporated in the eigenfunction itself. Specifically, the normal mode assumption employed here is

$$q' = q(\mu,\theta)\, e^{i(\alpha z - \omega t)} \tag{3.104}$$

After substituting the normal mode assumption into the disturbance equations, we obtain the following eigenfunction equations:

$$\begin{aligned} &-i\omega\rho + \left[\frac{\partial\bar{\rho}}{\partial\mu} + \left(\Gamma^1_{11} + \Gamma^2_{12}\right)\bar{\rho}\right]u_\mu + \left[\frac{\partial\bar{\rho}}{\partial\theta} + \left(\Gamma^1_{12} + \Gamma^2_{22}\right)\bar{\rho}\right]u_\theta \\ &+ \left[\frac{\partial\bar{u}_\theta}{\partial\theta} + \left(\Gamma^1_{12} + \Gamma^2_{22}\right)\bar{u}_\theta\right]\rho + \bar{\rho}\frac{\partial u_\mu}{\partial\mu} + \frac{\bar{\rho}\partial u_\theta}{\partial\theta} + \bar{u}_\theta\frac{\partial\rho}{\partial\theta} \\ &= -\alpha\left[i\bar{\rho}u_z + i\bar{u}_z\rho\right] \end{aligned} \tag{3.105}$$

$$\begin{aligned} &-i\omega\bar{\rho}u_\mu + \bar{\rho}\bar{u}_\theta\frac{\partial u_\mu}{\partial\theta} + 2\bar{\rho}\Gamma^1_{12}\bar{u}_\theta u_\mu + 2\bar{\rho}\Gamma^1_{22}\bar{u}_\theta u_\theta \\ &+ g^{11}\frac{\partial p}{\partial\mu} + g^{12}\frac{\partial p}{\partial\theta} = -\alpha i\bar{\rho}\bar{u}_z u_\mu \end{aligned} \tag{3.106}$$

$$\begin{aligned} &-i\omega\bar{\rho}u_\theta + \bar{\rho}\left[\frac{\bar{\partial}_\theta}{\partial\mu} + 2\Gamma^2_{12}\bar{u}_\theta\right]u_\mu + \bar{\rho}\left[\frac{\partial\bar{u}_\theta}{\partial\theta} + 2\Gamma^2_{22}\bar{u}_\theta\right]u_\theta \\ &+ \bar{\rho}\bar{u}_\theta\frac{\partial u_\theta}{\partial\theta} + \bar{u}_\theta\frac{\partial\bar{u}_\theta}{\partial\theta}\rho + g^{12}\frac{\partial p}{\partial\mu} + g^{22}\frac{\partial p}{\partial\theta} = -\alpha i\bar{\rho}\bar{u}_z u_\theta \end{aligned} \tag{3.107}$$

$$-i\omega\bar{\rho}u_z+\bar{\rho}\frac{\partial\bar{u}_z}{\partial\mu}u_\mu+\bar{\rho}\bar{u}_\theta\frac{\partial u_z}{\partial\theta}=-\alpha\left[i\bar{\rho}\bar{u}_z u_z+ip\right] \tag{3.108}$$

$$\begin{aligned}
&-i\omega M^2 p+i\omega\bar{T}\rho+\left[\bar{\rho}\frac{\partial\bar{T}}{\partial\mu}-(k-1)M^2\frac{\partial\bar{p}}{\partial\mu}\right]u_\mu\\
&+\left[\bar{\rho}\frac{\partial\bar{T}}{\partial\theta}-(k-1)M^2\frac{\partial\bar{p}}{\partial\theta}\right]u_\theta+\bar{\rho}\frac{\partial\bar{T}}{\partial z}u_z\\
&+\left[-\frac{kM^2\bar{u}_\theta}{\bar{\rho}}\frac{\partial\bar{\rho}}{\partial\theta}+C_e\bar{\rho}^{\nu_1+\nu_2}\bar{T}^{\alpha_k}e^{-\frac{E_a}{R_uT_0\bar{T}}}\left(\frac{\alpha_k}{\bar{T}}+\frac{E_a}{R_uT_0\bar{T}^2}\right)\frac{kM^2}{\bar{\rho}}\right]p\\
&+\left[-\bar{u}_\theta\frac{\partial\bar{T}}{\partial\theta}+\bar{u}_\theta\frac{\bar{T}}{\bar{\rho}}\frac{\partial\bar{\rho}}{\partial\theta}+\bar{u}_\theta\frac{\partial\bar{T}}{\partial\theta}+C_e\bar{\rho}^{\nu_1+\nu_2}\bar{T}^{\alpha_k}e^{-\frac{E_a}{R_uT_0\bar{T}}}\frac{\nu_1+\nu_2}{\bar{\rho}}\right.\\
&\left.-C_e\bar{\rho}^{\nu_1+\nu_2}\bar{T}^{\alpha_k}e^{-\frac{E_u}{R_uT_0\bar{T}}}\left(\frac{\alpha_k}{\bar{T}}+\frac{E_a}{R_uT_0\bar{T}^2}\right)\frac{\bar{T}}{\bar{\rho}}\right]\rho\\
&+M^2\bar{u}_\theta\frac{\partial p}{\partial\theta}-\bar{u}_\theta\bar{T}\frac{\partial\rho}{\partial\theta}=-\alpha\left[iM^2\bar{u}_z p-i\bar{u}_z\bar{T}\rho\right]
\end{aligned} \tag{3.109}$$

This is a set of homogeneous linear partial differential equations. The proper boundary conditions used are those which require the uniqueness of the solution at the center line (represented by the location of $\mu = 0$) and the disappearance of the disturbance at the infinity (represented by the location of $\mu = \infty$). Accordingly, we have

$$\frac{\partial u_z}{\partial\theta}=\frac{\partial p}{\partial\theta}=0, \qquad \text{at } \mu=0 \tag{3.110}$$

and

$$u_\mu = u_\theta = u_z = p = 0, \qquad \text{at } \mu = \infty \tag{3.111}$$

In order to avoid the singularities at $\mu = 0$, the radial solution region is confined to

$$\mu_{min} \le \mu \le \mu_{max} \tag{3.112}$$

where μ_{min} is a small generalized radial coordinate; μ_{max} is the generalized radial coordinate large enough so that the basic streamwise velocity is a constant at that location. Also because the basic flow always has a period of π, it is only necessary to solve the resulting eigenvalue problem in the region

$$0 \le \theta \le \pi \tag{3.113}$$

The equations for the disturbance eigenfunctions and the associated boundaries conditions constitutes an eigenvalue problem. The solution of this eigenvalue problem is the topic of the next section.

3.4 Solution of Eigenvalue Problem

It was mentioned in the last section that the normal mode assumption was applied in the derivation of the governing equations for the disturbance eigenfunctions. In addition, it is also necessary to specify the mode of the disturbance. Each mode has

particular symmetry properties. The reason for dividing the solution into various frequencies and modes is that the solution of the disturbance equations is not unique. In reality the solution consists of many frequencies and many modes.

For elliptical jets, there exist many mode classification schemes, such as the ce, se scheme used by Morris [1984], and the ++, +-, -+, -- scheme used by Koshigeo [1986]. Morris' mode classification scheme is based on the symmetry properties of the Mathieu functions which are the asymptotic solutions for the pressure eigenfunction of the stability problems of the elliptical jet. Koshigeo's mode classification scheme is based on the symmetry properties of the pressure function. In the case with a swirl, some of the symmetry properties of the non-swirling flow no longer exist. Therefore, it is necessary to adopt a different mode classification scheme to handle the situation in which there is a swirl.

In the work described here, the solution of the stability problem is divided into two modes, i.e., the mode in which the solution of the eigenfunctions have a period of π, and the mode in which the solution of the eigenfunctions have a period of 2π. The first mode is called the π mode and the second mode is called the 2π mode. For the π mode, $q(\theta) = q(\theta + \pi)$, where q is the eigenfunction of any flow parameters. For the 2π mode, the eigenfunctions not only have a period of 2π, but are antisymmetric about the center line. So, $q(\theta) = -q(\theta + \pi)$ for the 2π mode. In each of the π and 2π mode, there are

many sub-modes. The π modes in which the eigenfunctions have the least azimuthal variation is called the fundamental π mode. The 2π mode in which the eigenfunctions have the least azimuthal variation is called the first azimuthal modes. When there is no swirl, one mode was found for the fundamental π mode, and two modes were found for the first 2π mode which we designate the sine and cosine modes. In the sine mode, the pressure eigenfunction has a symmetry property similar to the sine function, that is, the pressure eigenfunction is symmetric about the major axis. In the cosine mode, the pressure eigenfunction has a symmetry property similar to the cosine function, that is, the pressure eigenfunction is symmetrical about the minor axis.

Because of the symmetry properties of the modes, it is only necessary to carry out the computation in the upper half plane. This is equivalent to the computation domain described in the last section.

It has been demonstrated [Khorrami, 1989, 1991; Macaraeg, 1988] that the spectral collocation method is effective in the solution of the stability problem of jet flow. In this work, both the Chebyshev and Fourier spectral collocation methods are applied in the solution of the eigenvalue problem. The Chebyshev collocation is used in the radial direction. The Fourier collocation method is used in the azimuthal direction because the flow is periodic in this direction.

Since the Chebyshev collocation method requires that the solution be carried out in between -1 and 1, a radial transformation $\mu = \mu(\xi)$ is applied to transform the radial solution region $\mu_{min} \le \mu \le \mu_{max}$ to $1 \ge \xi \ge -1$, where ξ is the new transformed radial coordinate. Besides satisfying the transforming requirement, the transformation should also guarantee that more grid points be distributed in the shear layer and less grid points be distributed outside the shear layer. This requires the derivative of $\frac{d\mu}{d\xi}$ be small enough in the shear layer region and large enough outside the shear layer region. The stretching was chosen to be:

$$\mu = -a_0 \sinh(b_0 \xi)\left[1 + e^{a_1(-\xi - b_1)}\right]\left[1 + e^{-a_2(-\xi + b_2)}\right] + 1 + \mu_{min} \qquad (3.114)$$

where the values of a_0, b_0, a_1, b_1, a_2 and b_2 can be chosen to satisfy the above requirement. With this coordinate transformation, the governing equations for the eigenfunctions can be expressed in terms of the transformed radial azimuthal coordinates.

In order to discretize the governing equations for the eigenfunctions, it is necessary to express the derivatives of the disturbance eigenfunctions with respect to the transformed radial coordinate and azimuthal coordinate in terms of these eigenfunctions themselves at the grid points (the collocation points). According to the Chebyshev spectral collocation method the derivatives of a quantity q with respect to the transformed radial coordinate ξ at the radial collocation points is

$$\frac{\partial q_{ik}}{\partial \xi} = \sum_{l=0}^{n_r} q_{lk} \left[D\,1_r \right]_{i,l} \tag{3.115}$$

In the above equation, subscript i and the first subscript of q represent the node number in the radial direction; subscript k and the second subscript of q represent the node number in the azimuthal direction; n_r is the number of the collocation points in radial direction. The transformed radial coordinate ξ_i at the collocation points i is:

$$\xi_i = \cos\frac{\pi i}{n_r} \tag{3.116}$$

$$(i = 0, \cdots, n_r)$$

where $\left[D\,1_r \right]_{i,l}$ is a function of i and l and is defined as

$$\left[D\,1_r \right]_{k,j} = \frac{c_k}{c_j} \frac{(-1)^{j+k}}{\xi_k - \xi_j} \tag{3.117}$$

$$(k \neq j)$$

$$\left[D\,1_r \right]_{j,j} = -\frac{\xi_j}{2\left[1 - \xi_j^2 \right]} \tag{3.118}$$

$$\left[D\,1_r \right]_{0,0} = \left[D\,1_r \right]_{n_r, n_r} = \frac{2n_r^2 + 1}{6} \tag{3.119}$$

$$c_0 = c_{n_r} = 2 \tag{3.120}$$

$$c_j = 1 \tag{3.121}$$

$$(1 \le j \le n_r - 1)$$

According to the Fourier spectral collocation method, the derivative of q with respect to θ at the azimuthal collocation points is:

$$\frac{\partial q_{ik}}{\partial \theta} = \sum_{j=0}^{2n_\theta - 1} q_{ij} \left[D\, 1_\theta \right]_{k,j} \tag{3.122}$$

where n_θ is the number of the collocation points in the azimuthal direction. $\left[D\, 1_\theta \right]_{k,j}$ is defined by:

$$\left[D\, 1_\theta \right]_{k,j} = \frac{1}{2}(-1)^{k+j} \cot \frac{\theta_k - \theta_j}{2} \tag{3.123}$$

$$(k \ne j)$$

$$\left[D\, 1_\theta \right]_{j,j} = 0 \tag{3.124}$$

The collocation points in the azimuthal direction are defined as follows:

$$\theta_k = \frac{\pi k}{n_\theta} \tag{3.125}$$

$$(k = 0, \cdots, 2n_\theta - 1)$$

The details of the above discretization scheme using the spectral collocation method are described by Voigt, et al. [1984].

From the results of the stability analysis circular jet, it is possible for the azimuthal eigenfunction to be infinite at the jet center line, the following velocity eigenfunctions are used in the actual computations:

$$v_{\mu} = u_{\mu} \tag{3.126}$$

$$v_{\theta} = u_{\theta}\mu \tag{3.127}$$

$$v_z = u_z \tag{3.128}$$

Substituting the expressions for the partial derivatives of a quantity with respect to the radial and azimuthal coordinates, we can obtain the discretized form of the governing equations for the disturbance eigenfunction in terms of the stretched coordinates:

$$\begin{aligned} &-i\omega\rho_{i,k} + \left[\frac{\partial\bar{\rho}}{\partial\mu} + \left(\Gamma_{11}^{1} + \Gamma_{12}^{2}\right)\bar{\rho}\right] v_{\mu\, i,k} + \left[\frac{\partial\bar{\rho}}{\partial\theta} + \left(\Gamma_{12}^{1} + \Gamma_{22}^{2}\right)\bar{\rho}\right]\frac{v_{\theta\, i,k}}{\mu_i} \\ &+ \left[\frac{\partial\bar{u}_{\theta}}{\partial\theta} + \left(\Gamma_{12}^{1} + \Gamma_{22}^{2}\right)\bar{u}_{\theta}\right]\rho_{i,k} + \frac{\bar{\rho}}{\dfrac{d\mu_i}{d\xi}}\sum_{l=0}^{n_r} v_{\mu\, l,k}\left[D\,1_r\right]_{i,l} \\ &+ \frac{\bar{\rho}}{\mu_i}\sum_{j=0}^{2n_{\theta}-1} v_{\theta\, i,j}\left[D\,1_{\theta}\right]_{k,j} + \bar{u}_{\theta}\sum_{j=0}^{2n_{\theta}-1}\rho_{i,j}\left[D\,1_{\theta}\right]_{k,j} = -\alpha\left[i\bar{\rho}v_{z\, i,k} + i\bar{u}_z\rho_{i,k}\right] \end{aligned} \tag{3.129}$$

$$-i\omega\bar{\rho}v_{\mu\,i,k}+\bar{\rho}\bar{u}_{\theta}\sum_{j=0}^{2n_{\theta}-1}v_{\mu\,i,j}\left[D\,1_{\theta}\right]_{k,j}+2\bar{\rho}\Gamma_{12}^{1}\bar{u}_{\theta}v_{\mu\,i,k}+2\bar{\rho}\Gamma_{22}^{1}\bar{u}_{\theta}v_{\theta\,i,k}$$

$$+\frac{g^{11}}{\dfrac{d\mu_i}{d\xi}}\sum_{l=0}^{n_r}p_{l,k}\left[D\,1_{r}\right]_{i,l}+g^{12}\sum_{j=0}^{2n_{\theta}-1}p_{i,j}\left[D\,1_{\theta}\right]_{k,j}=-\alpha i\bar{\rho}\bar{u}_{z}u_{\mu\,i,k} \qquad (3.130)$$

$$-\frac{i\omega\bar{\rho}u_{\theta\,i,k}}{\mu_i}+\bar{\rho}\left[\frac{\partial\bar{u}_{\theta}}{\partial\mu}+2\Gamma_{12}^{2}\bar{u}_{\theta}\right]v_{\mu\,i,k}+\bar{\rho}\left[\frac{\partial\bar{u}_{\theta}}{\partial\theta}+2\Gamma_{22}^{2}\bar{u}_{\theta}\right]\frac{v_{\theta\,i,k}}{\mu_i}$$

$$+\frac{\bar{\rho}\bar{u}_{\theta}}{\mu_i}\sum_{j=0}^{2n_{\theta}-1}v_{\theta\,i,j}\left[D\,1_{\theta}\right]_{k,j}+\bar{u}_{\theta}\frac{\partial\bar{u}_{\theta}}{\partial\theta}\rho_{i,k}+\frac{g^{12}}{\dfrac{d\mu_i}{d\xi}}\sum_{l=0}^{n_r}p_{l,k}\left[D\,1_{r}\right]_{i,l}$$

$$+g^{22}\sum_{j=0}^{2n_{\theta}-1}p_{i,j}\left[D\,1_{\theta}\right]_{k,j}=-\alpha i\bar{\rho}\bar{u}_{z}\frac{v_{\theta\,i,k}}{\mu_i} \qquad (3.131)$$

$$-i\omega\bar{\rho}v_{z\,i,k}+\bar{\rho}\frac{\partial\bar{u}_{z}}{\partial\mu}v_{\mu\,i,k}+\bar{\rho}\bar{u}_{\theta}\sum_{j=0}^{2n_{\theta}-1}v_{z\,i,j}\left[D\,1_{\theta}\right]_{k,j}=-\alpha\left[i\bar{\rho}\bar{u}_{z}u_{z\,i,k}+ip_{i,k}\right] \qquad (3.132)$$

$$-i\omega M^2 p_{i,k} + i\omega \bar{T}\rho_{i,k} + \left[\bar{\rho}\frac{\partial \bar{T}}{\partial \mu} - (k-1)M^2\frac{\partial \bar{p}}{\partial \mu}\right] v_{\mu\, i,k}$$

$$+ \left[\bar{\rho}\frac{\partial \bar{T}}{\partial \theta} - (k-1)M^2\frac{\partial \bar{p}}{\partial \theta}\right]\frac{v_{\theta\, i,k}}{\mu_i} + \bar{\rho}\frac{\partial \bar{T}}{\partial z} v_{z\, ik}$$

$$+ \left[-\frac{kM^2\bar{u}_\theta}{\bar{\rho}}\frac{\partial \bar{\rho}}{\partial \theta} + C_e\bar{\rho}^{\nu_1+\nu_2}\bar{T}^{\alpha_k} e^{-\frac{E_a}{R_u T_0 \bar{T}}}\left(\frac{\alpha_k}{\bar{T}} + \frac{E_a}{R_u T_0 \bar{T}^2}\right)\frac{kM^2}{\bar{\rho}}\right] p_{i,k}$$

$$+ \left[-\bar{u}_\theta\frac{\partial \bar{T}}{\partial \theta} + \bar{u}_\theta\frac{\bar{T}}{\bar{\rho}}\frac{\partial \bar{\rho}}{\partial \theta} + \bar{u}_\theta\frac{\partial \bar{T}}{\partial \theta} + C_e\bar{\rho}^{\nu_1+\nu_2}\bar{T}^{\alpha_k} e^{-\frac{E_a}{R_u T_0 \bar{T}}}\frac{\nu_1+\nu_2}{\bar{\rho}}\right.$$

$$\left. - C_e\bar{\rho}^{\nu_1+\nu_2}\bar{T}^{\alpha_k} e^{-\frac{E_u}{R_u T_0 \bar{T}}}\left(\frac{\alpha_k}{\bar{T}} + \frac{E_a}{R_u T_0 \bar{T}^2}\right)\frac{\bar{T}}{\bar{\rho}}\right]\rho_{i,k}$$

$$+ M^2\bar{u}_\theta \sum_{j=0}^{2n_\theta - 1} p_{i,j}\left[D\,1_\theta\right]_{k,j} - \bar{u}_\theta\bar{T}\sum_{j=0}^{2n_\theta - 1}\rho_{i,j}\left[D\,1_\theta\right]_{k,j}$$

$$= -\alpha\left[iM^2\bar{u}_z p_{i,k} - i\bar{u}_z\bar{T}\rho_{i,k}\right] \tag{3.133}$$

where all the basic flow parameters are evaluated at node i, k. The above discretized form of the disturbance equation and its boundary condition can also been written in a matrix form:

$$\mathbf{A}(\omega)\mathbf{u} = \alpha\mathbf{B}(\omega)\mathbf{u} \tag{3.134}$$

where

$$\mathbf{u} = \begin{bmatrix} p_{0,0} \\ \cdots \\ p_{n_r-1,n_\theta-1} \\ v_{\mu\,0,0} \\ \cdots \\ v_{\mu\,n_r-1,n_\theta-1} \\ v_{\theta\,0,0} \\ \cdots \\ v_{\theta\,n_r-1,n_\theta-1} \\ v_{z\,0,0} \\ \cdots \\ v_{z\,n_r-1,n_\theta-1} \\ \rho_{0,0} \\ \cdots \\ \rho_{n_r-1,n_\theta-1} \end{bmatrix} \tag{3.135}$$

which is an algebraic eigenvalue problem. Here **A** and **B** are matrices; **u** is a column vector consisting of eigenfunctions.

It is necessary to include a small external basic streamwise velocity to make **B** non-singular. This will introduce some spurious modes. But the physical modes will not be affected. If we choose an initial guess s and solve this eigenvalue problem, it is easy to prove that the result is the same as the largest eigenvalue and the associated eigenfunctions of the following eigenvalue problem:

$$(\mathbf{B}^{-1}A - s\mathbf{I})^{-1}\mathbf{u} = \alpha'\mathbf{u} \tag{3.136}$$

where

$$\alpha = s + \frac{1}{\alpha'} \tag{3.137}$$

The solution of this algebraic eigenvalue problem is obtained with power method. That is:

$$\mathbf{u}_{i+1} = (\mathbf{B}^{-1} - s\mathbf{I})^{-1}\mathbf{u}_i \tag{3.138}$$

In the actual computation, a LU decomposition was carried out for matrix $\mathbf{A} - s\mathbf{B}$, so that

$$\mathbf{A} - s\mathbf{B} = \mathbf{LU} \tag{3.139}$$

then a iteration was made such that

$$\mathbf{LU}\mathbf{u}_{i+1} = \mathbf{B}\mathbf{u}_i \tag{3.140}$$

for $i = 0, 1, 2 \cdots$ until convergence is reached.

After the eigenfunction $\mathbf{u}$ is obtained, the eigenvalue can be computed using

$$\alpha = \frac{\mathbf{u}_{i+1}^T \mathbf{A}\mathbf{u}_{i+1}}{\mathbf{u}_{i+1}^T \mathbf{B}\mathbf{u}_{i+1}} \tag{3.141}$$

For an elliptical jet of a specified aspect ratio, the solution is first carried out for an aspect ratio slightly larger than 1. This enables the eigenvalue of the corresponding circular jet to be used as the initial guess of the elliptical jet. Then the aspect ratio is increased a small amount and the eigenvalue from previous solution is used as the new initial guess.

This process needs to be repeated until the required aspect ratio is reached.

3.5 Basic Flow

The task of linear stability analysis is to find the behavior of the disturbances to the basic steady flow. So, the specification of the basic flow is required before the linear stability analysis can be carried out.

For the basic streamwise velocity, we used Michalke's second velocity profile as we did for the circular jet. But instead of using the circular radial coordinate, the basic steady streamwise velocity is assumed to be a function of the generalized radial coordinate. That is:

$$\bar{u}_z = 0.5\left\{1 + \tanh\left[\frac{1}{4\theta_\mu}\left[\frac{1}{\mu} - \mu\right]\right]\right\} \tag{3.142}$$

where θ_μ is the momentum thickness in μ, and in contrast with Equation 2.47 the non-dimensionalized equivalent jet radius which is unity has been explicitly assumed.

The basic azimuthal velocity at $\theta = 0$ is assumed to be

$$\bar{u}_\theta = \frac{\Phi}{2\pi\mu^2}\left[1 - e^{-\mu^2}\right] \tag{3.143}$$

where Φ is a parameter which controls the amount of the swirl. The azimuthal variation of the basic azimuthal velocity can be obtained from the continuity equation of the basic flow:

$$\frac{\partial \bar{\rho}\bar{u}_\theta}{\partial\theta} + (\Gamma^1_{12}\bar{\rho} + \Gamma^2_{22}\bar{\rho})\bar{u}_\theta = 0 \tag{3.144}$$

If the swirl is small, then the variations of the pressure in the radial and azimuthal direction is also small. In this case, the basic pressure can be assumed to be constant. In this work, the maximum basic azimuthal velocity is assumed to be 6% of the maximum basic streamwise velocity.

The basic mass fraction of the fuel is also assumed to follow a hyperbolic tangent profile:

$$Y_F = 0.5\left\{1 + \tanh\left[\frac{1}{4\delta_Y}\left[\frac{1}{\mu+\delta} - \mu - \delta\right]\right]\right\} \tag{3.145}$$

The basic mass fraction of the oxidizer is assumed to follow:

$$Y_O = \begin{cases} 0 & (\mu \le \delta) \\ 0.5\left\{1 - \tanh\left[\frac{1}{4\delta_Y}\left(\frac{1}{\mu - \delta} - \mu + \delta\right)\right]\right\} & (\mu > \delta) \end{cases} \tag{3.146}$$

where δ_Y represents the width the mass fractions of the fuel and oxidizer spread; δ represents amount of the deviation of the mass fractions from the location of the shear layer. The mass fraction of the product is determined by the requirement that the sum of the mass fractions of all the chemical species is unity. Figure 3.7 shows the distributions of mass fractions of the fuel and oxidizer.

The basic temperature is assumed to be proportional to the mass fraction of the product:

$$\bar{T} = \bar{T}_{\text{nocomb}} + C_t(1 - Y_F - Y_O) \tag{3.147}$$

where $\bar{T}_{\text{nocomb}}$ represent the temperature in the shear layer according to the Crocco-Busemann relationship; C_t is a constant determined in such a way that the maximum basic temperature at the center of the shear layer is a certain fraction higher than that at the jet center line. That is:

$$T_{\text{nocomb}} = T^* + (1 - T^*)\bar{u}_z(z) + \frac{k-1}{2}M^2\bar{u}_z(\mu)\left[1 - \bar{u}_z(\mu)\right] \tag{3.148}$$

$$T^* = \frac{T_\infty}{T_0} \tag{3.149}$$

$$C_t = \frac{0.1Q_0}{\max(\,1 - Y_F - Y_O\,)} \tag{3.150}$$

$$\frac{\partial \bar{T}}{\partial \mu} = \frac{\partial T_{\text{nocomb}}}{\partial \mu} - C_t\left[\frac{\partial Y_F}{\partial \mu} + \frac{\partial Y_O}{\partial \mu}\right] \tag{3.151}$$

$$\frac{\partial Y_F}{\partial \mu} = 0.5\frac{\dfrac{1}{4\delta_Y}\left[-\dfrac{1}{(\mu+\delta)^2} - 1\right]}{\cosh^2\left[\dfrac{1}{4\delta_Y}\left[\dfrac{1}{\mu+\delta} - \mu - \delta\right]\right]} \tag{3.152}$$

$$\frac{\partial Y_O}{\partial \mu} = \begin{cases} -0.5\dfrac{\dfrac{1}{4\delta_Y}\left[-\dfrac{1}{(\mu-\delta)^2} - 1\right]}{\cosh^2\left[\dfrac{1}{4\delta_Y}\left[\dfrac{1}{\mu+\delta} - \mu + \delta\right]\right]} & (\mu > \delta) \\ 0 & (\mu \le \delta) \end{cases} \tag{3.153}$$

Assuming that the variation of the basic pressure due to the swirl is small, the basic density can be determined using:

$$\bar{\rho} = \frac{\tilde{\rho}}{\rho_0} = \frac{\dfrac{\tilde{p}}{R_M T_0 \bar{T}}}{\dfrac{\tilde{p}_0}{R_M T_0}} = \frac{1}{\bar{T}} \tag{3.154}$$

3.6 Vorticity Field

The vorticity eigenfunction can be obtained from the velocity eigenfunctions. First the velocity eigenfunctions in the Cartesian coordinate system u_x, u_y and u_z can be obtained from

$$u_x = u_\mu \frac{\partial x}{\partial \mu} + u_\theta \frac{\partial x}{\partial \theta} \tag{3.155}$$

$$u_y = u_\mu \frac{\partial y}{\partial \mu} + u_\theta \frac{\partial y}{\partial \theta} \tag{3.156}$$

$$u_z = u_z \tag{3.157}$$

The partial derivatives of these velocity eigenfunctions in the generalized cylindrical coordinate system are:

$$\frac{\partial u_x}{\partial \mu} = \frac{\partial u_\mu}{\partial \mu}\frac{\partial x}{\partial \mu} + u_\mu \frac{\partial^2 x}{\partial \mu^2} + \frac{\partial u_\theta}{\partial \mu}\frac{\partial x}{\partial \theta} + u_\theta \frac{\partial^2 x}{\partial \mu \partial \theta} \tag{3.158}$$

$$\frac{\partial u_x}{\partial \theta} = \frac{\partial u_\mu}{\partial \theta}\frac{\partial x}{\partial \mu} + u_\mu \frac{\partial^2 x}{\partial \mu \partial \theta} + \frac{\partial u_\theta}{\partial \theta}\frac{\partial x}{\partial \theta} + u_\theta \frac{\partial^2 x}{\partial \theta^2} \tag{3.159}$$

$$\frac{\partial u_y}{\partial \mu} = \frac{\partial u_\mu}{\partial \mu}\frac{\partial y}{\partial \mu} + u_\mu \frac{\partial^2 y}{\partial \mu^2} + \frac{\partial u_\theta}{\partial \mu}\frac{\partial y}{\partial \theta} + u_\theta \frac{\partial^2 y}{\partial \mu \partial \theta} \tag{3.160}$$

$$\frac{\partial u_y}{\partial \theta} = \frac{\partial u_\mu}{\partial \theta}\frac{\partial y}{\partial \mu} + u_\mu \frac{\partial^2 y}{\partial \mu \partial \theta} + \frac{\partial u_\theta}{\partial \theta}\frac{\partial y}{\partial \theta} + u_\theta \frac{\partial^2 y}{\partial \theta^2} \tag{3.161}$$

The partial derivative of these velocity eigenfunctions with respect to the Cartesian coordinates are:

$$\frac{\partial u_x}{\partial x} = \frac{\partial u_x}{\partial \mu}\frac{\partial \mu}{\partial x} + \frac{\partial u_x}{\partial \theta}\frac{\partial \theta}{\partial x} \tag{3.162}$$

$$\frac{\partial u_x}{\partial y} = \frac{\partial u_x}{\partial \mu}\frac{\partial \mu}{\partial y} + \frac{\partial u_x}{\partial \theta}\frac{\partial \theta}{\partial y} \tag{3.163}$$

$$\frac{\partial u_y}{\partial x} = \frac{\partial u_y}{\partial \mu}\frac{\partial \mu}{\partial x} + \frac{\partial u_y}{\partial \theta}\frac{\partial \theta}{\partial x} \tag{3.164}$$

$$\frac{\partial u_y}{\partial y} = \frac{\partial u_y}{\partial \mu}\frac{\partial \mu}{\partial y} + \frac{\partial u_y}{\partial \theta}\frac{\partial \theta}{\partial y} \tag{3.165}$$

$$\frac{\partial u_z}{\partial x} = \frac{\partial u_z}{\partial \mu}\frac{\partial \mu}{\partial x} + \frac{\partial u_z}{\partial \theta}\frac{\partial \theta}{\partial x} \tag{3.166}$$

$$\frac{\partial u_z}{\partial y} = \frac{\partial u_z}{\partial \mu}\frac{\partial \mu}{\partial y} + \frac{\partial u_z}{\partial \theta}\frac{\partial \theta}{\partial y} \tag{3.167}$$

Since

$$x = x(\mu, \theta) \tag{3.168}$$

$$y = y(\mu, \theta) \tag{3.169}$$

The derivatives of the generalized cylindrical coordinate μ and θ with respect to the Cartesian coordinates x and y can be determined from solving the following equations:

$$1 = \frac{\partial x}{\partial \mu}\frac{\partial \mu}{\partial x} + \frac{\partial x}{\partial \theta}\frac{\partial \theta}{\partial x} \tag{3.170}$$

$$0 = \frac{\partial x}{\partial \mu}\frac{\partial \mu}{\partial y} + \frac{\partial x}{\partial \theta}\frac{\partial \theta}{\partial y} \tag{3.171}$$

$$0 = \frac{\partial y}{\partial \mu}\frac{\partial \mu}{\partial x} + \frac{\partial y}{\partial \theta}\frac{\partial \theta}{\partial x} \tag{3.172}$$

$$1 = \frac{\partial y}{\partial \mu}\frac{\partial \mu}{\partial y} + \frac{\partial y}{\partial \theta}\frac{\partial \theta}{\partial y} \tag{3.173}$$

The partial derivatives of the velocity eigenfunctions with respect to the streamwise coordinate can be determined from the normal mode assumption, that is,

$$\frac{\partial u_x}{\partial z} = i\alpha u_x \tag{3.174}$$

$$\frac{\partial u_y}{\partial z} = i\alpha u_y \tag{3.175}$$

$$\frac{\partial u_z}{\partial z} = i\alpha u_z \tag{3.176}$$

Finally, the vorticity eigenfunctions can be determined as

$$\Omega_x = \frac{\partial u_z}{\partial y} - \frac{\partial u_y}{\partial z} \tag{3.177}$$

$$\Omega_y = \frac{\partial u_x}{\partial z} - \frac{\partial u_z}{\partial x} \tag{3.178}$$

$$\Omega_z = \frac{\partial u_y}{\partial x} - \frac{\partial u_x}{\partial y} \tag{3.179}$$

3.7 Validation of Code

First let us compare the dispersion relationship of a circular jet from the elliptical code and the circular jet code which was described in Chapter 2. Table 3.1 shows this comparison for the $m = 0$ mode of the incompressible circular jet with a normalized (with the jet radius) momentum thickness $\theta_{cir} = 0.1$. The $m = 0$ mode corresponds to the fundamental π mode of the elliptical jet when the aspect ratio is unity. From Table 3.1 we see that the growth rates and the phase speeds of the circular jet from the two codes are in agreement up to the third decimal place.

The comparison of the pressure eigenfunctions which are obtained from the two codes are given in Figure 3.8. Excellent agreement is obtained.

Now the $m = 1$ mode will be considered. The growth rate and phase speed of the

$m = 1$ mode of the circular jet (again with momentum thickness $\theta_{cir} = 0.1$) is given in Table 3.2. Similar to the $m = 0$ mode, the growth rates and phase speeds agree up to the third third decimal place.

As a final verification of the current results, a comparison of the dispersion relationship with the Koshigoe's results for an $AR = 2$ elliptical jet with uniform and very thin momentum thickness. The growth rate and phase speed obtained from Koshigoe's figure appear as symbols on the dispersion relationship curves in Figure 3.9. In general, the agreement is good. The small differences in the growth rate is thought to be caused by the difference in the form of velocity profile.

In this work, 30 points were used in the radial direction; 10 points were used in the upper half plane of the cross section of the jet. To verify that the calculations were sufficiently resolved, the number of points in both the radial and azimuthal directions were increased. The results are shown in Tables 3.3 and 3.4. From these results we see little effect from increasing the number of points. This verifies the original choice of radial and azimuthal spacing.

Chapter 4. Results

4.1 Introduction

The procedure described in Chapter 3 has been used to study the behavior of elliptical jets. In this chapter, the momentum thickness is denoted by θ. By the context it will be clear when θ refers to the momentum thickness and when it refers to the azimuthal coordinate.

As will be demonstrated shortly, it is important to compare jets of different aspect ratios on a consistent basis. In this chapter this will be taken to be as follows:

1. All jets will have equal flow area (see Section 3.2);
2. All jets will have equal centerline Mach number;
3. All jets will have equal momentum area (see Section 3.2) and an equivalent circular momentum thickness of 0.0707 ($R/\theta = 14.14$);
4. All jets will have equal disturbance kinetic energy at the nozzle exit as explained in the following

With linear stability analysis, we can obtain the dispersion relationship and the eigenfunction which represent the level of the disturbance. It will be necessary, however, to independently specify the level of the disturbance in comparison with the basic flow. Since the solution of stability problem can only be obtained up to an arbitrary multiplicative constant, the product of any constant and the eigenfunction is also an

eigenfunction of the stability problem. In this work, the maximum magnitude of the streamwise velocity disturbance of the circular jet at the nozzle exit is set to be 2% of the center line basic streamwise velocity and the multiplicative constant for any aspect ratio jet will be adjusted in that the disturbance kinetic energy (DKE)

$$\text{DKE} = 0.5(|u_x'|^2 + |u_y'|^2 + |u_z'|^2)$$

is constant.

4.2 Equal Momentum Thickness vs. Equal Momentum Area Comparison

Figure 4.1 shows the comparison of growth rates of jets of different aspect ratios on the basis of equal uniform momentum thickness. The horizontal axis represent the scaled non-dimensional frequency $\frac{\omega\theta_{cir}}{U_z(0)}$. Here, θ_{cir} is the momentum thickness of the corresponding circular jet. The vertical axis is the scaled nondimensional growth rate $-\alpha_i\theta_{cir}$. We can see that if the minimum momentum thickness is kept the same while the aspect ratio is increased from 1 to 2, the growth rate decreases. When the aspect ratio is further increased to 3, the growth rate returns to about the same level of the circular jet. However, if the momentum area is kept the same, the results will be different. Figure 4.2 shows the comparison of growth rates of the circular and elliptical jets on the basis of equal momentum area. In contrast to the case with a equal momentum thickness, when the aspect ratio is increased from 1 to 2, the growth rate remains at about the same level. When the aspect ratio is further increased to 3, the growth rate increases significantly.

This shows that different results can be obtained using different methods of comparison. In the following, the results of the stability analysis will be presented on the basis of equal momentum area.

4.3 Influence of Aspect Ratio

The influence of the aspect ratio on the growth rate can be seen in Figure 4.2. In addition to the observation discussed in the last section that increasing the aspect ratio increases the growth rate, we find that the most amplified frequency, which is defined as the frequency at which the growth rate is at a maximum, is almost the same regardless of the value of the aspect ratio. The growth rates in the lower frequency region are less affected by the aspect ratio than the growth rates in the higher frequency region.

Figure 4.3 shows the scaled phase speeds $c_{ph}/U_z(0)$ as a function of the scaled frequency for the three cases in Figure 4.1. When the aspect ratio is increased from 1 to 2, the phase speed becomes slightly lower at the most amplified frequency. In the lower frequency region, the decrease in the phase speed is much more significant than that in the higher frequency region. This results in a less dispersive propagation of the disturbances for the elliptical jet. Less dispersive propagation of disturbances means that the disturbances of higher or lower frequencies travel at about more or less the same speed.

The growth rate and phase speed constitute the dispersion relationship of the stability problem, however, the distribution of disturbance in the flow field depends on the eigenfunction. Of particular interest is the velocity eigenfunction which is defined as the square root of the sum of the squares of the real and imaginary parts of the eigenfunctions of the individual velocity components.

In Figures 4.4 - 4.6, the distributions of the velocity eigenfunctions of the jets of equal momentum area are plotted. For the circular jet, it is apparent that the velocity eigenfunction is azimuthally uniform. For the elliptical jets, the velocity eigenfunctions are azimuthally non-uniform with the degree of non-uniformity increasing with aspect ratio. The maximum velocity eigenfunction occurs on the minor axis and the minimum velocity eigenfunction occurs on the major axis.

Because the eigenfunctions of the circular jet is azimuthally uniform, the development of vortical structures of the circular jet is also azimuthally uniform. This is shown in Figure 4.7 in which the surface of constant vorticity is plotted. In contrast, Figure 4.8 shows the surface of the constant vorticity of $AR = 2$ elliptical jet. The development of the vortical structures are clearly azimuthally non-uniform. They appear earlier on the minor axis than on the major axis. The reason is that the velocity eigenfunction is largest on the minor axis. This causes the disturbance to grow more rapidly in the minor axis region.

The non-uniform development of the vortical structures shown in Figure 4.8 is called out-of-plane motion. This can be easily seen by examining the streakline pattern. Figures 4.9 and 4.10 show the streaklines of an incompressible jet of aspect ratio of 2 in the major and minor axis planes, respectively. In these figures we see that the structures form first on the minor axis and thus the structures on the major axis appear to lead those on the minor axis. It is worth remarking that rollup is clearly seen in the linear stability analysis results even though rollup is recognized to be a non-linear phenomena.

This out-of-plane motion of the vortical structures has also been observed experimentally by Hussain and Husain [1989] and explained by the self induction of the vortex ring.

4.4 Influence of Momentum Thickness Distribution

In the last section, the influence of aspect ratio on jets with uniform momentum thickness was examined. In this section, the influence of different momentum thickness distribution around jet periphery on the stability properties of the $AR = 2$ elliptical jet will now be described.

Figure 4.11 shows the comparison of the growth rate of $AR = 2$ elliptical jets with three different momentum thickness distributions, i.e., $\theta_y/\theta_x = 1.0$, 0.8, and 1.2. For

$\theta_y/\theta_x = 0.8$, which represent the case in which the momentum thickness is smaller on the minor axis than on the major axis, the growth rate is larger than those of the uniform momentum thickness for which $\theta_y/\theta_x = 1.0$. However, if the minimum momentum thickness occurs on the major axis for which $\theta_y/\theta_x = 1.2$, the growth rate becomes lower than the one with uniform momentum thickness. Just as the influence of the aspect ratio, the greatest effect of varying the momentum thickness distributions on the growth rate is in the higher frequency region.

Figure 4.12 shows the influence of different momentum thickness distribution on the phase speed of the $AR = 2$ elliptical jet. Contrary to the response of growth rate to the variation of the momentum thickness distribution, the phase speed is the same above the most amplified frequency. Since the difference in phase speeds in the lower and higher frequency regions is much larger for the elliptical jet with a minimum momentum thickness on the minor axis, disturbance of the elliptical jet with a minimum momentum thickness on the minor axis is much more dispersive than the ones with uniform or minimum momentum thickness on the major axis.

The velocity eigenfunction of the elliptical jet with a minimum momentum thickness on the minor axis is plotted in Figure 4.13. Compared to Figure 4.5 in which the velocity eigenfunction of the elliptical jet with a uniform momentum thickness is plotted, the eigenfunction of the elliptical jet with a minimum momentum thickness on

the minor axis is more concentrated in the minor axis region and more azimuthally non-uniform. This is expected because the gradient of the basic streamwise velocity is larger on the minor axis than on the major axis and the disturbances are easier to grow in the minor axis region than in the major axis region.

With a minimum momentum thickness on the major axis, the gradient of the basic streamwise velocity is larger on the major axis, so the velocity eigenfunction should be larger there. However, this is not seen in Figure 4.14. This is because the momentum thickness on the major axis has not been reduced enough to shift the location of the maximum velocity eigenfunction to the major axis. From the stability analysis of the circular jet [Michalke, 1984], the larger the value of R/θ is, the more unstable the flow is. For the elliptical jet, R can be regarded as the local radius of curvature and is greatest on the minor axis. If the momentum thickness is uniform, R/θ is largest on the minor axis. To completely move the location of the maximum velocity eigenfunction from the minor axis to the major axis, the momentum thickness on the major axis must be sufficiently small. This is not the case here and in Figure 4.14, the magnitude of the velocity eigenfunction looks more azimuthally uniform than the cases with uniform momentum thickness and minimum momentum thickness on the minor axis.

In Figures 4.15 and 4.16 surfaces of constant vorticity for the cases with a minimum momentum thickness on the minor and major axes. Note that despite the fact

that the momentum thickness is smaller on the major axis for the case shown in Figure 4.16, the value of the eigenfunction on the minor axis is large enough to cause the structures to appear first on the minor axis as in the case with a minimum momentum thickness on the minor axis shown in Figure 4.15.

4.5 Behavior of First Azimuthal Modes

In Figure 4.17, the growth rates of the sine and cosine modes of an elliptical jet with uniform momentum thickness are compared with that of the $m = 1$ mode of a corresponding circular jet. Immediately we can see that the most amplified frequency of the sine mode is smaller than that of the cosine mode of the elliptical jet. However, the most amplified frequency of the sine mode is almost the same as that of the $m = 1$ mode of the corresponding circular jet. The growth rate of the sine mode is always greater than that of the $m = 1$ mode of the circular jet. For the elliptical jet, the sine mode has a greater growth rate than that of the cosine mode, particularly in the most amplified frequency region and low frequency region. But this difference in growth rate becomes smaller in the higher frequency region. Above $\frac{\omega\theta}{U_z(0)} = 0.2$, the difference in the growth rates of the sine and cosine modes is negligible. In addition, we can note that the growth rate of the circular jet lies between the those of the sine and cosine modes below the most amplified frequency of the circular jet. In the higher frequency region, the circular jet has a smaller growth rate than both of the sine and cosine modes.

Figure 4.18 shows the comparison of the phase speeds of the sine and cosine modes of the $AR = 2$ elliptical jet with that of the $m = 1$ mode of the circular jet. From this figure we can see that the phase speed of the sine mode is smaller than that of the cosine mode of the elliptical jet. The phase speeds of the $m = 1$ mode of the circular jet lies between those of sine and cosine modes of the elliptical jet. Figures 4.19 and 4.20 show the distributions of the velocity eigenfunctions of the sine and cosine modes of the elliptical jet. For the sine mode, the velocity eigenfunction has a maximum value on the minor axis and a very small value on the major axis. For the cosine mode, the maximum value of the velocity eigenfunction occurs on the major axis. The eigenfunction of the cosine mode is very small on the minor axis. Because the phase speed of the sine mode is smaller than that of the cosine mode and the velocity eigenfunction of the sine mode is concentrated in the minor axis region, the disturbances on the minor axis travel more slowly than those on the major axis.

Figures 4.21 and 4.22 show the surfaces of constant vorticity of the sine and cosine mode of the $AR = 2$ elliptical jet. Since the eigenfunction of the sine mode is symmetrical about the minor axis, its surface of constant vorticity is symmetrical about the minor axis. Similarly, the surface of constant vorticity of the cosine mode is symmetrical about the major axis.

4.6 Influence of Swirl

The influence of swirl on the growth rate and phase speed of the fundamental π mode is shown in Figures 4.23 and 4.24. Two levels of swirl were considered: no swirl and 6% swirl. Here the 6% swirl means that the maximum basic azimuthal velocity is 6% that of the basic streamwise velocity. From Figure 4.23 we can see that the swirl decreased the growth rate of the fundamental π mode of the elliptical jet in the most amplified frequency region and the lower frequency region; In the higher frequency region, the swirl increases the growth rate by a small amount. However, we can note that the overall variation of the growth rate as a result of the introduction of swirl is small. This is similar to the results of Khorrami's investigation [1991] of the swirling circular jet. From Figure 4.24 we can see that the swirl increases the phase speed of the fundamental π mode by a small amount over the entire frequency range.

In Figure 4.25, the velocity eigenfunction of the swirling elliptical jet is plotted. Because of the presence of the swirl, the velocity eigenfunction is no longer symmetrical about the major or minor axis. One can easily imagine why some symmetries are lost if there is a swirling basic flow in the elliptical jet. Suppose the swirl is in the counter-clockwise direction, then the swirling direction in the first quadrant is toward the minor axis, the swirling direction in the second quadrant is toward the major axis. Thus the flow properties in the first and second quadrants must be different. However, since the swirling direction of the third quadrant is toward the minor axis which is the same as that

of the first quadrant, the symmetry property about the coordinate origin still exists.

Figure 4.26 shows the surface of constant vorticity of the $AR = 2$ elliptical jet with 6% swirl. The asymmetry shown in this surface is a result of both the swirling basic flow and the asymmetrical eigenfunctions.

Overall, the influence of swirl on the dispersion relationship of the fundamental π mode is small. However, the swirl increases the asymmetry of the flow. This causes the structures of the flow to be more complicated.

For the first azimuthal modes of jets with a swirl, the stability properties are direction dependent. For the circular jet, the mode in which the disturbance travels in the same direction of the swirl is called the positive (+) mode, while the mode in which the disturbance travels in the opposite direction of the swirl is called the negative (-) mode. For the elliptical jet, the same convention is used. In Figure 4.27, the comparison of the growth rates of the positive and negative modes of the elliptical jet with 6% swirl with those of the circular jet with 6% swirl is made. The most amplified frequency of the negative mode of the elliptical jet is almost the same as those of the two first azimuthal mode of the swirling circular jet. The most amplified frequency of the positive mode of the elliptical jet is larger than the three modes discussed above.

Similar to the case of the circular jet, the negative mode of the elliptical jet has a greater growth rate than the positive mode. This is also believed to be a result of the fact the disturbance of the negative mode is traveling in the opposite direction of the swirl. In the low frequency region, the difference in the growth rates of the the positive and negative mode is larger for the elliptical jet. In addition, the growth rate of the negative mode of the elliptical jet is larger than both the two first azimuthal modes of the circular jet; the growth rate of the positive mode of the elliptical jet is smaller than both the two first azimuthal modes of the circular jet in the low frequency region; In the higher frequency region, the difference in the growth rate of both the positive and negative modes of the elliptical jet is smaller, and the growth rates are higher than those of the circular jet. Therefore, if only the first azimuthal modes were present in the elliptical jet, the large scale structures would be dominated by the negative mode. The smaller structures will be formed because both the positive and negative mode of the elliptical jet have closer growth rate in the high frequency region.

Figure 4.28 shows the phase speeds of the positive and negative modes of the $AR = 2$ elliptical jet in comparison with those of the corresponding modes of the circular jet. Just as in the case of the circular jet, the phase speed of the positive mode of the elliptical jet is larger than that of the negative mode. Moreover, the difference in the phase speed of the positive and negative modes is larger for the elliptical jet than for the circular jet.

The velocity eigenfunction of the positive first azimuthal mode of the elliptical jet is shown in Figure 4.29. It is apparent that the distribution of the velocity eigenfunction is asymmetrical. The velocity eigenfunction of the negative first azimuthal mode is shown in Figure 4.30. We can notice from these Figures 4.29 and 4.30 that the distributions of the positive and negative first azimuthal modes resemble those of the cosine and sine modes of the elliptical jet with no swirl.

In the above discussion, we have claimed that one of the first azimuthal mode of the swirling elliptical jet is the positive mode and the other is the negative mode. In reality, it is very difficult to determine if a certain mode is the positive mode or the negative mode by just looking at the distribution of the eigenfunction. The method that the author used in determining in which direction the disturbance travels is to find the coefficients of the trigonometric expansion of the eigenfunction in the azimuthal direction and compare the relative size of these coefficients. Table 4.1 contain the coefficients of this trigonometric expansion of the streamwise velocity eigenfunction for the positive mode. It can be seen in this table that the coefficient of the $e^{\theta i}$ term is larger than the coefficient of the the $e^{-\theta i}$ term. Thus this mode should be the positive mode. The negative mode can be similarly determined by examining the coefficients listed in Table 4.2.

Figures 4.31 and 4.32 show the surfaces of constant vorticity of the positive and

negative first azimuthal modes of the elliptical jet with 6% swirl. From these figures we also see that the surfaces of constant vorticity of the positive and negative first azimuthal modes resemble those of the cosine and sine modes of the elliptical jet without swirl except that the structures are shifted in the direction of the swirl.

4.7 Influence of Heat Release

The influence of the heat release on the growth rate of the fundamental π mode of the $AR = 2$ elliptical jet is shown in Figure 4.33. When the heat release Q_0 is increased, the growth rate decreases in the high frequency region. Here $Q_0 = 2$ and 10 correspond to the amounts of heat release which cause the maximum basic temperature to increase by 20% and 100%, respectively. The growth rate in the lower frequency region is not influenced by the heat release. Since the growth rate is smaller when the heat release is higher, it has a stabilizing effect on the elliptical jet flow. The phase speeds of the fundamental π mode of the elliptical jets with different levels of heat release are shown in Figure 4.34. Contrary to the growth rate, the phase speed of the elliptical jet is not sensitive to the different amount of the heat release in the high frequency region. In the low frequency region, however, the phase speed becomes smaller as the heat release becomes higher. Since the difference between the phase speeds in the low frequency and high frequency regions is smaller for the elliptical jet with higher heat release than for the elliptical jet with lower or no heat release, the heat release makes the jet flow less dispersive.

Even though the dispersion relationship of the fundamental π mode is influenced by the heat release, the eigenfunctions are not changed much by the introduction of heat release. This conclusion can be obtained by comparing the Figure 4.35, in which the velocity eigenfunction of the fundamental π mode of the elliptical jet with heat release is plotted, with the Figure 4.5. This means that the flow structures induced by the fundamental π mode of elliptical jets are the same regardless of the level of the heat release present in the flow.

By comparing Figure 4.36 which shows the surface of constant vorticity of the elliptical jet with heat release with Figure 4.8 which shows the surface of constant vorticity of the elliptical jet without heat release, we find that the presence of the heat release delays the development of the vortical structures of the flow. This delay is a result of the smaller growth rate of the elliptical jet with heat release.

The influence of the non-dimensional activation energy $\beta = E_a/R_u T_{\max}$ on the growth rate and phase speed of the fundamental π mode is shown in Figures 4.37 and 4.38. The activation energy is the energy barrier which the molecules of the reactants must surpass in order to form the product. From Figure 4.37 we can see that when β is lower, the growth rate is also lower. The reason is that lower activation energy means that the chemical reaction and therefore the energy release is facilitated. Similar to the energy release, the activation energy only influences the growth rate in the high

frequency region. From Figure 4.38 we can see that the activation energy does not influence the phase speed of the fundamental π mode.

The influence of the Damkohler number D_a on the growth rate and phase speed of the fundamental π mode is shown in Figures 4.39 and 4.40. The Damkohler number is a measure of the relative rate of the chemical process in the flow with respect to the convective process. The larger the Damkohler number is, the faster the chemical reaction occurs. For the fundamental π mode of the elliptical jet, increasing the Damkohler number increases the growth rate by a small amount in the high frequency region. The influence of the Damkohler number on the growth rate in the low frequency region is negligible. However, for the circular jet with a heat release, Shin and Ferziger [1991] found that the Damkohler number has little effect on the growth rate and phase speed. Just as in the case of a circular jet, the Damkohler number has negligible effect on the phase speed of the fundamental π mode of the $AR = 2$ elliptical jet.

The above discussion of the influence of the heat release on the stability properties of the jet flow is for the fundamental π mode. The influence of this parameter on the stability properties of the sine and cosine modes is the same as on the fundamental π mode. That is, increasing the heat release decreases the growth rate in the high frequency region and decreases the phase speeds in the low frequency region; decreasing the activation energy decreases the growth rate in the high frequency region and decreases

the phase speed in the low frequency region; and increasing the Damkohler number increases the growth rate in the high frequency region by a small amount. We obtained these results from Figures 4.41 - 4.52.

4.8 Mode Competition

It has been shown in experiments [Austin and Ho, 1992] that elliptical jets have finer structures than circular jets. Linear stability analysis provides an explanation for this behavior. For the circular jet, the $m = 0$ and $m = 1$ modes have different growth rates as we can see in Figure 4.53. For the elliptical jet of uniform momentum thickness, however, Figure 4.54 shows that the fundamental π mode and the sine mode have about the same growth rates and most amplified frequencies. Moreover, comparing Figures 4.18 and 4.3, it can be seen that the phase speeds of the fundamental π and sine modes are different. Thus according to Koshigoe's criteria [1988] linear stability analysis suggests that the large scale structures will be finer in an elliptical jet thus supports Austin and Ho's experimental observations.

It has been found, however, that these results are largely dependent upon the thickness of the shear layer. Calculations similar to those described above were repeated for a shear layer of approximately twice the current thickness. It was found in this case that the growth rate of the first azimuthal mode was much greater than the growth rate of

the fundamental π mode. This suggests that the mode competition would decrease.

4.9 Insights into Entrainment Process

Entrainment can be defined as the increase in the effective width of a jet as a result of the engulfment of the surrounding fluid by the large scale structures in the jet.

Figure 4.55 shows the entrainment measurements of Ho and Gutmark [1987] for the circular and elliptical jets. The ordinate is the ratio of the difference between the mass flow rates at a specified streamwise location and the nozzle exit to the the mass flow rate at the nozzle exit. From this figure we can see that the elliptical jet has a much larger entrainment than the circular jet. And this lager entrainment of the elliptical jet is largely due to the much larger entrainment in the minor axis region,

With linear stability analysis, however, it is impossible to predict the entrainment. The reason is the temporal periodicity implied by the normal mode assumption. Since it is impossible to calculate the amount of entrainment, we have computed several quantities which we believe are suggestive of entrainment; namely, the total, cross-plane, streamwise component of vorticity, and what we call the vorticity containing area.

We calculated the vorticity containing area by counting the number of cells on

which the time-averaged vorticity magnitude is larger than a minimum threshold value. This counting process is carried out in a uniform Cartesian coordinate system in which the real flow was constructed using linear stability results. The threshold value was set to be 10% of the maximum basic vorticity in the shear layer. From Figure 4.56 we can see that the vorticity-containing area is larger for the elliptical jet than for the circular jet. Moreover, we can see that it is larger in the minor axis region than in the major axis region. Since the entrainment is a measure of the global interaction of a jet with its surroundings and the vorticity is a measure of the local interaction of the fluid particles with their surroundings, the larger vorticity-containing region means that the local interaction of fluid particles extends to a larger area and suggests a larger entrainment of the jet.

Figure 4.57 shows the streamwise growth of the integral of the total vorticity of the elliptical and circular jets. The total vorticity used here is defined as the sum of the basic steady vorticity and the disturbance vorticity. It is clear that the vorticity level of the elliptical is larger than that of the circular jet. This also suggests the larger entrainment of elliptical jet because the vorticity level is a measure of the intensity of the local interaction of the fluid particles and larger intensity of the interaction of the fluid particles means larger entrainment.

To examine the vorticity in detail, the vorticity can be split into two parts, i.e., the

cross-plane vorticity and the streamwise vorticity. Figures 4.58 shows the streamwise growth of the cross-plane vorticity of the circular and elliptical jets. We can see that the cross-plane vorticity is larger than that of the circular jet.

Figure 4.59 shows the streamwise growth of the streamwise vorticity of the circular and elliptical jets. It is very clear that the streamwise vorticity of the circular jet is zero. This is because the eigenfunction of the circular jet is azimuthally uniform. This uniformity of the circular jet produces zero streamwise vorticity. However, the elliptical jet has a strong inherent non-uniformity which produces a non-zero cross-plane disturbance velocity. The non-zero cross-plane velocity causes the streamwise vorticity to appear for the elliptical jet.

The sign of the streamwise vorticity present in an elliptical jet can be explained by examining the way in which vortex roll-up occurs. Recall that roll-up occurs first on the minor axis and thus when completed the elliptial vortex ring has an out-of-plane shape in which the major axis "leads" the minor axis. This "bending" of the vortex ring produces a negative streamwise component of the originally azimuthal vorticity in the first quadrant and a positive streamwise component of the vorticity in the second quadrant. This is exactly what is shown in Figure 4.60 which shows the distribution of the streamwise vorticity at about two diameters downstream from the nozzle exit. In Figure 4.60, the flow is flowing out of the paper. We can see that the streamwise vorticities in the first

and second quadrants are in the negative and positive streamwise direction, This is expected to push high velocity fluid out of the minor axis region and cause the outside fluid to move along with the jet, thus producing a higher level of entrainment on the minor axis than on the major axis. This is the mechanism which is responsible for axis switching in an elliptical jet. Axis switching was observed in many experiments and was thought to be the cause of the higher entrainment of the elliptical jet. But according to the above discussion, it is a result of higher entrainment on the minor axis.

Figure 4.61 shows a surface of the constant streamwise vorticity magnitude of the elliptical jet. This surface also shows that the streamwise vorticity is zero on the major and minor axes and concentrated between the major and minor axes.

4.10 Suggestions for Enhancing Entrainment of Elliptical Jets

From the results of the last section, it clear that larger entrainment is associated with larger vorticity. But we believe that the entrainment of the elliptical jet can only be effectively enhanced by increasing the level of the streamwise vorticity. This is because the streamwise vorticity contributes to the non-uniform development of the vortical structures which the cross-plane vorticity does not. According to the previous discussions, the higher streamwise vorticity can be obtained by enhancing the non-uniformity and asymmetry of the eigenfunctions of the flow. And these non-uniformity

and asymmetry can be increased by increasing the aspect ratio, thinning the momentum thickness on the minor axis, and adding swirl. Since heat release has a stabilizing effect on the jet, it is advantageous to delay the occurrence of combustion until the fuel and the oxidizer are sufficiently mixed.

Chapter 5. Summary

Linear stability analysis has been used to study the stability properties of circular and elliptical jets. For the circular jet, the shooting method developed by Michalke was extended to account for the presence of the swirl. For the elliptical jet, a method was developed which combines the best features and capabilities of previous investigations and takes into account of the influence of aspect ratio, momentum thickness distribution, swirl and heat release. The calculations reveals that thinning the momentum thickness on the minor axis concentrates the velocity eigenfunction distribution in the minor axis region and has a greater effect on the stability properties than thinning the momentum thickness on the major axis. Two first azimuthal mode were found for the 2π mode. The sine mode has a larger growth rate, a maximum velocity eigenfunction on the minor axis, and a smaller phase speed, while the cosine mode has a smaller growth rate, a maximum velocity eigenfunction on the major axis, and a larger phase speed. Swirl has little effect on the dispersion relationship of the fundamental π mode of elliptical jets. However, the eigenfunctions are no longer symmetrical about the major and minor axis of the jet because of the presence of the swirl. For the first azimuthal mode, the swirl causes the negative mode to have a larger growth rate than the positive mode. The difference in phase speed of the first azimuthal modes of the swirling elliptical is larger than that of the swirling circular jet. The eigenfunctions of the first azimuthal modes of the elliptical jet with a swirl is asymmetrical. It was found that the heat release has a stabilizing effect on

the jet flow. Decreasing the activation energy causes the flow to be more stable in the high frequency region. Increasing the Damkohler number increases the growth rate by a small amount in the high frequency region. The eigenfunction distribution of the elliptical jet with a heat release is almost identical to that of the elliptical jet without heat release. Thus the flow structures are expected to be qualitatively the same whether or not there exists a heat release in the flow. It was also found that the linear stability analysis provides an insight of why the elliptical jet has a larger entrainment than the circular jet. Specifically, the vorticity-containing region and the vorticity level (in particular the streamwise vorticity) is larger in an elliptical jet than in a circular jet. To enhance the entrainment of the elliptical jet, it is necessary to increase the streamwise component of vorticity which in turn enhances the non-uniform development of the vortical structures in the flow. The non-uniform development of the vortical structures can be enhanced by increasing the non-uniformity and asymmetry of the velocity eigenfunction by increasing the aspect ratio, non-uniformly distributing the momentum thickness, and adding swirl. The stabilizing effect of heat release can be reduced by delaying the occurrence of combustion.

References

T. Austin and C. M. Ho, "Controlled Entrainment in a 2:1 Aspect-Ratio Subsonic Elliptic Nozzle," *AIAA 92-0537*

G. K. Batchelor and A. E. Gill, "Analysis of the Stability of Axisymmetric Jets," *Journal of Fluid Mechanics, 14, 529, 1962.*

R. S. Baty and P. J. Morris, "Instability of Jets of Arbitrary Geometry," *AIAA 89-1796.*

G. L. Brown and A. Roshko, "On Density Effects and Large Structures in Turbulent Mixing Layers," *Journal of Fluid Mechanics, Vol. 64, 1974, pp. 775-816.*

D. G. Crighton, "Instability of an Elliptical Jet," *Journal of Fluid Mechanics, Vol. 59, 1973, 665-672.*

M. Favre-Marinet, "Coherent Structures in a Round Jet," in *VKI Turbulent Shear Flows, 1989* Avail: NTIS HC A21/MF AO3.

F. F. Grinstein and K. Kailasanath, "Chemical Energy Release and Dynamics of Transitional, Reactive Shear Flows," *Physics of Fluids* A 4(10), October 1992.

C. E. Grosch and T. L. Jackson, "Inviscid Spatial Stability of a Three-Dimensional Compressible Mixing Layer," *Journal of Fluid Mechanics* vol. 231, pp. 35-50, 1991.

A. K. Gupta, *Flowfield Modeling and Diagnostics*, Abacus Press, Turnbridge Wells, Kent, 1985.

C. M. Ho and E. Gutmark, "Vortex Induction and Mass Entrainment in a Small-Aspect-Ratio Elliptical Jet," *Journal of Fluid Mechanics, 1987, 179: 383-405.*

Fazle Hussain and Hyder S. Husain, "Elliptical Jets. Part 1. Characteristics of Unexcited and Excited Jets," *Journal of Fluid Mechanics*, vol. 208, 1989, pp. 257-320.

T. L. Jackson and C. E. Grosch, "Inviscid Spatial Stability of a Compressible Mixing Layer. Part 2. The Flame Sheet Model," *Journal of Fluid Mechanics*, vol. 217, 1990, pp. 391-420.

T. L. Jackson and C. E. Grosch, "Inviscid Spatial Stability of a Compressible Mixing Layer. Part 3. Effect of Thermodynamics," *Journal of Fluid Mechanics*, vol. 224, 1991, pp. 159-175.

M. R. Khorrami, "Application of Spectral Collocation Techniques to the Stability of Swirling Flows," *Journal of Computational Physics* 81, 206-229, 1989.

M. R. Khorrami, "Stability of a Compressible Swirling Jet," *AIAA 91-1770*

S. Koshigoe and A. Tubis, "Wave Structures in Jets of Arbitrary Shape. I. Linear Inviscid Spatial Instability Analysis," *Physics of Fluids 29 (12), December 1986.*

S. Koshigoe and A. Tubis, "Wave Structures in Jets of Arbitrary Shape. II. Applications of a Generalized Shooting Method to Linear Stability Analysis," *Physics of Fluids 30 (6), June 1987.*

S. Koshigoe, A. Tubis and C. M. Ho, " Vortex Deformation in Elliptic-Core Jets from the Perspective of Linear Instability Analysis," *Phys. Fluids* 31 (9), September 1988.

Martin Lessen and Pawan Jit Singh, "The Stability of Axisymmetric Free Shear Layers," *Jounal of Fluid Mechanics,* vol. 60, part 3, pp.433-457, 1973.

S. Mahalingam, B. Cantwell and J. Ferziger, "Effects of Heat Release on the Structure and Stability of a Coflowing, Chemically Reacting Jet," *AIAA 89-0661.*

S. Mahalingam, B. J. Cantwell, and J. H. Ferziger, "Full Numerical Simulation of Coflowing, Axisymmetric Jet Diffusion Flames," *Physics of Fluids,* A, Vol. 2, No.5, May 1990

S. Mahalingam, B. J. Cantwell, and J. H. Ferziger, "Stability of Low-Speed Reacting Flows," *Physics of Fluids,* A, 3(6), June 1991.

P. A. McMurtry, W. H. Jou, J. J. Riley and R. W. Metcalfe, "Direct Numerical Simulation of a Reacting Mixing Layer with Chemical Heat Release," *AIAA 85-0143*

A. Michalke and G. Hermann, "On the Inviscid Instability of a Circular Jet with External Flow," *Journal of Fluid Mechanics, 114, 345-359, 1982.*

A. Michalke, "Survey on Jet Instability Theory," *Prog. Arospace Sci.* vol. 21, pp. 159-199, 1984.

P. J. Morris, "Instability of Elliptical Jets," *AIAA 86-1868.* or *AIAA Journal,* vol. 26, No. 2, February 1988, pp. 172.

P. J. Morris and D. G. Miller, "Wavelike Structures in Elliptical Jets," *AIAA 84-0399.*

H. S. Mukunda, J. Philip Drummond, "Two-Dimensional Stability of Laminar Flames," *NASA Technical Paper 3131, 1992*

R. A. Petersen and M. M. Samet, "On the Preferred Mode of Jet Instability," *Journal of Fluid Mechanics,* vol. 194, pp. 153-173, 1988.

O. H. Planche and W. C. Reynolds, "Heat Release Effects on Mixing in Supersonic Reacting Free Shear-Layers," *AIAA 92-0002*

K. C. Schadow, K. J. Wilson, M. J. Lee, E. Gutmark, "Enhancement of Mixing in Reacting Fuel-Rich Plumes Issued from Elliptical Nozzles," *Journal of Propulsion and Power,* Volume 3, Number 2, March-April 1987, page 145

H. Schlichting, *Boundary layer theory,* New York, McGraw-Hill, 1968.

F. S. Sherman, *Viscous Flow,* McGraw-Hill, Ch. 13, 1990.

D. S. Shin and J. H. Ferziger, "Stability of Compressible Reacting Mixing Layer," *AIAA 91-0372*

D. Shin and J. Ferziger, "Linear Stability of the Reacting Mixing Layer," *AIAA 92-0992* or *AIAA Journal* v 29 n10 October 1991.

C. Wu, S. Farokhi and R. Taghavi, "On Spatial Instability of a Swirling Jet --- Theory and Experiment," *AIAA 91-1771*

Table 3.1. The comparison of the elliptical jet code with the circular jet code.
$AR = 1$, $m = 0$, $\theta = 0.1$, $M = 0$

ω	$-\alpha_i$		c_{ph}	
	Circular Jet Code	Elliptical Jet Code	Circular Jet Code	Elliptical Jet Code
0.6	0.218294	0.217623	0.958427	0.959271
1.0	0.599945	0.597471	0.864588	0.865539
1.4	0.906868	0.904315	0.653268	0.655063
1.8	0.762780	0.760541	0.587832	0.588617

Table 3.2. The comparison of the elliptical jet code with the circular jet code.
$AR = 1$, $m = 1$, $\theta = 0.1$, $M = 0$

ω	$-\alpha_i$		c_{ph}	
	Circular Jet Code	Elliptical Jet Code	Circular Jet Code	Elliptical Jet Code
0.6	0.454302	0.453059	0.696882	0.697764
1.0	0.683225	0.681218	0.648609	0.649666
1.4	0.773053	0.771640	0.595955	0.597140
1.8	0.663886	0.659630	0.572907	0.572748

Table 3.3. The influence of the number of grid points.
$AR = 2$, $\omega = 1.8$, fundamental π mode, $M = 0$

	$-\alpha_i$	c_{ph}
$n_r = 30$, $n_\theta = 10$	1.42346	0.568095
$n_r = 46$, $n_\theta = 10$	1.42419	0.568103
$n_r = 30$, $n_\theta = 16$	1.42352	0.568103

Table 3.4. The influence of the number of grid points.
$AR = 2$, $\omega = 1.8$, sine mode, $M = 0$

	$-\alpha_i$	c_{ph}
$n_r = 30$, $n_\theta = 10$	1.41893	0.553429
$n_r = 46$, $n_\theta = 10$	1.42050	0.553546
$n_r = 30$, $n_\theta = 16$	1.41893	0.553430

Table 3.5. The influence of the number of grid points.
$AR = 2$, $\omega = 2.1$, cosine mode, $M = 0$

	$-\alpha_i$	c_{ph}
$n_r = 30$, $n_\theta = 10$	1.19702	0.627786
$n_r = 46$, $n_\theta = 10$	1.19614	0.627954
$n_r = 30$, $n_\theta = 16$	1.19703	0.627795

Table 4.1. The coefficients in the azimuthal Fourier expansion of the steamwise velocity eigenfunction of the positive first azimuthal mode of the $AR = 2$ elliptical jet with 6% swirl at the shear layer.

Terms	Coefficient	
	Real	Imaginary
$e^{-9\theta i}$	-.328155e-02	0.320498e-02
$e^{-7\theta i}$	-.152739e-01	-.585223e-02
$e^{-5\theta i}$	-.720380e-02	-.609676e-01
$e^{-3\theta i}$	0.129231e+00	-.102662e+00
$e^{-\theta i}$	0.270945e+00	0.512883e-01
$e^{\theta i}$	0.349930e+00	0.379724e-01
$e^{3\theta i}$	0.124607e+00	-.307712e+00
$e^{5\theta i}$	-.821938e-01	0.790138e-02
$e^{7\theta i}$	0.648595e-02	0.132355e-01
$e^{9\theta i}$	0.155799e-02	0.162309e-02

Table 4.2. The coefficients in the azimuthal Fourier expansion of the steamwise velocity eigenfunction of the negative first azimuthal mode of the $AR = 2$ elliptical jet with 6% swirl at the shear layer.

Terms	Coefficient	
	Real	Imaginary
$e^{-9\theta i}$	0.215304e-02	0.166588e-02
$e^{-7\theta i}$	-.117850e-01	-.116100e-02
$e^{-5\theta i}$	-.110410e-02	-.403713e-01
$e^{-3\theta i}$	0.123223e+00	-.787449e-02
$e^{-\theta i}$	0.145275e+00	0.457173e+00
$e^{\theta i}$	-.138915e+00	-.411175e+00
$e^{3\theta i}$	-.982866e-02	0.584277e-01
$e^{5\theta i}$	0.157217e-01	-.108323e-01
$e^{7\theta i}$	0.270052e-02	-.262431e-02
$e^{9\theta i}$	0.799358e-03	0.118153e-02

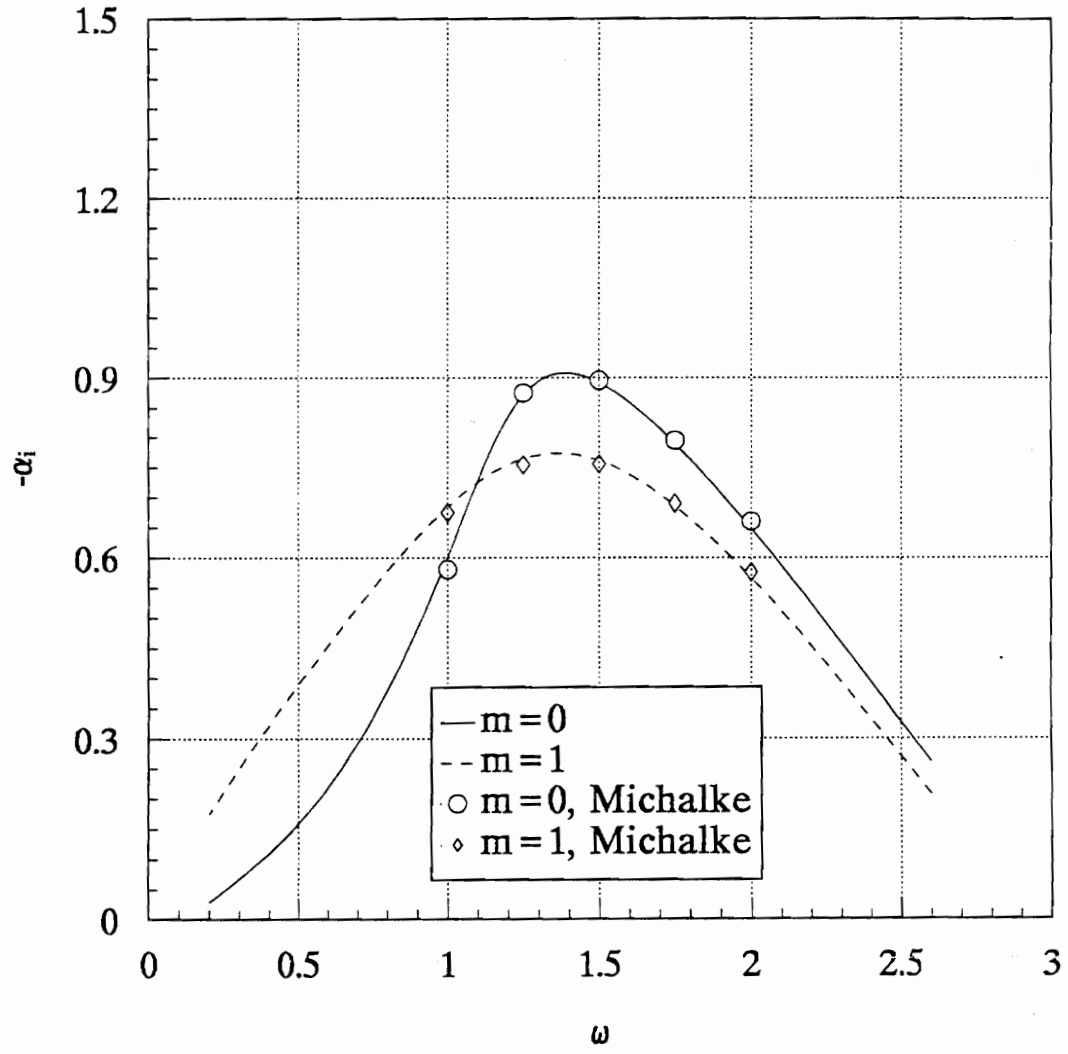

Figure 2.1. The comparison of the growth rate of the $m = 0, 1$ modes obtained from the author's code and Michalke's paper.

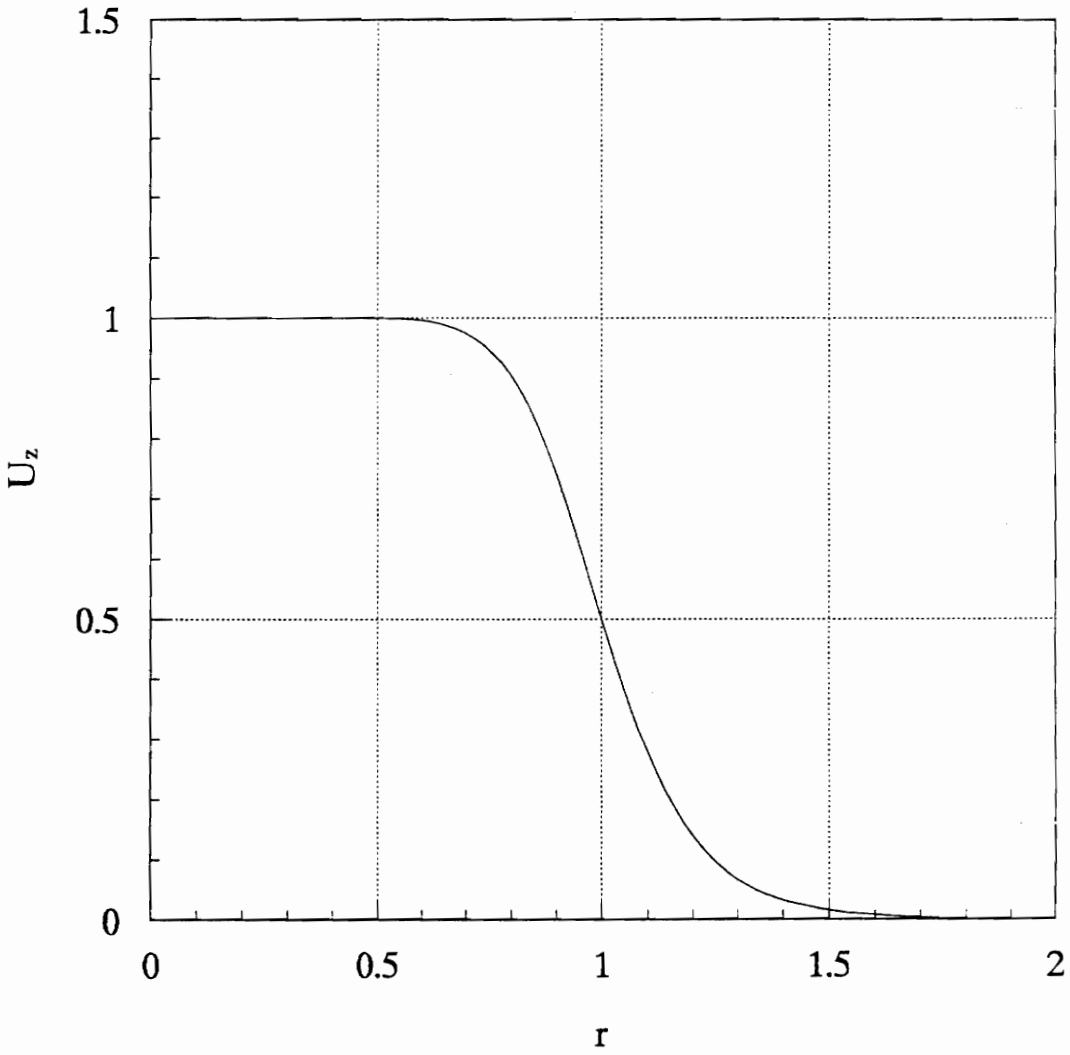

Figure 2.2. The basic steady streamwise velocity distribution.

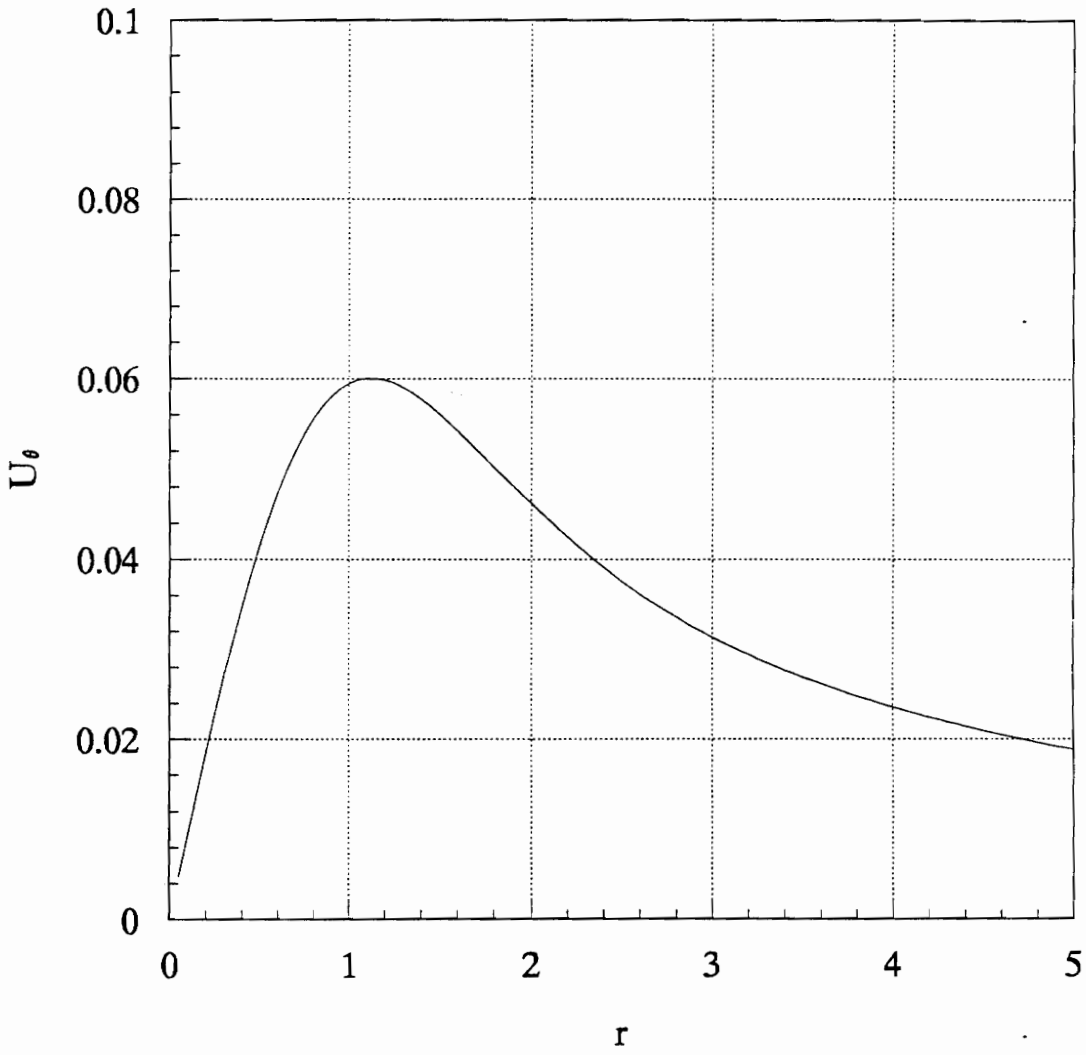

Figure 2.3. The basic steady azimuthal velocity distribution.

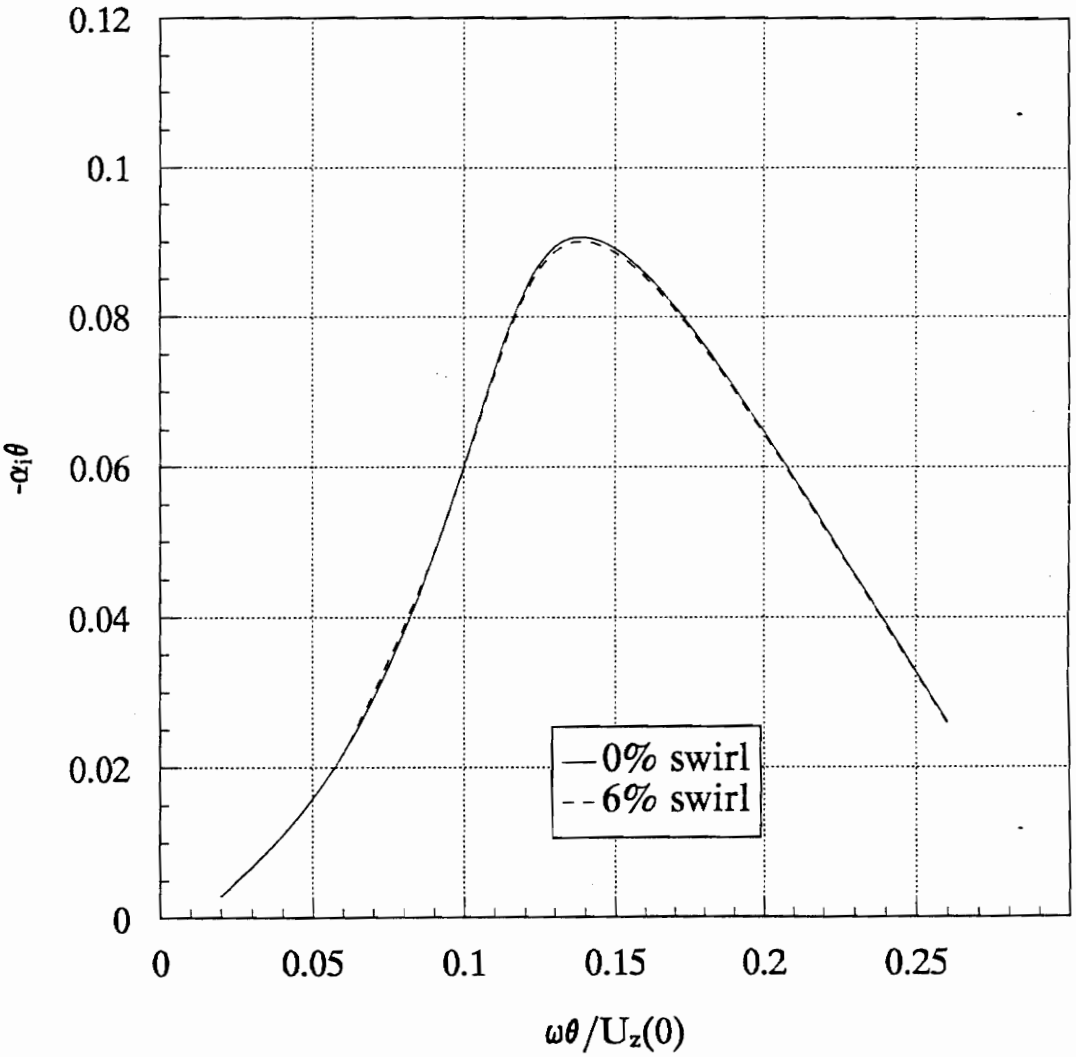

Figure 2.4. The influence of the swirl on the growth rate of the $m = 0$ mode.

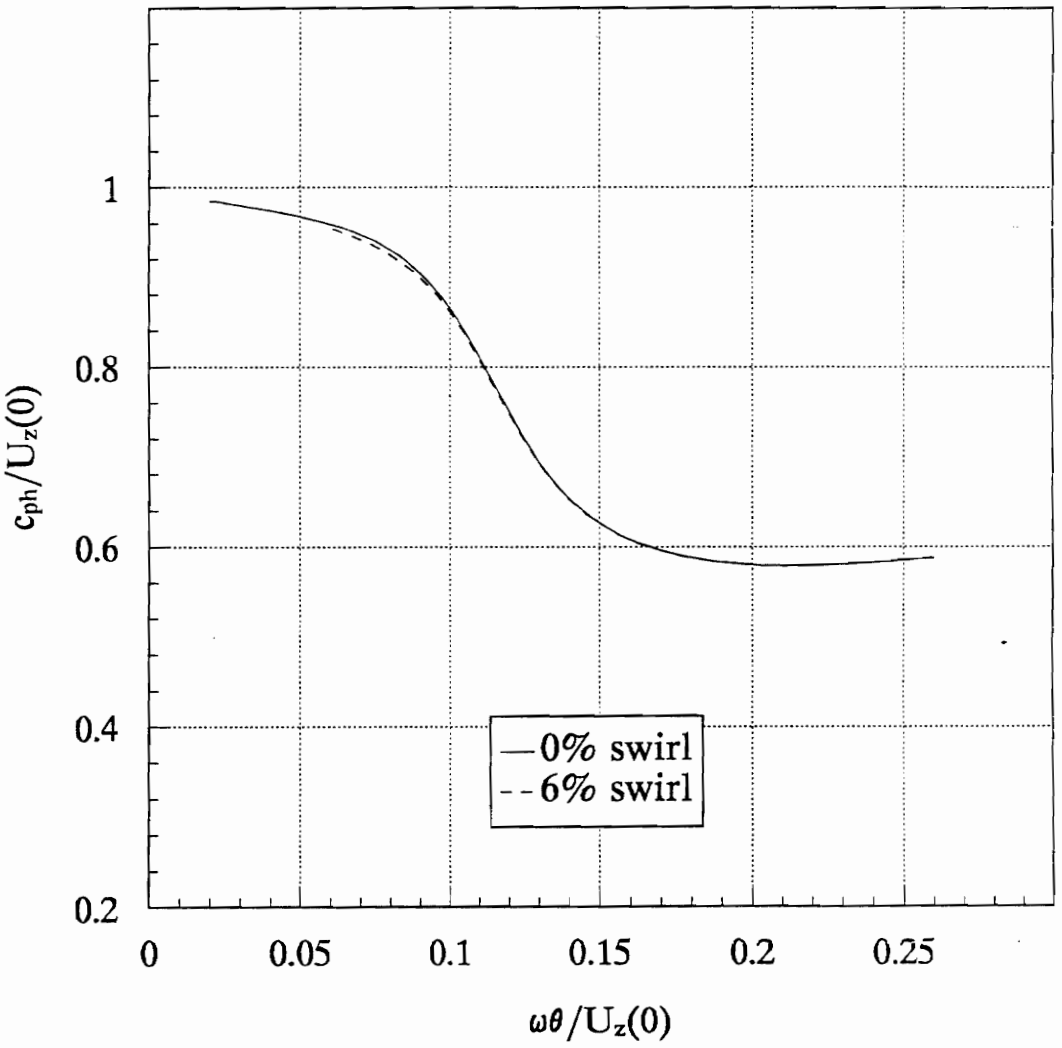

Figure 2.5. The influence of the swirl on the phase speed of the $m = 0$ mode.

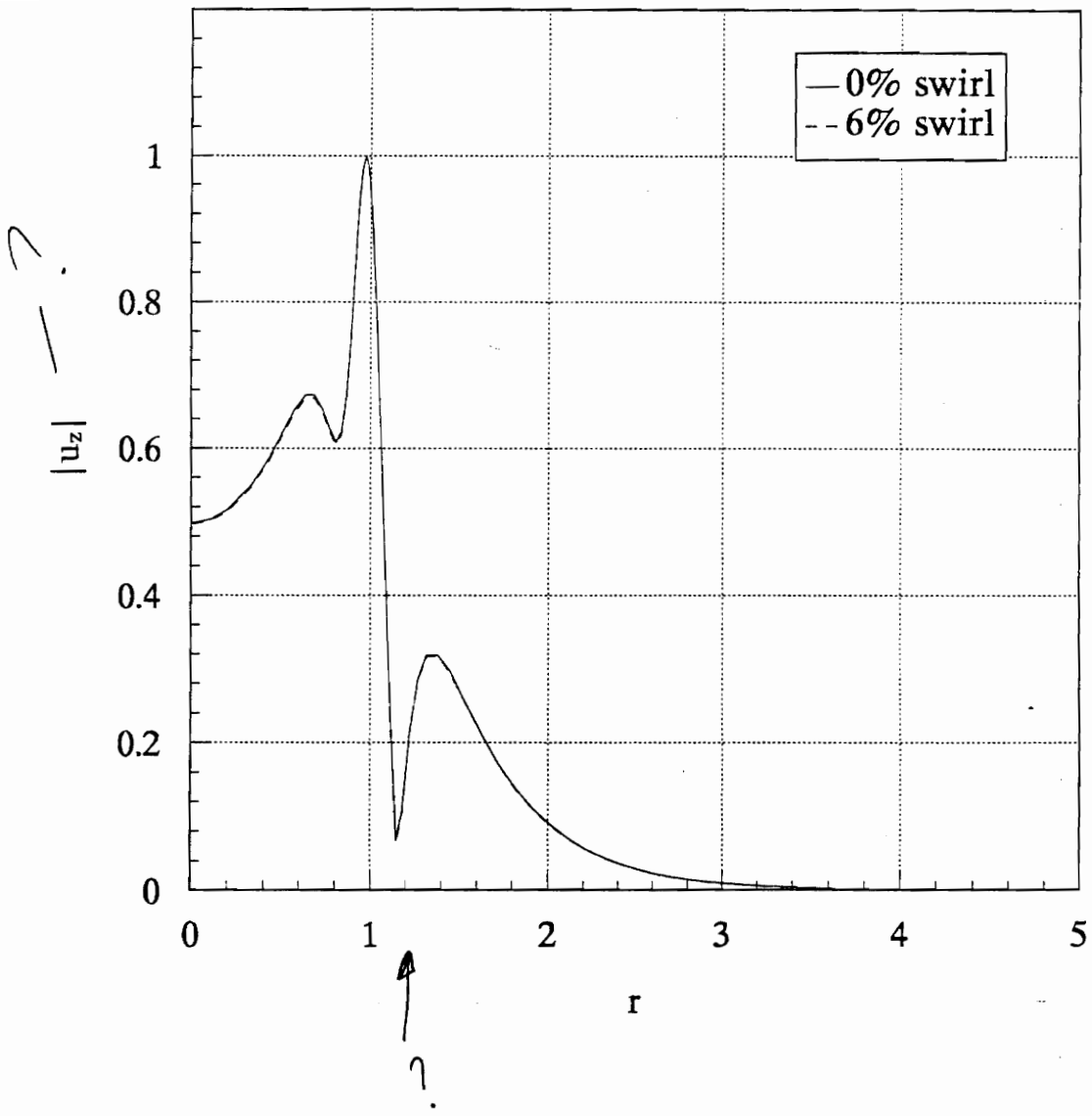

Figure 2.6. The distribution of the pressure eigenfunction of the $m = 0$ mode.

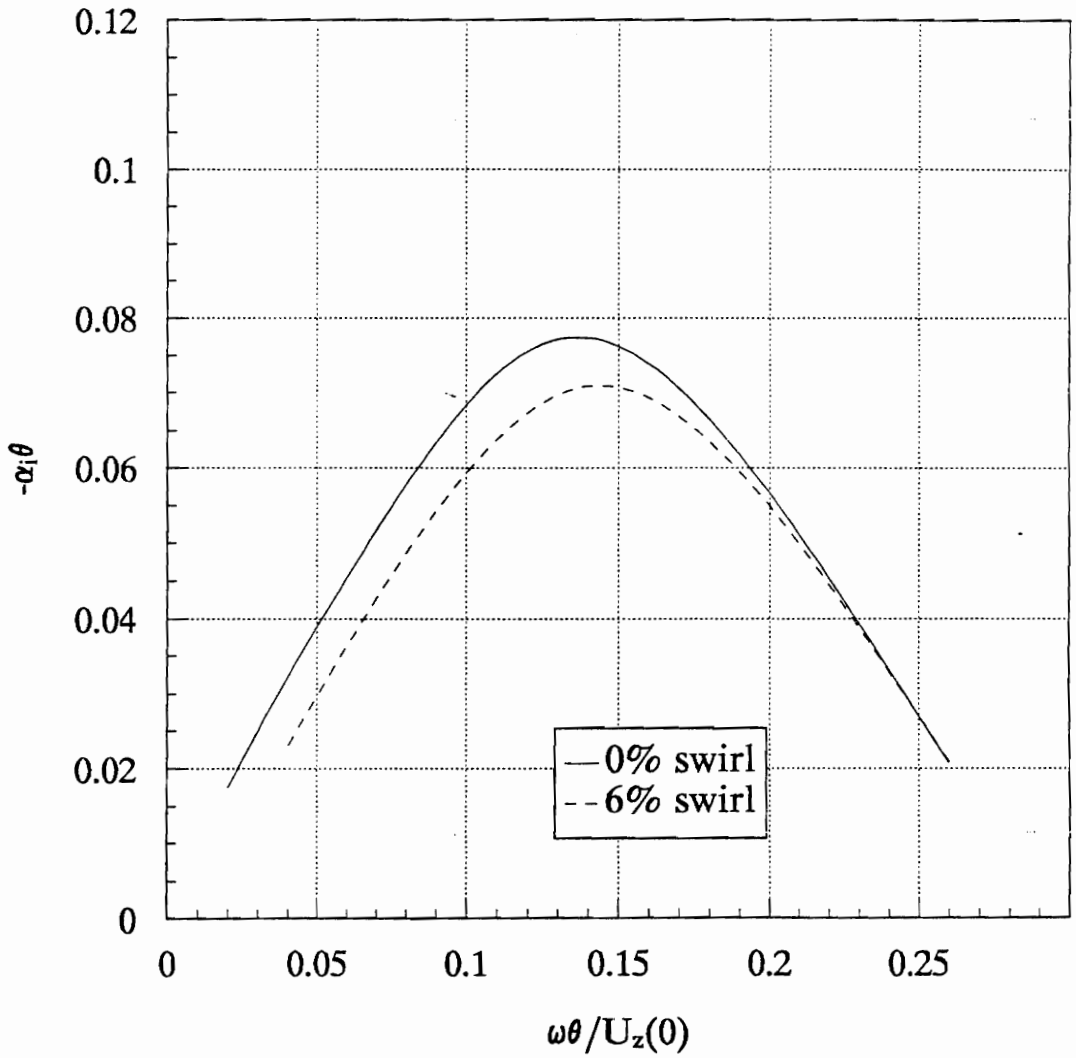

Figure 2.7. The influence of the swirl on the growth rate of the positive first azimuthal mode.

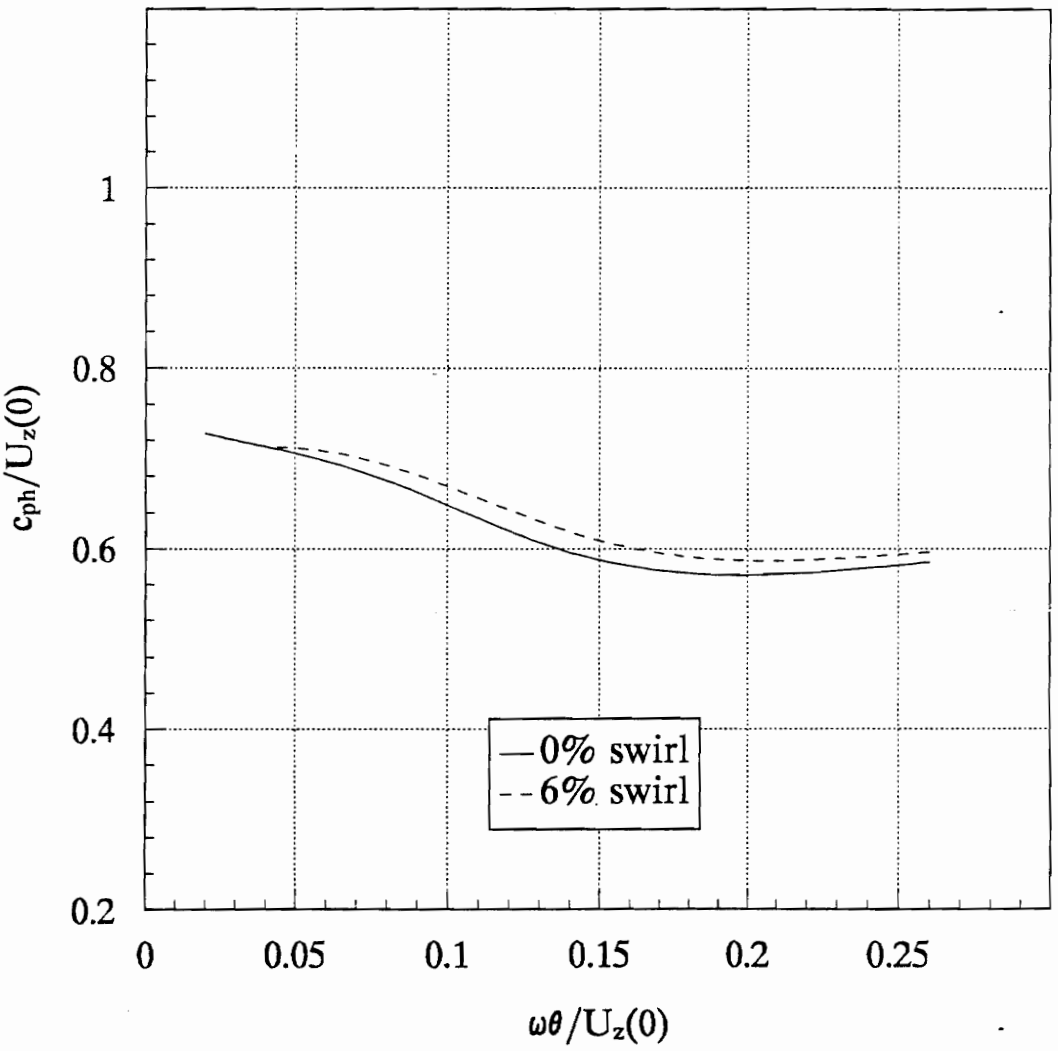

Figure 2.8. The influence of the swirl on the phase speed of the positive first azimuthal mode.

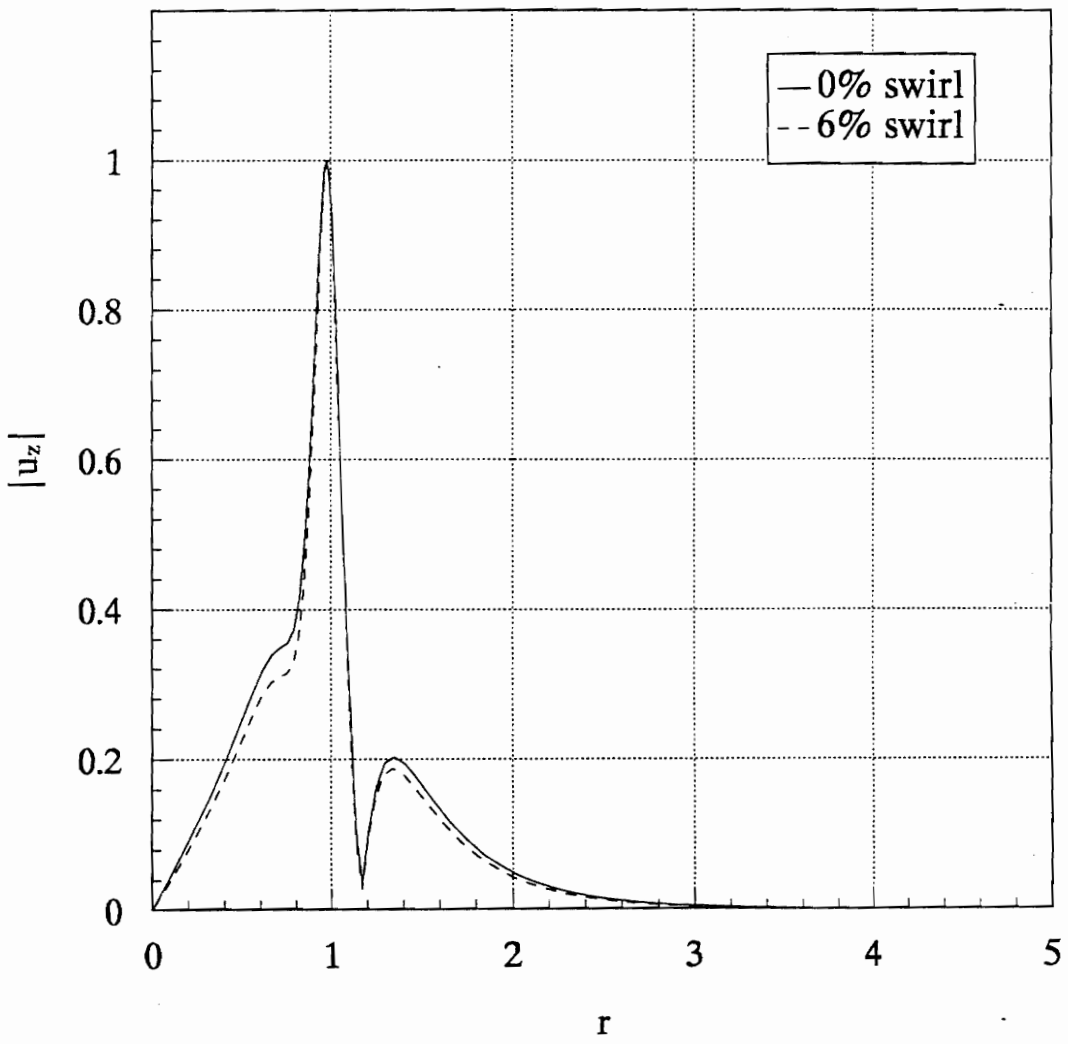

Figure 2.9. The distribution of the pressure eigenfunction of the positive first azimuthal mode.

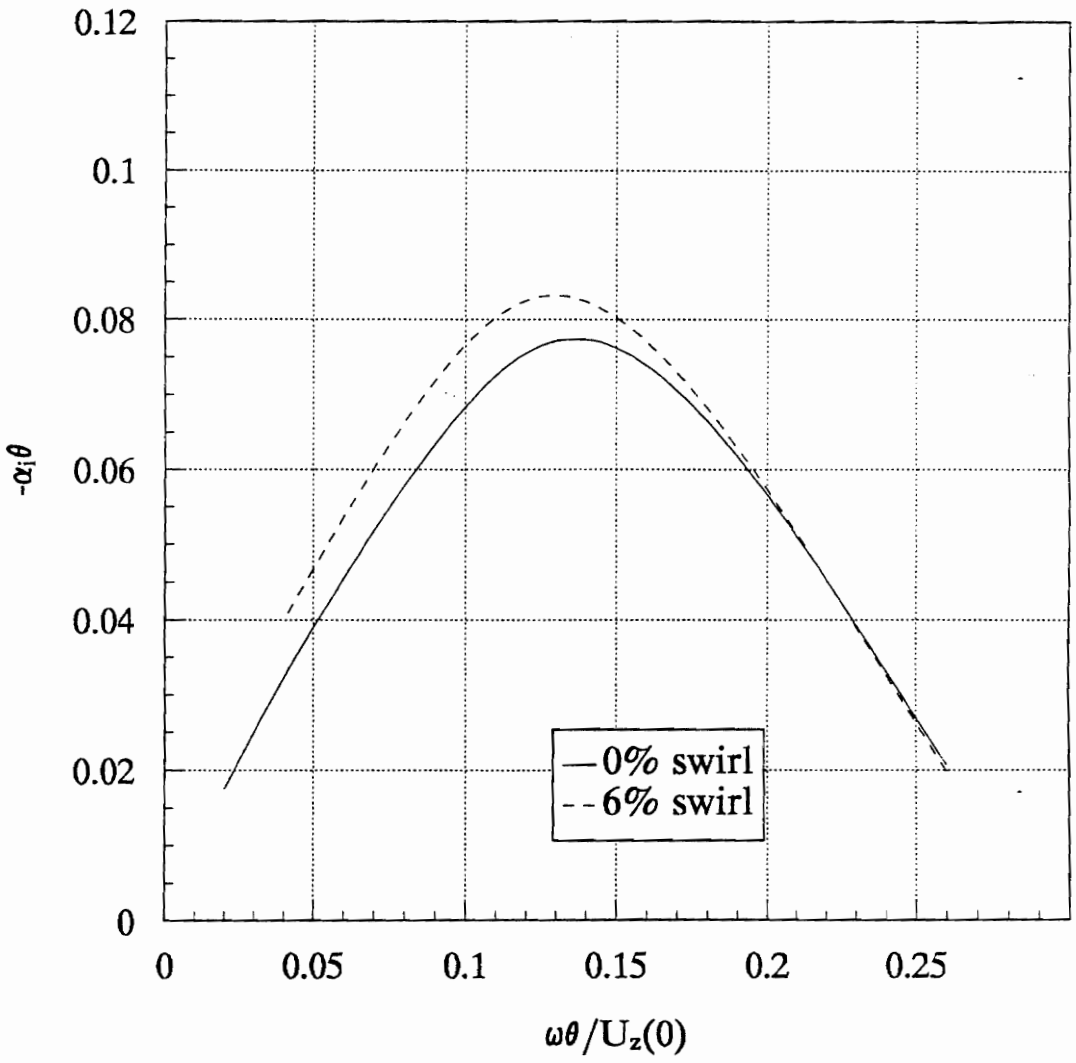

Figure 2.10. The influence of the swirl on the growth rate of the negative first azimuthal mode.

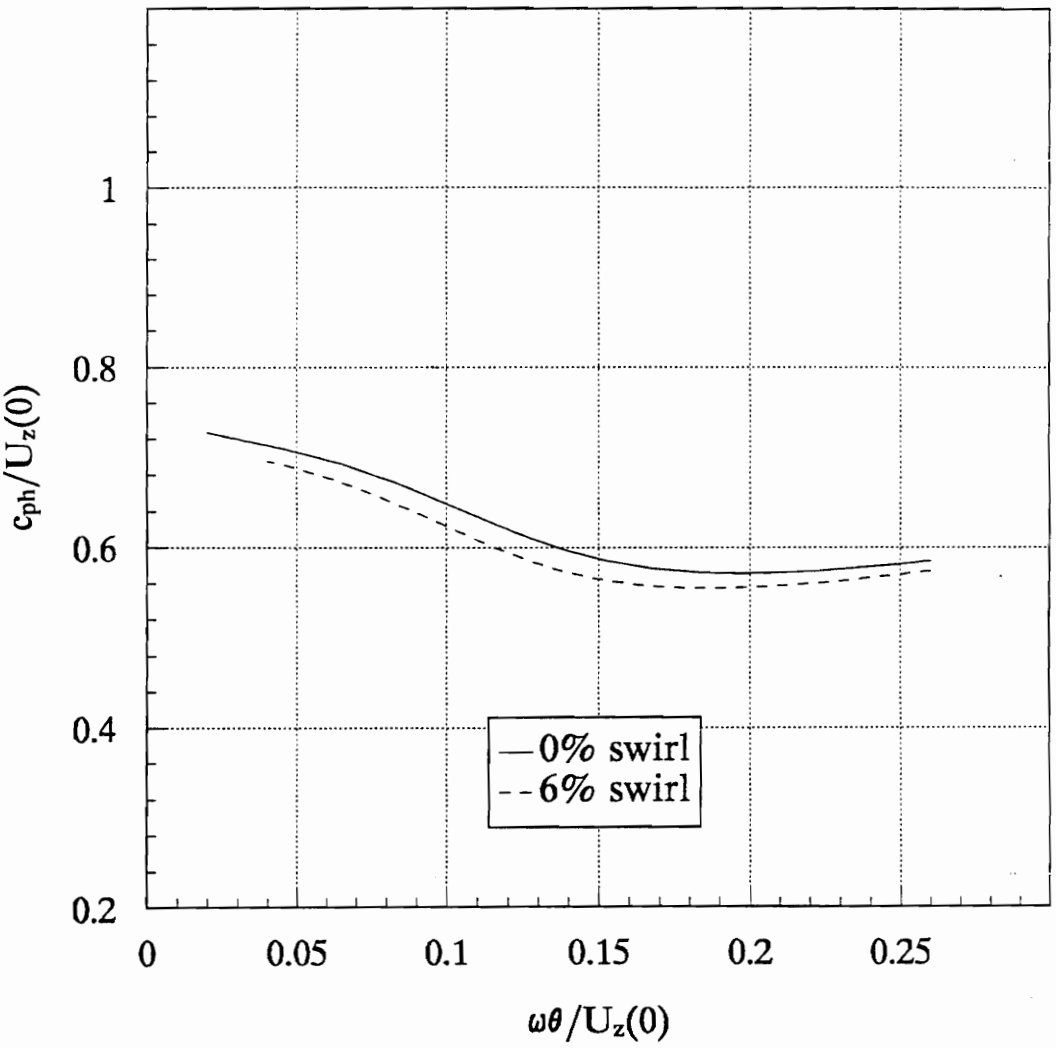

Figure 2.11. The influence of the swirl on the phase speed of the first azimuthal mode.

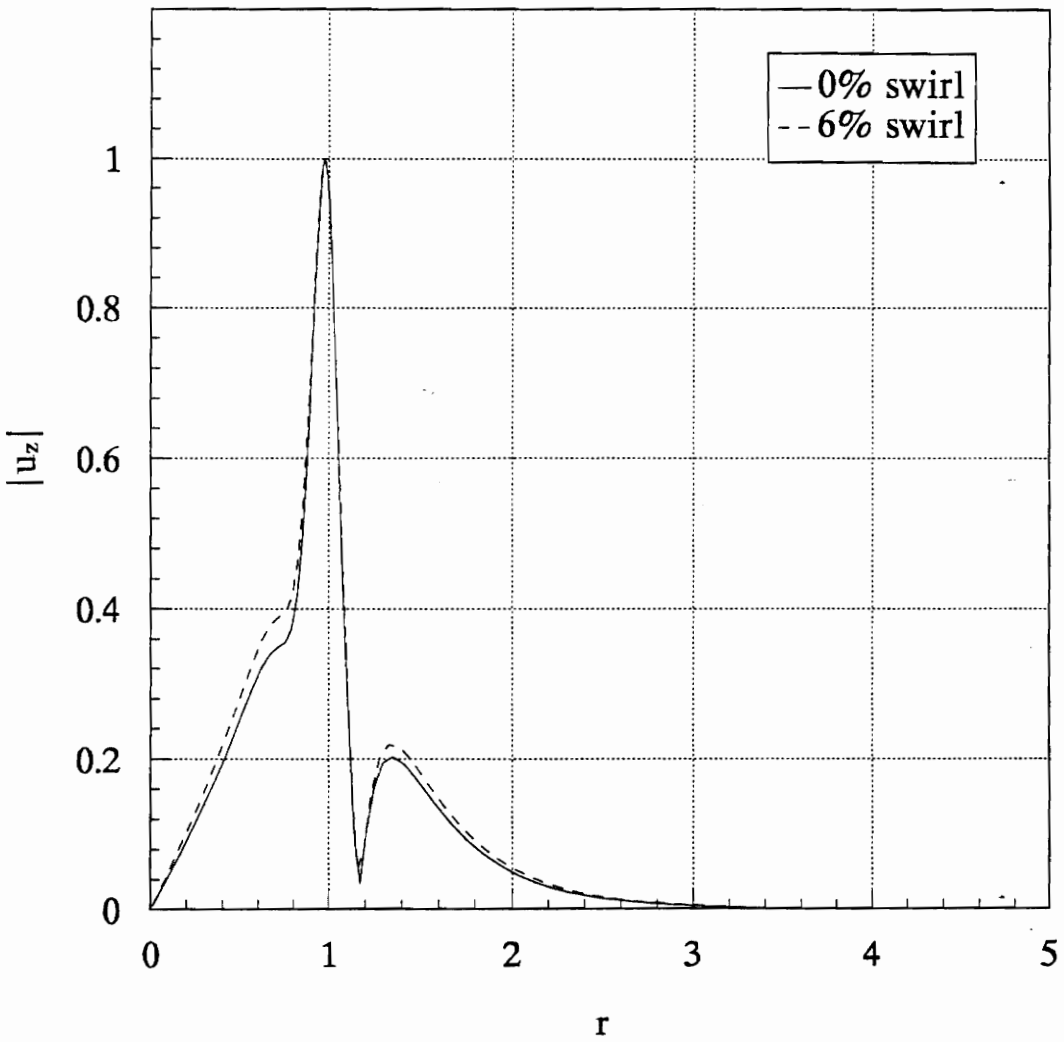

Figure 2.12. The distribution of the pressure eigenfunction of the negative first azimuthal mode.

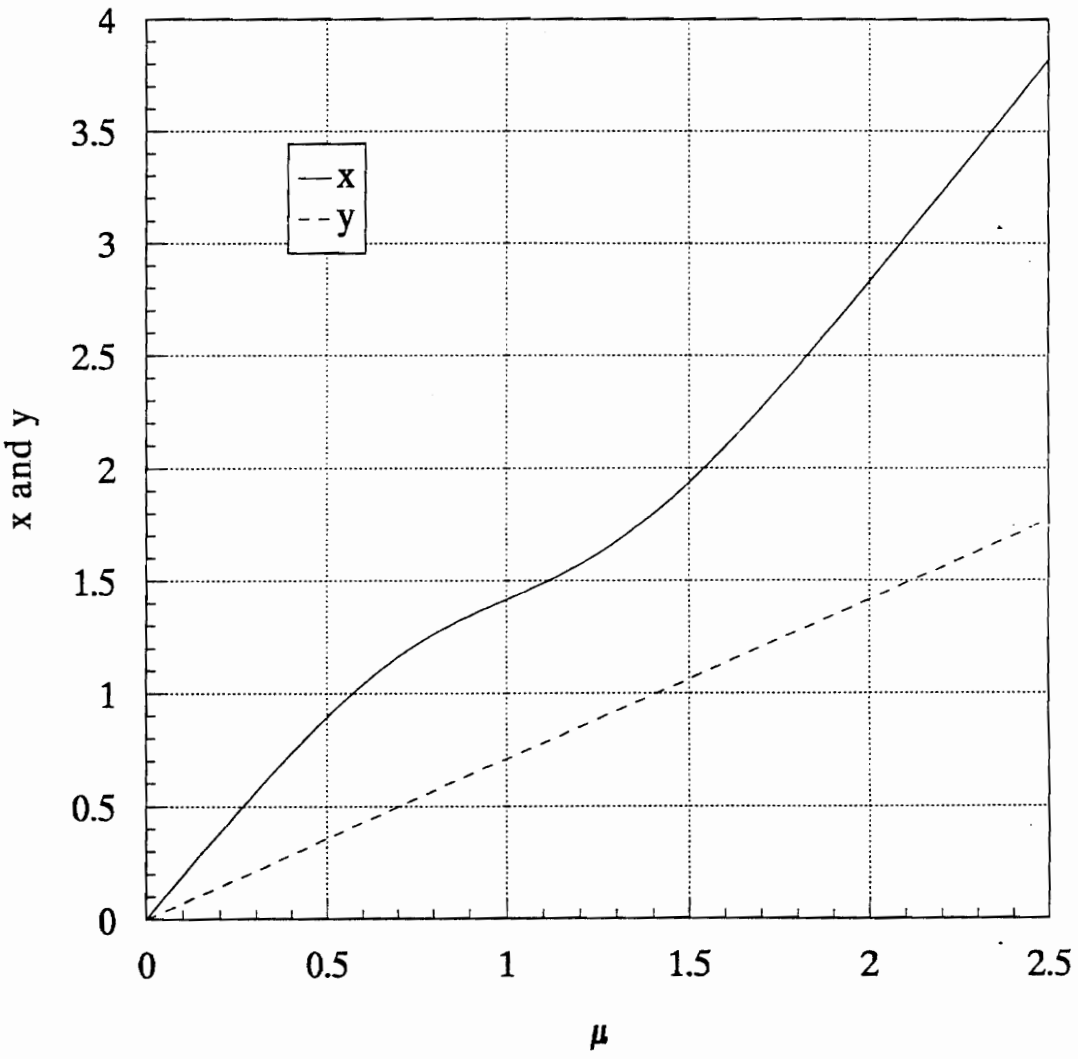

Figure 3.1. The x and y coordinates on the major and minor axes against the generalized radial coordinate μ.

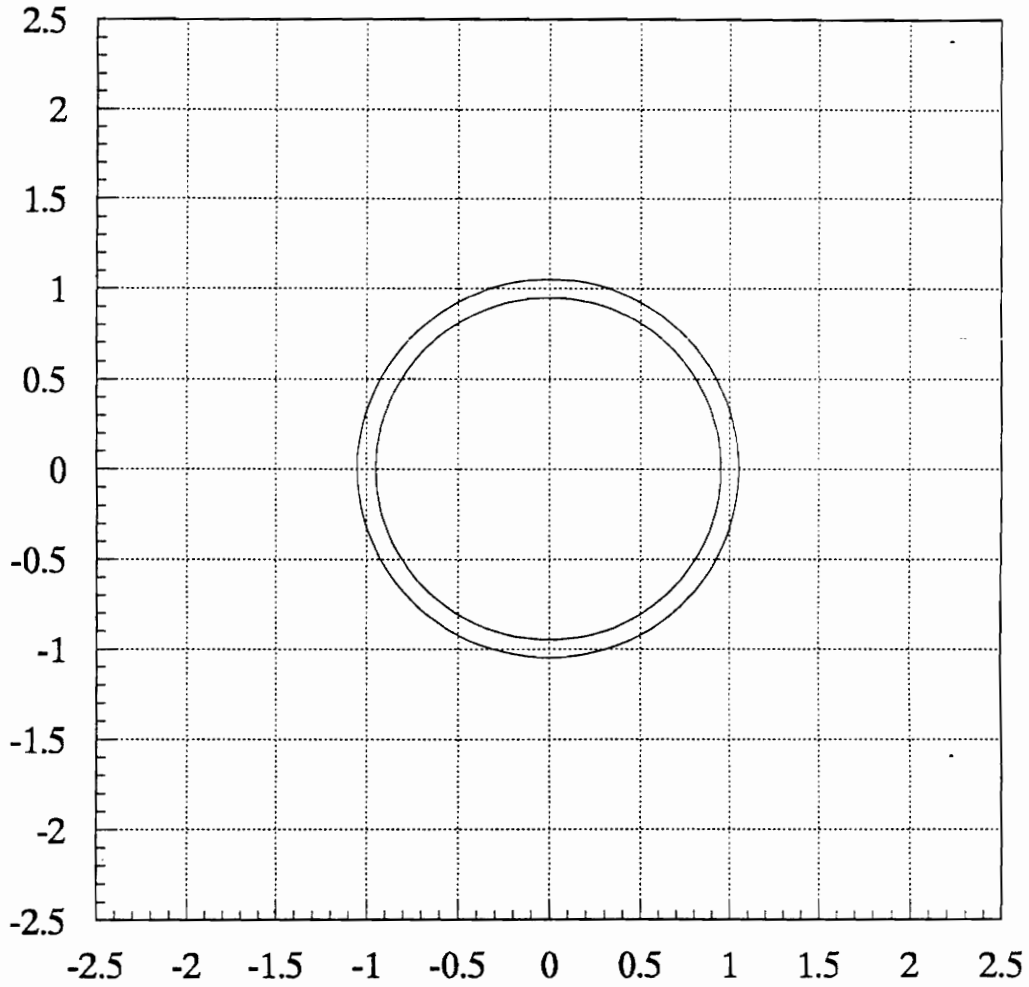

Figure 3.2. The momentum thickness distribution of the circular jet.

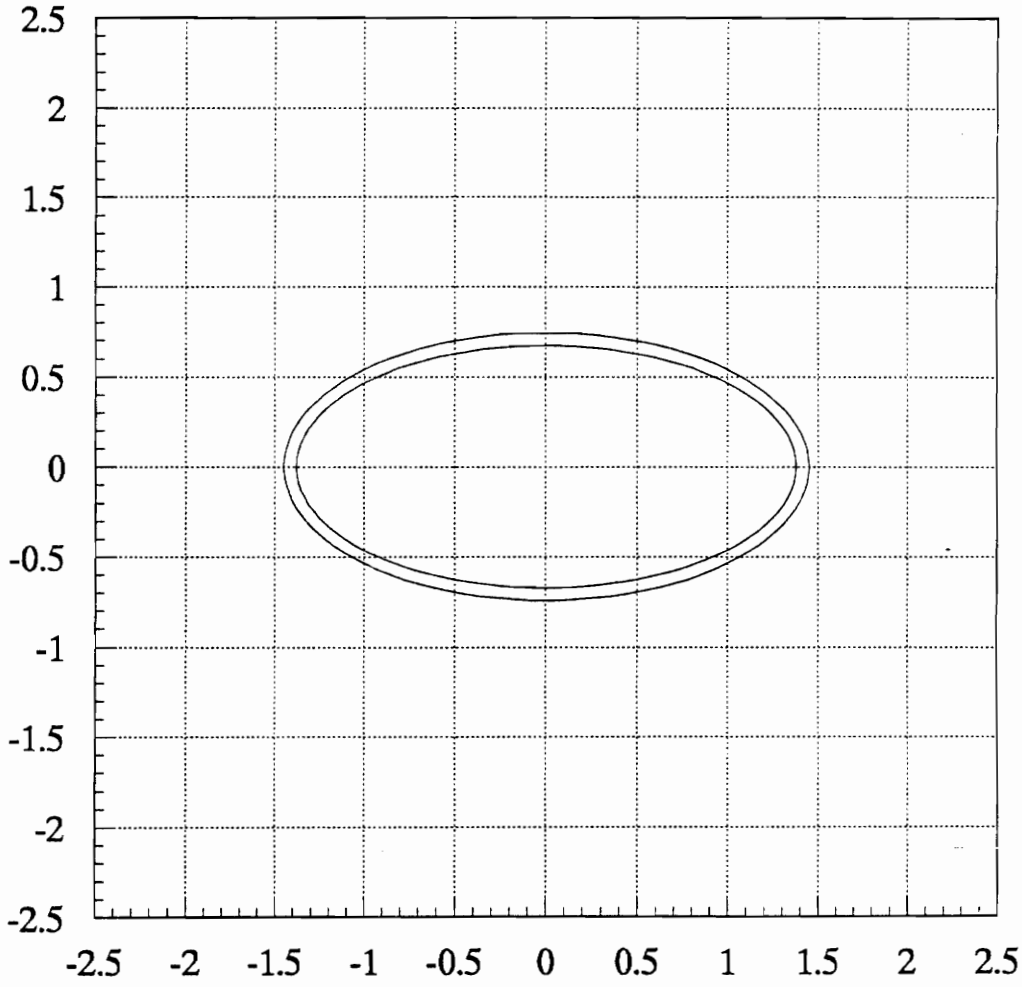

Figure 3.3. The momentum thickness distribution of the $AR = 2$ elliptical jet with $\theta_y/\theta_x = 1.0$.

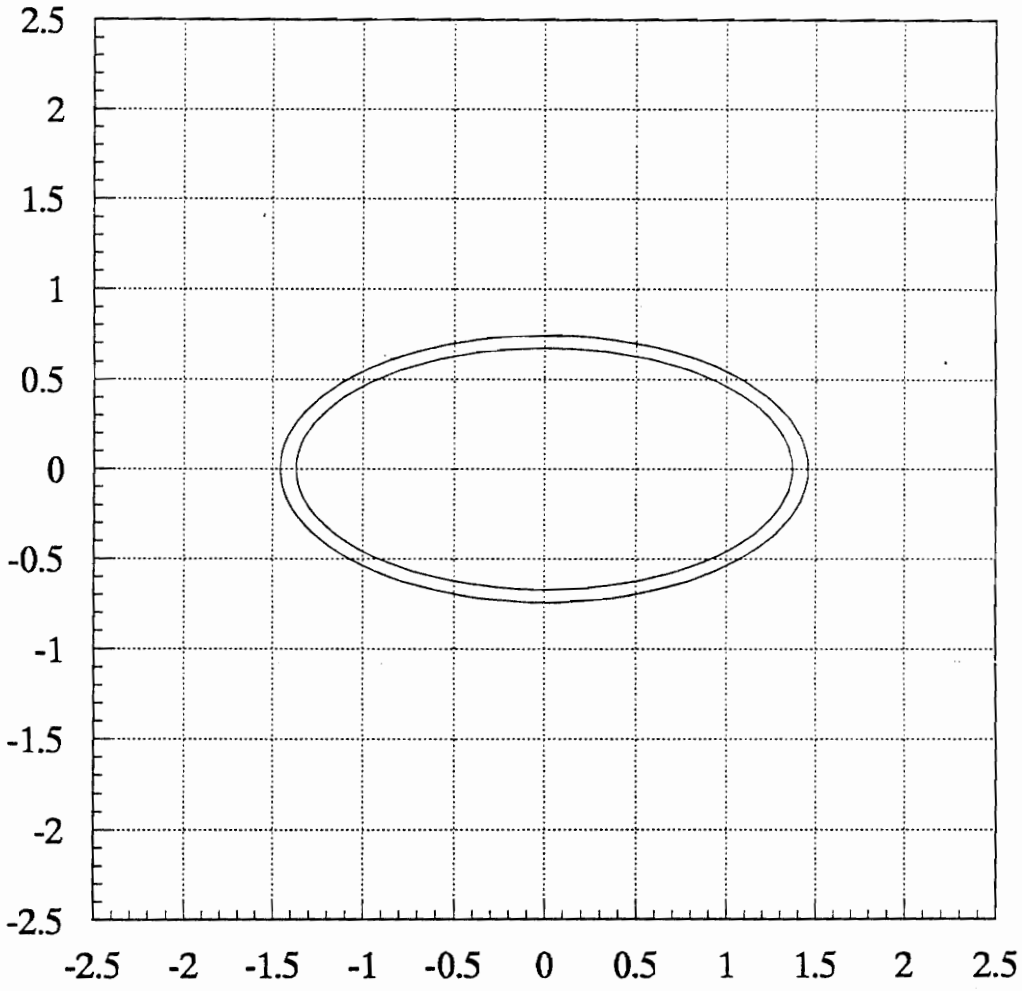

Figure 3.4. The momentum thickness distribution of the $AR = 2$ elliptical jet with $\theta_y/\theta_x = 0.8$.

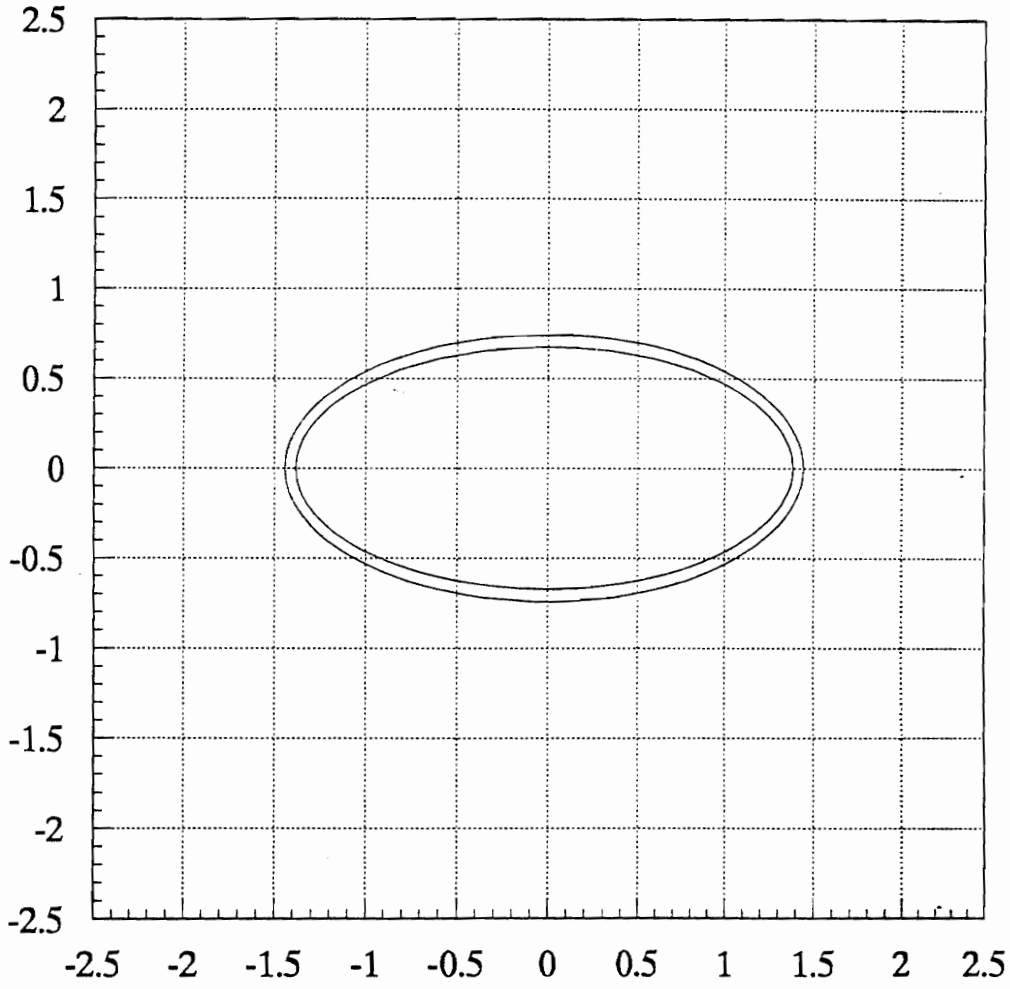

Figure 3.5. The momentum thickness distribution of the $AR = 2$ elliptical jet with $\theta_y/\theta_x = 1.2$.

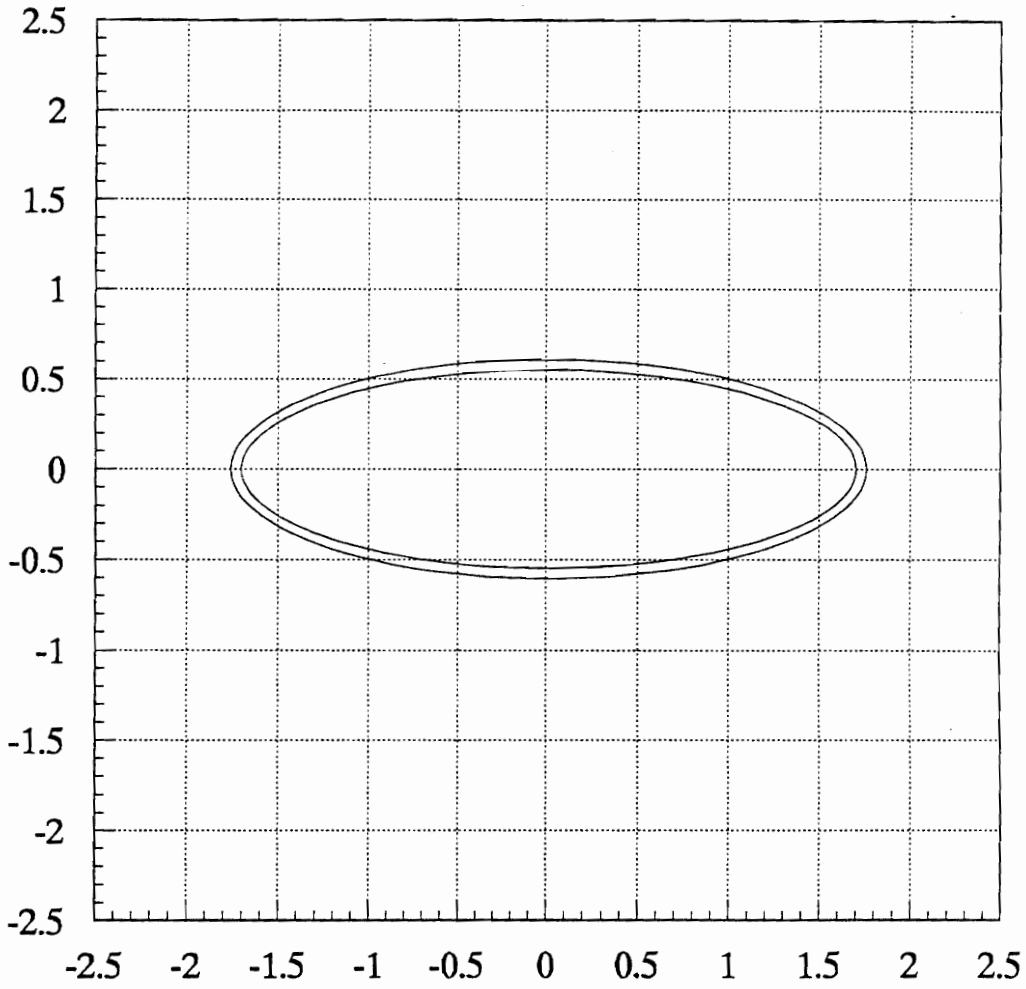

Figure 3.6. The momentum thickness distribution of the $AR = 3$ elliptical jet with $\theta_y/\theta_x = 1.0$.

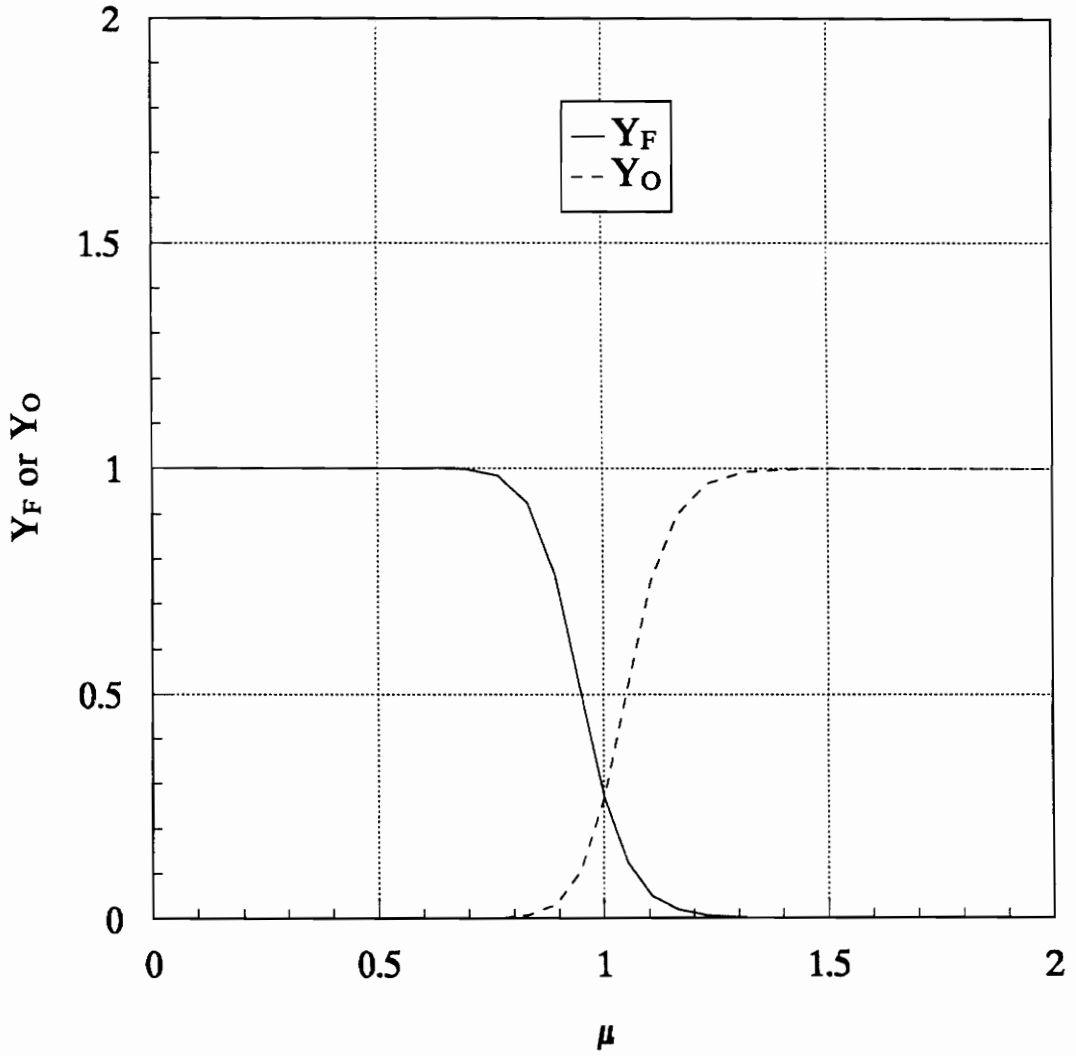

Figure 3.7. The distributions of the mass fractions of the fuel and oxidizer.

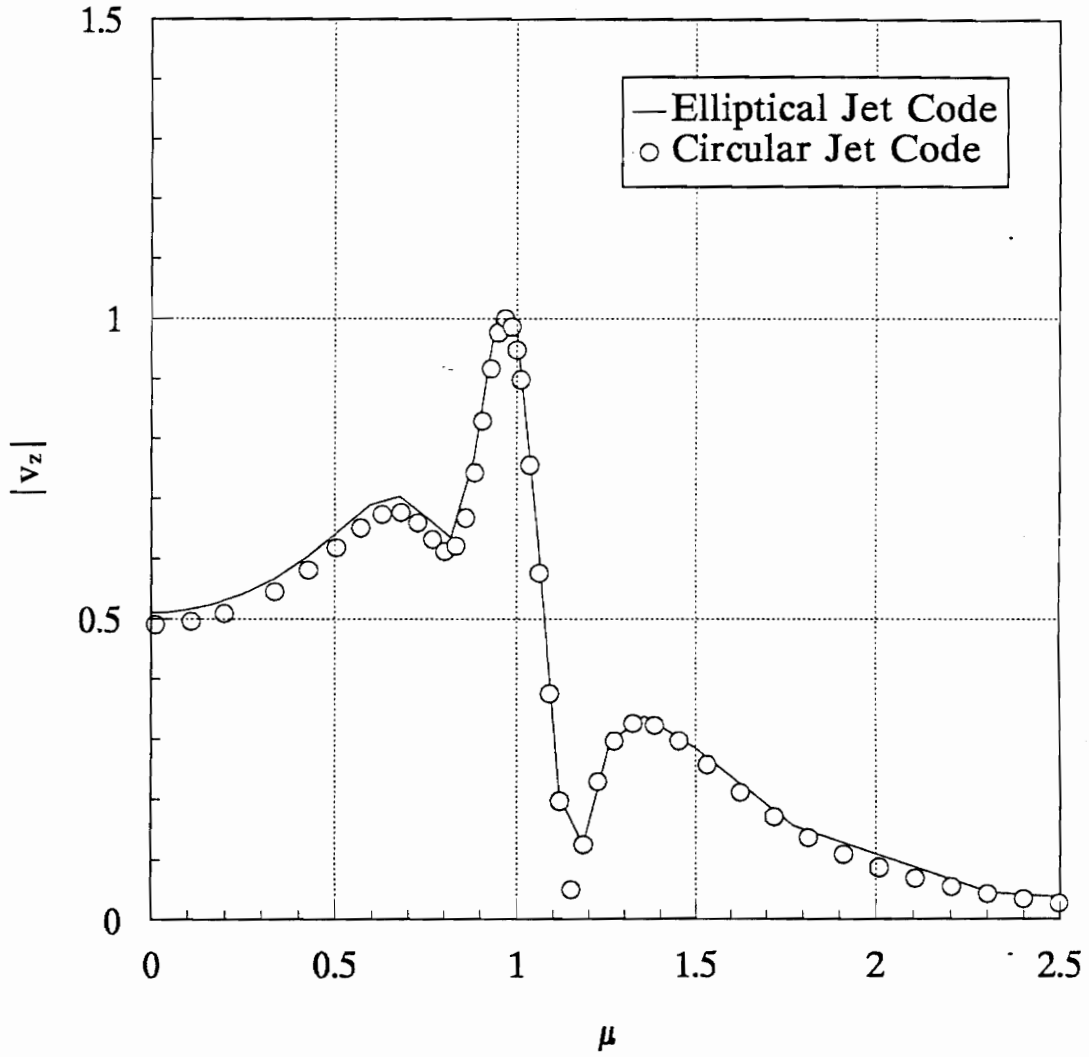

Figure 3.8. The comparison of the magnitude of the streamwise velocity eigenfunction obtained using the elliptical jet code described in Chapter 3 and the circular jet code described in Chapter 2.

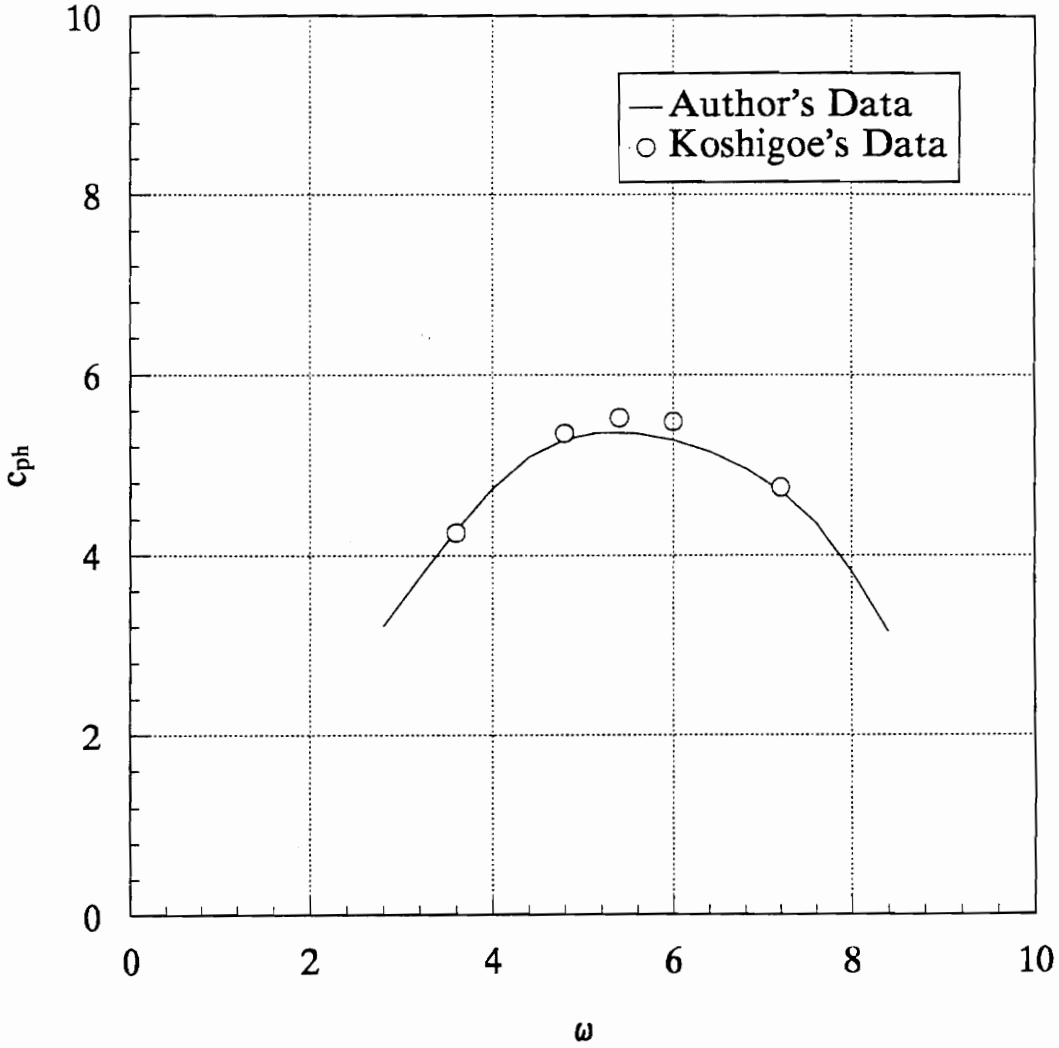

Figure 3.9. The comparison of the growth rate from the author's code and Koshigoe's paper.

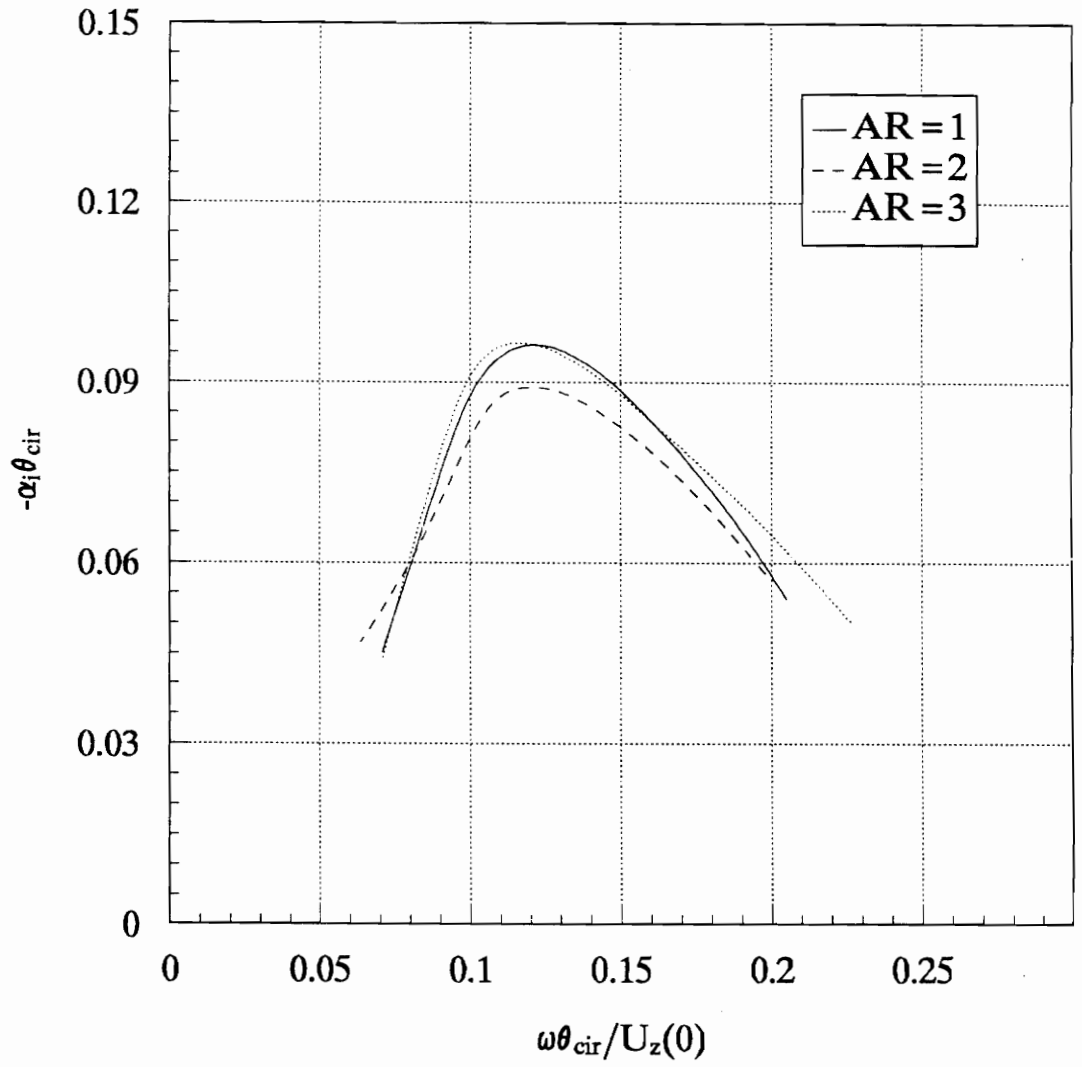

Figure 4.1. The comparison of the growth rates on the constant momentum thickness.

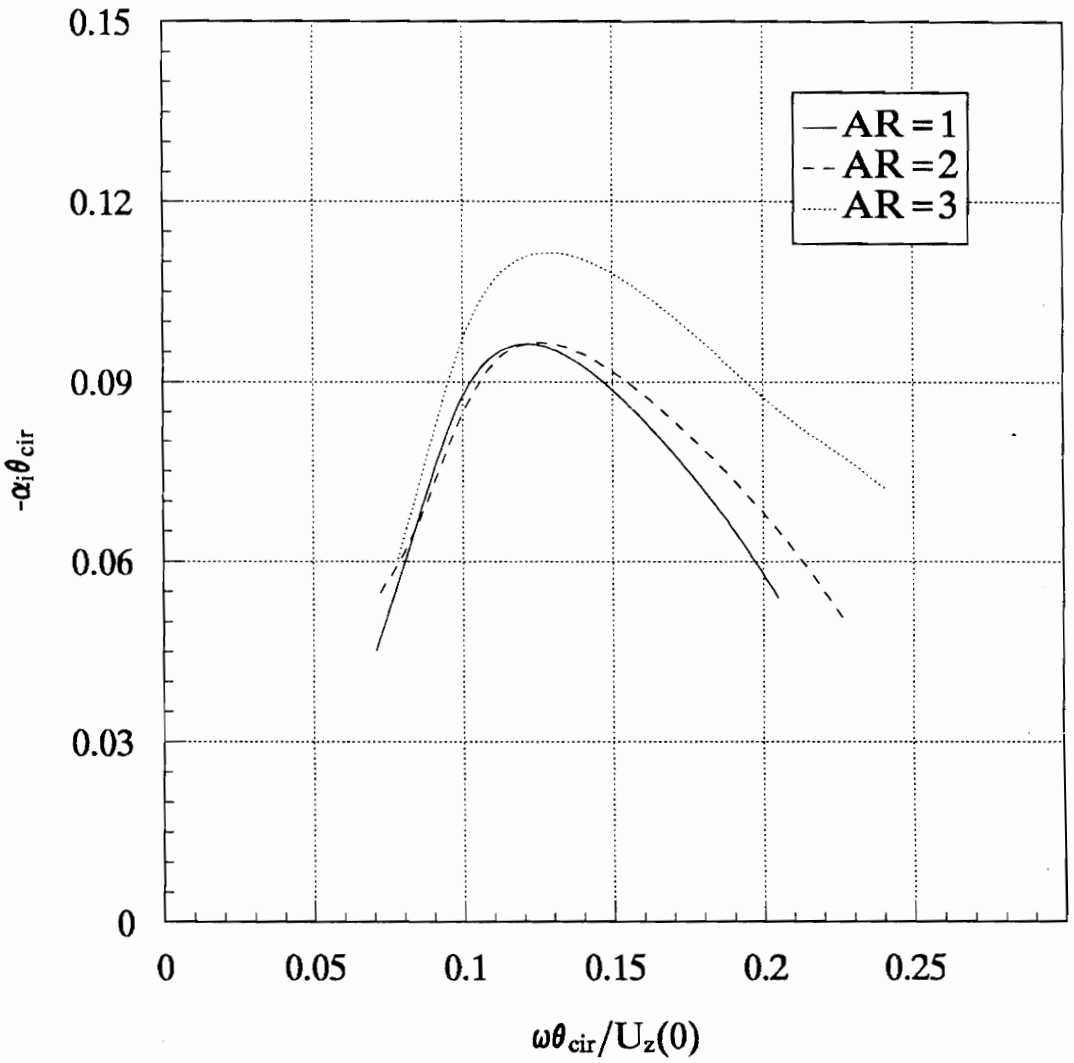

Figure 4.2. The influence of the aspect ratio on the growth rates of the fundamental π modes of the jets with equal momentum area.

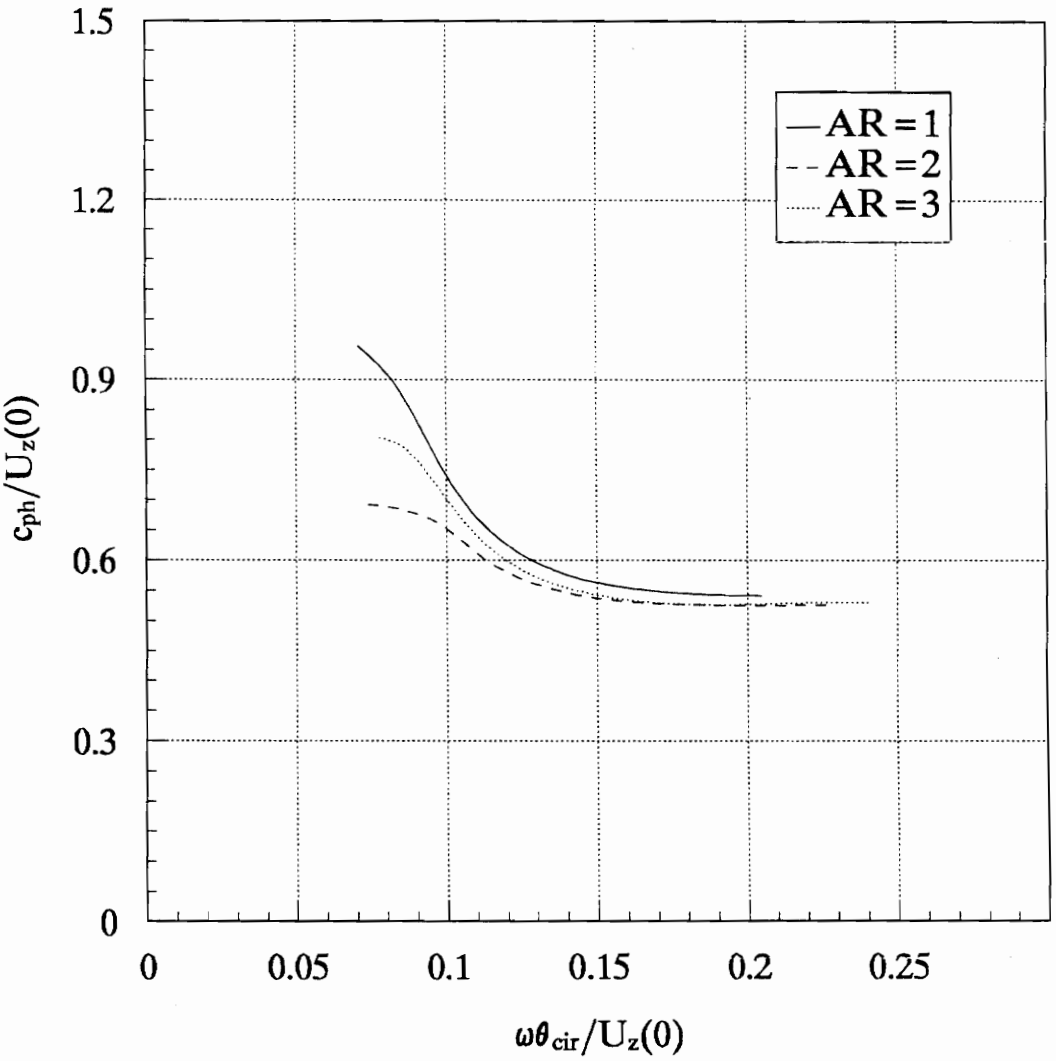

Figure 4.3. The influence of the aspect ratio on the phase speeds of the fundamental π modes of the jets with equal momentum area.

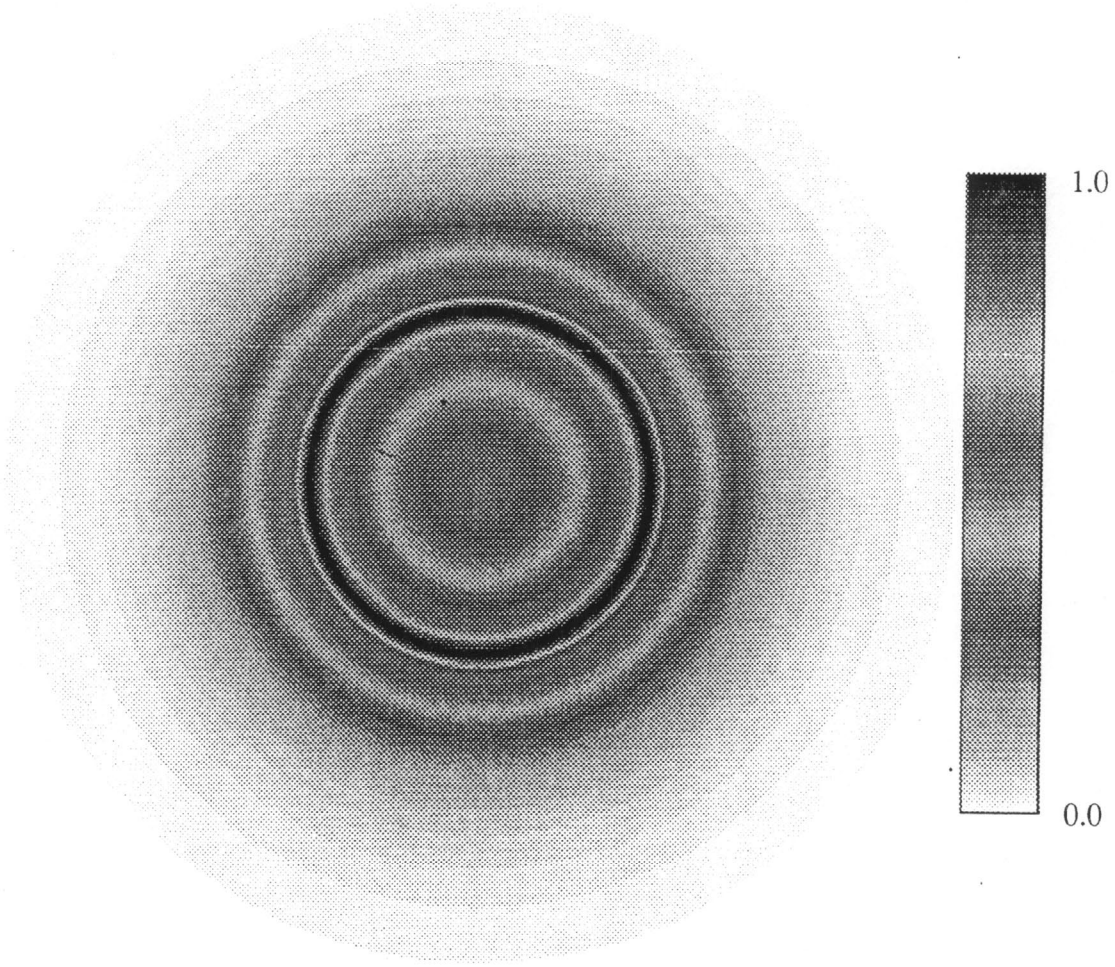

Figure 4.4. The distribution of the velocity eigenfunction of the $m = 1$ mode of the circular jet.

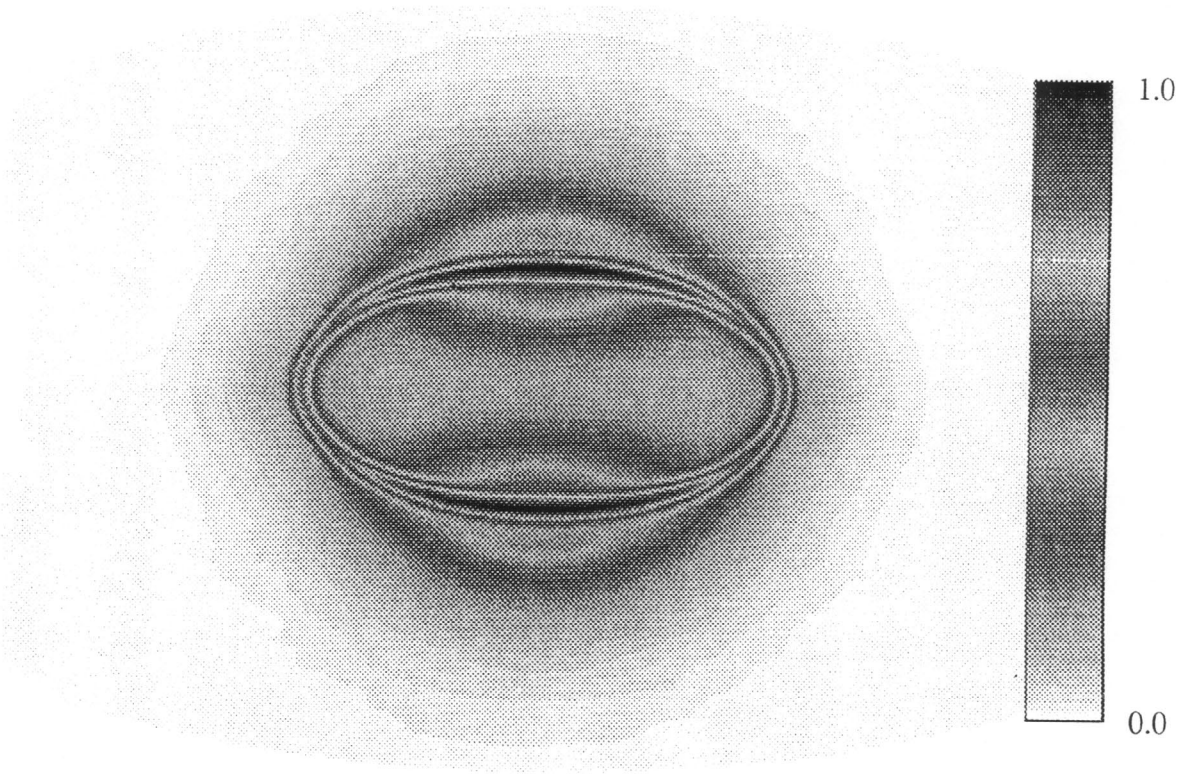

Figure 4.5. The distribution of the velocity eigenfunction of the fundamental π mode of the $AR = 2$ elliptical jet.

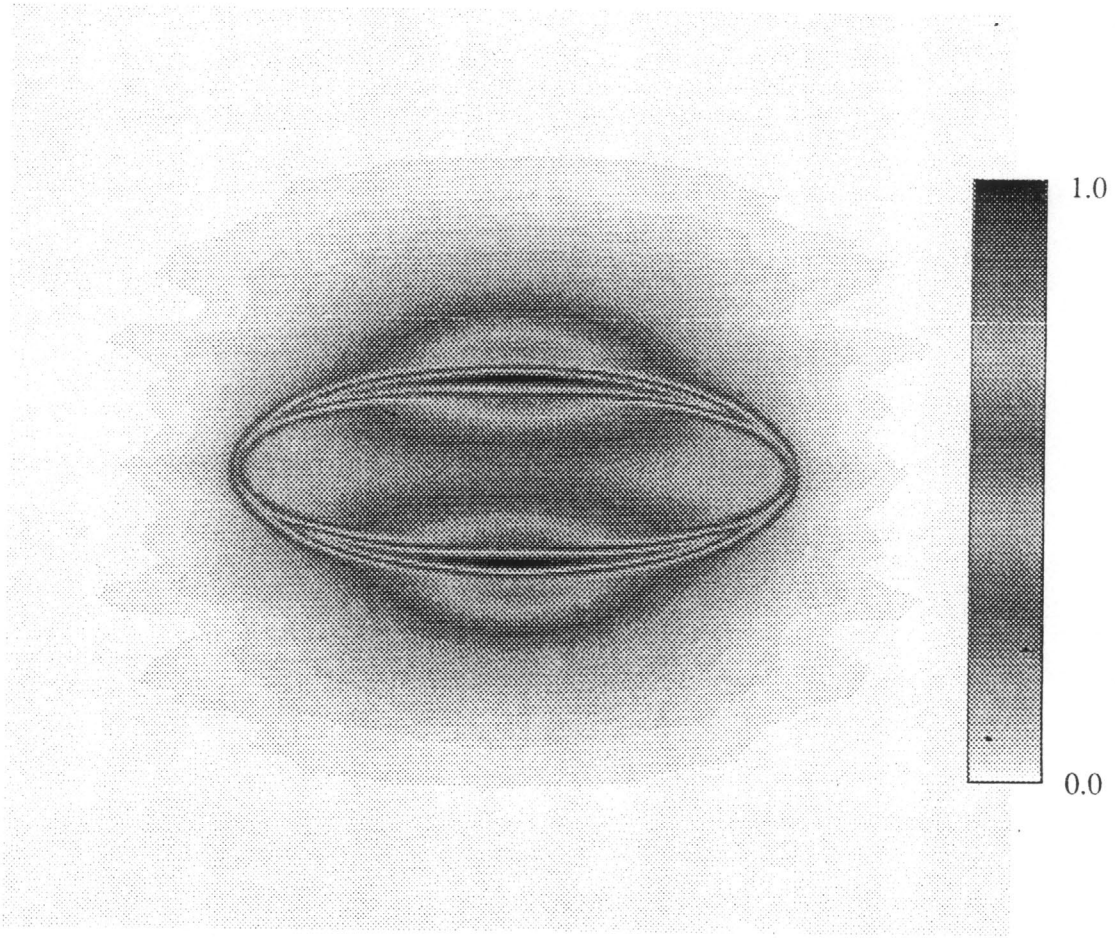

Figure 4.6. The distribution of the velocity eigenfunction of the fundamental π mode of the $AR = 3$ elliptical jet.

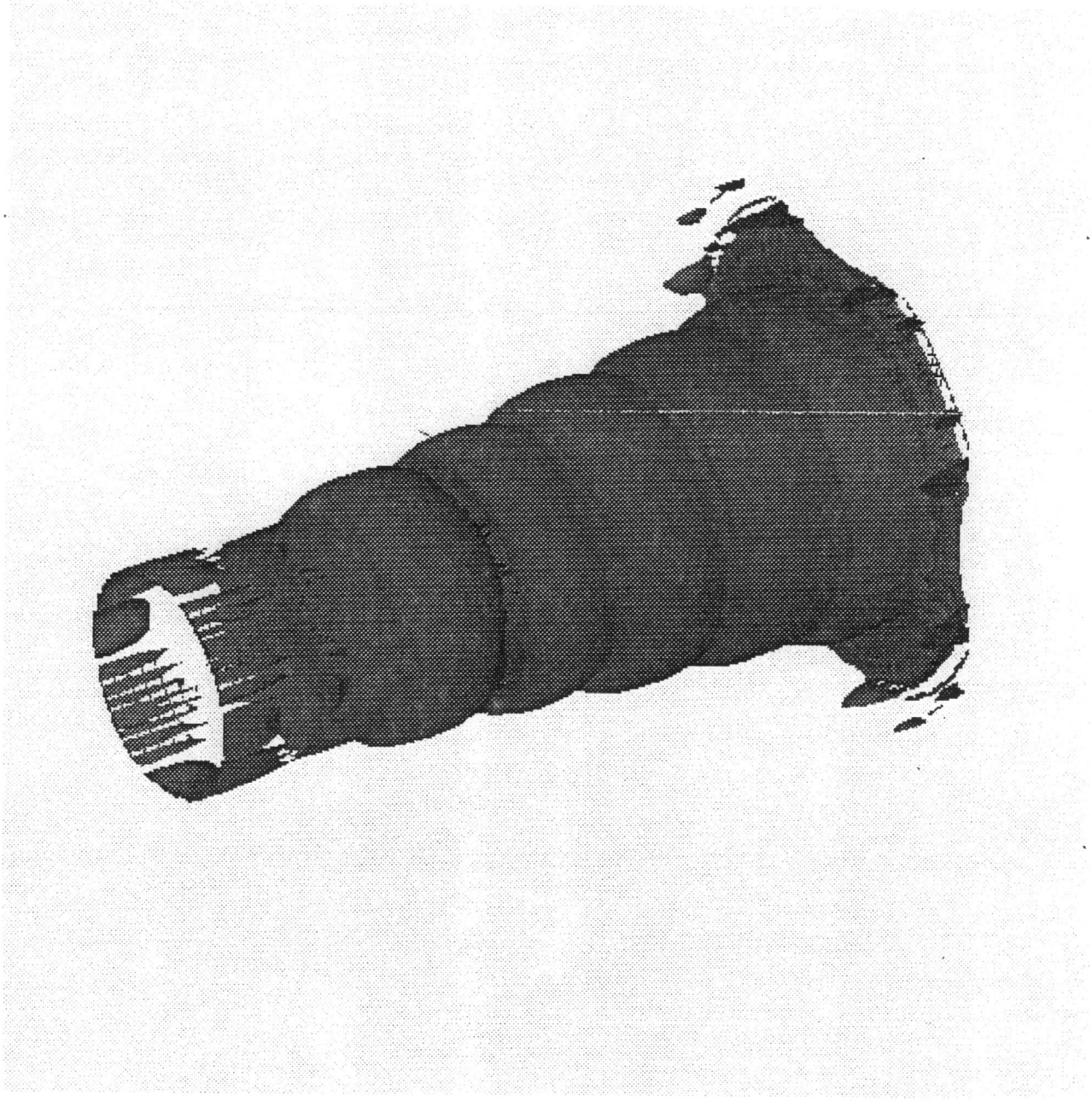

Figure 4.7. The surface of constant vorticity of the $m = 0$ mode of the circular jet.

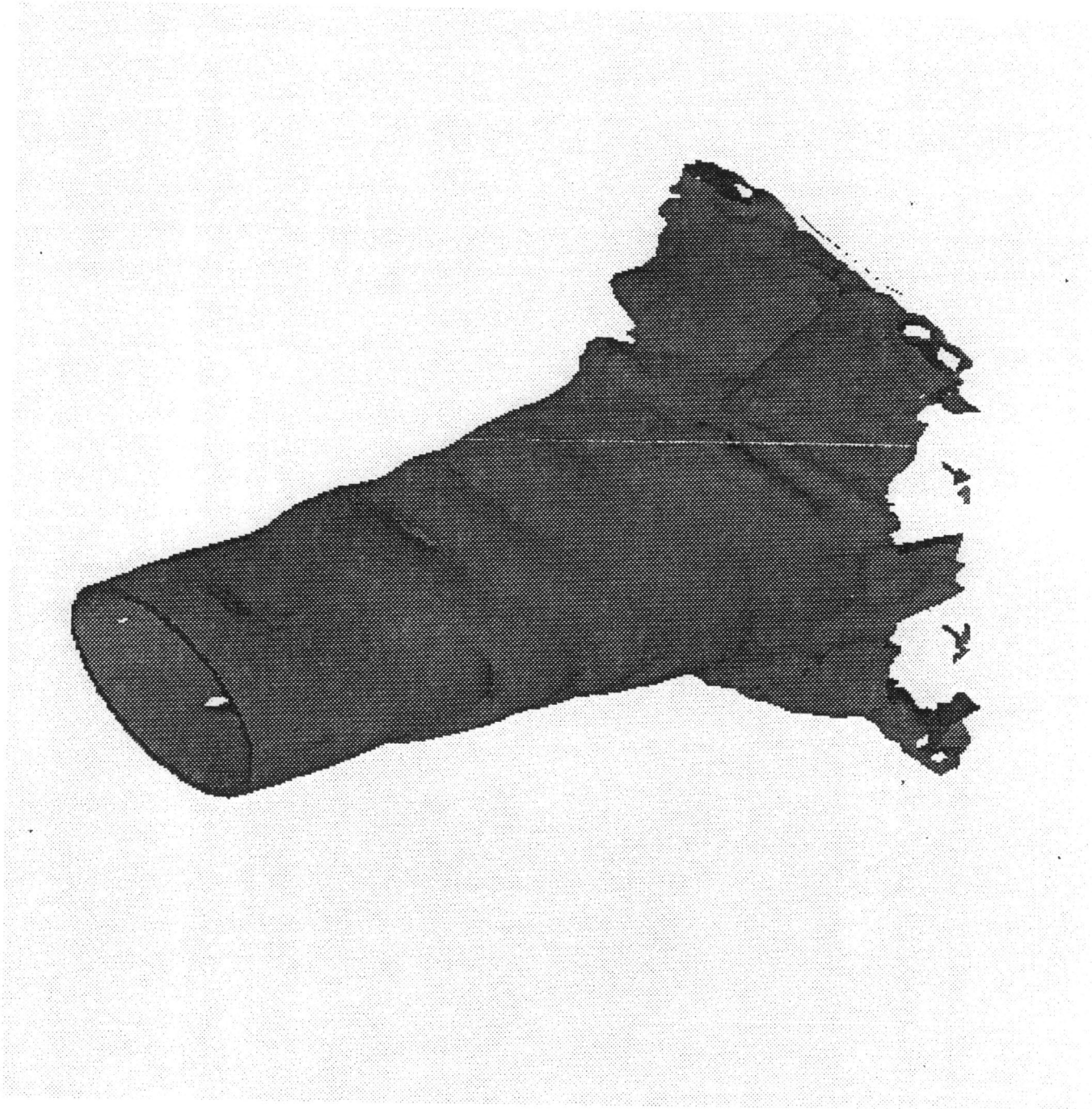

Figure 4.8. The surface of constant vorticity of the fundamental π mode of the $AR = 2$ elliptical jet.

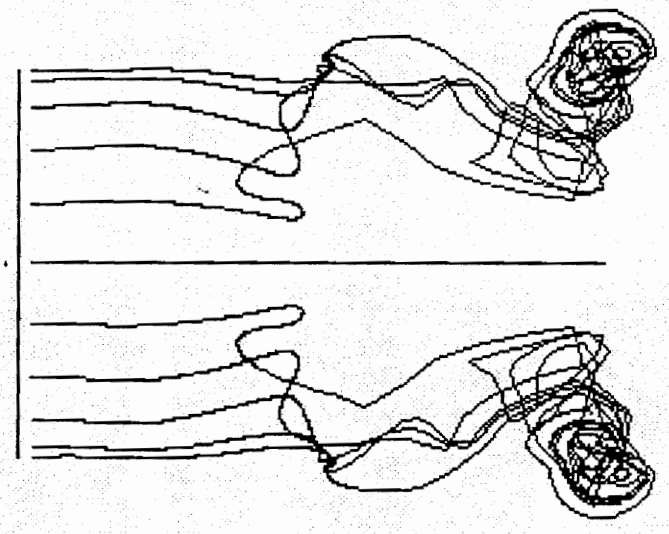

Figure 4.9. The streaklines of the $AR = 2$ elliptical jet with uniform momentum thickness projected on the major axis.

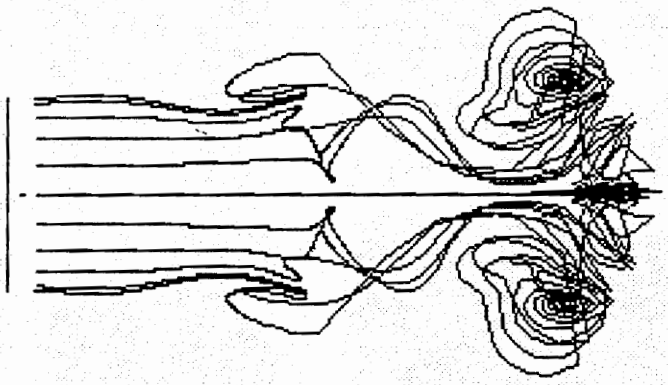

Figure 4.10. The streaklines of the $AR = 2$ elliptical jet with uniform momentum thickness projected on the minor axis.

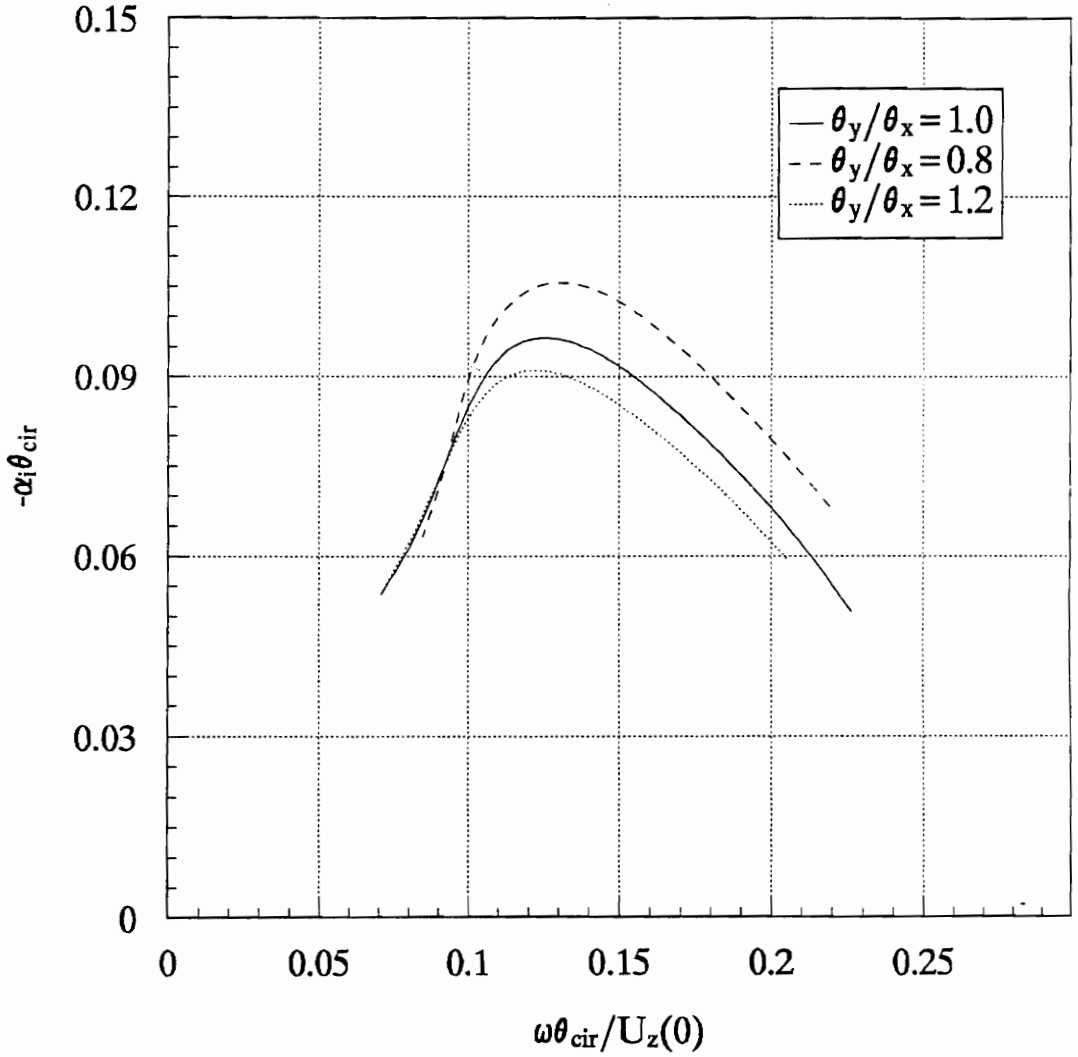

Figure 4.11. The influence of the momentum thickness distribution on the growth rate of the fundamental π mode of the $AR = 2$ elliptical jet.

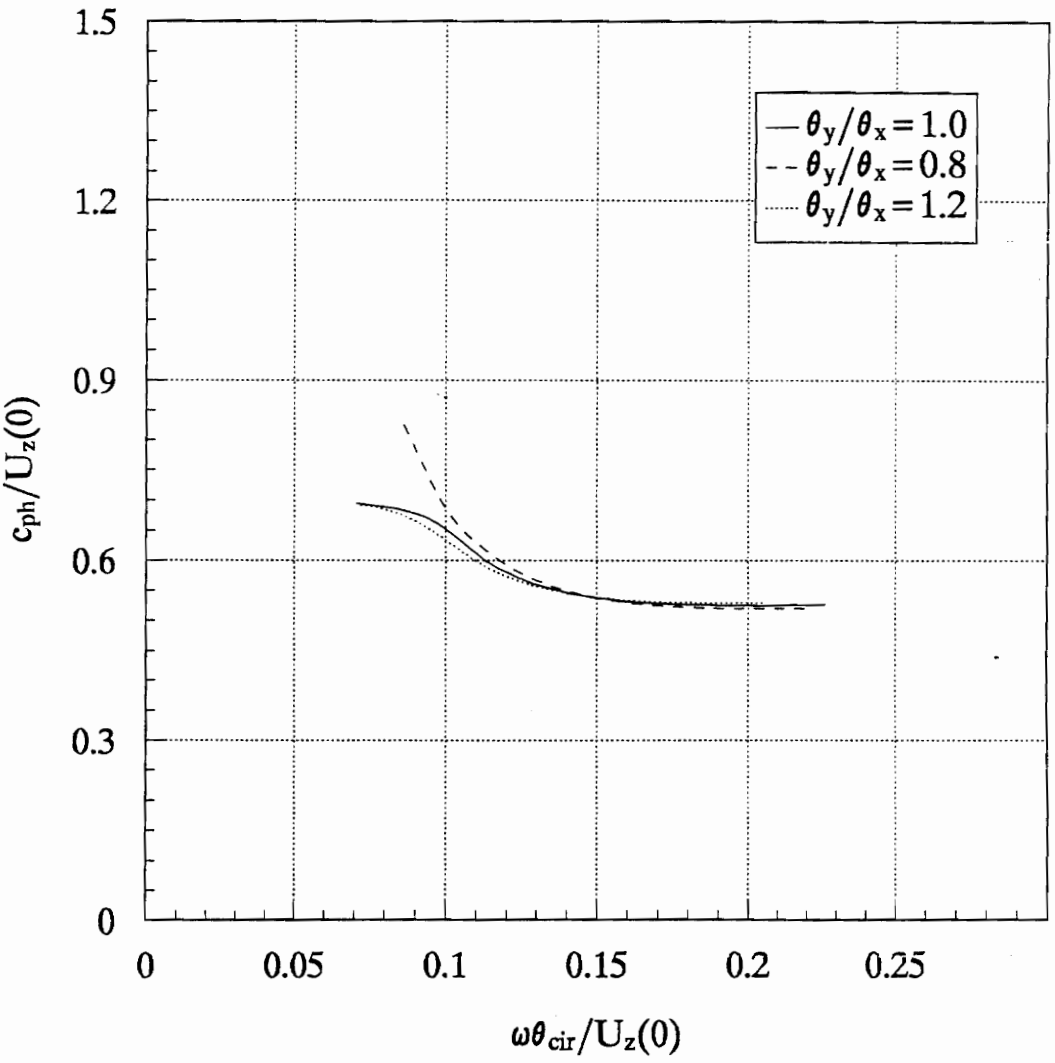

Figure 4.12. The influence of the momentum thickness distribution on the phase speed of the fundamental π mode of the $AR = 2$ elliptical jet.

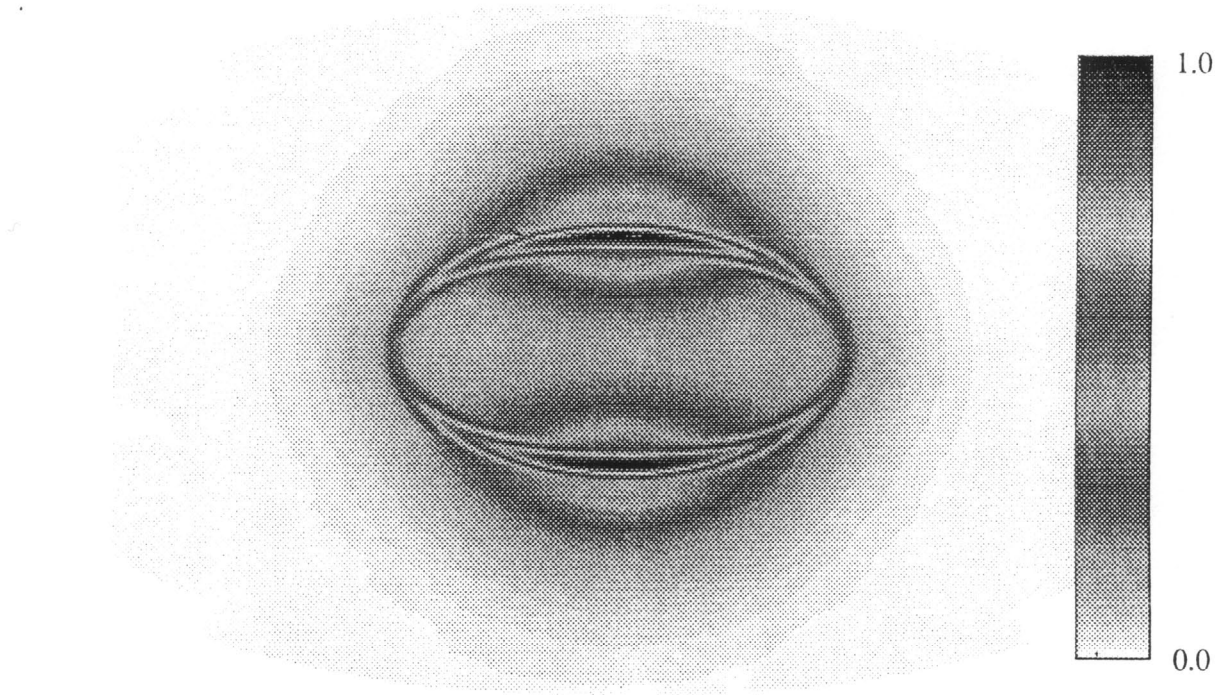

Figure 4.13. The distribution of the velocity eigenfunction of the fundamental π mode of the $AR = 2$ elliptical jet with a minimum momentum thickness on the minor axis. $\theta_y/\theta_x = 0.8$

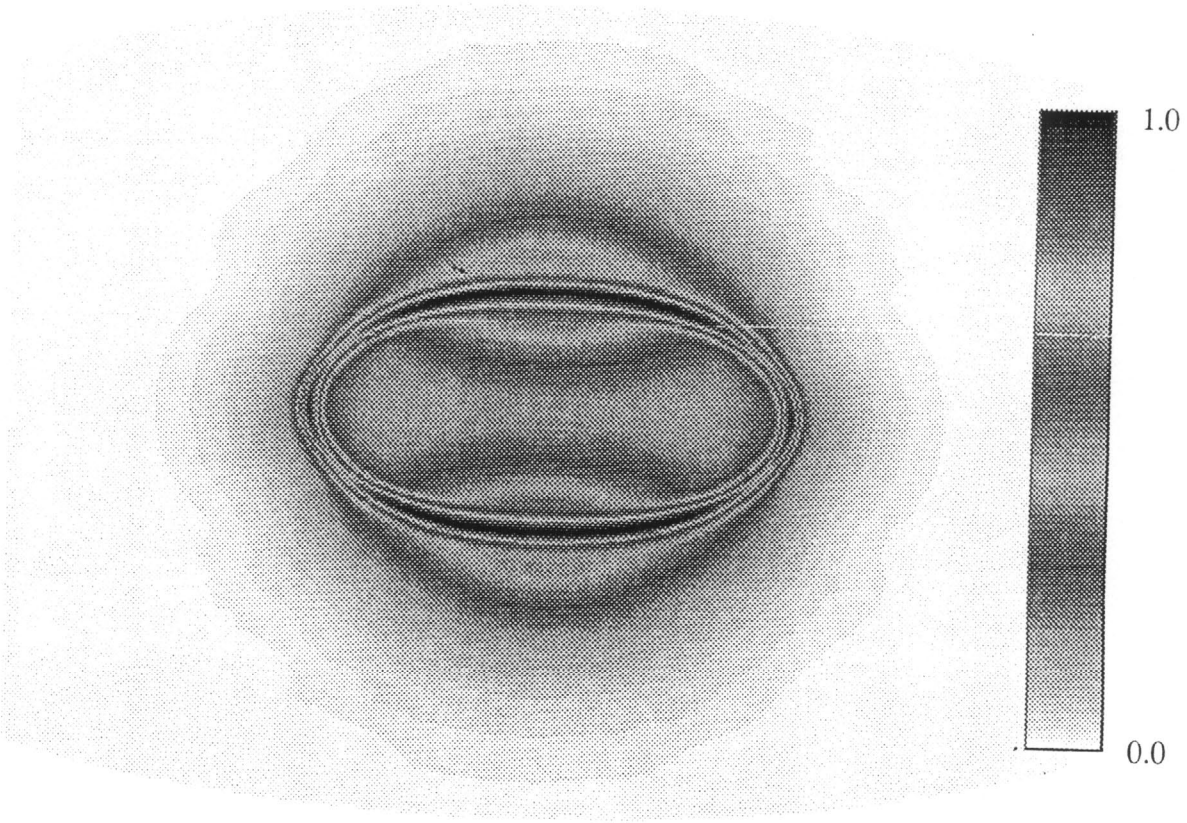

Figure 4.14. The distribution of the velocity eigenfunction of the fundamental π mode of the $AR = 2$ elliptical jet with a minimum momentum thickness on the major axis. $\theta_y/\theta_x = 1.2$

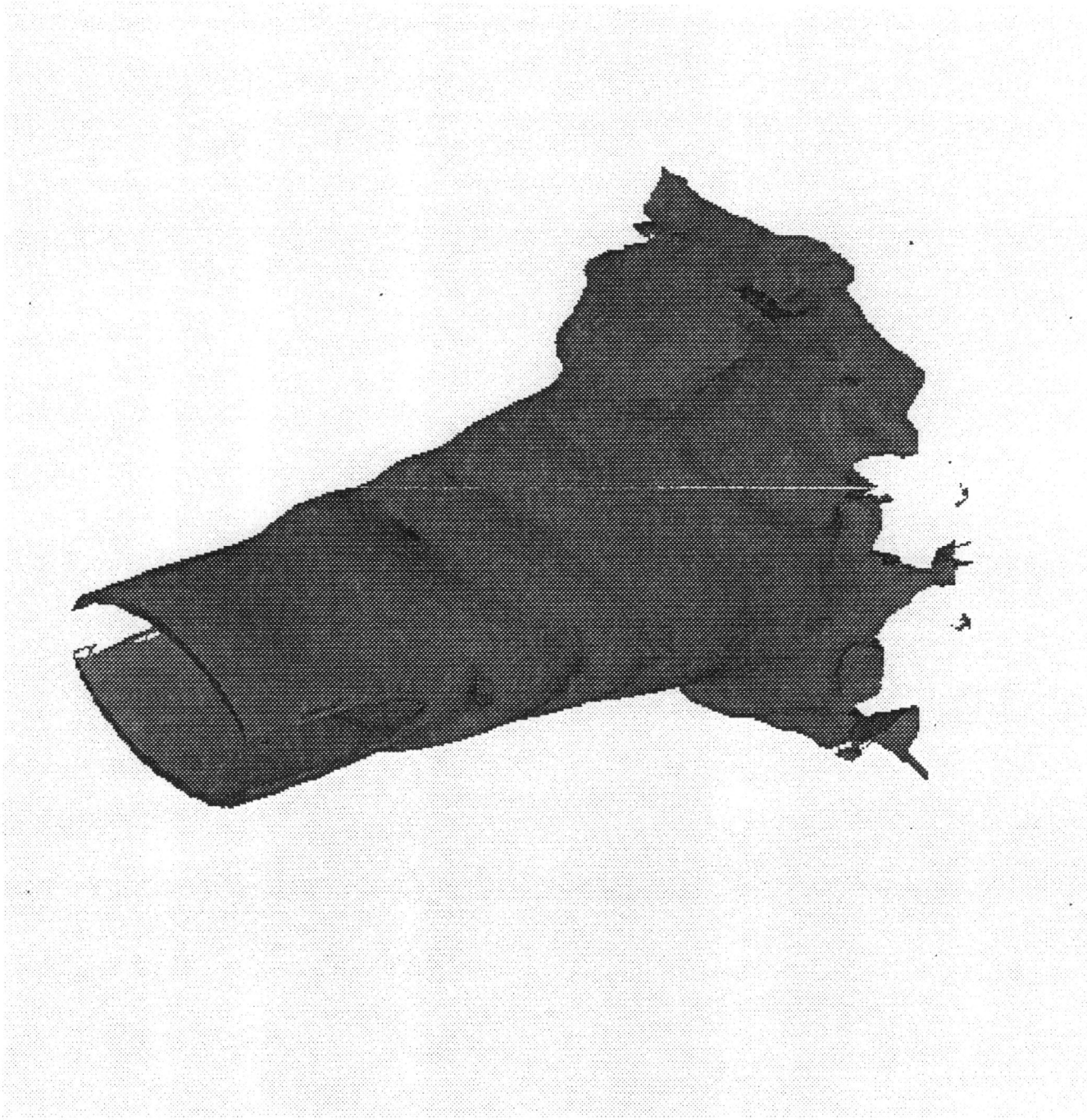

Figure 4.15. The surface of constant vorticity of $AR = 2$ elliptical jet with the minimum momentum thickness on the minor axis. $\theta_y/\theta_x = 0.8$

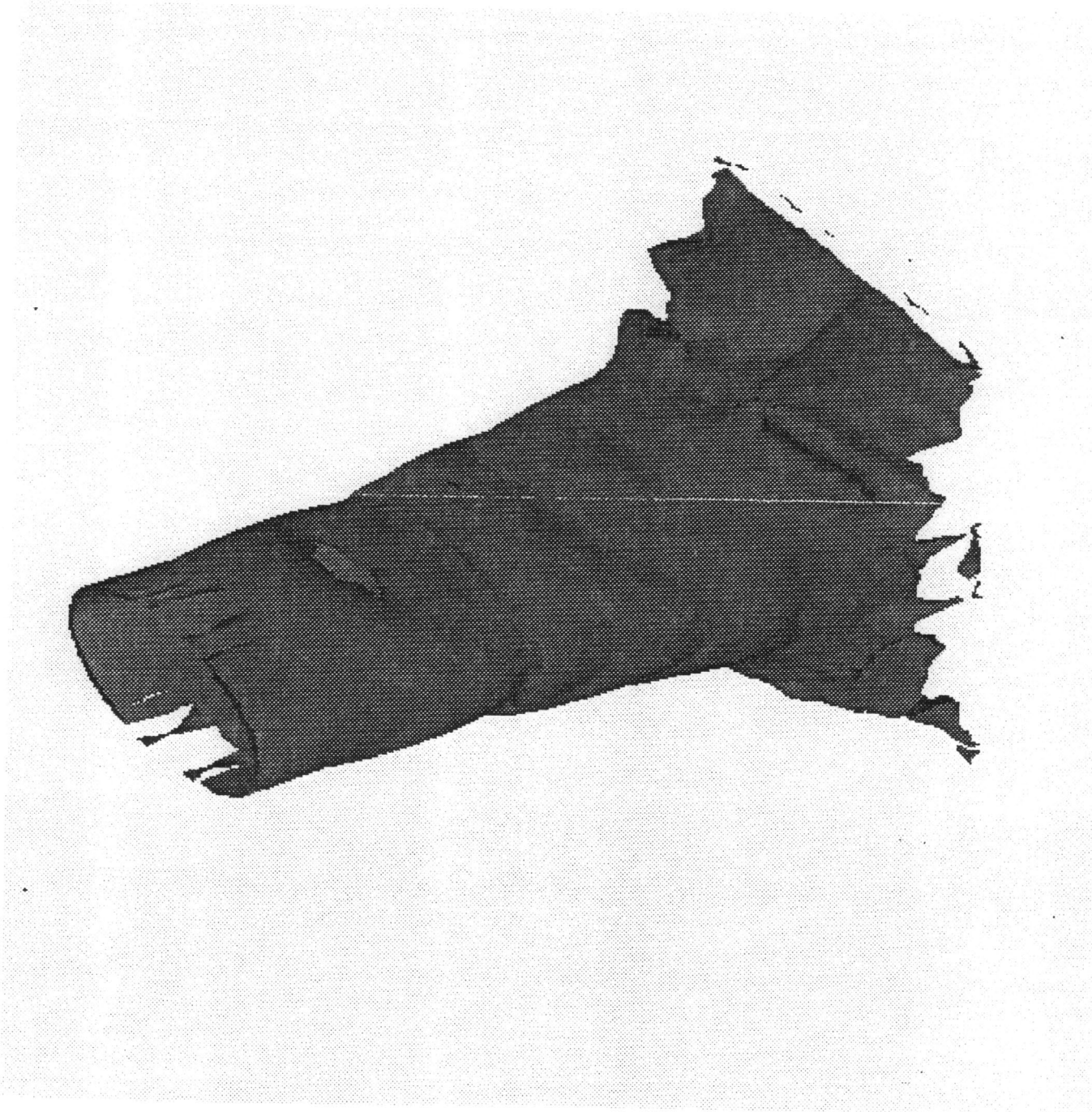

Figure 4.16. The surface of constant vorticity of $AR = 2$ elliptical jet with the minimum momentum thickness on the major axis. $\theta_y/\theta_x = 1.2$

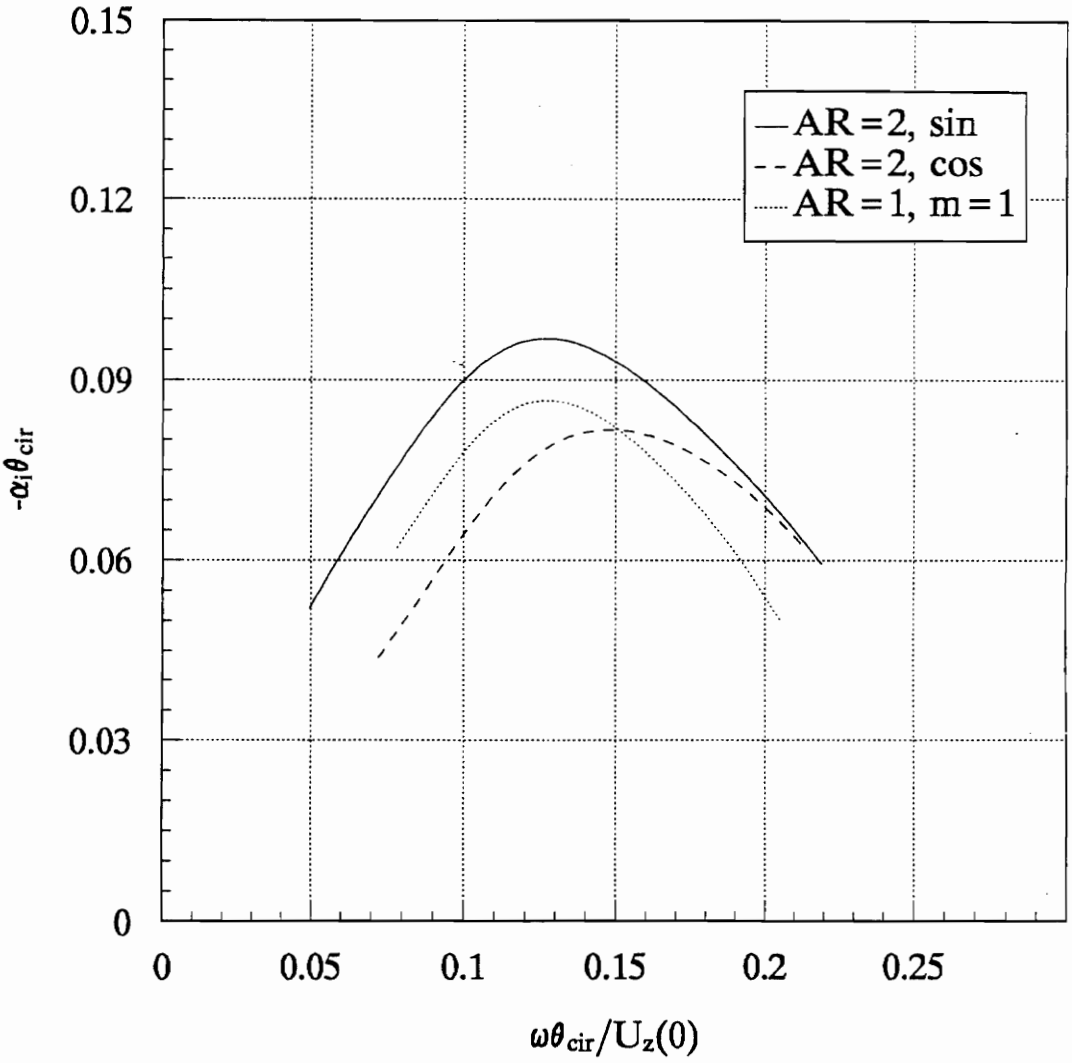

Figure 4.17. The comparison of the growth rates of the first azimuthal modes of the circular and elliptical jets with uniform momentum thickness.

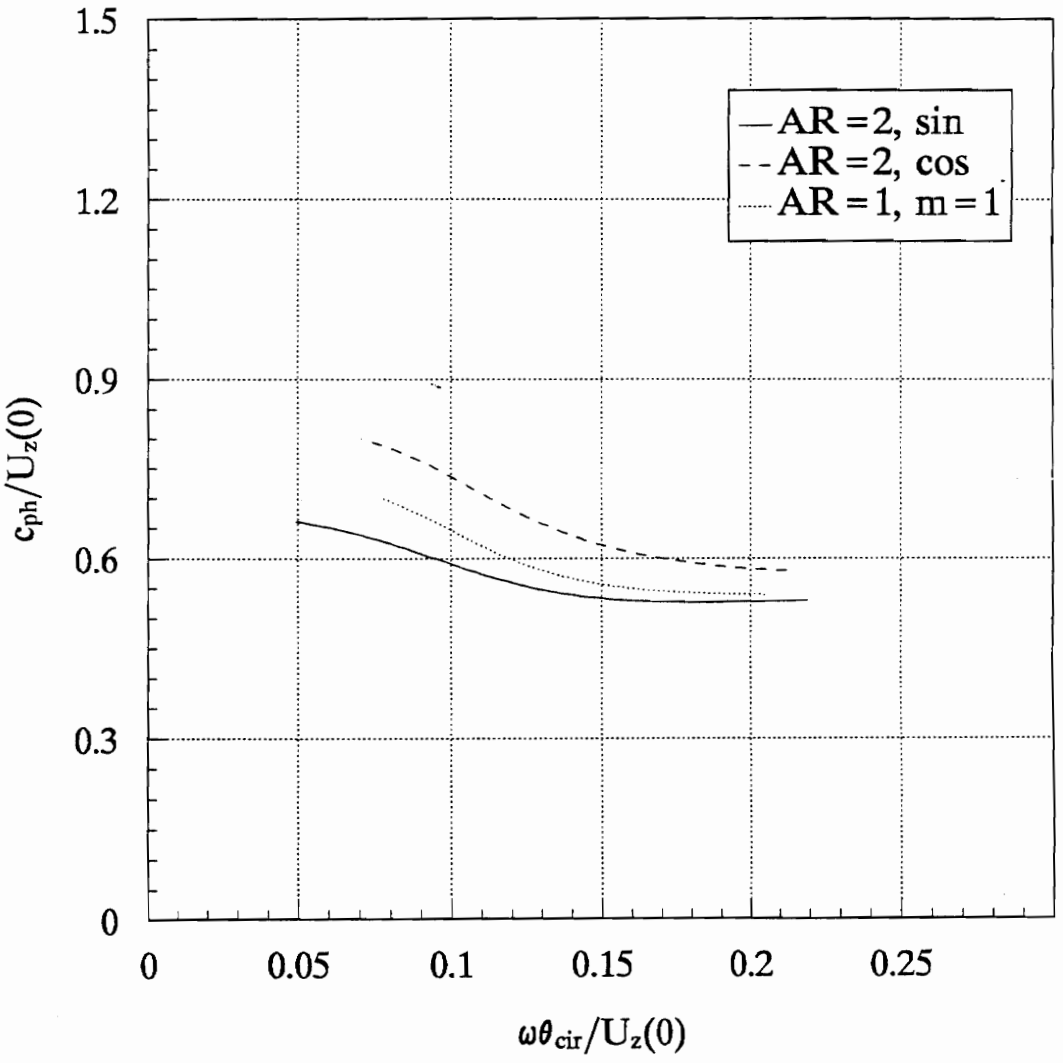

Figure 4.18. The comparison of the phase speeds of the first azimuthal modes of the circular and elliptical jets with uniform momentum thickness.

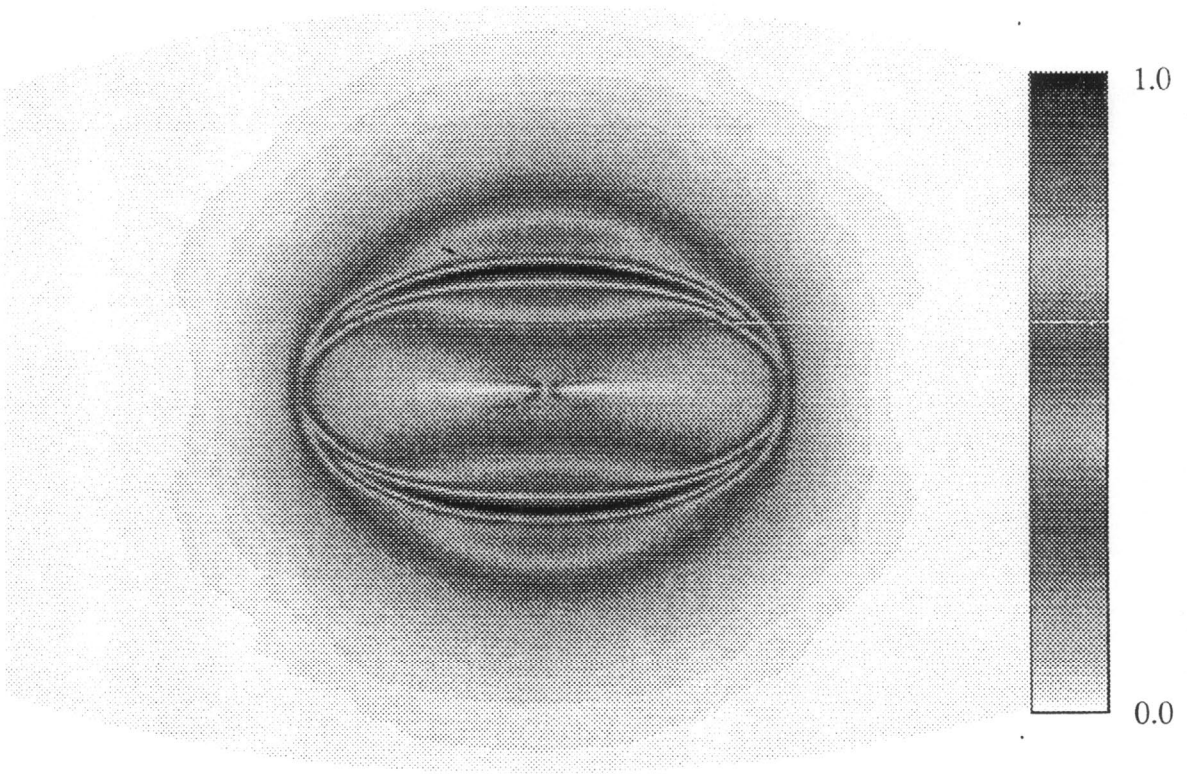

Figure 4.19. The distribution of the velocity eigenfunction of the sine mode of the $AR = 2$ elliptical jet with uniform momentum thickness.

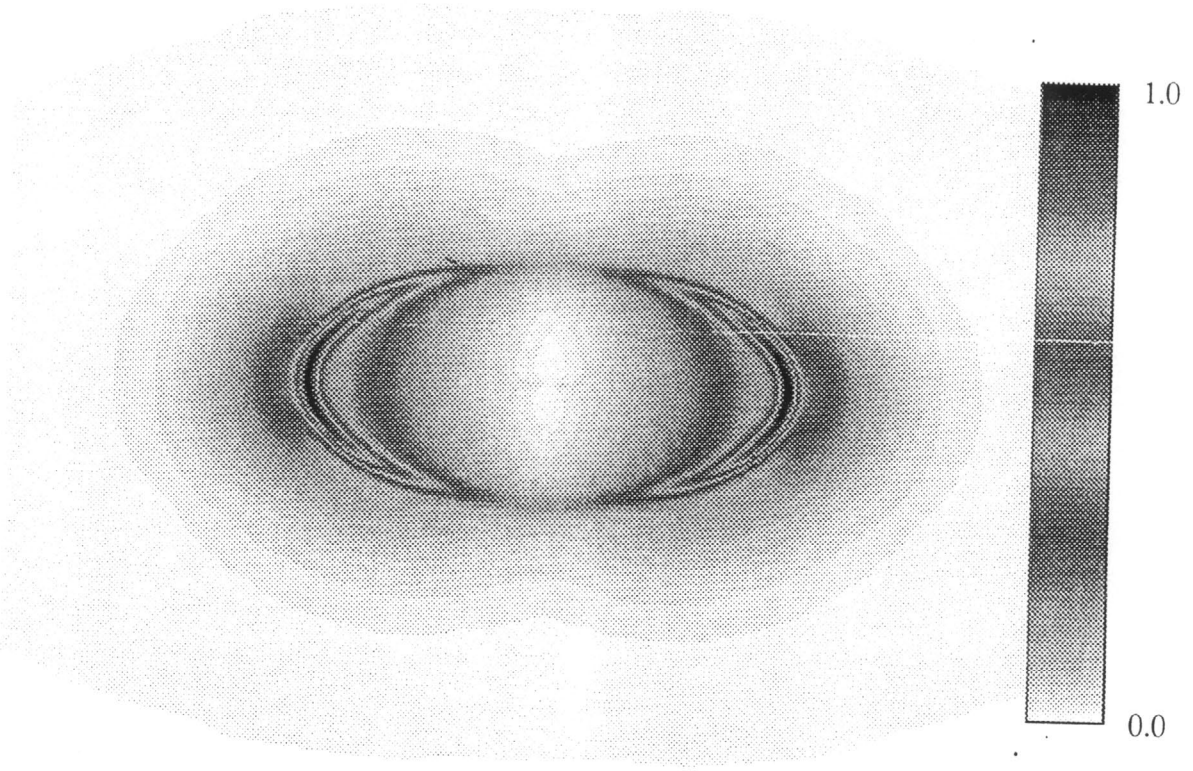

Figure 4.20. The distribution of the velocity eigenfunction of the cosine mode of the $AR = 2$ elliptical jet with uniform momentum thickness.

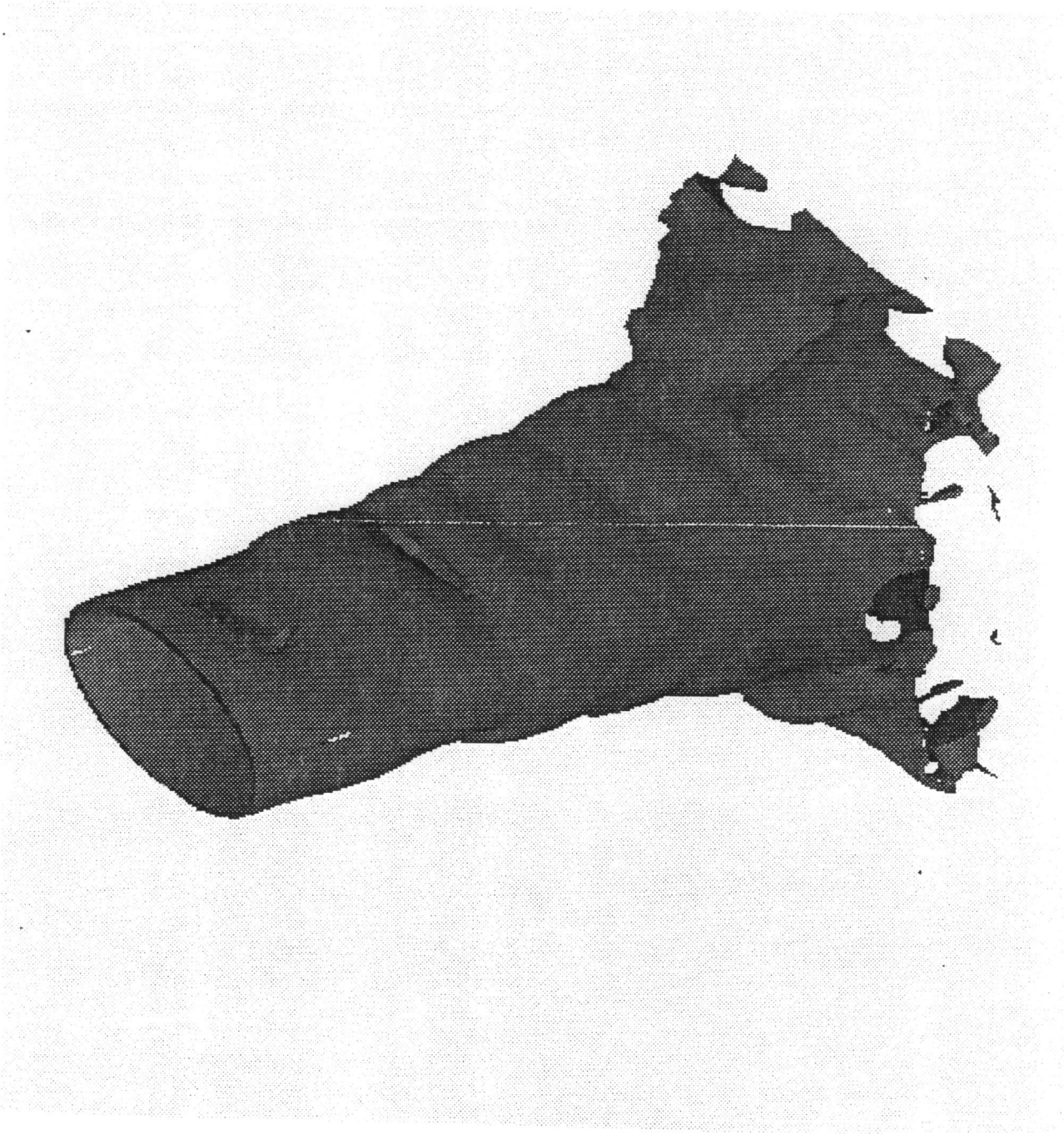

Figure 4.21. The surface of the constant vorticity of the sine mode of the $AR = 2$ elliptical jet with uniform momentum thickness.

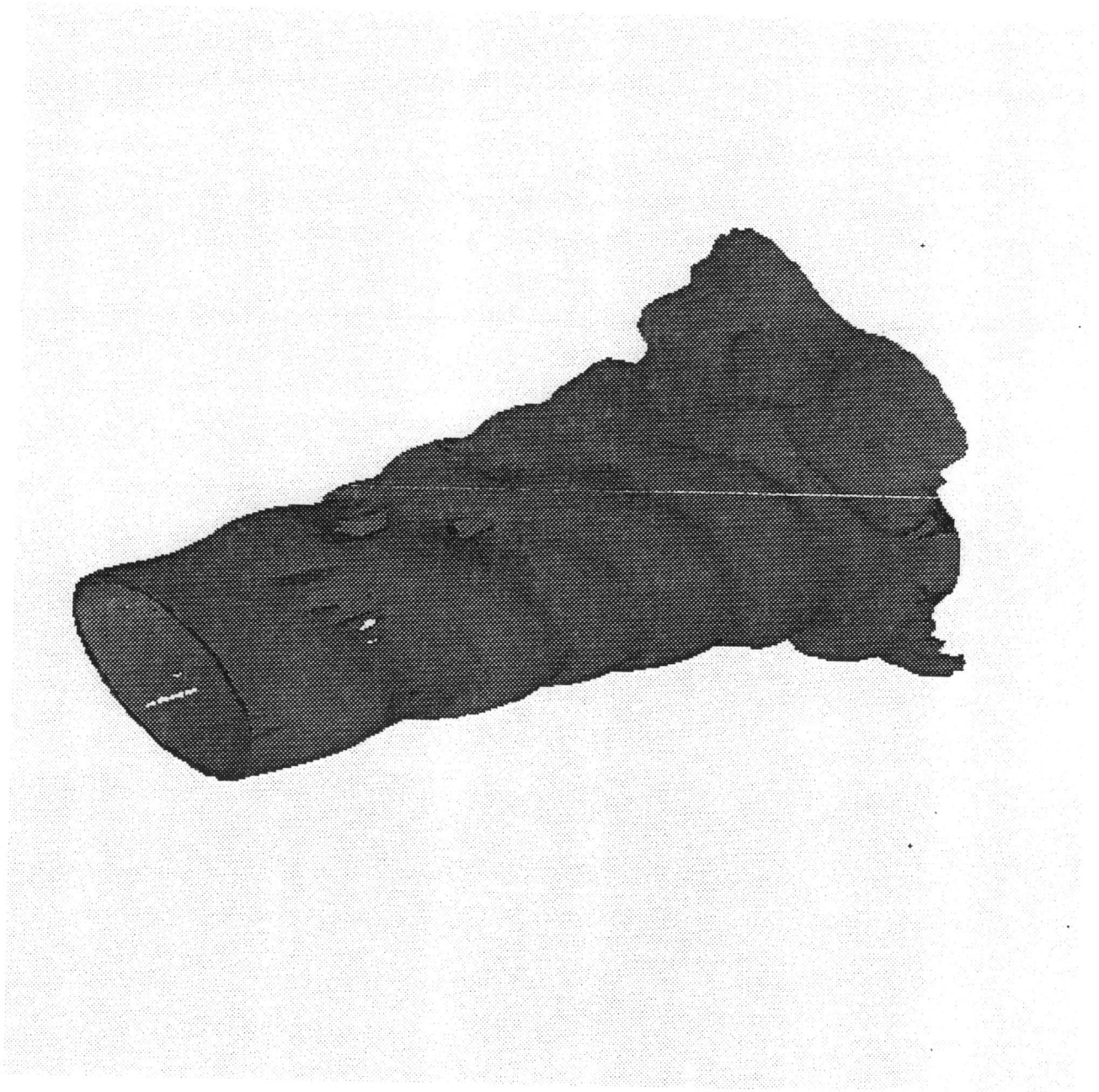

Figure 4.22. The surface of the constant vorticity of the cosine mode of the $AR = 2$ elliptical jet with uniform momentum thickness.

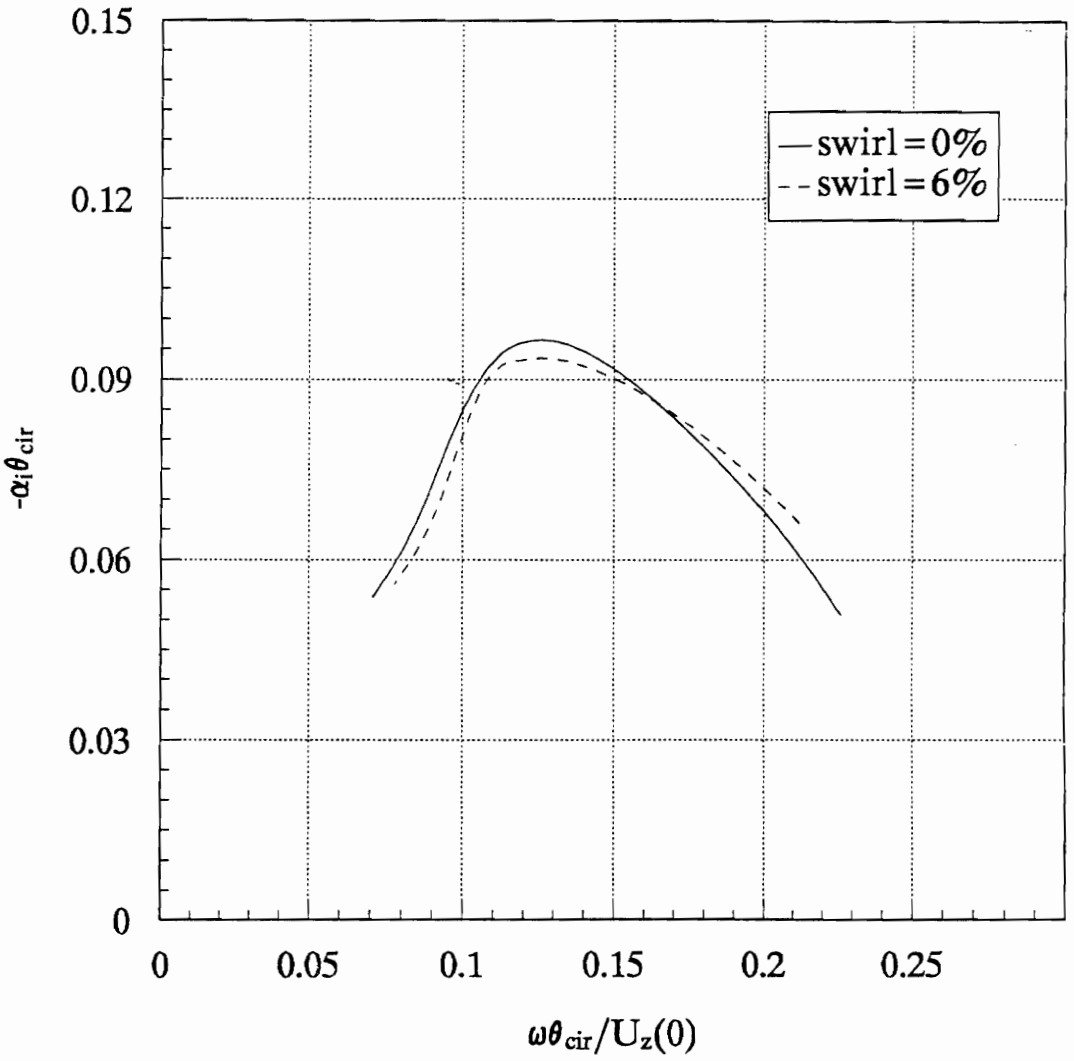

Figure 4.23. The influence of the swirl on the growth rate of the fundamental π mode of the $AR = 2$ elliptical jet with uniform momentum thickness.

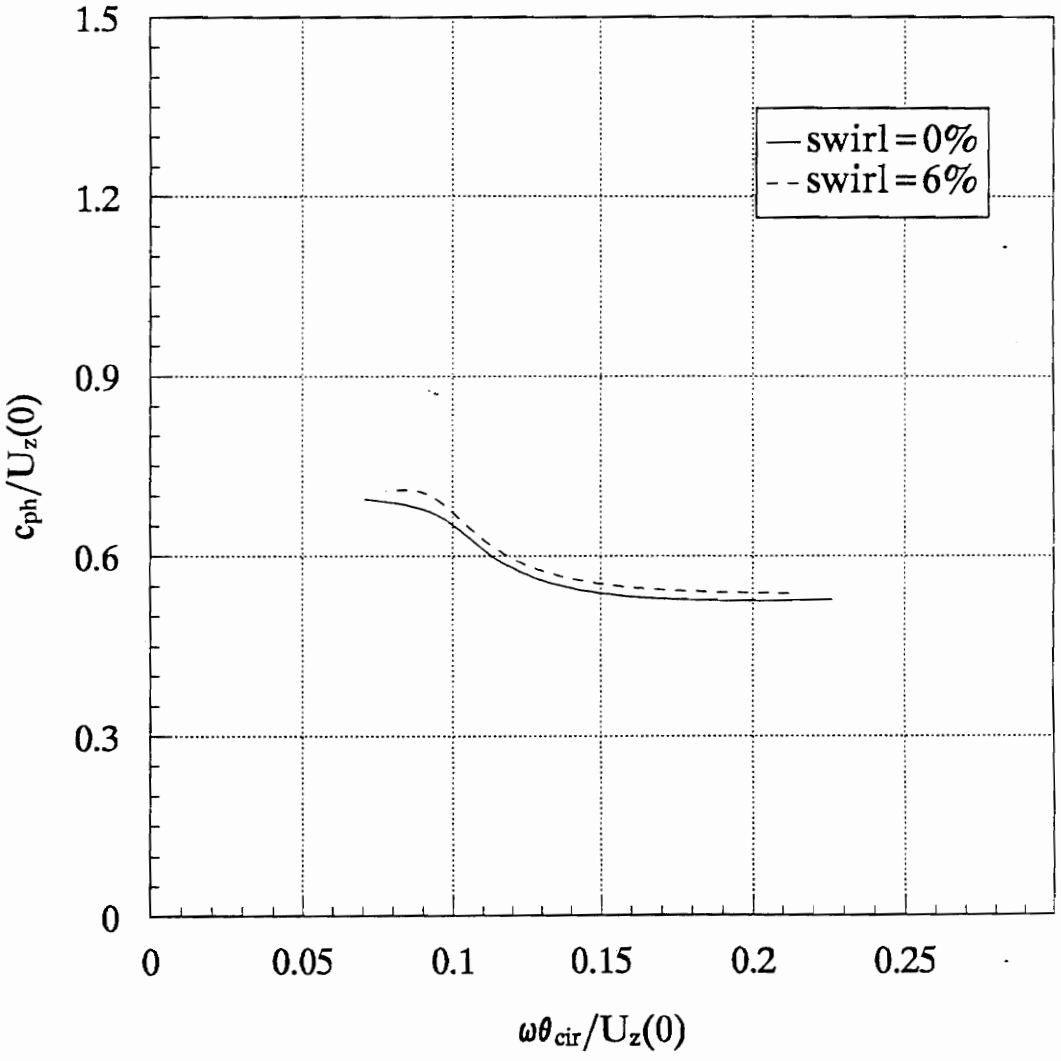

Figure 4.24. The influence of the swirl on the phase speed of the fundmental π mode of the $AR = 2$ elliptical jet with uniform momentum thickness.

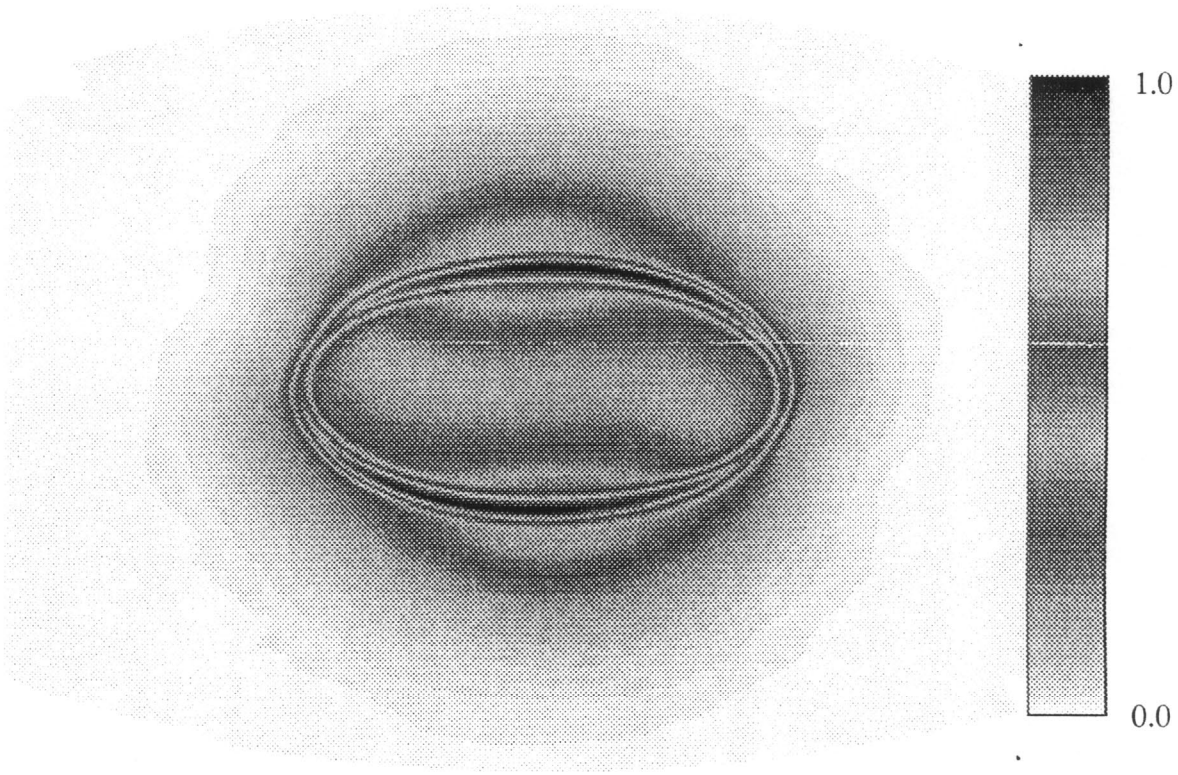

Figure 4.25. The distribution of the velocity eigenfunction of the fundamental π mode of the $AR = 2$ elliptical jet with uniform momentum thickness and 6% swirl.

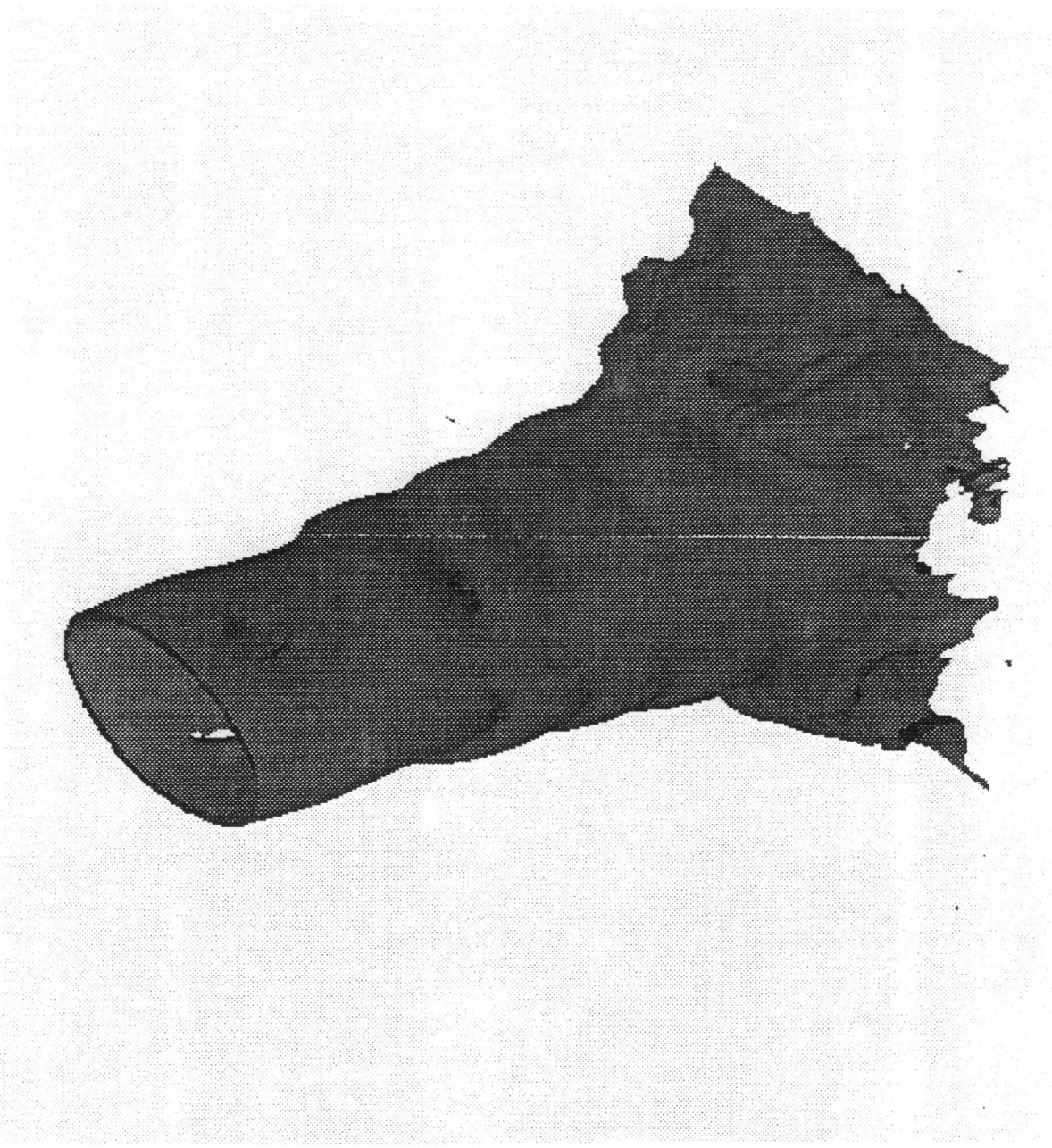

Figure 4.26. The surface of the constant vorticity of the fundamental π mode of the $AR = 2$ elliptical jet with uniform momentum thickness and 6% swirl.

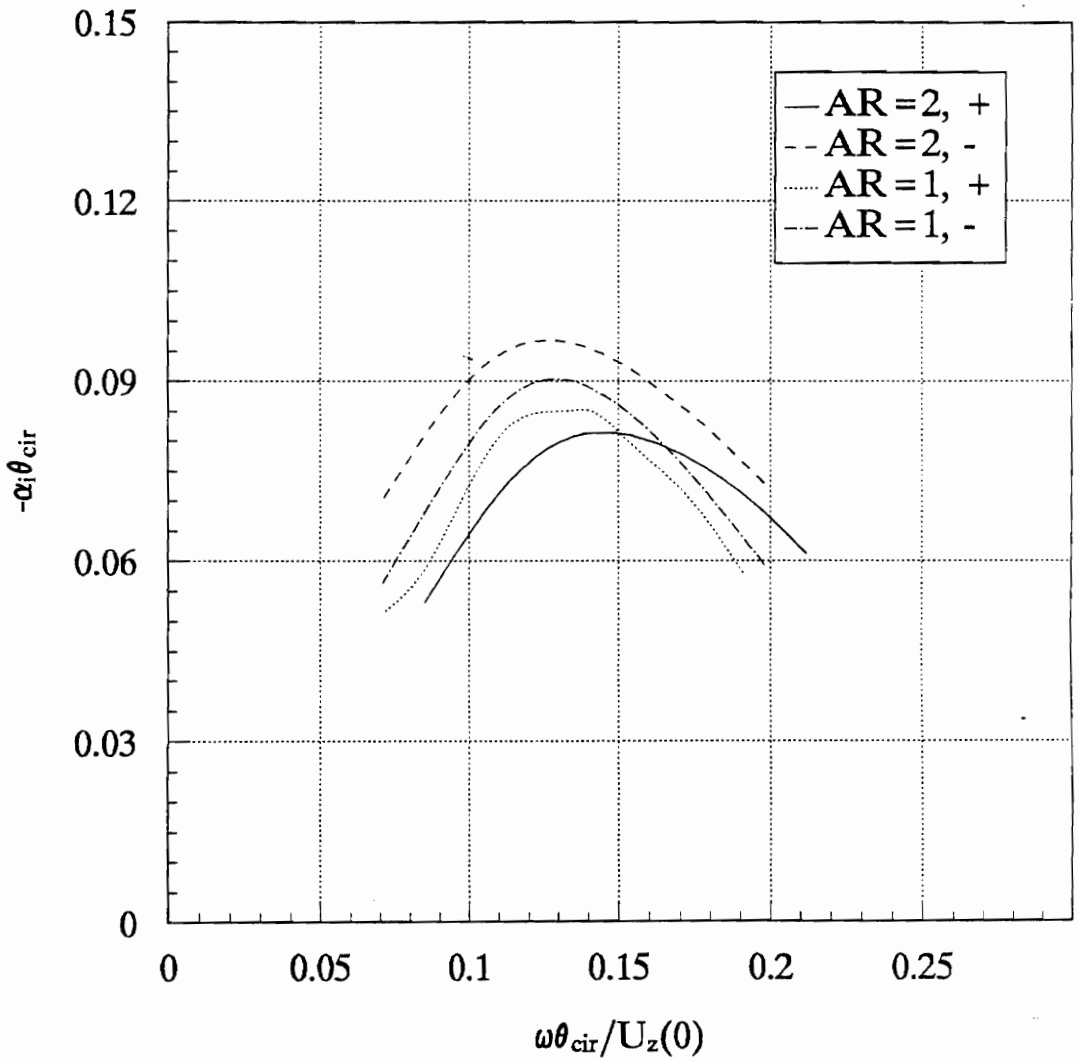

Figure 4.27. The comparison of the growth rates of the positive and negative first azimuthal modes of the $AR = 2$ elliptical jet with uniform momentum thickness with those of the circular jet.

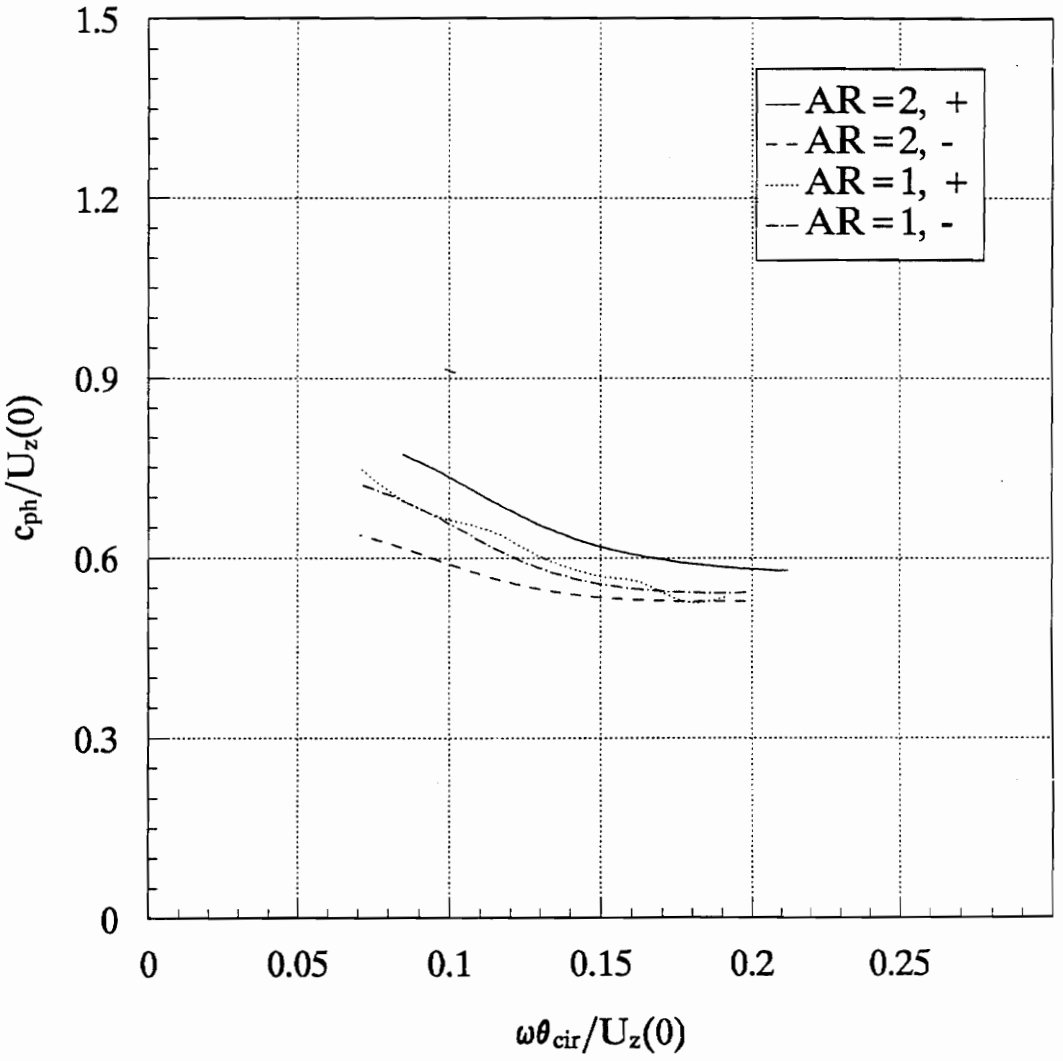

Figure 4.28. The comparison of the phase speeds of the positive and negative first azimuthal modes of the $AR = 2$ elliptical jet with uniform momentum thickness with those of the circular jet.

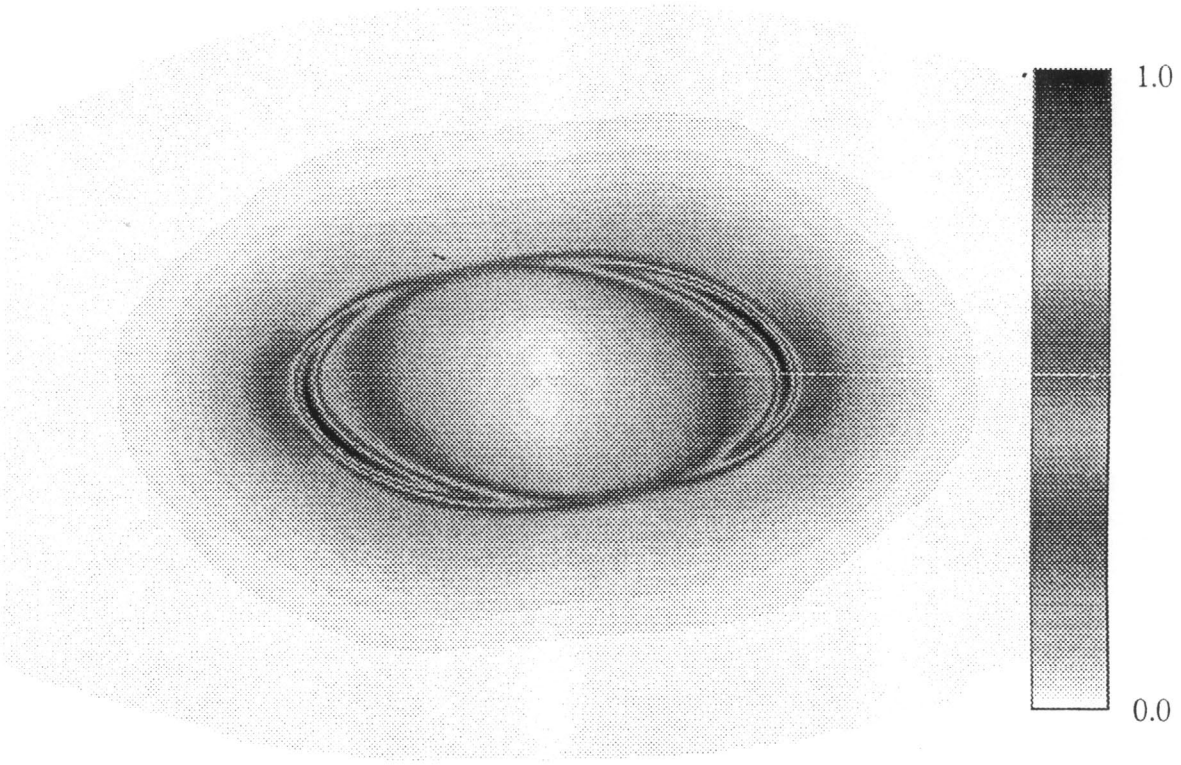

Figure 4.29. The distribution of the velocity eigenfunction of the positive first azimuthal mode of the $AR = 2$ elliptical jet with uniform momentum thickness and 6% swirl.

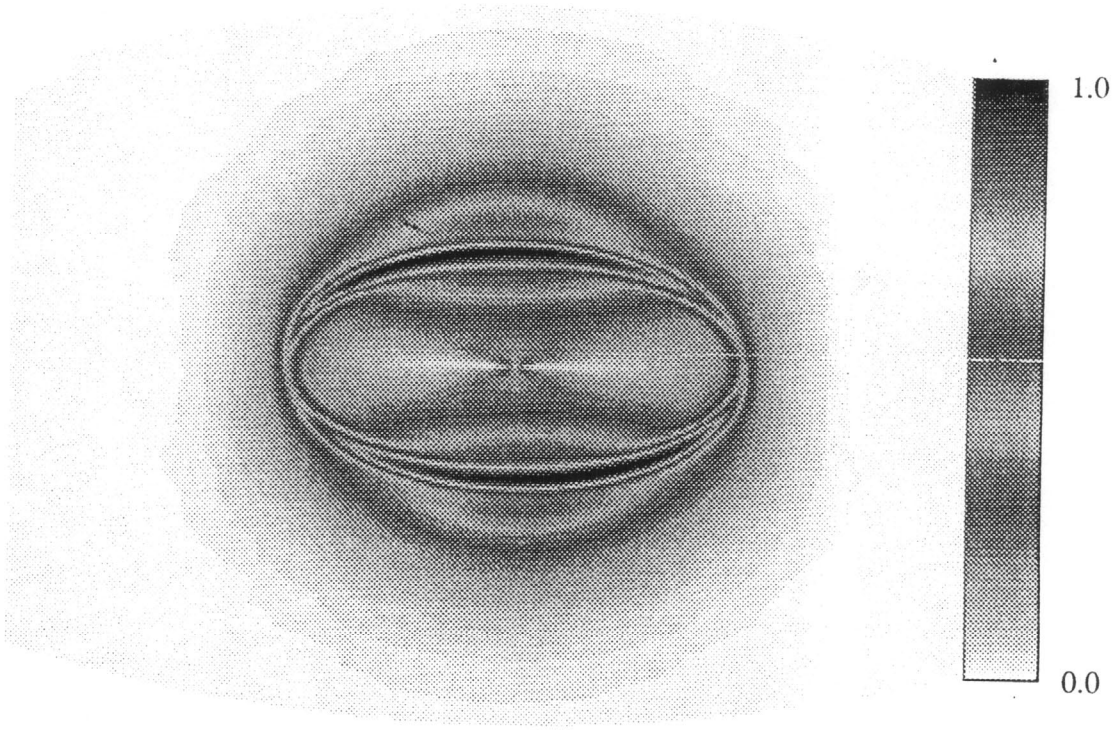

Figure 4.30. The distribution of the velocity eigenfunction of the negative first azimuthal mode of the $AR = 2$ elliptical jet with uniform momentum thickness and 6% swirl.

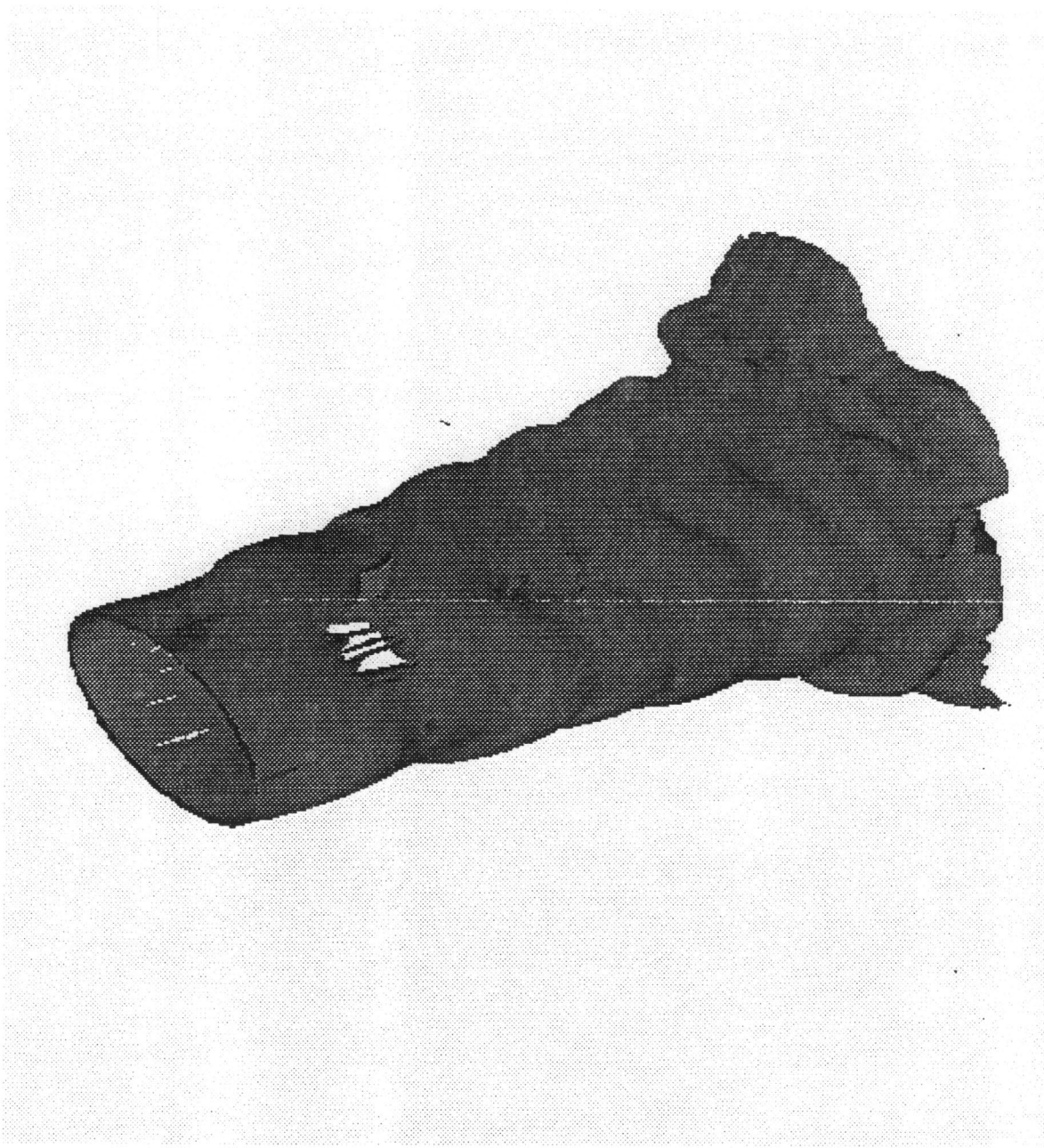

Figure 4.31. The surface of constant vorticity of the positive first azimuthal mode of the $AR = 2$ elliptical jet with uniform momentum thickness and 6% swirl.

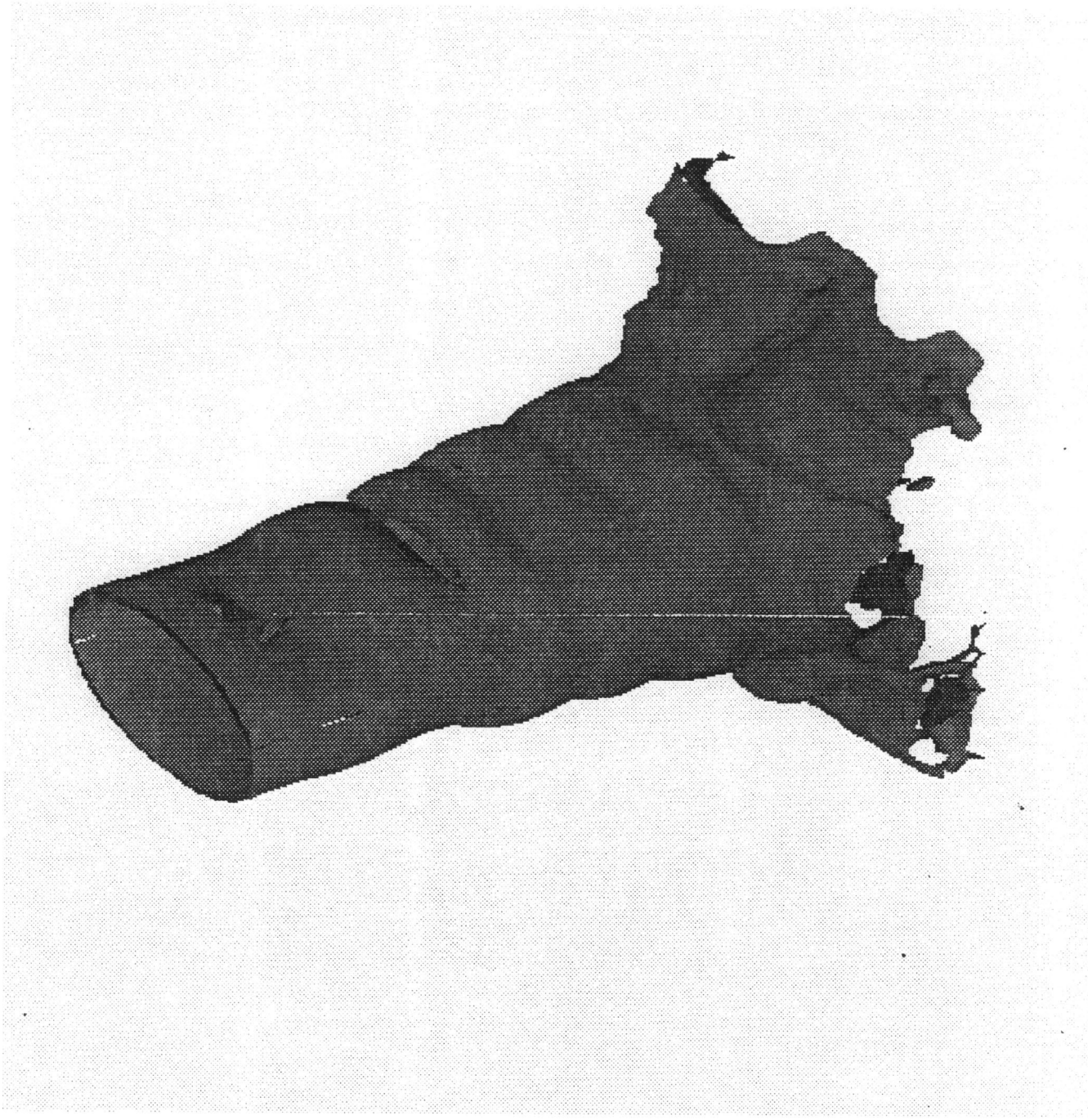

Figure 4.32. The surface of constant vorticity of the negative first azimuthal mode of the $AR = 2$ elliptical jet with uniform momentum-thickness and 6% swirl.

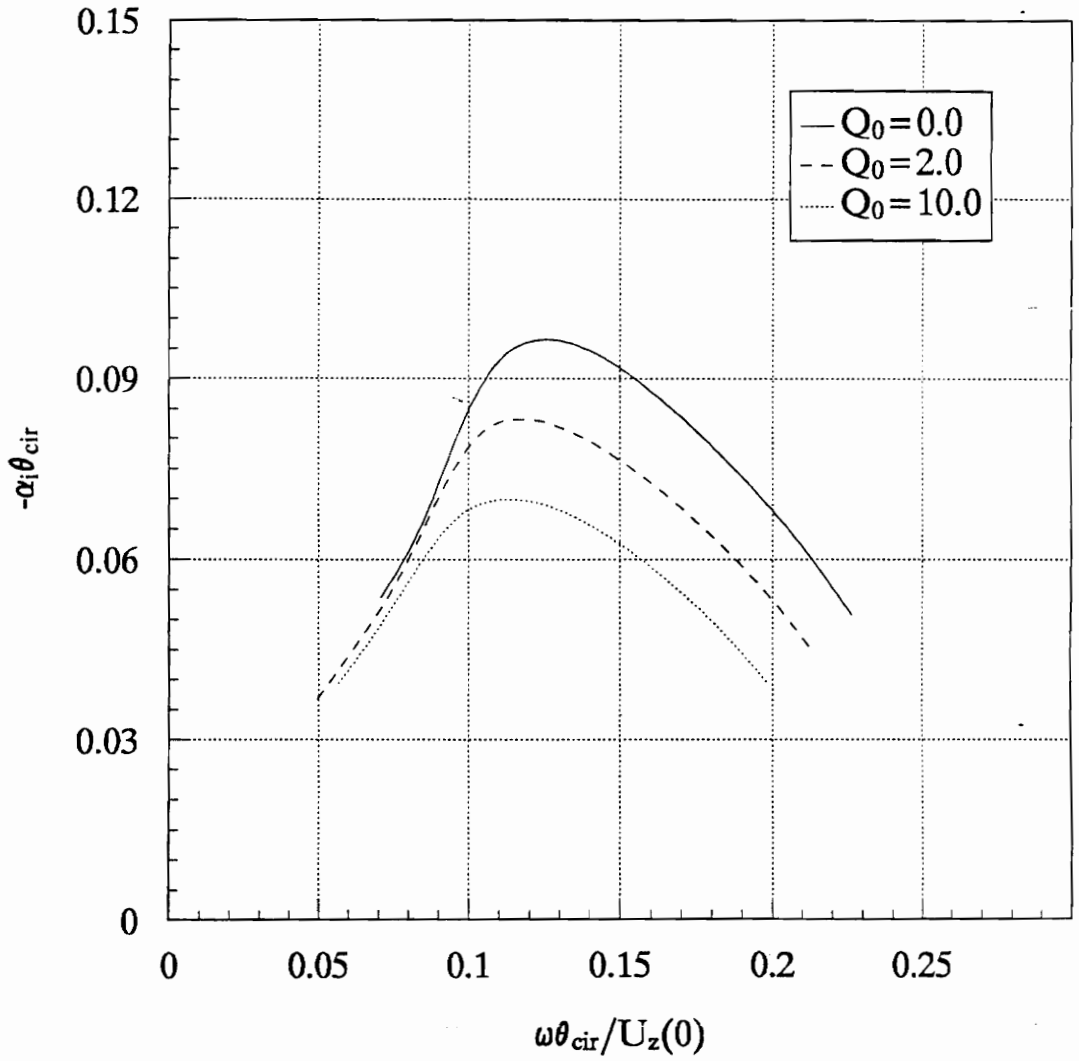

Figure 4.33. The influence of the heat release on the growth rate of the fundamental π mode of the $AR = 2$ elliptical jet with uniform momentum thickness.

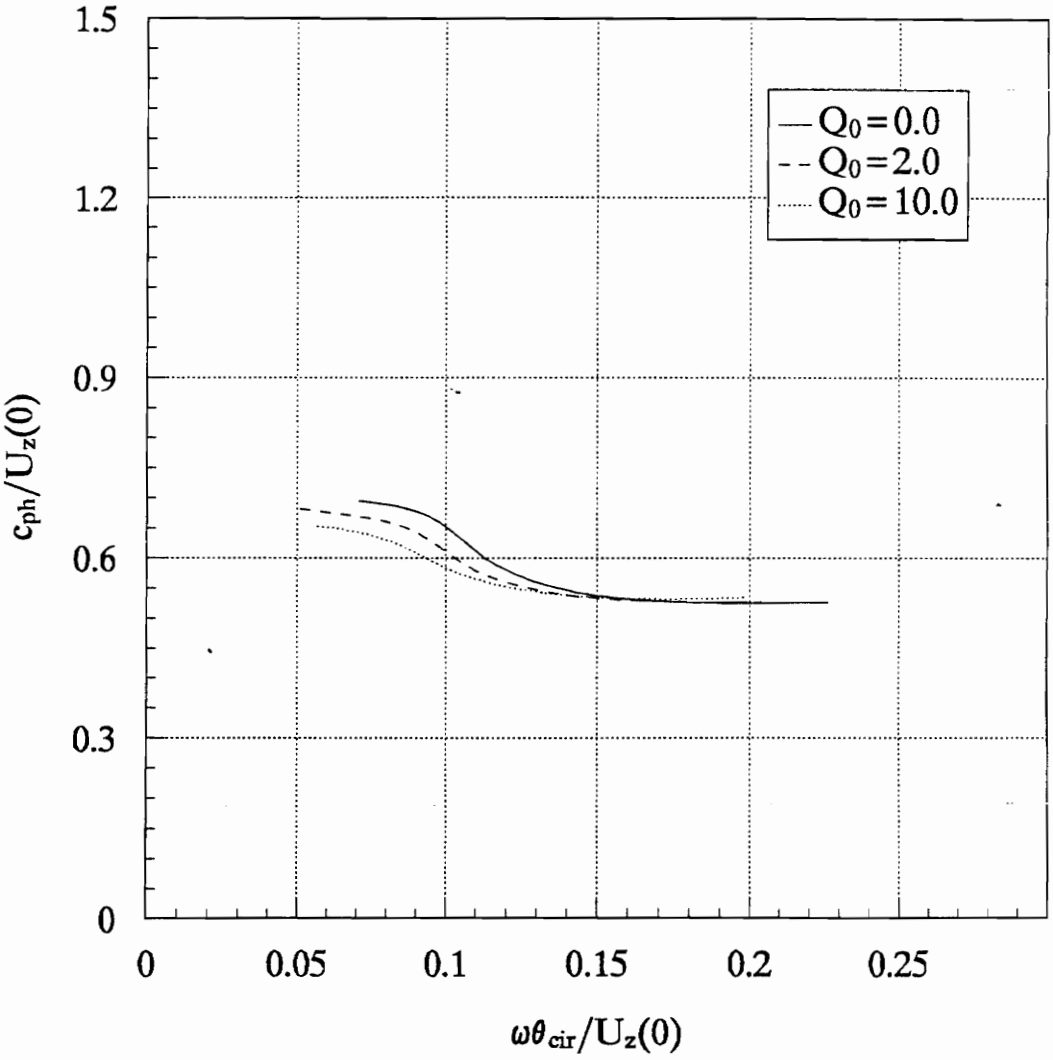

Figure 4.34. The influence of the heat release on the phase speed of the fundamental π mode of the $AR = 2$ elliptical jet with uniform momentum thickness.

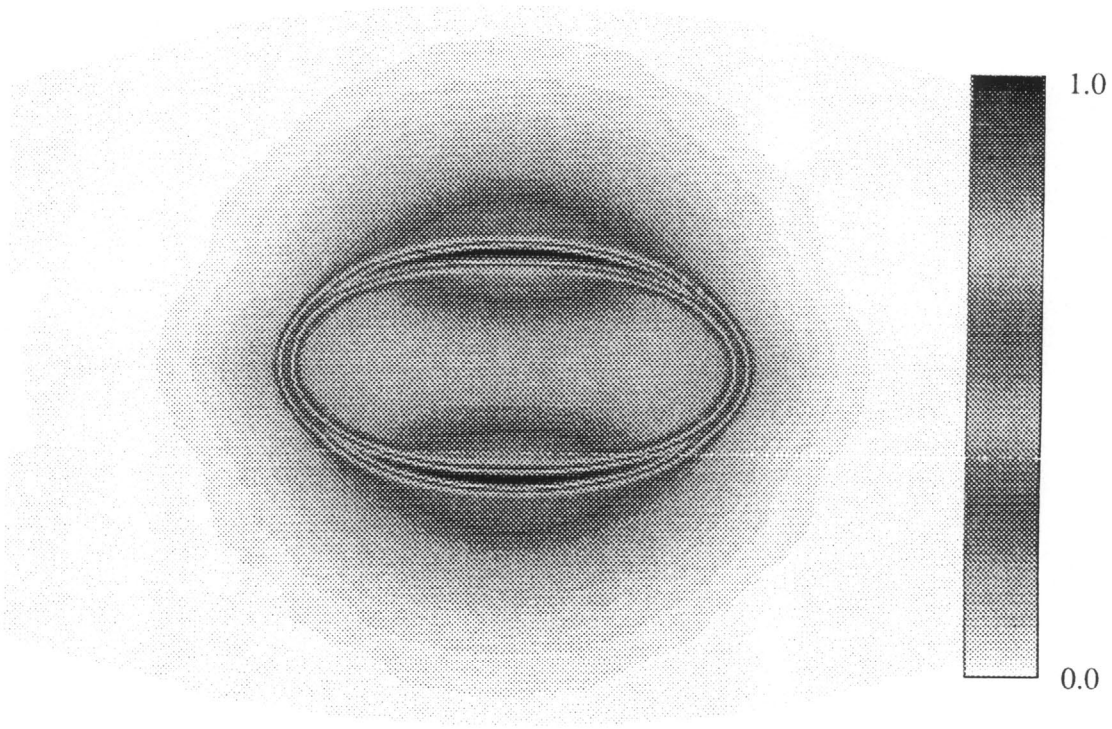

Figure 4.35. The distribution of the velocity eigenfunction of the $AR = 2$ elliptical jet with uniform momentum thickness and heat release.

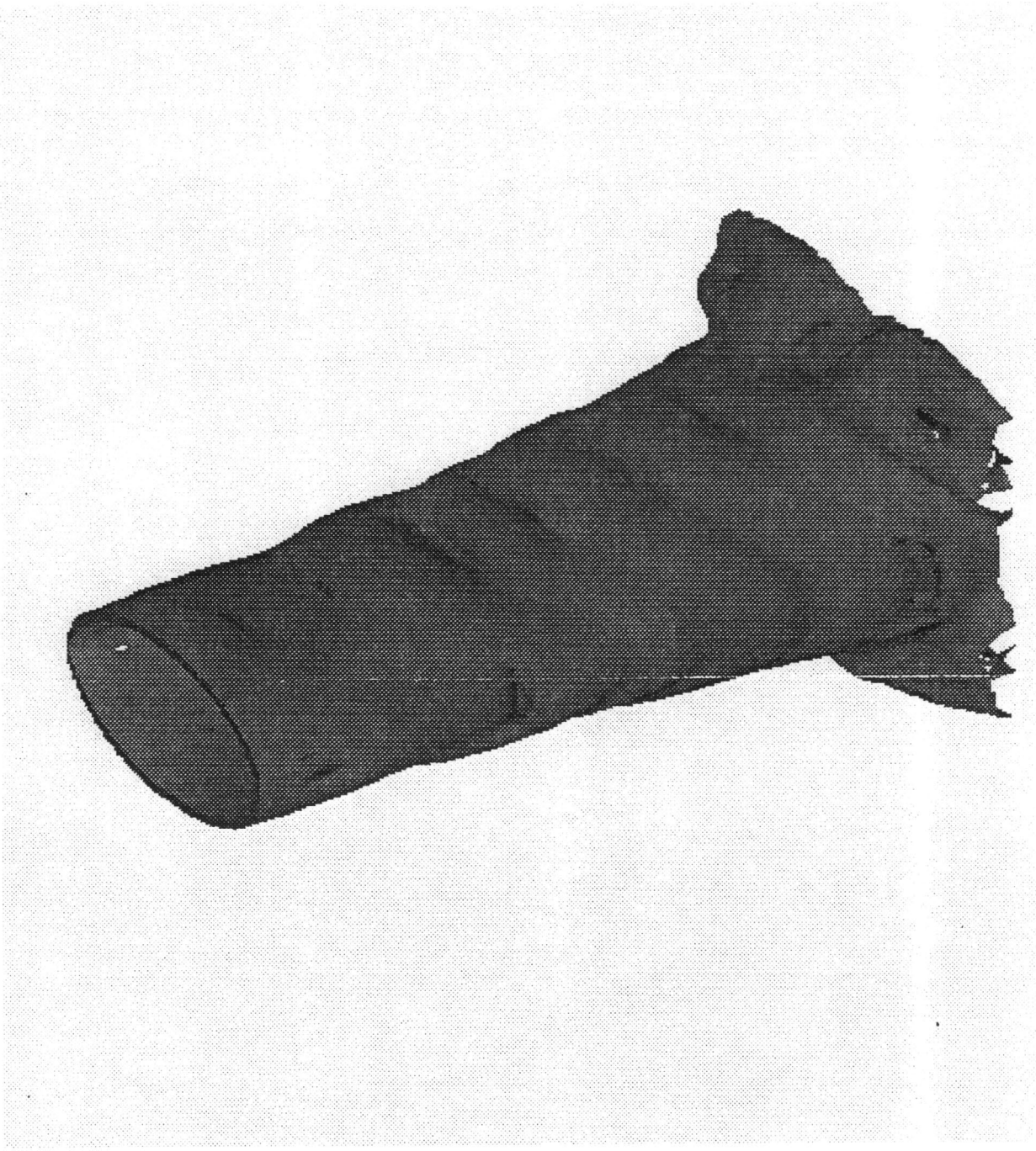

Figure 4.36. The surface of constant vorticity of the fundamental π mode of the $AR = 2$ elliptical jet with uniform momentum thickness and heat release.

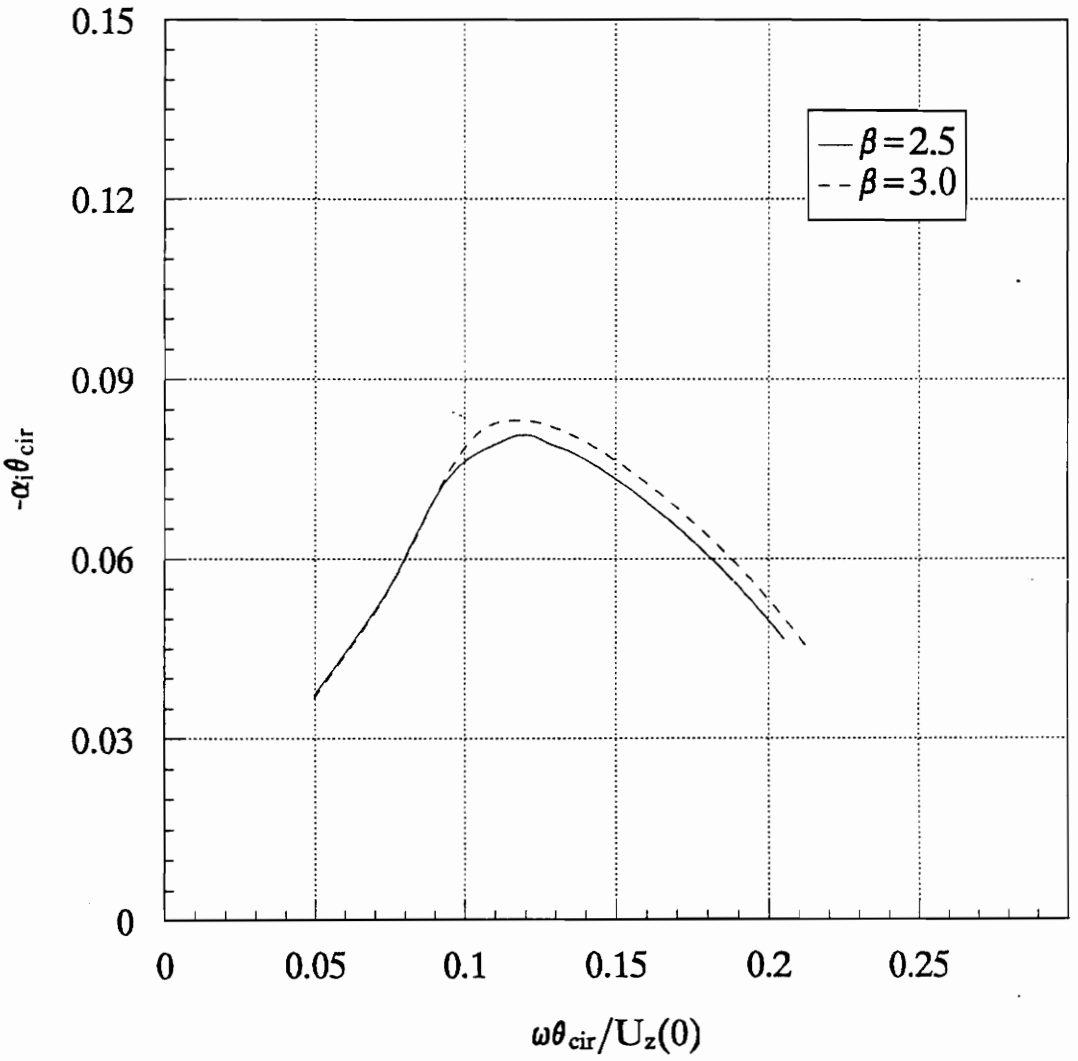

Figure 4.37. The influence of the activation energy on the growth rate of the fundamental π mode of the $AR = 2$ elliptical jet with uniform momentum thickness.

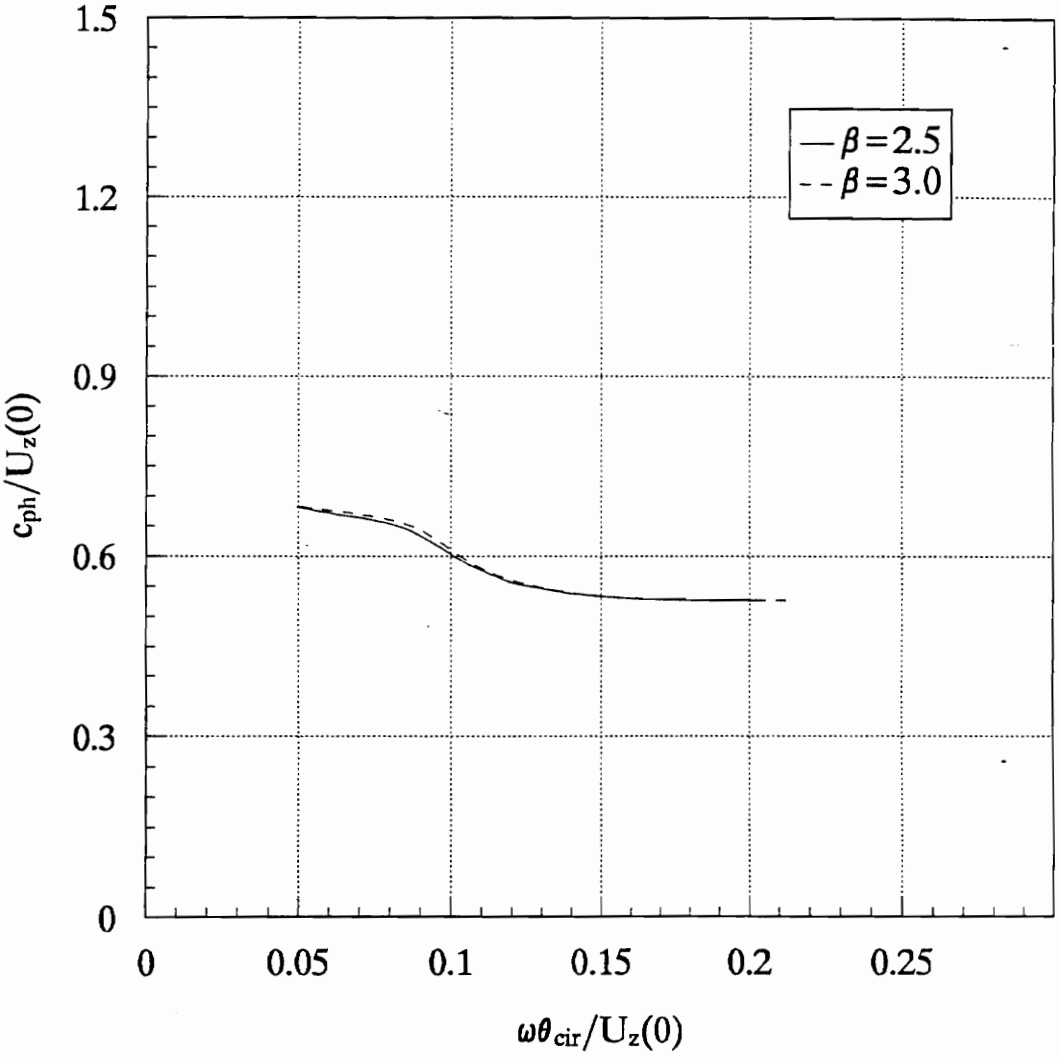

Figure 4.38. The influence of the activation energy on the phase speed of the fundamental π mode of the $AR = 2$ elliptical jet with uniform momentum thickness.

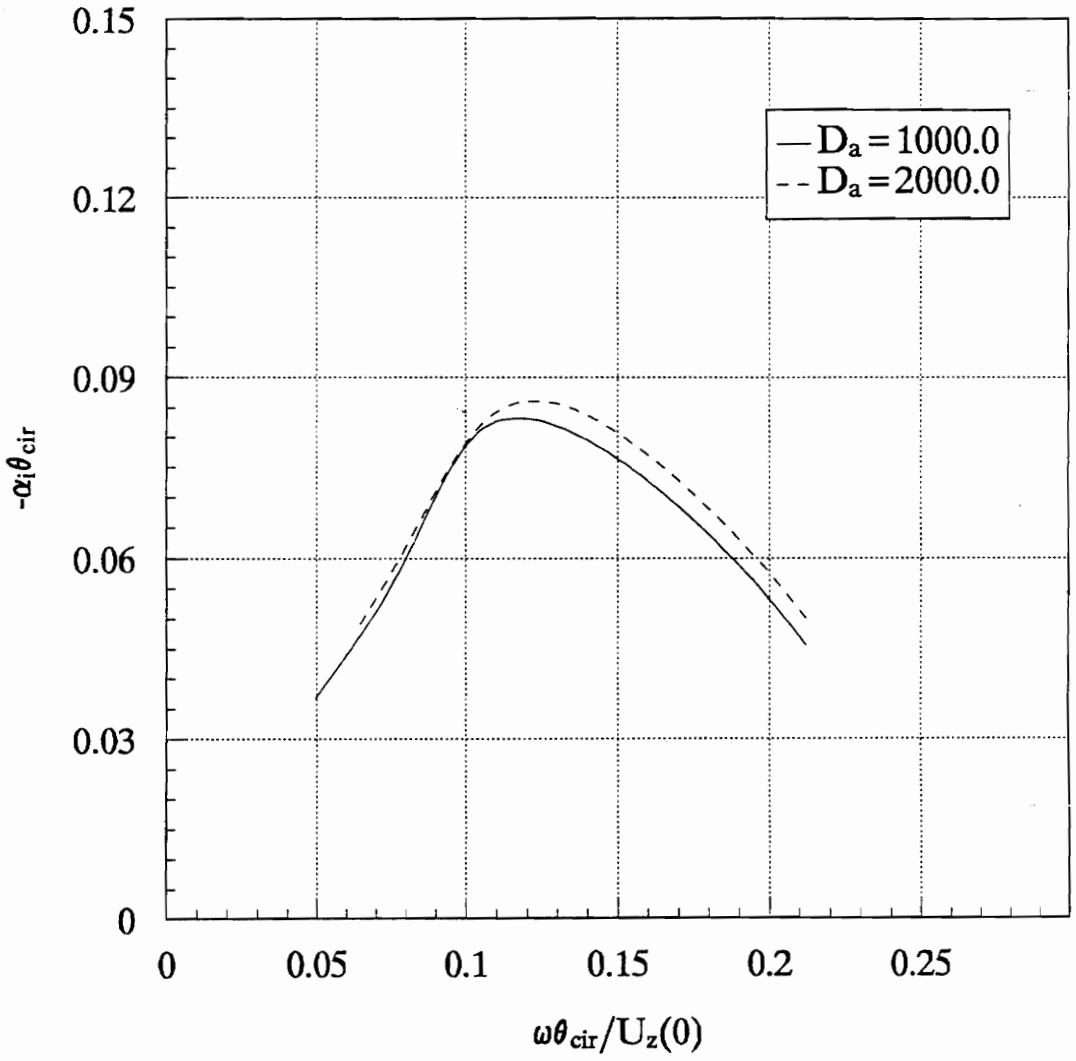

Figure 4.39. The influence of the Damkohler number on the growth rate of the fundamental π mode of the $AR = 2$ elliptical jet with uniform momentum thickness.

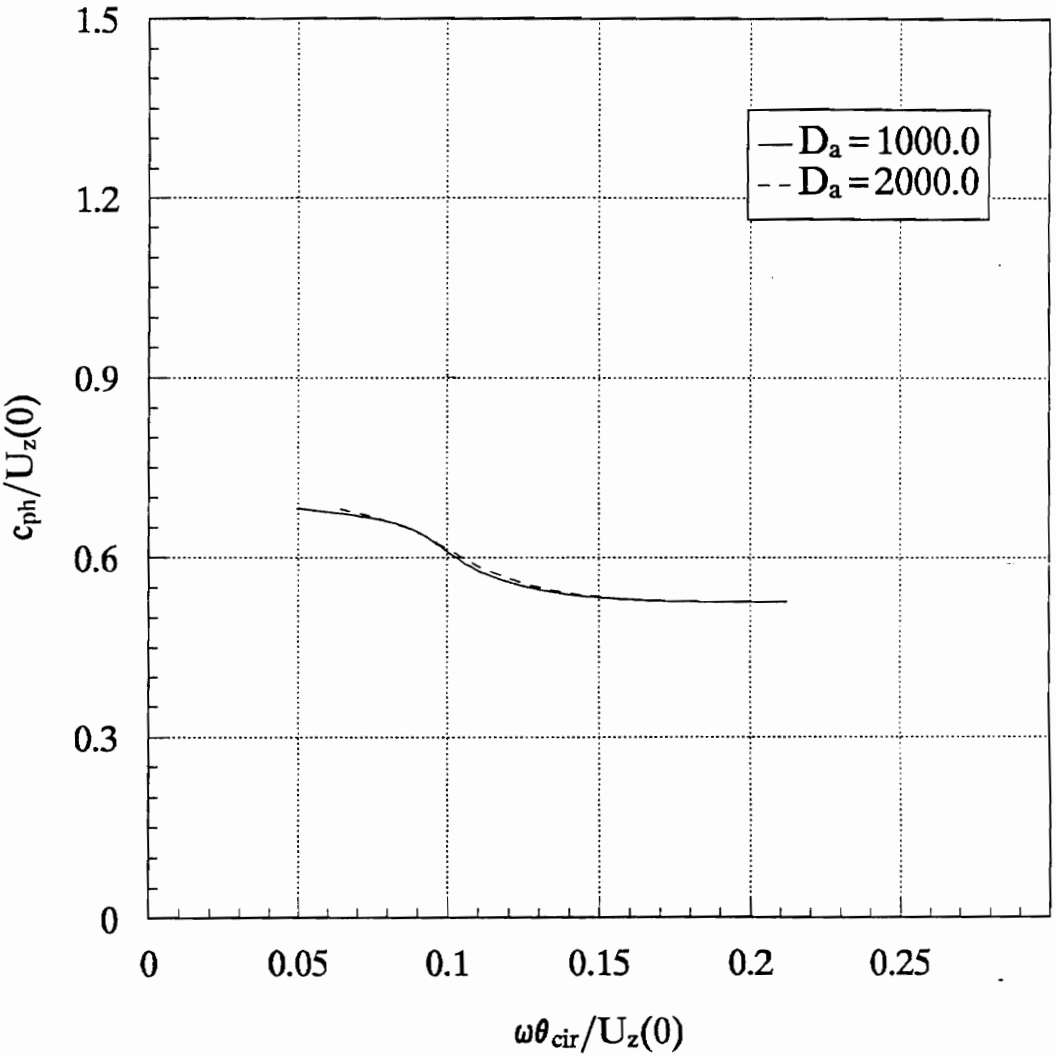

Figure 4.40. The influence of the Damkohler number on the phase speed of the fundamental π mode of the $AR = 2$ elliptical jet with uniform momentum thickness.

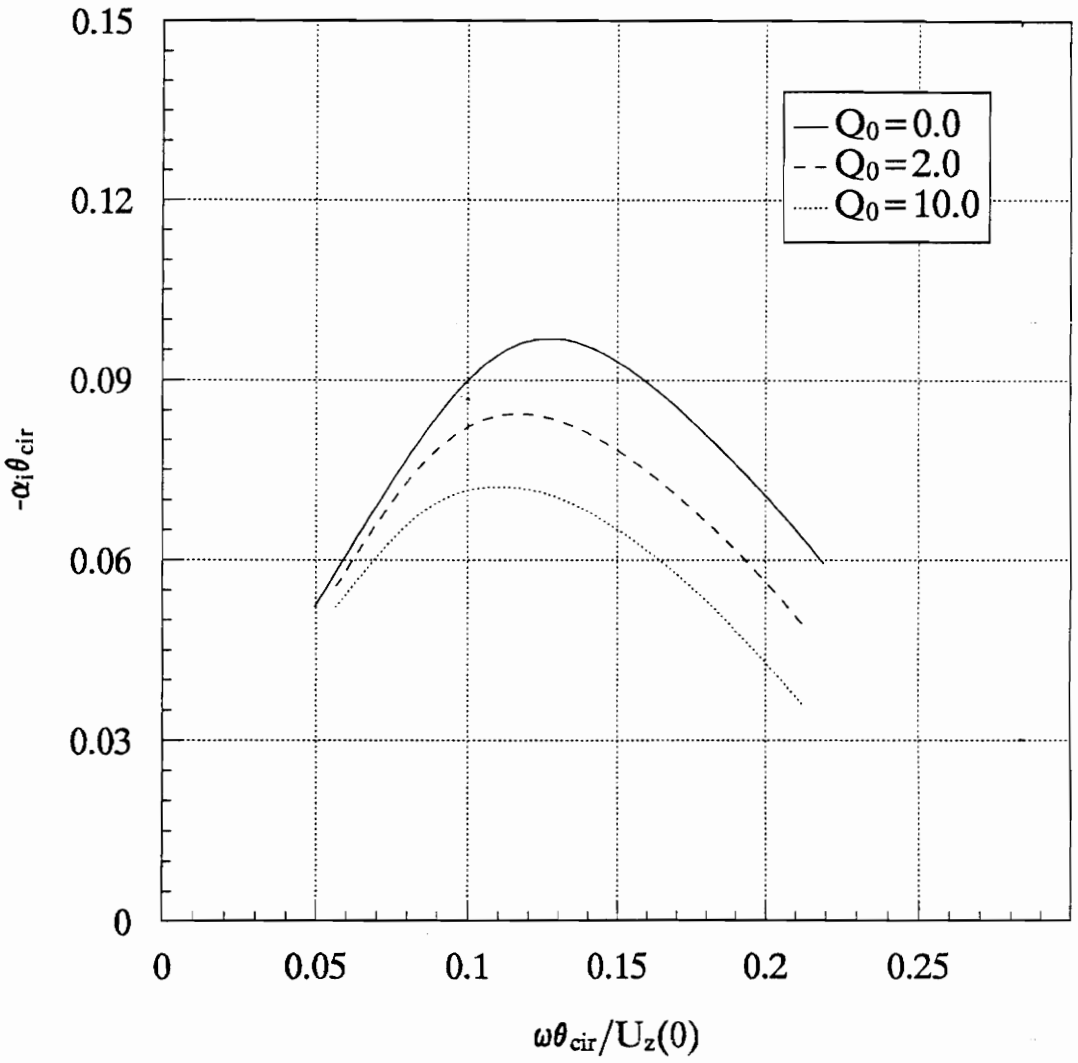

Figure 4.41. The influence of the heat release on the growth rate of the sine mode of the $AR = 2$ elliptical jet with uniform momentum thickness.

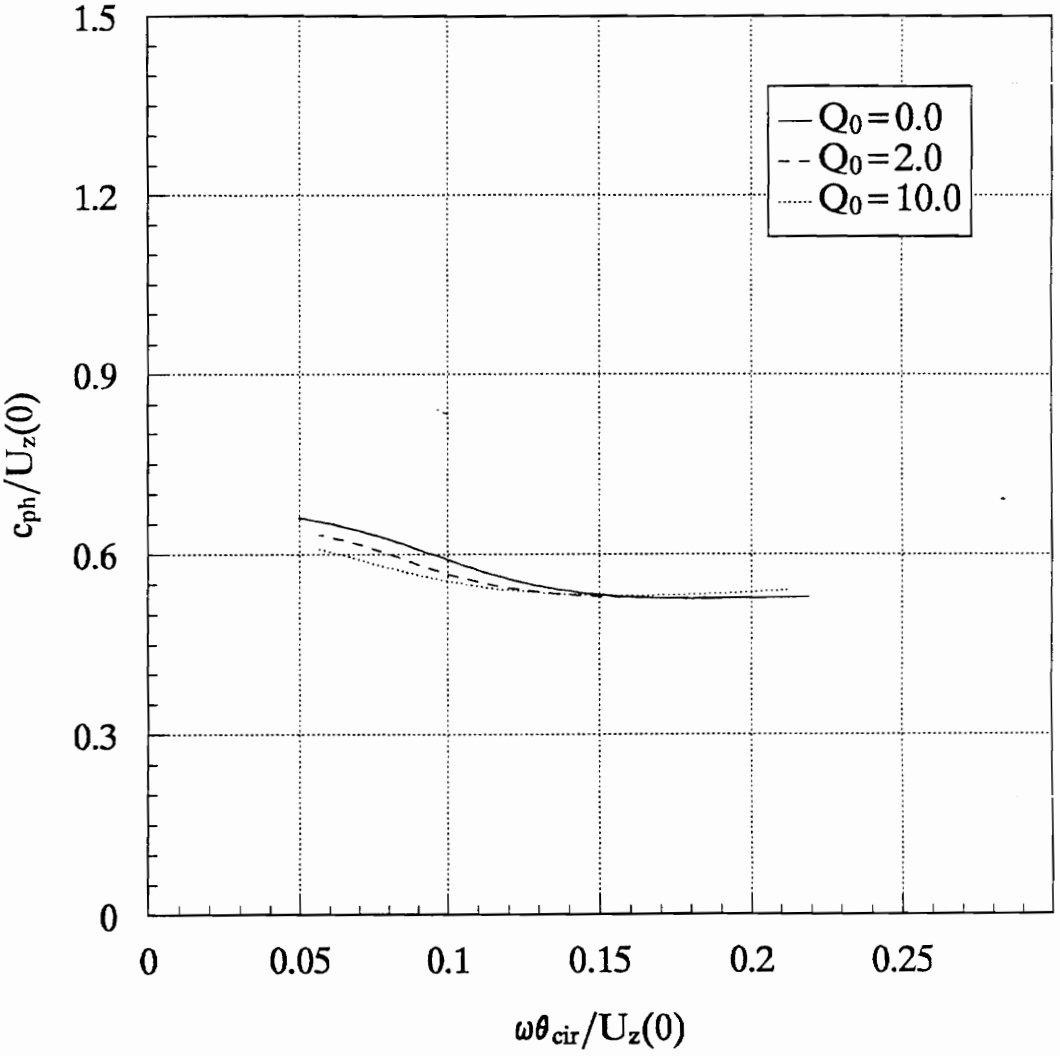

Figure 4.42. The influence of the heat release on the phase speed of the sine mode of the $AR = 2$ elliptical jet with uniform momentum thickness.

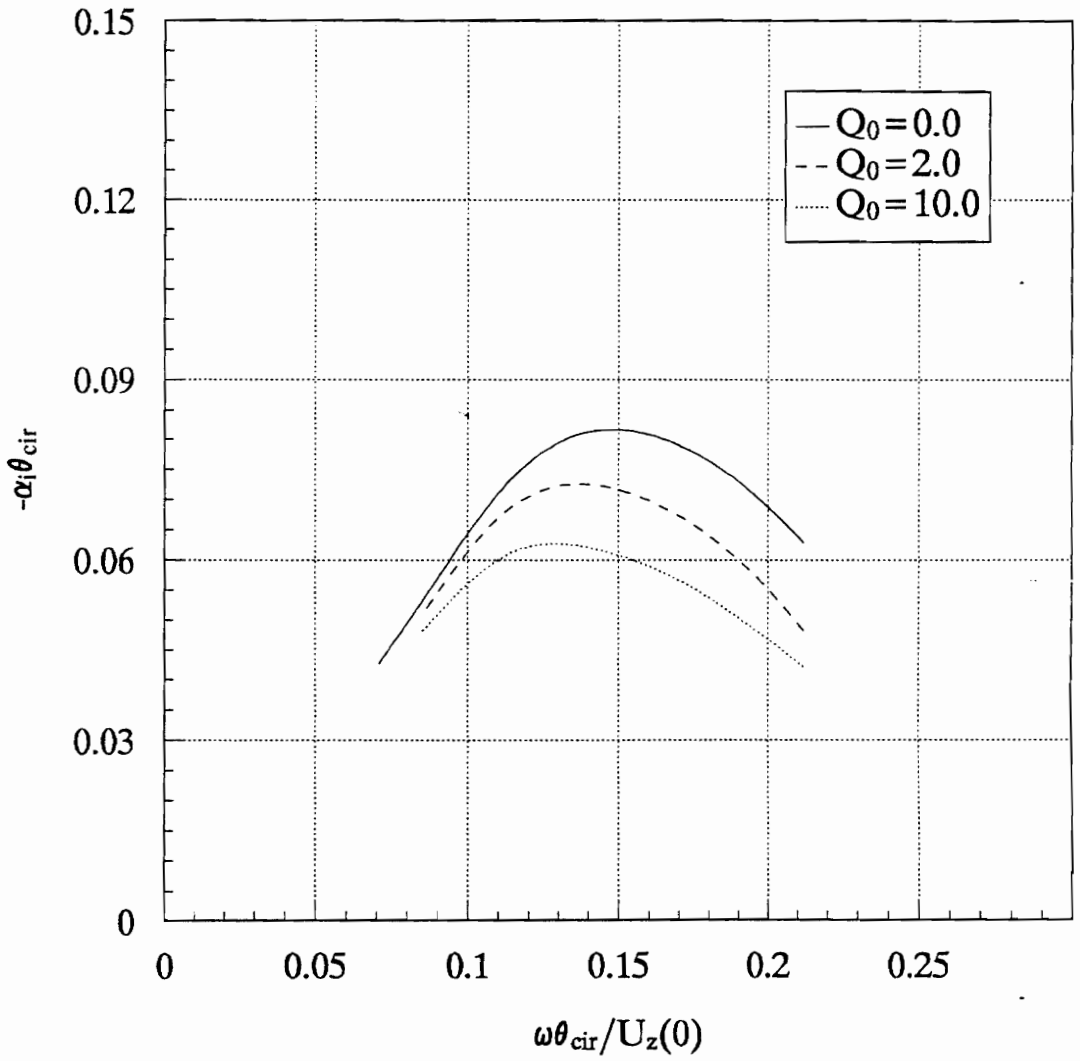

Figure 4.43. The influence of the heat release on the growth rate of the cosine mode of the $AR = 2$ elliptical jet with uniform momentum thickness.

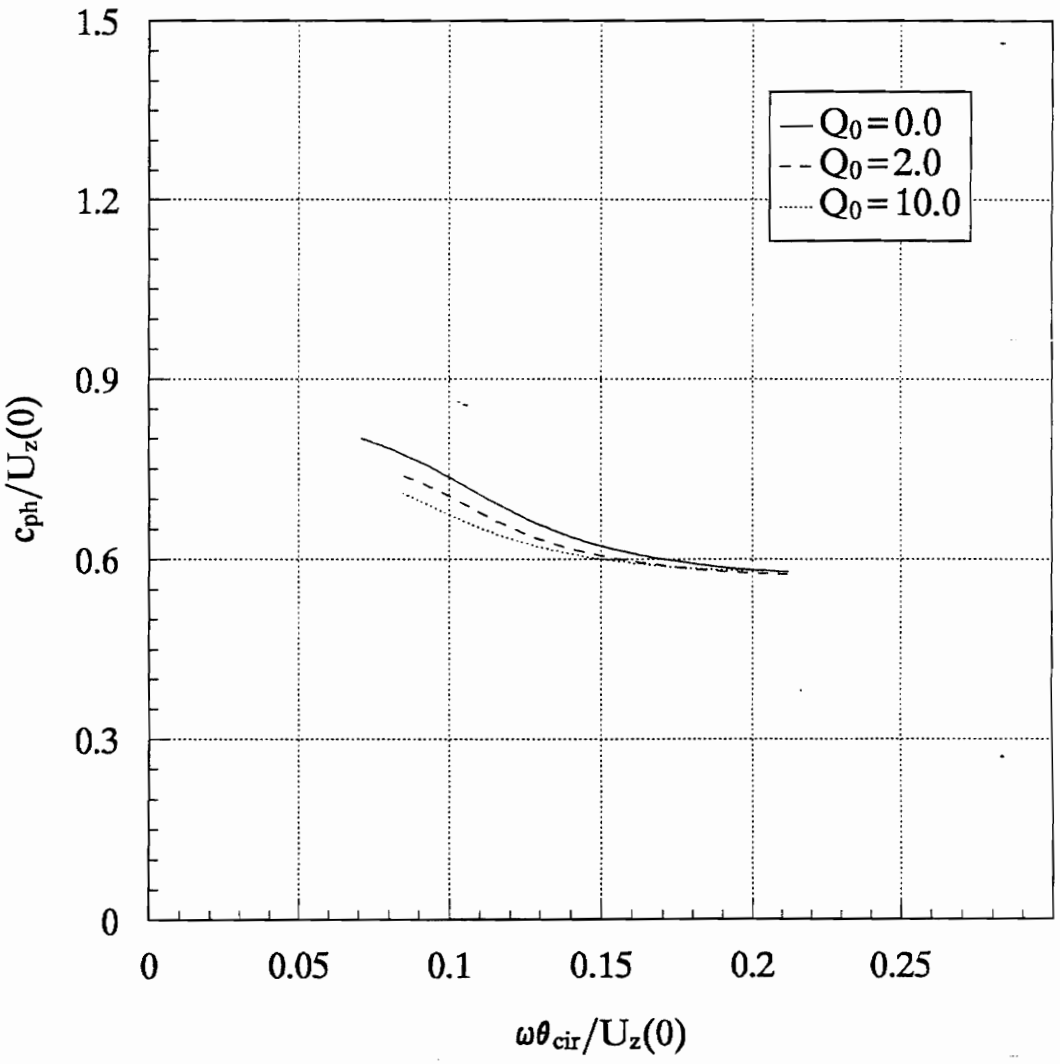

Figure 4.44. The influence of the heat release on the phase speed of the cosine mode of the $AR = 2$ elliptical jet with uniform momentum thickness.

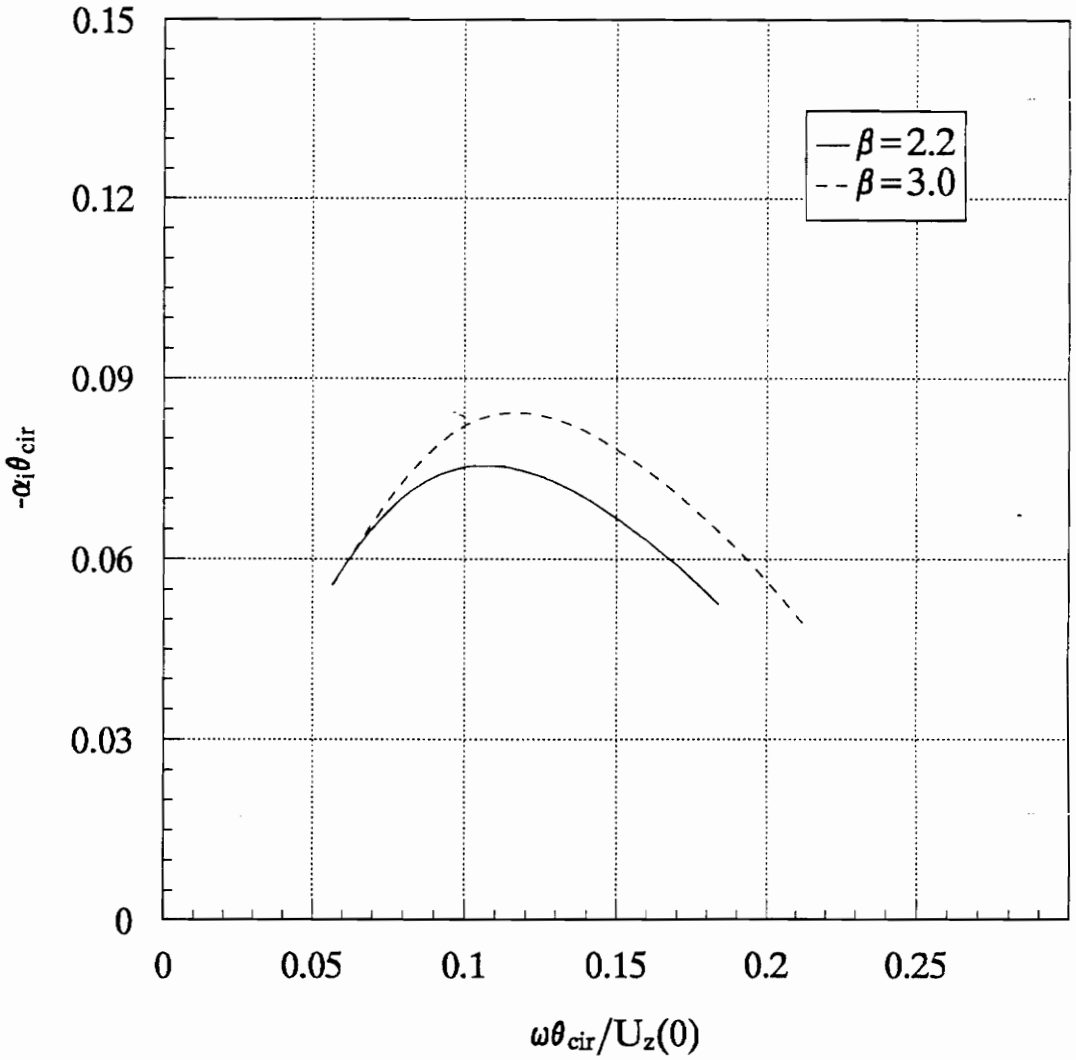

Figure 4.45. The influence of the activation energy on the growth rate of the sine mode of the $AR = 2$ elliptical jet with uniform momentum thickness.

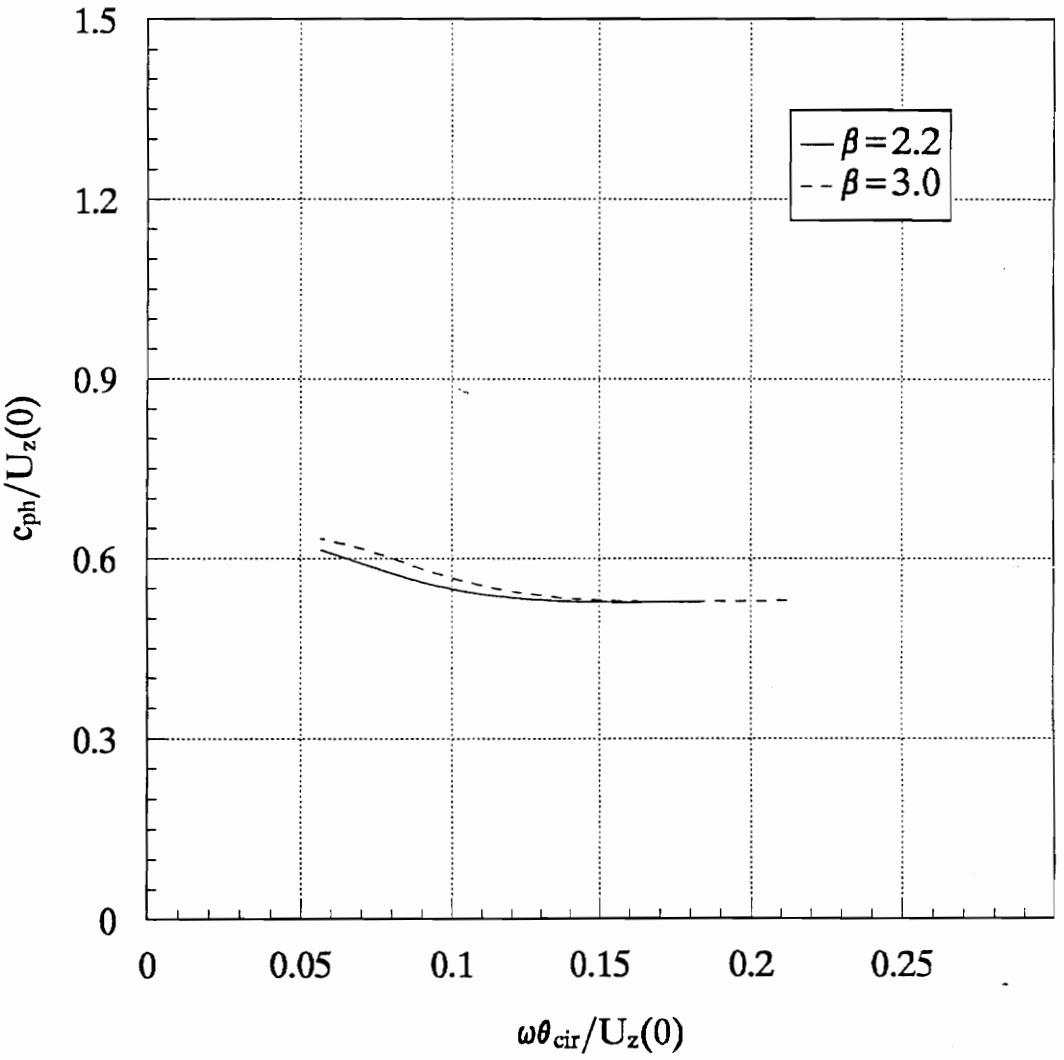

Figure 4.46. The influence of the activation energy on the phase speed of the sine mode of the $AR = 2$ elliptical jet with uniform momentum thickness.

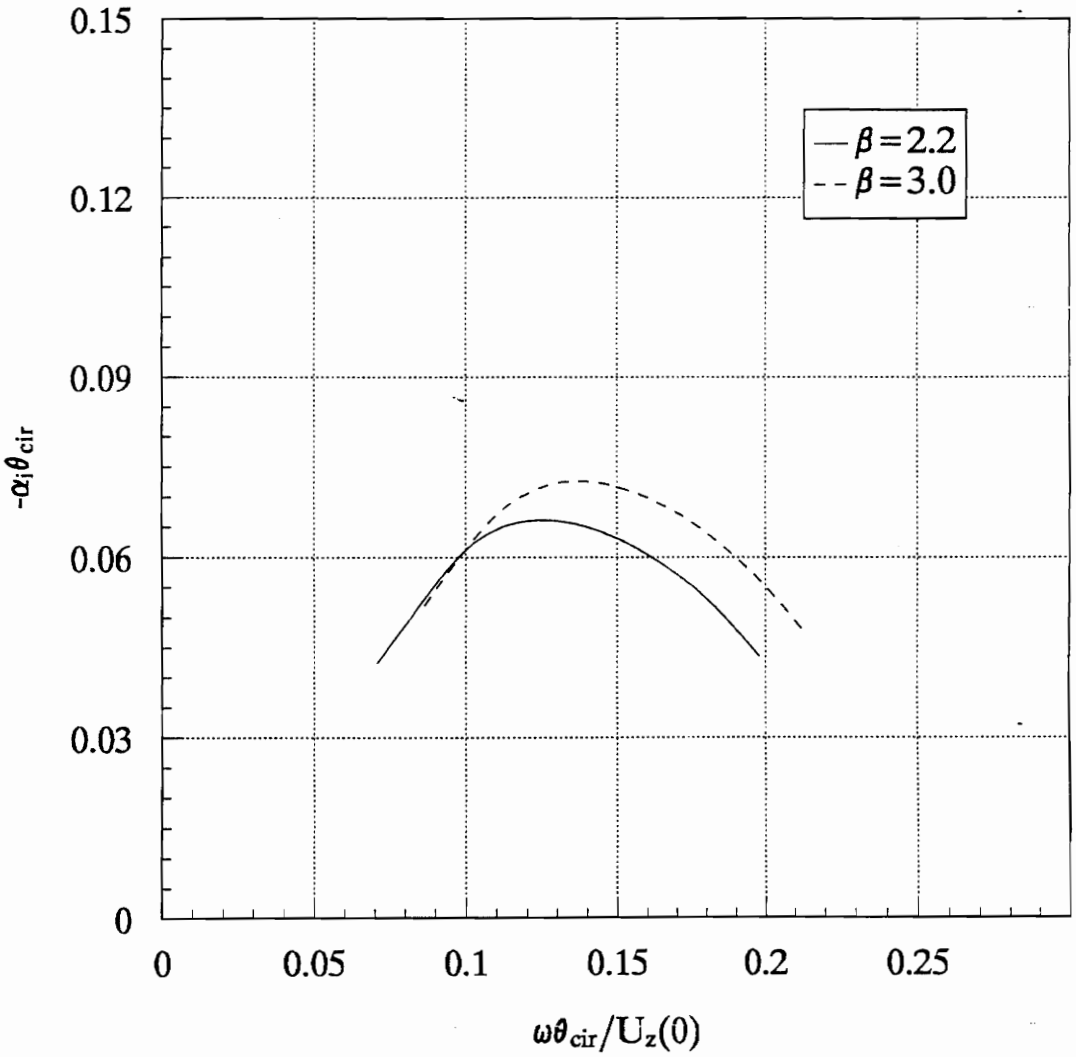

Figure 4.47. The influence of the activation energy on the growth rate of the cosine mode of the $AR = 2$ elliptical jet with uniform momentum thickness.

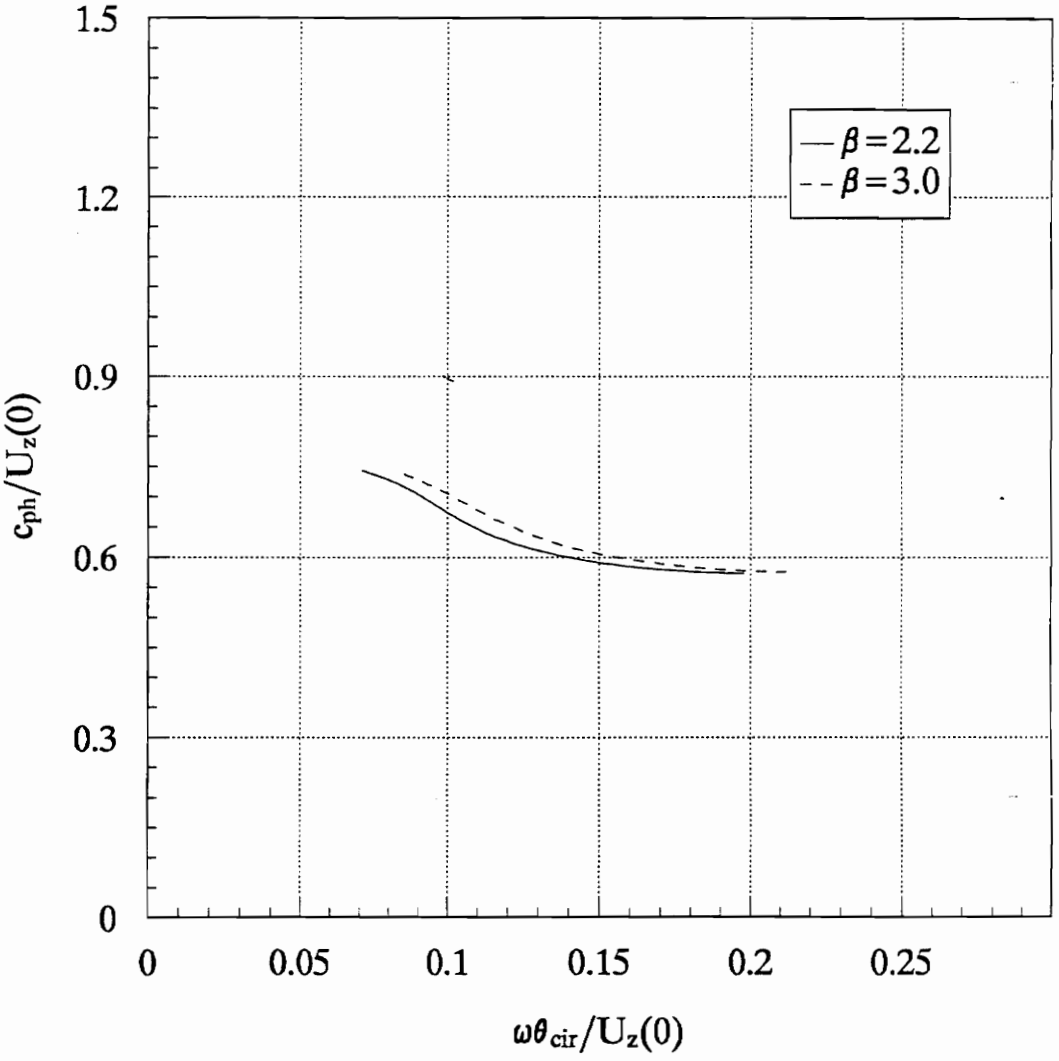

Figure 4.48. The influence of the activation energy on the phase speed of the cosine mode of the $AR = 2$ elliptical jet with uniform momentum thickness.

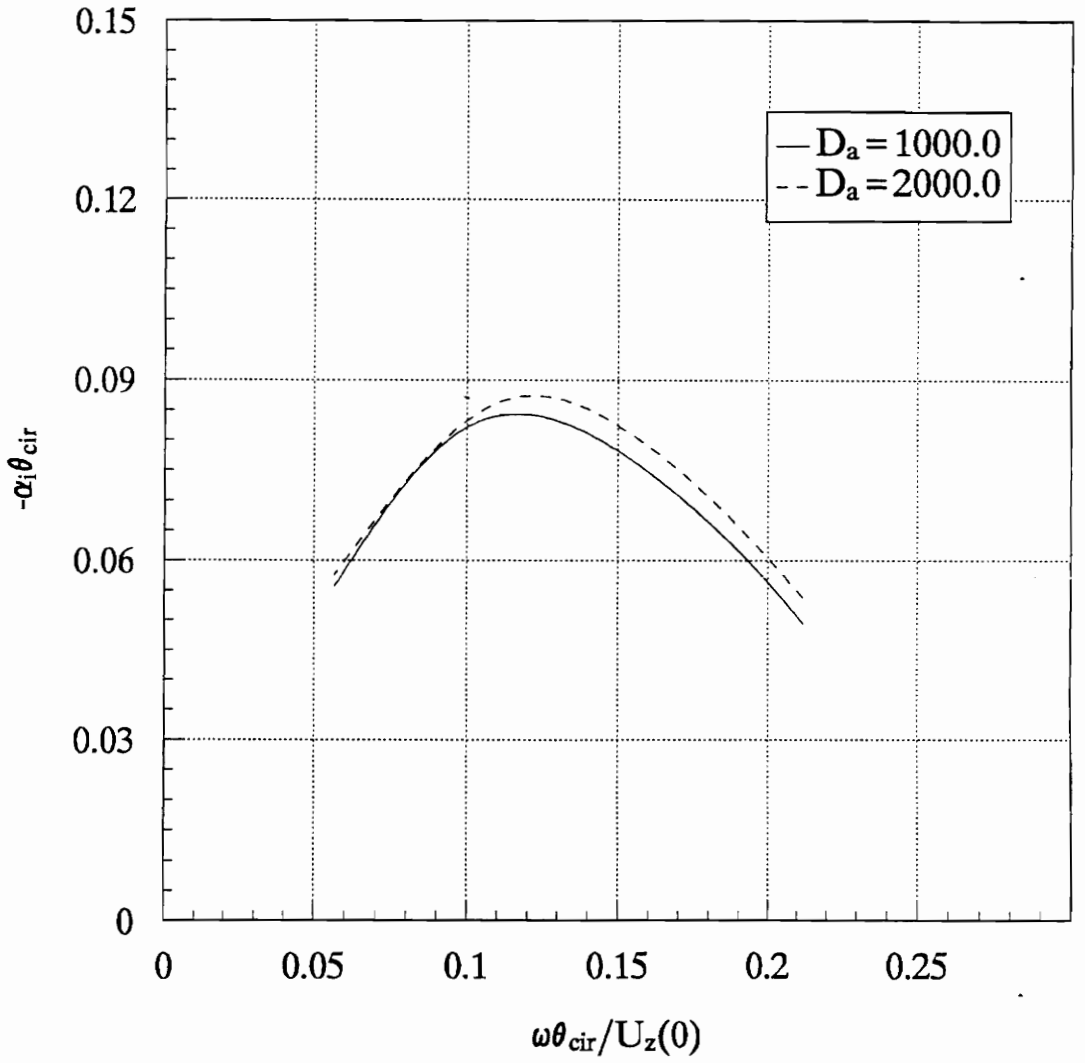

Figure 4.49. The influence of the Damkohler number on the growth rate of the sine mode of the $AR = 2$ elliptical jet with uniform momentum thickness.

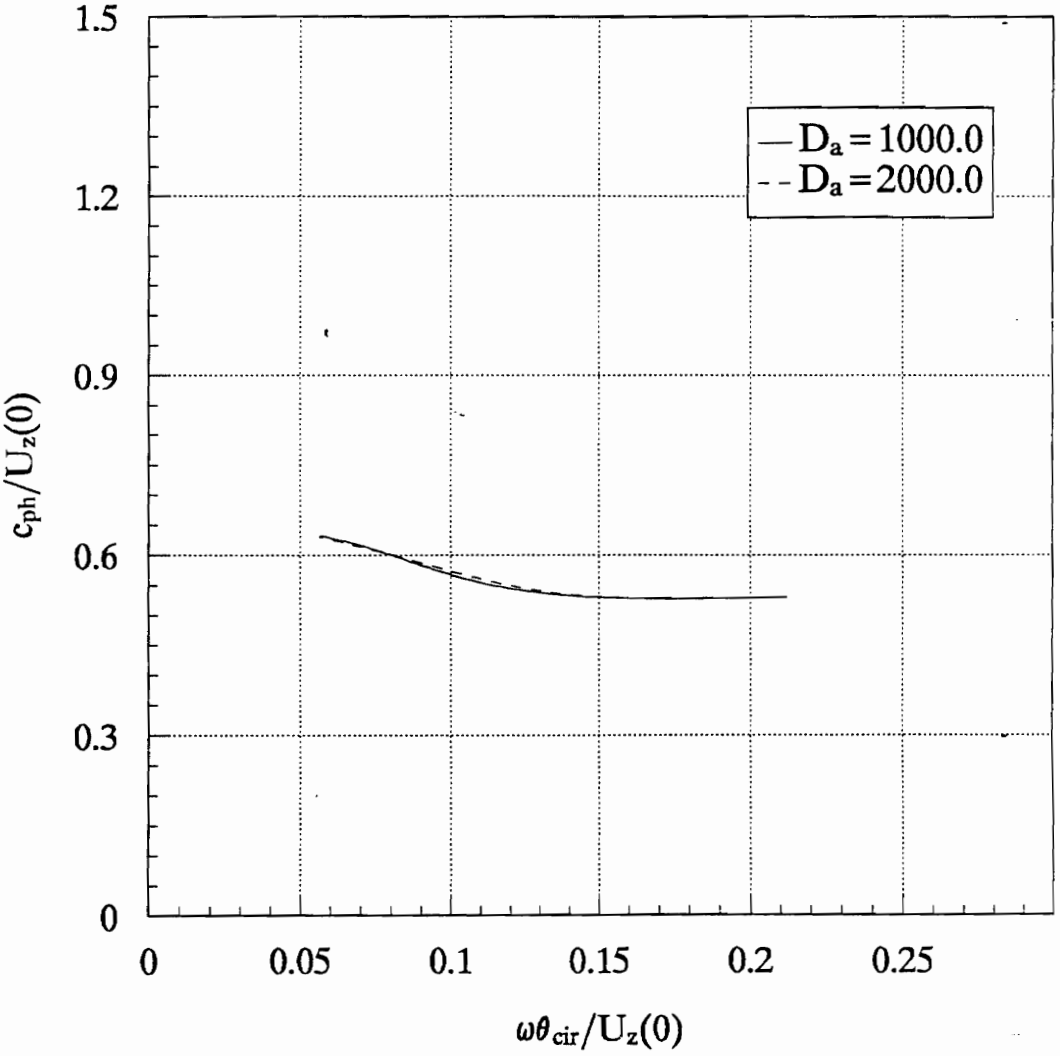

Figure 4.50. The influence of the Damkohler number on the phase speed of the sine mode of the $AR = 2$ elliptical jet with uniform momentum thickness.

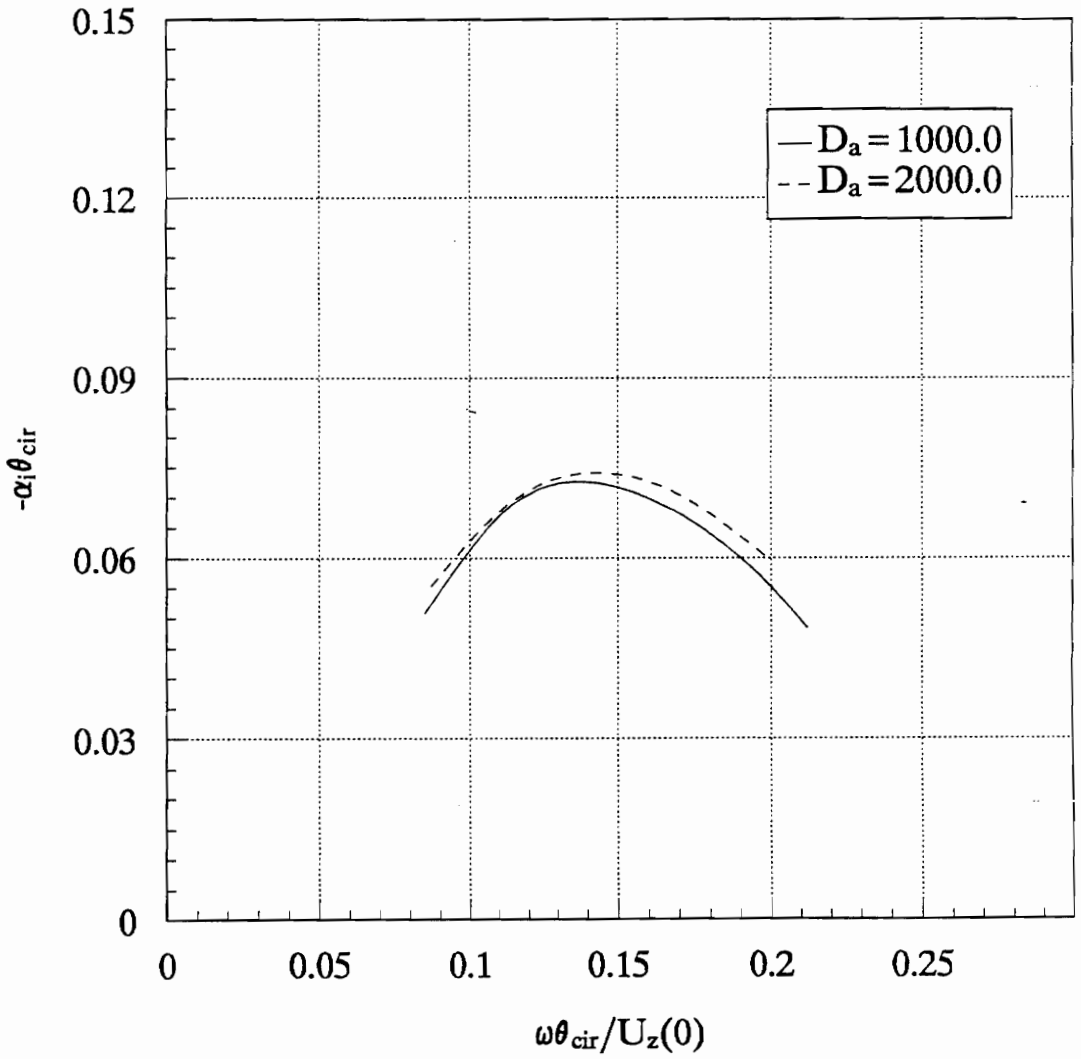

Figure 4.51. The influence of the Damkohler number on the growth rate of the cosine mode of the $AR = 2$ elliptical jet with uniform momentum thickness.

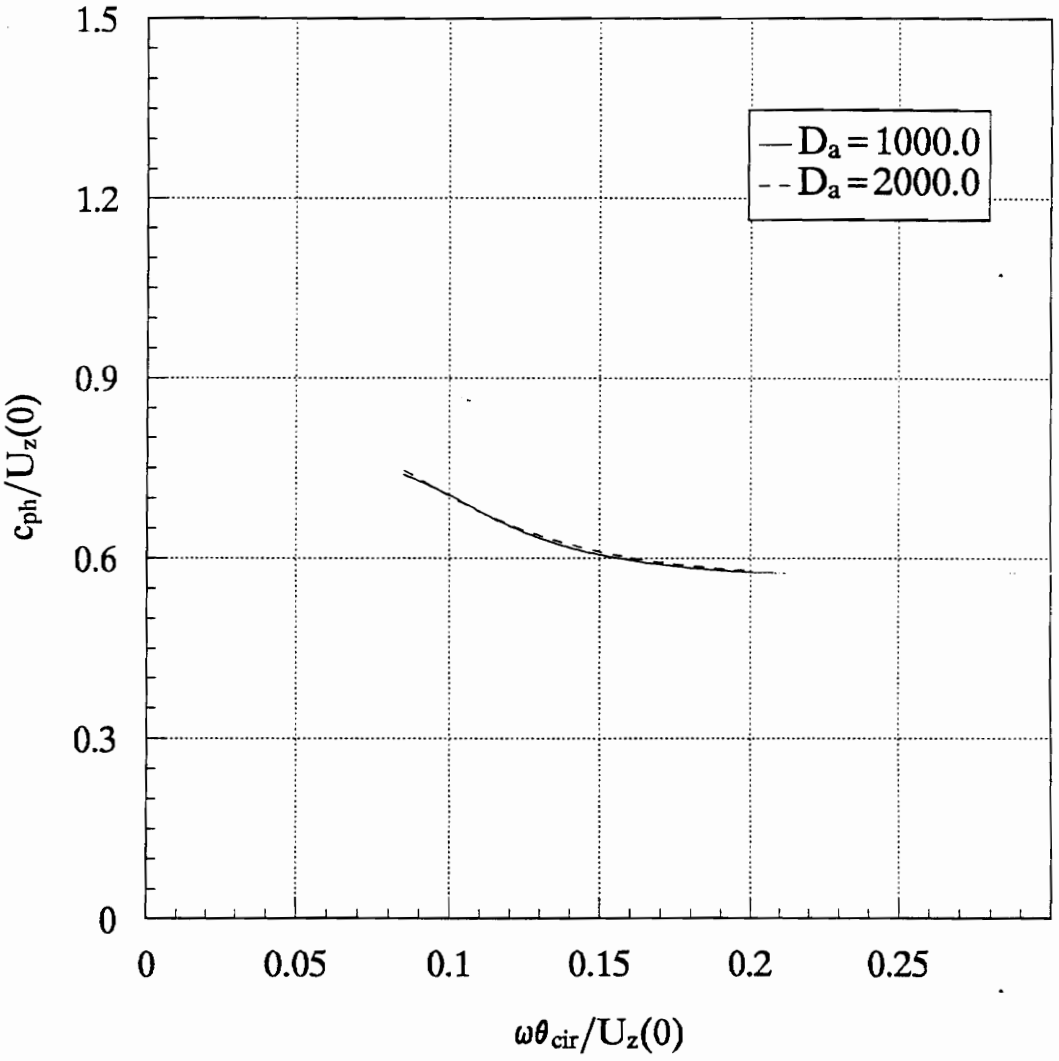

Figure 4.52. The influence of the Damkohler number on the phase speed of the cosine mode of the $AR = 2$ elliptical jet with uniform momentum thickness.

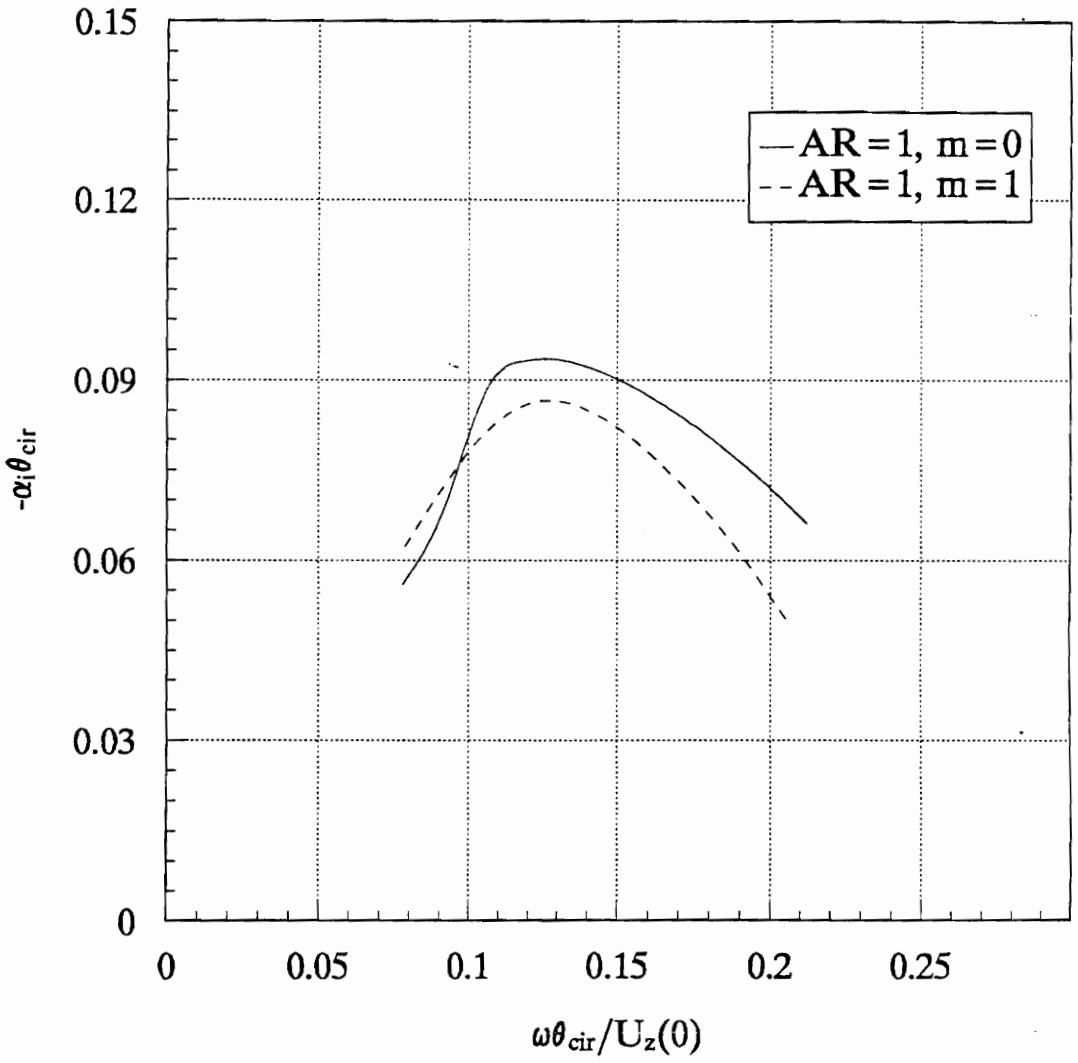

Figure 4.53. The relative size of the growth rates of different modes of the circular jet.

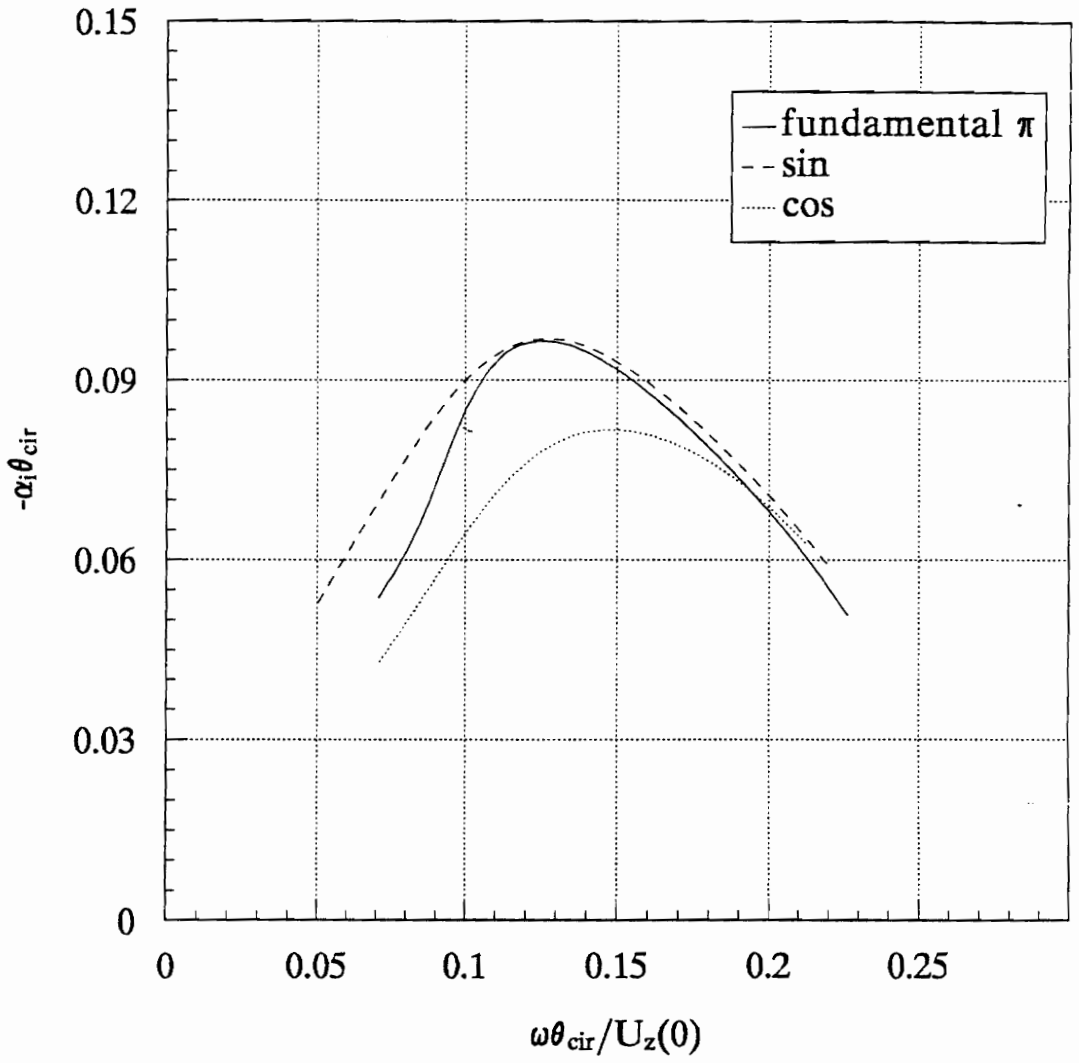

Figure 4.54. The relative size of the growth rates of different modes of the $AR = 2$ elliptical jet.

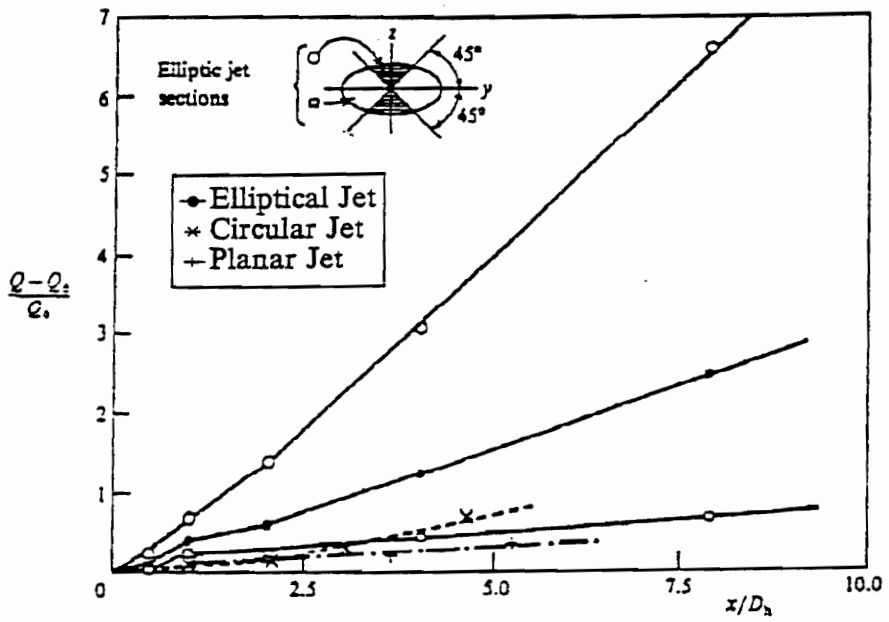

Figure 4.55. The entrainments of the circular jet and $AR = 2$ elliptical jet obtained by Ho and Gutmark.

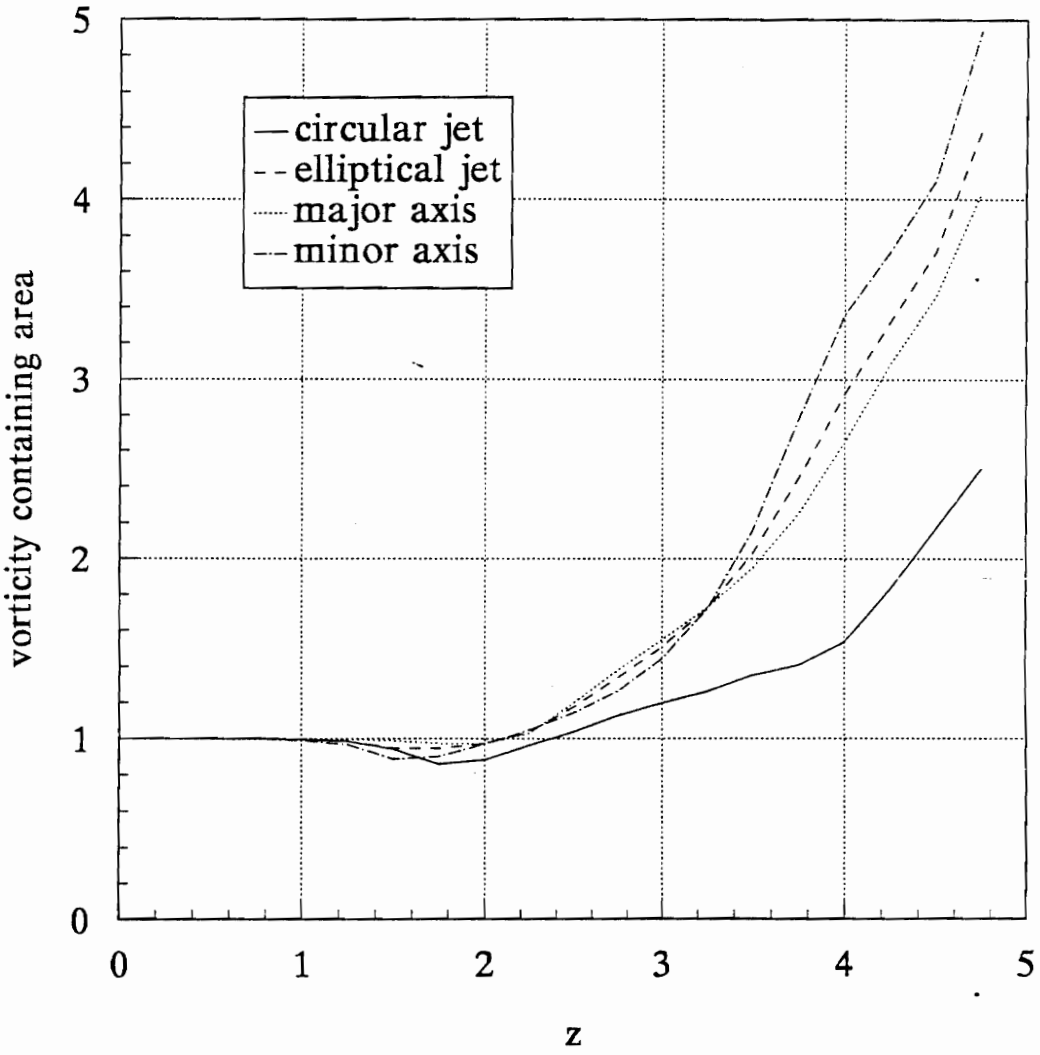

Figure 4.56. The streamwise growth of the vorticity-containing cross-sectional area of the circular jet and the $AR = 2$ elliptical jet.

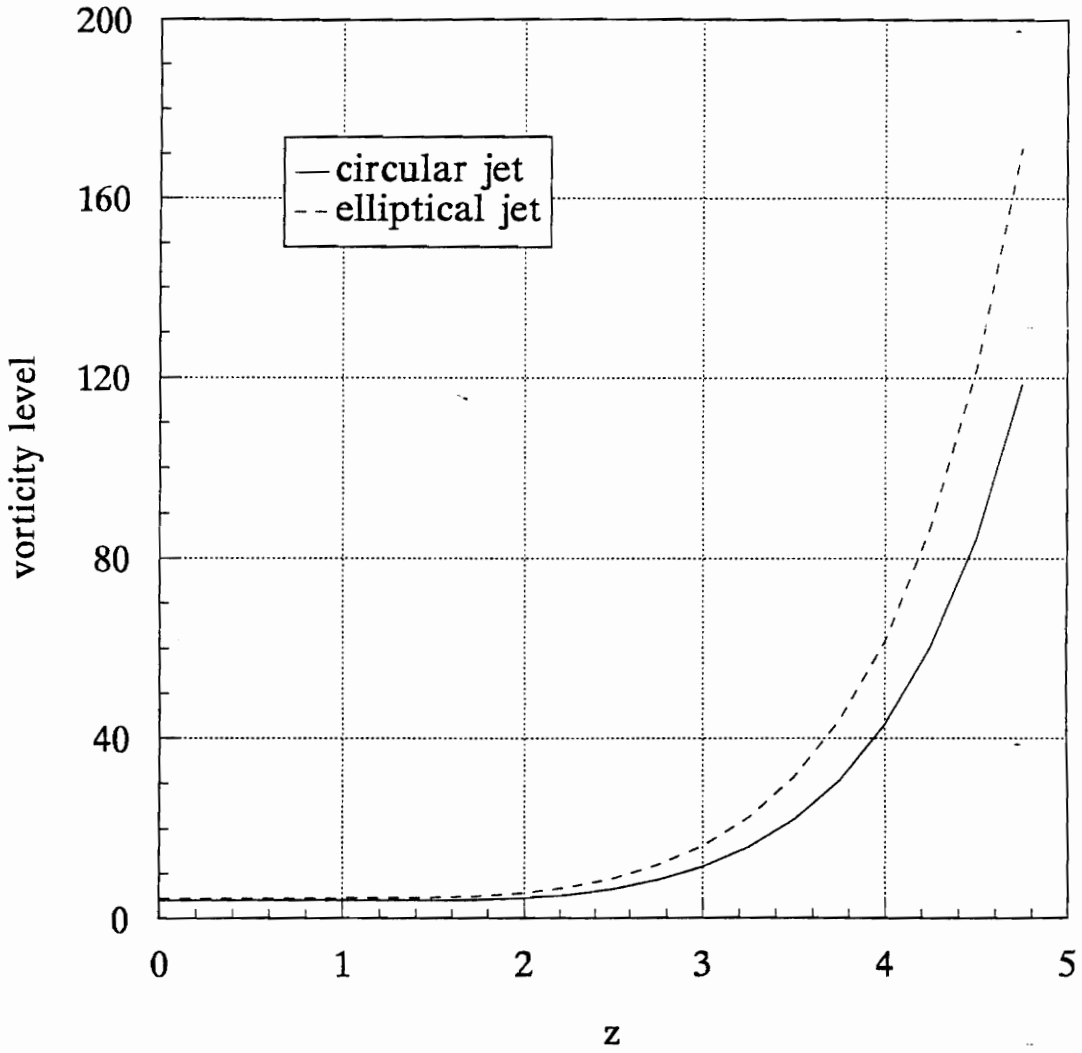

Figure 4.57. The streamwise growth of the integrals of the total vorticity of the circular jet and the $AR = 2$ elliptical jet.

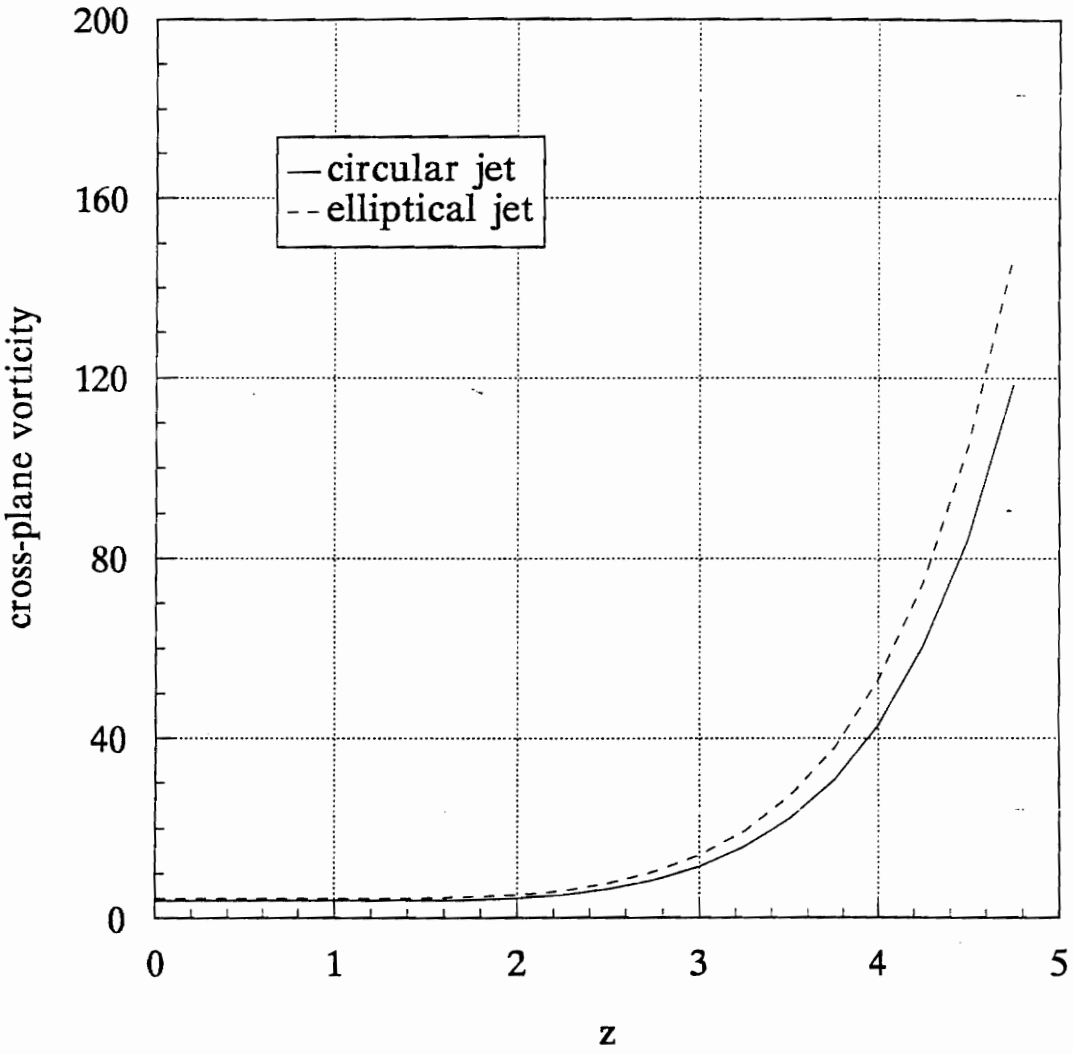

Figure 4.58. The streamwise growth of the cross-plane vorticity of the $AR = 2$ elliptical jet with uniform momentum thickness.

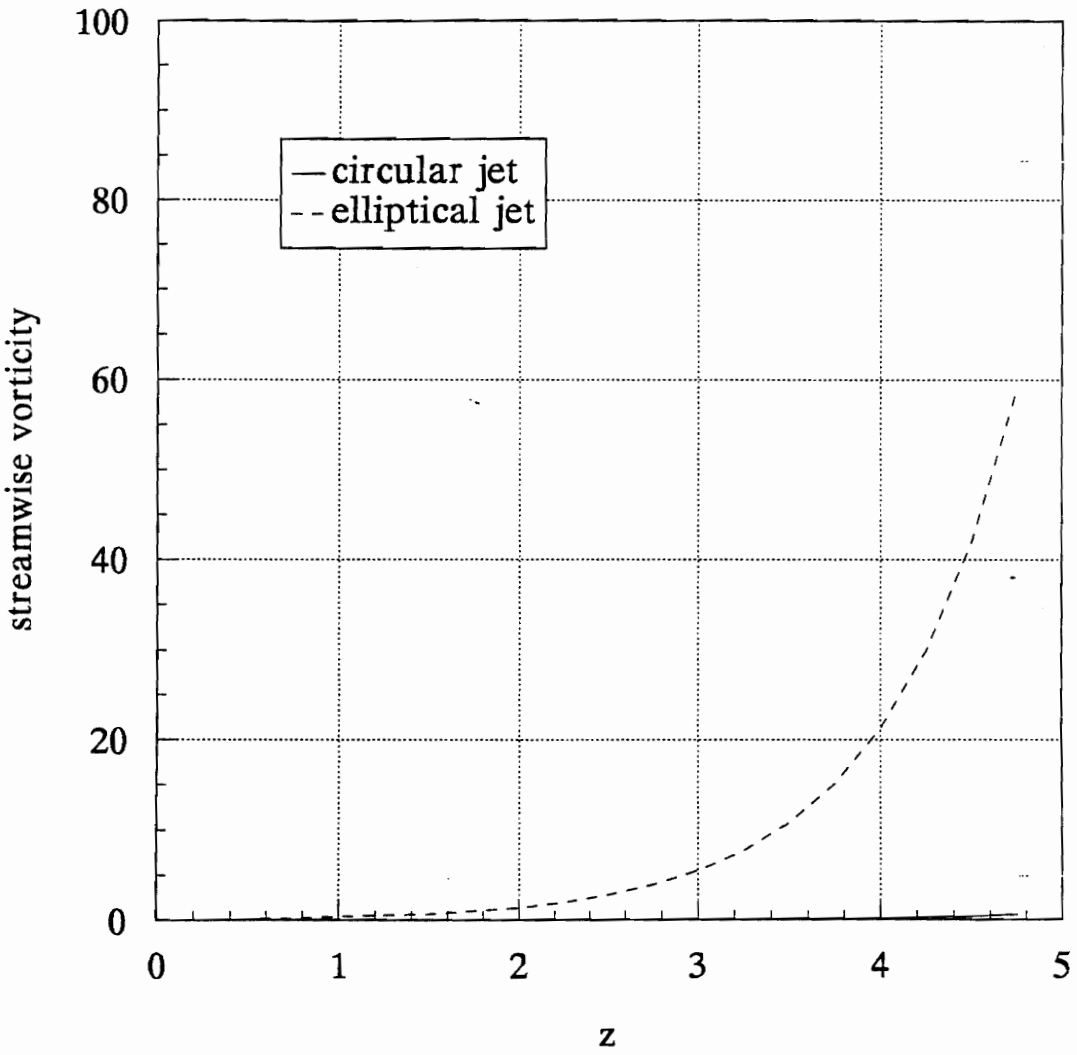

Figure 4.59. The streamwise growth of the streamwise vorticity of the $AR = 2$ elliptical jet with uniform momentum thickness.

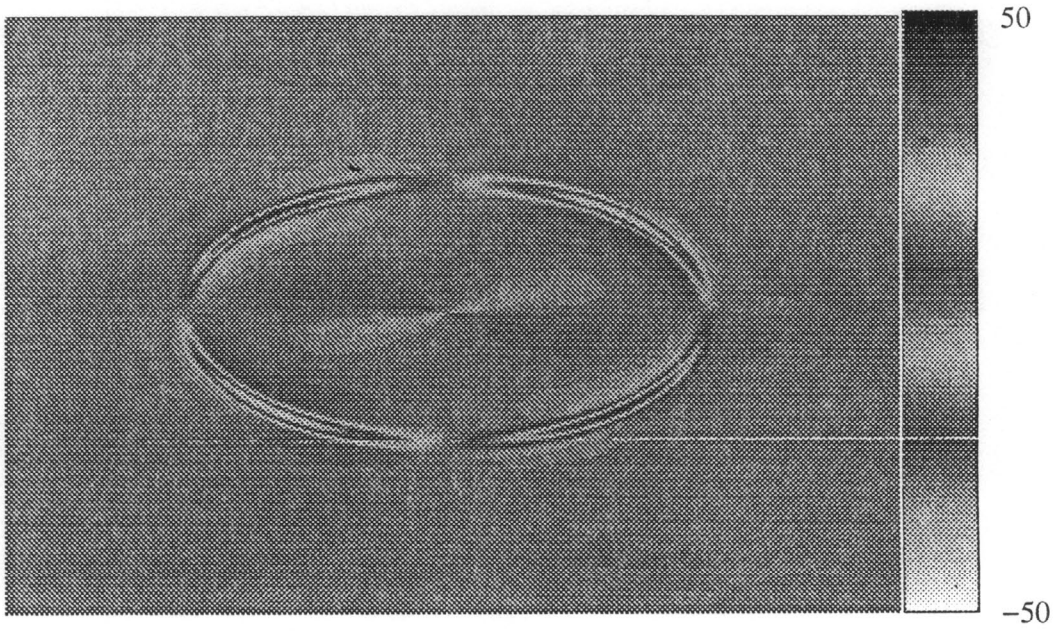

Figure 4.60. The distribution of the streamwise vorticity of the $AR = 2$ elliptical jet two diameters downstream the nozzle exit.

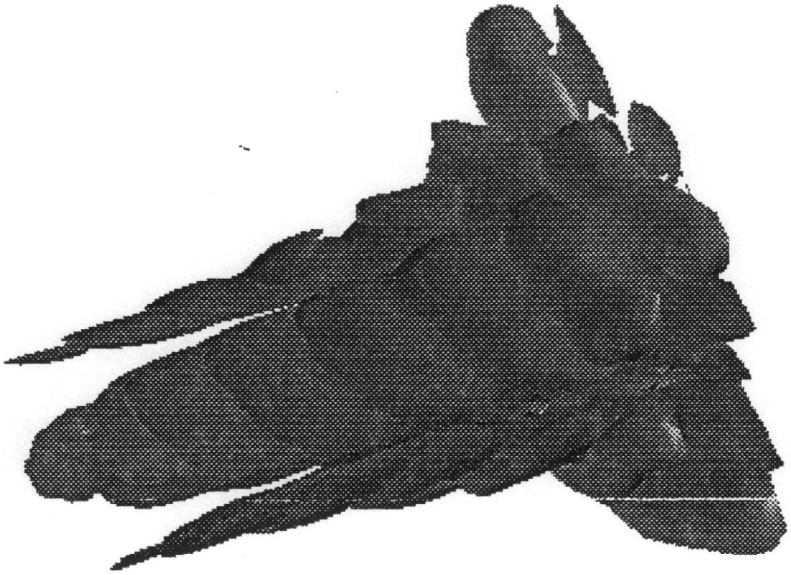

Figure 4.61. The surface of constant streamwise vorticity magnitude of the $AR = 2$ elliptical jet.

Vita

The author was born to Yanwei Huang and Qimei Wu on October 11, 1962 in Chengdu, China. He spent his childhood and received his pre-college education there. In 1978, the author became a student in the University of Science and Technology of China in Hefei, China. In 1982, he obtained a Bachelor of Science in Engineering Thermophysics there. In the same year, he was accepted for graduate study in the Institute of Engineering Thermophysics of Chinese Academy of Sciences in Beijing, China. In the three years that followed, he developed CFD codes for computing the compressible flow and solid particle trajectories in gas turbines. He obtained a Master of Science in Engineering Thermophysics there in 1985. From then to 1987, he was an instructor in the Chengdu University of Science and Technology in Chengdu teaching undergraduate courses. In 1987, he became a computer application engineer in the Chengdu Institute of Computer Application of Chinese Academy of Sciences in Chengdu. In the four years afterwards, he completed many projects in microcomputer and microprocessor applications such as the development of a serial communication software, the hardware and software development of a magnetic strip card reader system, controllers of a three-dimensional CNC lathe with up to seven axes, a smart CRT display device of a poloragraph, and a patented electronic lock with a magnetic strip card reader. In 1991, he began his Ph.D. study in the Mechanical Engineering Department of Virginia Polytechnic Institute and State University and carried out a linear stability analysis of elliptical jet flow with swirl and heat release, and scientific visualization. After his Ph.D.

study, the author will become a research scientist in DynaFlow, Inc. in Columbus, Ohio developing CFD and stability software, and their graphical user interface.